2017

Multi-transit Echo Suppression for Passive Wireless Surface Acoustic Wave Sensors Using 3rd Harmonic Unidirectional Transducers and Walsh-Hadamard-like Reflectors

Luis Manuel Rodriguez Cordoves
University of Central Florida

MULTI-TRANSIT ECHO SUPPRESSION FOR PASSIVE WIRELESS SURFACE ACOUSTIC WAVE SENSORS USING 3RD HARMONIC UNIDIRECTIONAL TRANDUCERS AND WALSH-HADAMARD-LIKE REFLECTORS

by

LUIS MANUEL RODRÍGUEZ CORDOVÉS
B.S.E.E. University of Central Florida, 2004
M.S.E.E. University of Central Florida, 2014

A dissertation submitted in partial fulfillment of the requirements
for the degree of Doctor of Philosophy
in the Department of Electrical Engineering and Computer Science
in the College of Engineering and Computer Science
at the University of Central Florida
Orlando, Florida

Fall Term
2017

Major Professor: Donald C. Malocha

ABSTRACT

A passive wireless surface acoustic wave sensor of a delay-line type is composed of an antenna, a transducer that converts the EM signal into a surface acoustic wave, and a set of acoustic reflectors that reflect the incoming signal back out through the antenna. A cavity forms between the transducer and the reflectors, trapping energy and causing multiple unwanted echoes. The work in this dissertation aims to reduce the unwanted echoes so that only the main transit signal is left—the signal of interest with sensor information.

The contributions of this dissertation include reflective delay-line device response in the form of an infinite impulse response (IIR) filter. This may be used in the future to subtract out unwanted echoes via post-processing. However, this dissertation will use a physical approach to echo suppression by using a unidirectional transducer. Thus a unidirectional transducer is used and also optimized for 3rd harmonic operation. Both the directionality and the coupling of the 3rd harmonic optimized SPUDT are improved over a standard electrode width controlled (EWC) SPUDT.

New type of reflectors for the reflective delay-line device are also presented. These use BPSK type coding, similar to that of the Walsh-Hadamard codes. Two types are presented, variable reflectivity and variable chip-lengths. The COM model is used to simulate devices and compare the predicted echo suppression level to that of fabricated devices. Finally, a device is mounted on a tunable antenna and the echo is suppressed on a wireless operating device.

ACKNOWLEDGEMENTS

I would like to first and foremost thank the Creator God, for creation and for being a personal God, my source of strength in life, and during this endeavor. Always providing a way, getting me past all of the obstacles and challenges that were encountered.

I would like to thank my family, my grandparents that were with me when this journey stared, but are no longer with me on this side of heaven. I'm very thankful for my mom especially, without her sacrifice, supporting role and encouragement this would not have been possible. The same goes for my dad. My brothers, my cousins, my uncle and aunt, all of my family has been a source of encouragement. I also thank my close friends from high school for their help in getting me through this. Special thanks also to Rene Perez, a friend of the family, and also my confidant regarding the research progress and challenges, always faithful in praying for me.

I thank Professor Don Malocha for being a source of instruction, encouragement, advice, help, and provision. He has not only provided me with an education and a life skill, but also with a really good working environment, with much grace and freedom balanced in with the responsibilities. I have learned much from him and through him. He has been there for me in difficult times. He has been like family, to me and many others, and has served his students with much sacrifice and endurance, I will be forever grateful for all that he has done. I have been helped and shaped also by the many students of our research group, past and present. I have been helped by all of them at some point or another, and I am forever grateful for that. Special acknowledgement to Brian Fisher, who welcomed me into his office when I 1st arrived, and not only shared his office with me for many years, but also shared much knowledge, giving me advice and lending me a hand whenever I needed it. Special thanks to Yuske Satoh for working with me

during my 1st year in the PhD program, before having to return to Japan. We had many good times together at RUF. I also thank Dr. Arthur Weeks for helping me through the later part of my PhD studies, he has been a blessing to me, I am very grateful for him. I'm also very grateful for the McKnight Doctoral Fellowship program for providing not only greatly needed funding, but also a caring community. Special thanks to Charles Jackson for being there for me in crucial times, and always very welcoming, as were many of the folks that were part of McKnight. I'll always cherish their amazingly inspiring and uplifting annual conferences.

There are other professors, like Dr. Sundaram, Dr. Gonzalez and Dr. Kasparis, who have encouraged me and helped me. I thank all of my past professors and teachers, including my 3rd and 4th grade ESOL teachers for being the most caring, and Mr. Miramonte in 12th grade English for being the coolest. I also thank all of my Sunday School teachers, and all of the brothers in the Faith, special thanks to Billy Randolph for the period of time we walked together in the first half of the PhD journey. Special thanks to my friends and neighbors Chris and Paul Papke for watching football and other sports with me, and going fishing to help me decompress after struggling with the books or research. Special thanks also to Jason Reinhart for many mountain biking trips, Sebring race campouts, encouragement and words of wisdom. Also thanks to Mark Lamothe for his friendship, hospitality, encouragement, and freediving trips. Many of the UCF staff, Clara from the cleaning staff, Diana Camerino, Giji Skaria, Sameer Nayfeh, Heather Houser, have also been great sources of encouragement to me, I am very thankful for them. I'd like to also thank Ed Dein for helping me and instructing me in the cleanroom in the early days. I am very grateful for many other students that I've encountered, and for many people I've met along the way, staff and friends, who at some point or another have been a real blessing to me. Thank you all.

TABLE OF CONTENTS

LIST OF FIGURES

LIST OF TABLES

CHAPTER 1:
INTRODUCTION

Surface acoustic wave (SAW) devices have been used for enabling technologies in the 20th century and are still pushing the limits of today. These technologies include radar systems, television and cellular phones. SAW devices are based on crystals that have a special property called piezoelectricity. Piezoelectricity comes about by asymmetry in the crystal lattice. A simplified model that illustrates the phenomenon is shown in Figure 1-1, taken from Figure 8.1 and 8.2 of Auld's *Acoustic Fields and Waves in Solids* [1].

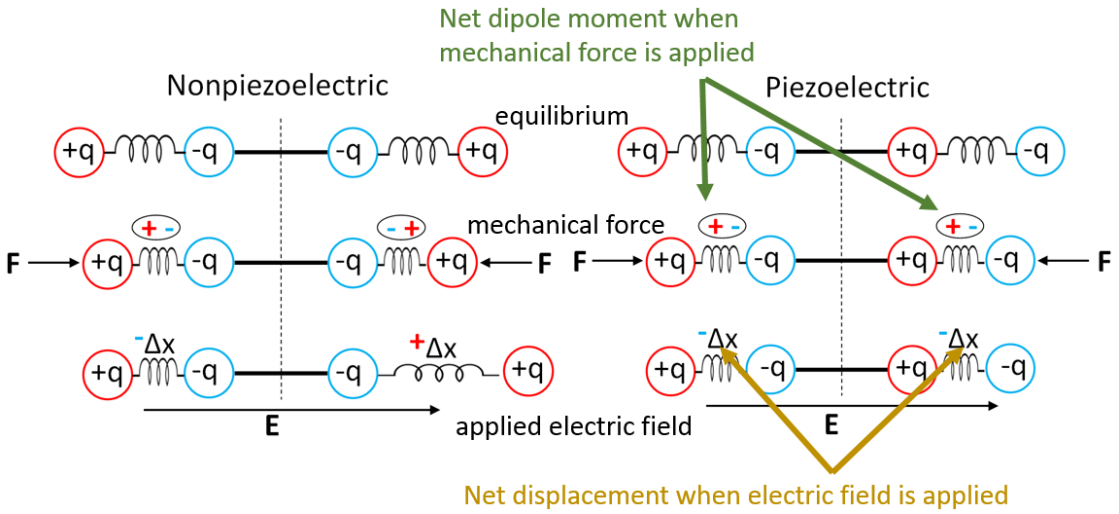

Figure 1-1. Simplified 1-dimentional model of an asymmetric crystal lattice that would produce piezoelectricity. The charges on the right side are attached to springs in a fashion that produces a net dipole moment when a mechanical force is applied, and a net displacement when an electric field is applied [1].

Piezoelectricity produces an electric charge when the material is deformed, and vice versa; when a wave is launched, an electric field is carried along with the mechanical wave. The devices pertaining to this dissertation make use of a wave that is trapped on the surface of the crystal. The velocity is about 4 orders of magnitude slower than an electromagnetic wave so many wavelengths are contained within a relatively small distance. This is a particular advantage for sensor

applications because there are many wavelengths over which the wave can interact with the environment. Many types of SAW sensors have been pioneered at the Consortium for Applied Acousto-electronic Technology (CAAT) at UCF (please see chapter 2 for references). Sensors have been made for gas sensing, measuring strain, measuring temperature, measuring the magnetic field of the earth. Another beauty of this technology is that these sensors can operate without a battery, thus are used as passive wireless sensors. This is of particular interest for harsh environments or places where it's impossible to gain access to change a battery. The aerospace and the automobile industry also have many potential applications. The work of this dissertation supports this emergent field of sensor technology, with the hope that the market demand will see SAW sensors as a viable solution.

A general overview of different sensing approaches and the different types of sensors is given in chapter 2. A discussion of the orthogonal frequency coded sensor and the general idea behind the interrogation scheme is given. For more in-depth descriptions of the sensor acquisition scheme, the references can be consulted. Also presented is a practical way of estimating the expected sensor precision by knowing the path loss of the wireless environment. Some of the current challenges are also mentioned so that informed decisions can be made by anyone aiming to continue development of this technology. Finally the main subject, the double transit echo, is presented. The rest of the chapters will contribute to finally building a device and physically demonstrating an optimized echo suppression level in a wireless SAW sensor.

Chapter 3 shows the P-matrix representation of the device response. It demonstrates how the analytical representation of the individual echoes can be calculated. From a power series representation of the device response, the individual echoes are seen. An echo transfer function is

found, and upon equating this to zero, the condition for echo suppression is found. It matches the previous result obtained from the original work, which was geared towards triple transit echo suppression in filters. From the original work on echo suppression, it was known that a directional transducer was more efficient at suppressing the multi-transit echoes that the bidirectional type. After a new SPUDT configuration is introduced, which is optimized for 3rd harmonic operation, chapter 4 is dedicated to showing coupling-of-modes (COM) model simulations. Different filters are built, 4f0 bidirectional transducer filters, the standard electrode width controlled (EWC) unidirectional transducer based filters, and 3rd harmonic optimized filters. The 1st and 3rd harmonic measured response is matched with the COM model and compared, with simulation parameters given. The device data will be attached as part of this electronic dissertation, and thus the interested reader can reproduce the simulation results. Details on how to construct the coupling-of-modes equations are given in Appendix F.

Chapter 5 introduces a new type of SAW reflector. It was difficult to make a 4-chip OFC reflector device within the 915MHz ISM bandwidth without significantly decreasing reflectivity. This leads to exploring the use BPSK type reflectors, with coding similar to that of the Walsh-Hadamard codes. Two types are presented, variable reflectivity and variable chip-lengths. What started as an effort at pulse shaping also resulted in finding new sets of orthogonal SAW reflectors. The COM model is used to simulate devices and compare to fabricated devices. In chapter 6 a device is mounted on a tunable antenna and the echo is suppressed on a wireless operating device.

CHAPTER 2:
BACKGROUND

This chapter attempts to familiarize a reader with interest on passive sensors, but with little acoustic sensor background, on passive SAW sensor systems—specifically the sensing platform developed at UCF over the last decade or so. Since several system prototypes and different types of sensors have been demonstrated, it's natural that industry will begin looking at the advantages of incorporating this technology. If a company, for example, needs to add a passive SAW sensor group into their R&D effort, hopefully this background will help give a brief but technical overview, helping them decide if this is something worth pursuing.

A general overview of different sensing approaches and the different types of sensors is given. A discussion of the orthogonal frequency coded sensor and the general idea behind the interrogation scheme is given. For more in-depth descriptions of the sensor acquisition scheme, the references can be consulted. Also presented is a practical way of estimating the expected sensor precision by knowing the path loss of the wireless environment. Some of the current challenges are also mentioned so that informed decisions can be made by anyone aiming to continue development of this technology. Finally, the main subject, the double transit echo, is presented. The rest of the chapters will contribute to finally building a device and physically demonstrating an optimized echo suppression level in a wireless SAW sensor.

A chapter summary is provided for each chapter. For this chapter and chapter 3 it's in the form of a list of important points or remarks, for a quick review of the matter. The points are listed in the order of appearance in the chapter, and serves as a kind of index.

2.1 Passive Wireless SAW Sensor Embodiments

The two main types of passive wireless SAW sensor topologies are the resonant and delay line type in a reflective 1-port configuration. The 1-port SAW resonator is composed of a transducer with long Bragg reflectors on either side.

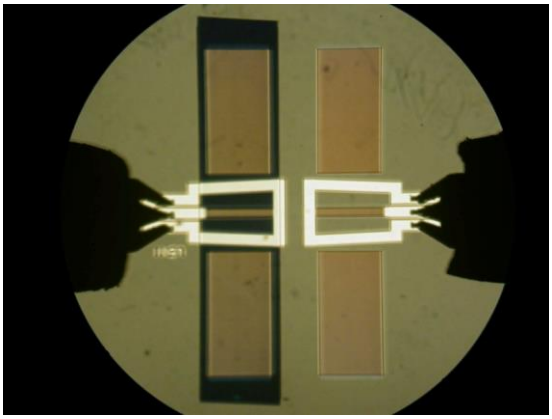

Figure 2-1. One-port SAW resonator. Long Bragg reflectors on either side of the IDT

The sensing mechanism for the resonator approach is based on frequency shift. The wave velocity changes under the reflectors or the whole propagation path, depending what part of the device is being influenced. The electrode material itself could be sensitive to some physical quantity. Magnetostriction, for example, involves a change of stress in a material due to changes in a present magnetic field. A metal like Cobalt would have this property [2]. In this case the surface wave under the reflectors and IDT would change velocity and result in a frequency shift of the resonant frequency. A resonant frequency shift can also be obtained if a gas sensing film is placed on top of the reflectors, causing a perturbation of the surface wave in this region [3]. When the measurand is temperature, a crystal that changes velocity due to temperature change is normally used. The rate of change of frequency versus change of temperature is quite linear for popular crystals such as lithium niobate. Thus the slope of the line in this relationship is given the name temperature

coefficient of frequency (TCF) or temperature coefficient of delay (TCD) [4]. The resonator in figure 2-1 is actually part of an experiment to test if the SiO2 film sputtered on top of the left resonator can temperature compensated.

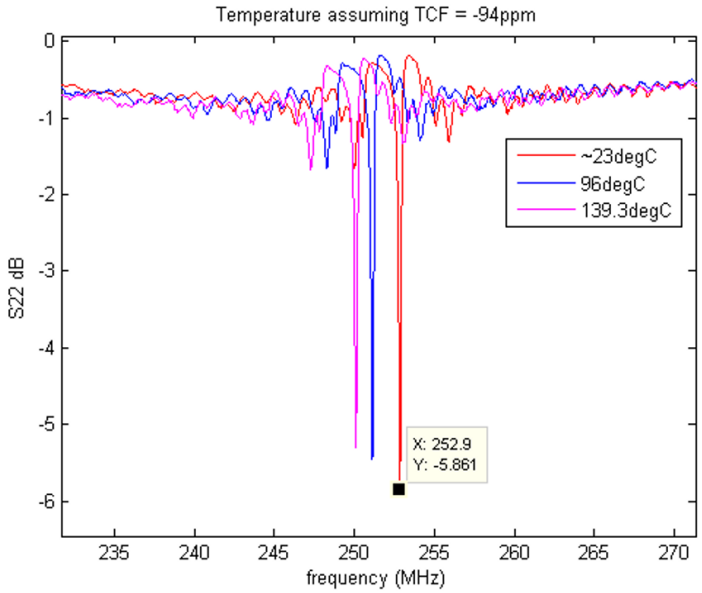

Figure 2-2. Magnitude of reflection coefficient for reference resonator on the right in Figure 1-1 at temperatures of 23^{0}C, 96^{0}C, and 139^{0}C.

Figure 2-2 shows the magnitude of the reflection coefficient for the reference resonator in figure 2-1. The S-parameter measurement is made at 3 different temperatures over a range of 115 °C, showing how the resonant frequency changes. In a passive wireless multi-sensor system these types of sensors require their own frequency range of operation. For the Y-Z lithium niobate based device of figure 2-2, the frequency range required for a 100 °C temperature range would be approximately 3-4MHz.

The other main type of passive wireless SAW sensor topology is the delay line configuration. It usually consists of a somewhat wideband IDT and a propagation path delay followed by acoustic reflectors. By the time the IDT ringing dies down substantially, the outgoing

surface wave that bounces off the reflectors, returns to the IDT and out of the electrical port. The sensing information is carried by the reflector response.

The delay line configuration lends itself to a greater variety of sensing approaches. With the delay line type of sensor, one can measure amplitude, time delay, or frequency shift of the reflected wave. When the sensing mechanism affects amplitude, a reference channel is usually used. The left device in figure 2-3 operates as a temperature sensor based on amplitude.

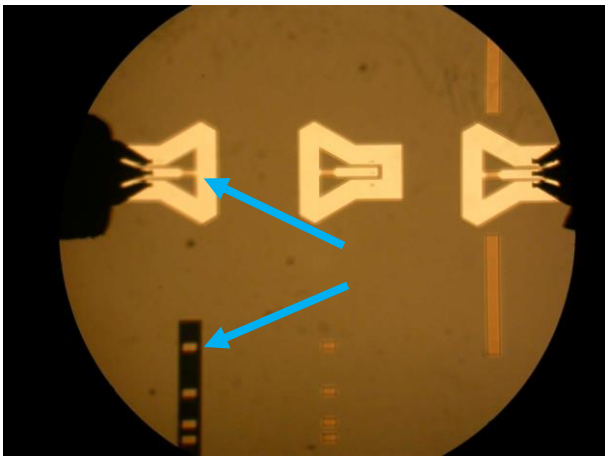

Figure 2-3. Reflective delay line device with top arrow pointing to IDT being probed. Bottom arrow is pointing to a set of reflectors covered with an SiO2 film. The device has an identical set of uncovered reference reflectors on the other side of the IDT. The reference reflectors are set at twice the distance and are outside the field of view of the microscope but would be similar to the uncovered reflectors of the adjacent middle device.

The top arrow points to the IDT and the bottom arrow points to a set of reflectors covered by a film of SiO2 3500 angstroms thick. This device operates at 915MHz center frequency. The time domain response at three different temperatures is shown in figure 2-4.

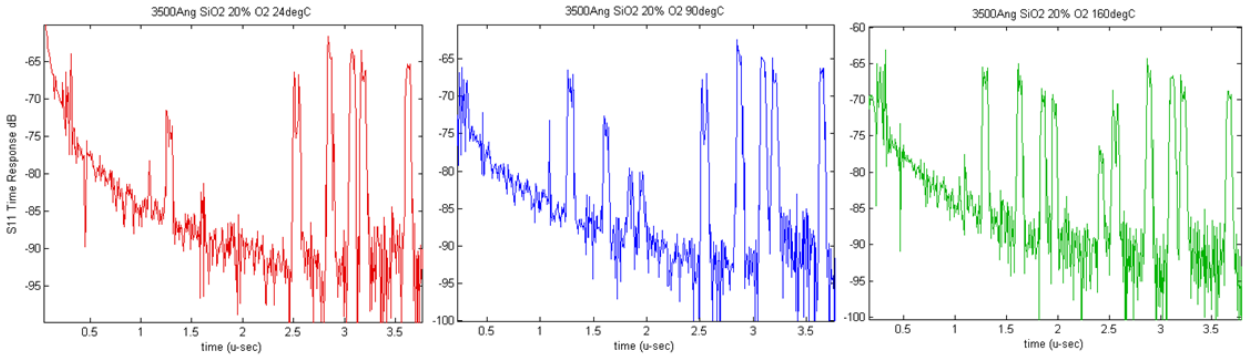

Figure 2-4. Time domain response of device in fig. 2-3 at three temperatures—24^{0}C, 90^{0}C, and 160^{0}C. The amplitude of the SiO2 covered reflectors (1st 5 pulses) increases with increasing temperature.

This device was actually part of an experiment in the effort to temperature compensate lithium niobate with SiO2, which has a TCF of an opposite sign to Y-Z lithium niobate. Unfortunately this particular film didn't temperature compensate, but it had the interesting property of decreasing propagation loss as temperature increased. If this were to be implemented as an actual temperature sensor, it would probably be better to place the film in the middle of the path so that each reflector signal would be attenuated the same amount. This device has a set of 5 reflectors on each side of the IDT. The side covered by the SiO2 film has a fifth reflector that is cut off from the microscope picture but can be seen on the time domain plots. The reference reflector bank on the other side is not shown on the microscope picture but can be seen in the time domain from 2.5 to 4usec. The downside to amplitude change is that low amplitude comes with a lower signal to noise ratio, and subsequently less precise measurement readout of the sensor. It is usually more practical to use amplitude change in an on-off type sensor, where a significant amplitude change identifies the presence of something, or that an event has occurred. Fisher used the amplitude approach to make a hydrogen gas sensor [5], cryogenic liquid level sensor [6], and a Reed switch closure sensor [7]. A sensor with a delay line measurement approach could also use a sensing film in the middle of the propagation path. Perhaps the presence of a gas or of a pathogen would cause a stiffness

change or a mass loading change in the film that would in turn cause a measurable delay because of the velocity change.

It is also possible to use two IDTs separated by an acoustic delay with both connected to the same electrical port. The incoming energy would split and go into each transducer and out the other while recombining at the electrical port. There are some downsides to this approach, like bulk waves which are easier to pick up by an IDT but not that well reflected by reflectors, so the time domain looks messier for a 2-IDT 1-port device. In a passive wireless multi-sensor system where there can be a lot of variation in signal level from one sensor to another because of free space EM path loss. There is a need to keep the reflector response/sensor signal separate from the contamination of spurious signals, like unwanted echoes—the main topic of this work and to be explained in detail in the upcoming sections.

Lastly to mention in this section is that the delay line type SAW sensor, just like the resonant type, can operate by frequency shift. Unlike the resonant type where a single point or only a few points in the reflected frequency spectrum are tracked, the reflective delay line type has an associated bandwidth. Instead of a single frequency, the shift in frequency of a whole bandwidth is tracked. This can be done with a simple center-of-mass tracking of the sensor signal spectrum, but a matched filter correlation approach is preferred because it can provide an improvement in SNR as well as provide coding for identification and some level of orthogonality [7]. The delay line based passive wireless sensor system is the choice sensor type for development by the CAAT group at UCF; particularly the Orthogonal Frequency Coded (OFC) passive wireless SAW sensor approach and variations [8-15]. It is quite versatile in being able to

be tailored for implementation in various applications and scenarios. It also does a good job in being able to resist jamming and fading caused by multipath interference.

2.2 OFC Coded Reflectors

An orthogonal frequency coded (OFC) SAW sensor configuration will look as follows:

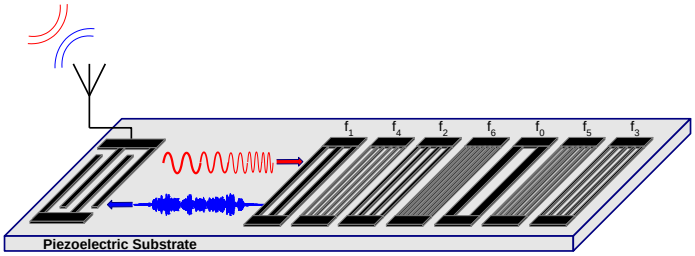

(a)

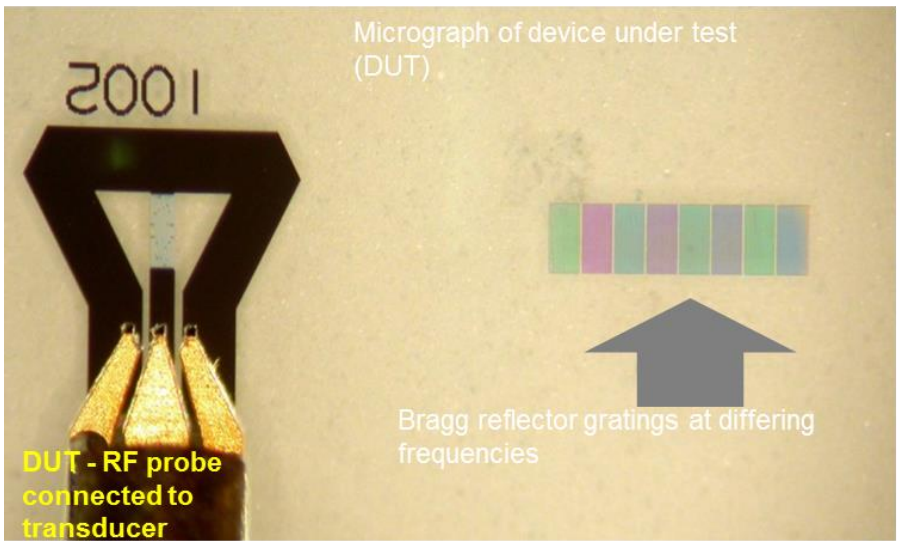

(b)

Figure 2-5. Example of a single track OFC device. The schematic representation (a) shows a wideband uniform IDT followed by a set of 7 Bragg reflectors. A built device (b) shows an apodized transducer and a set of 8 OFC reflectors diffracting different colors of light.

A wideband IDT, a propagation path delay, and a set of OFC coded reflectors. This name is given because each reflector, or chip (a communications term, sequence of chips making up a bit), is a

Bragg reflector with a special center frequency. Consider a time limited, nonzero time function defined in equation 2-1 [16]:

$$h(t) = \sum_{n=0}^{N} a_n \cdot \phi_n(t), \qquad |t| \le \frac{\tau}{2}$$

$$= 0, \qquad |t| \ge \frac{\tau}{2} \qquad \text{,where} \quad \phi_n(t) = \cos\left(\frac{n\pi t}{\tau}\right) \tag{2-1}$$

The function $\phi_n(t)$ represents a complete orthogonal basis set with real coefficients a_n. The members of the basis set are orthogonal over the given time interval if

$$\int_{\frac{-\tau}{2}}^{\frac{\tau}{2}} \phi_n(t) \cdot \phi_m(t) dt \quad = \quad K_n \quad , n = m \qquad \text{,where } K_n = constant$$

$$= \quad 0 \quad \text{, otherwise} \tag{2-2}$$

Given the basis set and constraints, $h(t)$ can take the forms

$$h1(t) = \sum_{n=0}^{N} a_n \cdot \cos\left(\frac{2n\pi t}{\tau}\right) \cdot \frac{rect(t)}{\tau} \quad and \tag{2-3}$$

$$h2(t) \ = \sum_{n=0}^{N} b_n \cdot \cos\left(\frac{(2m+1)\pi t}{\tau}\right) \cdot \frac{rect(t)}{\tau} \tag{2-4}$$

Each cosine term in $h1(t)$ and $h2(t)$ represents a time-gated sinusoid whose local center frequencies are given by

$$f_n = \frac{n}{\tau} \quad and \quad f_m = \frac{2m+1}{2\tau} \tag{2-5}$$

In the frequency domain, the basis terms $h1(t)$ and $h2(t)$ are transformed as Sampling or sin(x)/x functions with null bandwidth of $2/\tau$ and 3dB bandwidth of $1/\tau$.

The response of each Bragg reflector on the device approximates a truncated cosine from the family of truncated cosines from equation 2-4. An example of basis functions from equation

2-4 is shown in figure 2-6a, where each basis function is offset by τ to give a stepped chirp signal. The frequency domain response of basis functions from $h2(t)$ with m = 66, 67, 68, 69, 70 is shown in figure 2-6b.

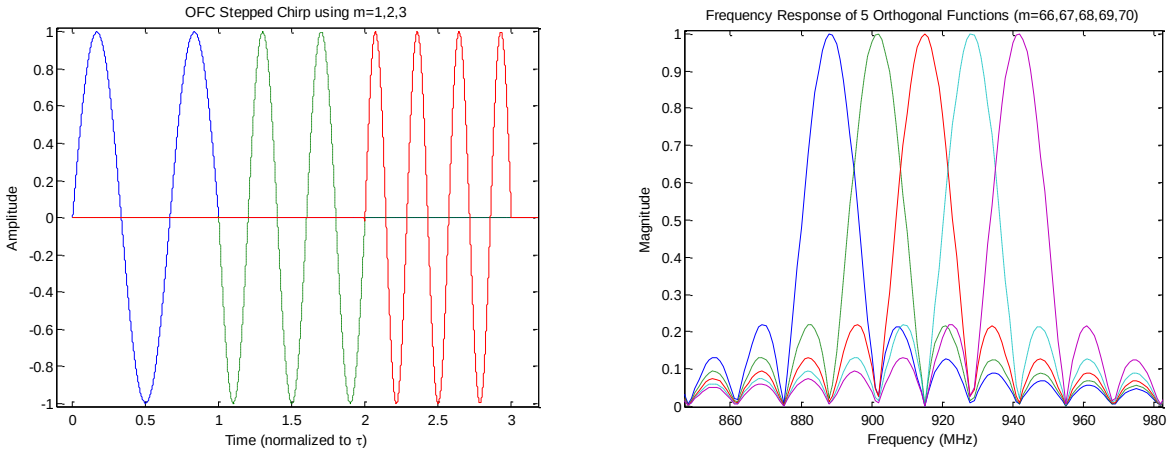

(a) (b)

Figure 2-6. Stepped chirp composed of time-delayed functions from $h2(t)$; m=1,2,3 (a). Frequency response of basis functions from $h2(t)$; m=66, 67, 68, 69, 70 (b).

One advantage of using an OFC design is that several reflectors can be placed back to back and still have significant in-band wave energy reach the farthest Bragg reflector. Each peak in frequency corresponds to a null of the other basis functions. The maximum reflected frequency component from each reflector bank undergoes complete transmission as it passes through the other reflectors.

There is some frequency overlap between the reflectors with frequency components deviating from the local center frequency of each reflector. This results in signal distortion in addition to stored energy caused by secondary reflections. The actual returned time signal looks as shown in figure 2-7, which was obtained wirelessly and the antenna response plus the EM path causes further distortion of the ideal response.

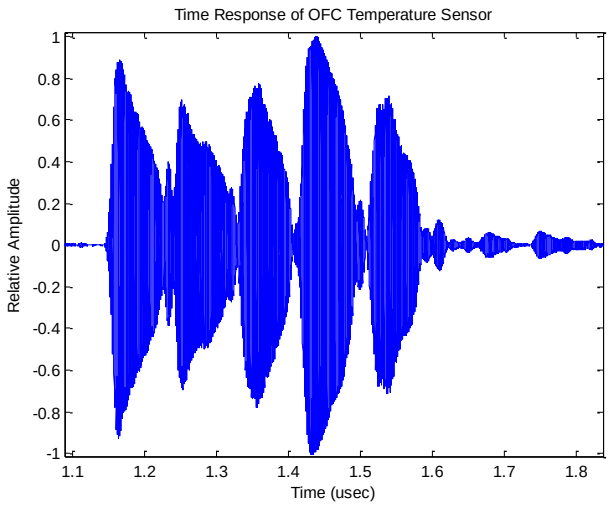

Figure 2-7. Measured time response of OFC sensor designed by M.W. Gallagher, MWG1001, showing the approximated truncated cosine response of the 5 Bragg reflectors.

Another advantage of designing the SAW temperature sensor with reflectors whose response closely resembles that of sequential orthogonal basis functions is coding [17]. The different orthogonal functions are referred to as chips. The chip sequence can be shuffled around from one device to another and thus each sensor can have its own identity.

2.3 Measurand Extraction

SAW devices built on Y-Z lithium niobate are natural temperature sensors. A temperature change will change the velocity under the reflector grating and thus the sensor frequency response. Temperature extraction will be used as an example of the approach used to extract the sensed parameter based on a frequency shift approach. After this section, some insight will be given into the system precision expected in a wireless configuration as distance is increased.

During the temperature extraction the returned signal is processed and convolved with an ideal rectangle-function-constructed matched filter, similar to figure 2-8a. In time, the correlation

is a convolution process of element-by-element multiplication and summation, then shifting the matched filter relative to the signal and performing the integration again and storing this value in an array. The convolution process will yield a peak value when the signal and matched filter line up. The idea of convolving the signal with the matched filter is to give a measure or detect if the signal of interest is present even if contaminated by noise or other signals, other sensors. Figure 2-8a shows the returned sensor signal with the truncated cosine-approximated matched filter, and figure 2-8b the correlation.

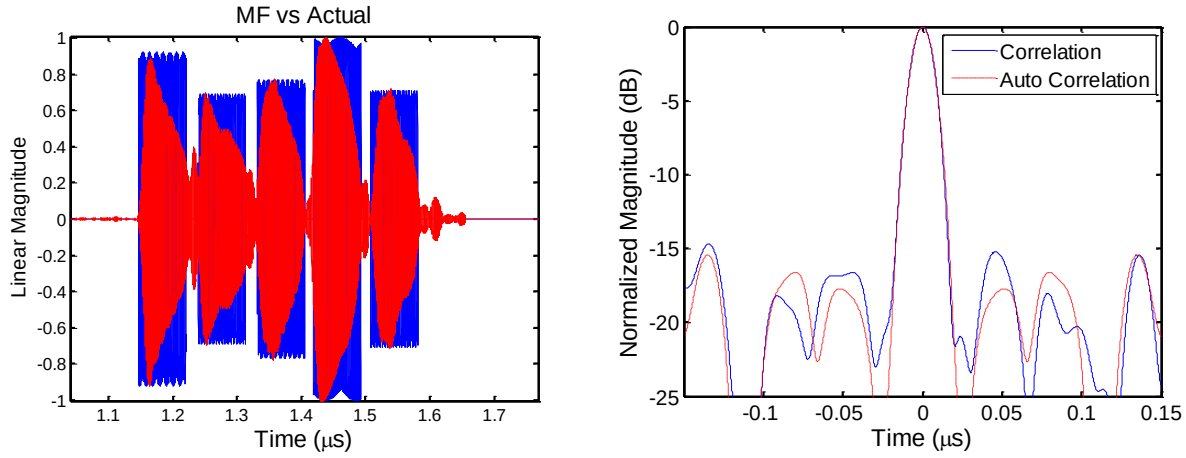

(a) (b)

Figure 2-8. (a) Measured OFC sensor time response (red) and corresponding matched filter (blue) created from truncated cosine functions. (b) Shows that the correlation of the measured sensor response with matched filter is very close to the auto-correlation of the ideal matched filter.

The red trace in Figure 2-8b is the ideal matched filter auto-correlation, the blue trace is the correlation of the sensor signal and the ideal matched filter. Figure 2-8b shows that even though the returned signal is not an ideal sequence of truncated cosines, the simply constructed matched filter correlation function is almost indistinguishable to the matched filter auto-correlation in the main lobe.

The returned sensor signal shown in figure 2-8a corresponds to one temperature value. Since the wave velocity in the crystal decreases linearly with increasing temperature, an increase

in temperature will result in a stretched version of itself [7, 18]. Temperature is extracted by creating compressed and expanded versions of the matched filter shown in figure 2-8a, but in the frequency domain for faster processing. A multiplication between the signal frequency response and the matched filter frequency response is performed for a given temperature range. The summation of this element by element multiplication is recorded and the highest value corresponds to the best matched filter [19]. The best matched filter is constructed with a given frequency scaling factor α. The temperature is calculated from the linear equation

$$Temp = {}^{(\alpha - 1)}/_{TCF} + ReferenceTemp \tag{2-6}$$

Each sensor is calibrated by taking two measurements of extracted temperature and two corresponding thermocouple measurements as the reference. From the two measurements the exact values for TCF and $RefereneTemp$ are obtained. Figure 2-9 is an example of a calibrated temperature run carried out in an environmental chamber.

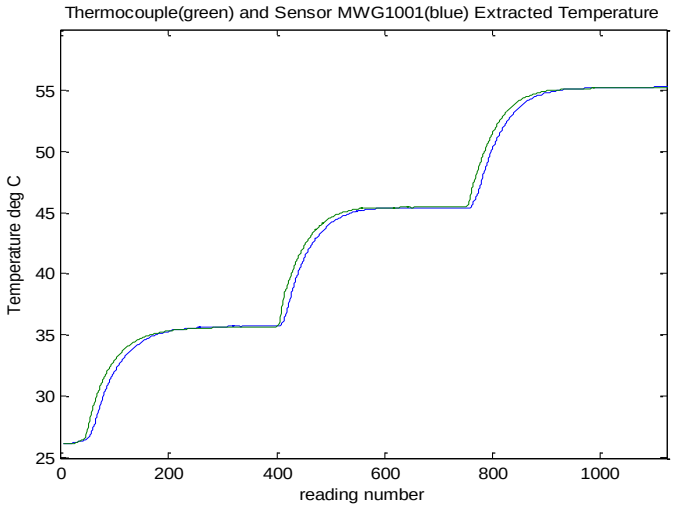

Figure 2-9. Evaluation of the performance of sensor MWG1001 inside an environmental chamber. The blue trace is the SAW sensor extracted temperature, showing some lag on a thermocouple reference attached to this device. Each reading number corresponds to about a second in time.

Each reading number took about a second to obtain. A VNA was used as the transceiver, controlled through GPIB by a Matlab program that also includes a post-processing algorithm to extract temperature [20, 21]. For a more economically practical application and also continually better performing in speed and range, a series of transceiver radios have been built by graduate students in the CAAT group through the years, the latest with a software defined radio (SDR) approach [22-26].

2.4 Passive Wireless SAW Sensor Precision

The path loss for free space electromagnetic propagation follows a $1/r^2$ relationship for power as distance increases. It becomes a $1/r^4$ relationship when the signal travels to the passive sensor, incurs some sensor insertion loss, and then travels back to the transceiver. Part of the task required for a practical implementation of passive wireless SAW sensors is understanding the precision of the extracted measurand as distance is increased. This relationship has been characterized for a particular OFC design for the measurement of temperature [21]. A 915 MHz SAW OFC sensor with 5 Bragg reflectors (chips), 68MHz bandwidth, and 440ns impulse response time length was used. The reflectors are separated into 2 acoustic tracks, 3 reflectors in 1 track and 2 in the other [27].

The extraction precision characterization was first performed under two primary scenarios. In one case the interrogation output power was kept constant as the distance from transceiver to sensor was increased in an open-air environment to simulate free space propagation loss. In the other case the sensor distance was kept constant at a short distance, and the output power from the transceiver was increased. Although dedicated radios have been designed for practical

interrogation of the passive SAW sensors, a VNA was used in S21 mode with the transmit antenna connected to port 1 and a receive antenna connected to port 2. The VNA was controlled with an external computer that also post processed the data and extracted the temperature using the method discussed in the previous section. The resulting wireless temperature measurements gave a relationship between standard deviation as seen in figure 2-10a and figure 2-10b.

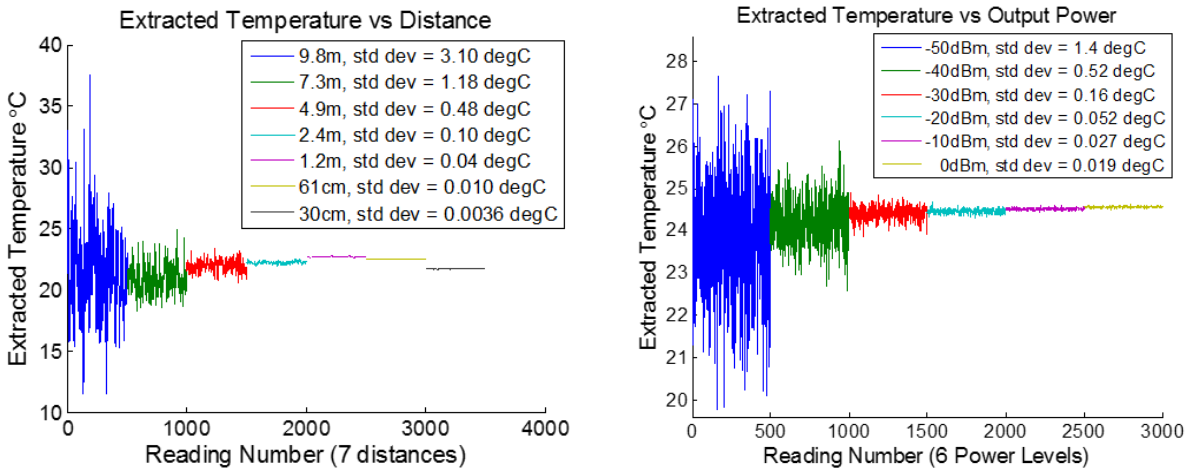

(a) (b)

Figure 2-10. (a) Temperature measurements showing the temperature deviation as a function of distance under constant output power of 0dBm. Each of the 7 sets is compensated for environment temperature drift. The corresponding reading number (RN) for the 7 distances are: RN 1-500, 9.8m; RN 501-1000, 7.3m; RN 1001-1500, 4.9m; RN 1501-2000, 2.4m; RN 2001-2500, 1.2m; RN 2501-3000, 61cm; RN 3001-3500, 30cm. (b) Temperature measurements showing the precision as a function of interrogation signal power. Also showing that the calculated temperature spread is approximately centered about the expected temperature. Each of the 6 sets is compensated for environment temperature drift. The corresponding reading number (RN) for the 6 power levels are: RN 1-500, -50dBm; RN 501- 1000, -40dBm; RN 1001-1500, -30dBm; RN 1501-2000, -20dBm; RN 2001- 2500, -10dBm; RN 2501-3000, 0dBm.

From the extracted temperature versus distance measurements in figure 2-10a, a SAW sensor signal SNR versus distance relationship was established (figure 2-11a). From the extracted temperature versus output power measurements in figure 2-10b, a SAW sensor signal SNR versus output power relationship was established (figure 2-11b).

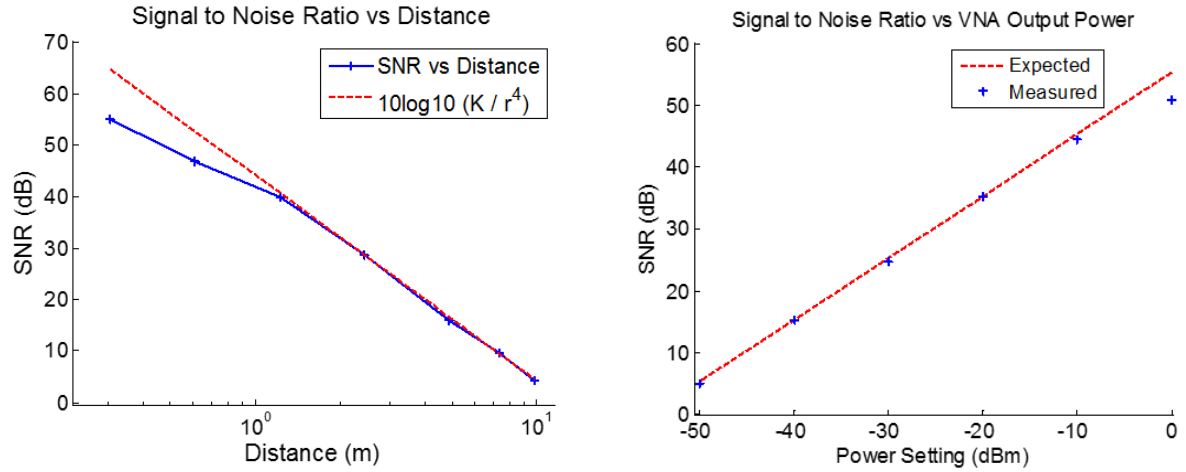

(a) (b)

Figure 2-11. (a) The plots of SNR vs. distance and the radar equation vs. distance. The agreement of the two curves shows that the radar equation is a good approximation for the path loss in the environment in which the measurements were taken. (b) Measured average SNR corresponding to each output power level of the power sweep of Fig. 2-10b.

By combining the results of figure 2-10ab and figure 2-11ab, a relationship between extracted temperature precision and sensor signal SNR is established and shown in figure 2-12.

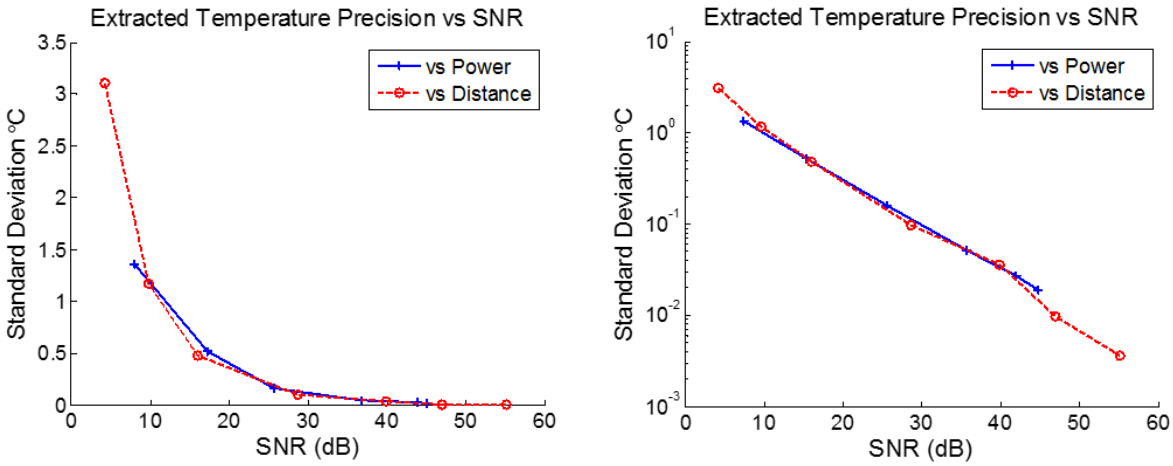

(a) (b)

Figure 2-12. (a) Standard deviation, in degrees centigrade, and SNR, obtained from 2 measurement approaches. Below a 5dB SNR near the curve knee, the temperature extraction scheme may lose lock and is unreliable data. (b) The same as figure on the left but in log scale.

Figure 2-12 shows that in both the varied power and the varied distance measurements, the precision of the extracted temperature by the SAW sensor is a function of SNR. By knowing this relationship in a particular sensor configuration, one can know how the sensor will operate in a

given application environment, and if it will meet the system requirements. And additional system requirement to consider is also how long one is willing to wait for each temperature measurement. Averaging, whether it is done by adding consecutive signals to increase the SNR or by a moving average of the extracted temperature, can also decrease the standard deviation of the reading. Integrating (or signal averaging) provides a means to increase the SNR at the expense of extra time required to obtain the measurement. The integration or summation of Gaussian noise increases the RMS noise amplitude by $\sqrt{n} \cdot A_{noise}$, where n is the number of integrations. Coherent sensor signal integrations increase the amplitude by $n \cdot A_{signal}$ when integrated. Dividing amplitudes and squaring for power as $[(n \cdot A\_signal)/(\sqrt{n} \cdot A\_noise)]$^2 gives an SNR increase of a factor of n by coherent integrations.

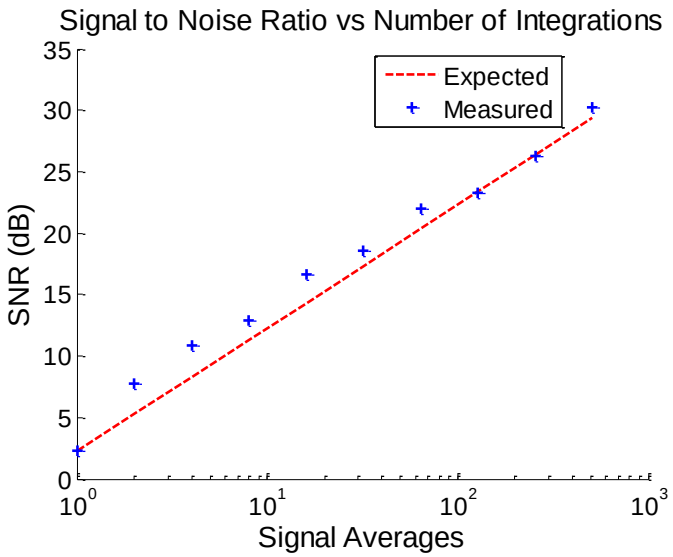

Figure 2-13. The measured SNR improvement as a function of integrations; an effective means to increase the operating range.

Averaging to increase the SNR ideally assumes that the temperature or whatever is being measured remains constant. Studies about effects of rate of change of temperature on temperature precision or accuracy have not been carried out. While rapidly changing temperature during oven controlled

experiments some anomalies have been observed in the temperature profile. Sharp temperature readout in the opposite direction of temperature movement followed by a sharp reversal until reaching proper temperature has been observed. The rate of change of temperature being measured has to be taken into account, especially if this causes the triggering of some alarm in a system into which a SAW sensor system has been integrated.

2.5 Double Transit Echo Problem

As discussed in the previous section, the effect of adding Gaussian or any other symmetric noise to the received sensor signal has the effect of spreading the temperature measurements some distance away from the true value measured in the absence of noise. But when the predominant noise or interference is deterministic, signal integration will not increase the SNR, and there may be an offset to the mean extracted temperature, depending on the interference level with respect to the desired signal. Unfortunately such type of interference is inherent in a passive SAW multi-sensor system with reflective delay line devices. It is mainly present because of the echoes that arise due to the cavity that is formed between the IDT and the reflectors. The desired signal is the main transit, the second transit is the double transit echo (DTE). The start of the DTE will show up at twice the start time of the main transit. Higher echoes are in practice negligible.

Multiple reflective delay line SAW sensors can operate simultaneously over the same frequency band because the sensor signal, the convolution of the IDT response and the reflector response, appears for approximately a finite time duration. After a single interrogation, all of the sensors within range will respond indiscriminately. The spatial delay between the IDT and reflectors has to be chosen so that sensor signals do not overlap.

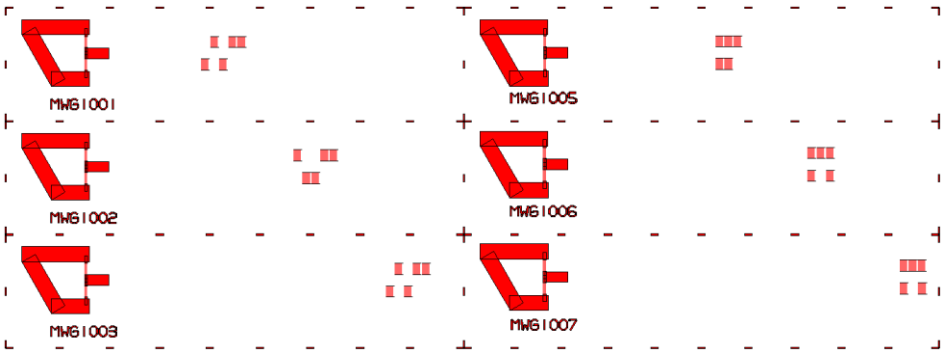

Figure 2-14. Device layout of the six dual track OFC and MOFC wireless temperature sensors

The photolithographic mask layout shown above in figure 2-14 for a set of six simultaneously working devices was designed by M. Gallagher. These are dual acoustic track OFC and modified OFC (MOFC) devices. The MOFC devices overlap Bragg reflectors to shorten the time response [27]. Figure 2-15 shows a received signal capture window, or frame, containing the summation of all 6 sensor signals.

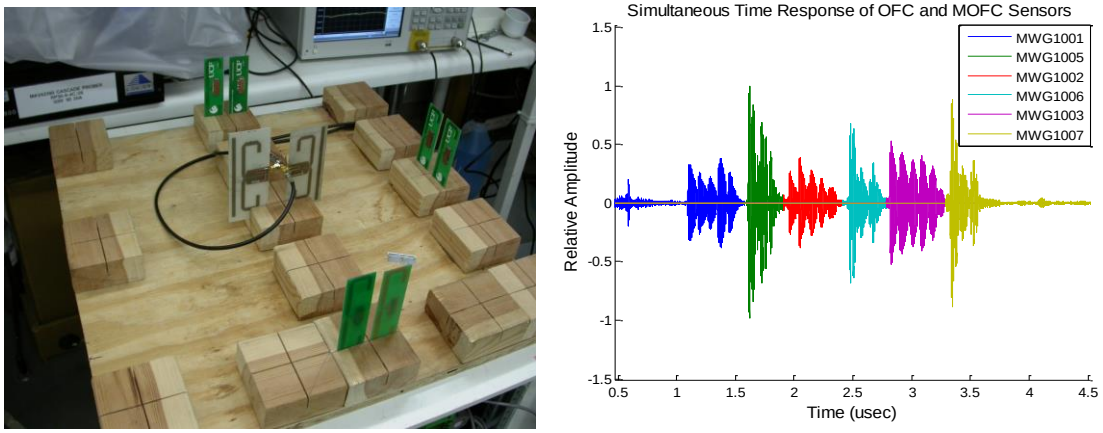

(a) (b)

Figure 2-15. (a) Sensor order starting bottom left and counterclockwise follows time response sequence on right: MWG1001, 1005, 1002, 1006, 1003, 1007. (b) Shows the time response of the simultaneous operation of the 6 sensors.

One of the main challenges of a passive wireless system is that dynamic ranges of received signals can change rapidly with sensor position, due to obstruction of line of sight or lossy barriers, or free space path loss. The degree of impact may be application dependent. If the sensor placement

relative to the receiver is constant, an attenuator could be used to tune the signal levels for the dynamic range of the receiver. Even with signal levels in the same order of magnitude, there can be inter-sensor interference. In figure 2-15b above, the DTE of the first two sensors is contaminating the last two sensor signals. A study on how much the affected sensors are affected has not been carried out. An initial estimate would be that the extracted temperature of the affected sensor might be offset by an amount similar to that given by the temperature deviation versus SNR previously shown in figure 2-12.

Reflectors have limitations on the shape and length of reflected waveforms that can be generated for use as sensor signals. At the current moment sensor signals are not overlapped in time because of issues posed by code collisions [28, 29]. The reflector response lengths are kept long enough to give good processing gain and maintain the loss low, but short enough to be able to accommodate multiple time slots for sensor signals. Available working bandwidth also plays an important role in determining the sensor response length. Many of these parameters come with tradeoffs and the application dictates how the design is handled. Even selective interrogation of passive sensors is a possibility—perhaps with pairing a coded IDT with a specific interrogation signal waveform [30, 31]. Consider the received signal composed of two sensor signals in figure 2-16.

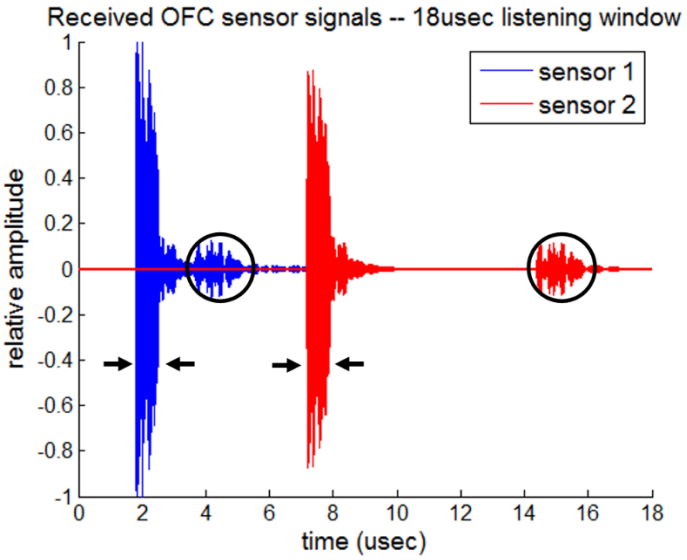

Figure 2-16. Two simulated OFC sensor signals and their double transit echo (circled).

Two sensors are within view of the transceiver; the capture window (or frame) is 18usec long. The usable sensor signal for processing is shown within the black arrows to be approximately 1usec. The ringing due to stored energy takes about another microsecond to die down. Then at double the time from when the main signal arrives at the IDT and out of the antenna, the double transit echo arrives. Because of the convolution-like operation that takes place as the signal arrives at either IDT or reflector, the DTE is about twice as long as the main signal. It essentially takes the place of a time slot where another sensor could be placed. In past sensor designs where the DTE interference was not willing to be tolerated, the sensors were laid out so that the 1st sensor had enough time delay to accommodate all the sensors before the 1st sensor's DTE appeared. This unfortunately sacrifices the possible time slots before and after the main transits.

Another issue that arises with the DTE can be seen in figure 2-17.

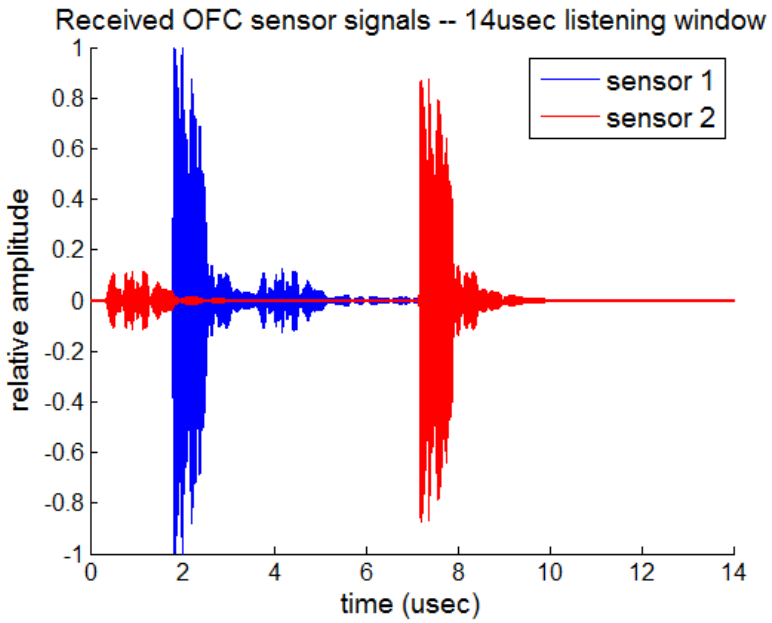

Figure 2-17. Similar to figure 2-16 but assuming the capture window of the receiver being 14usec instead of 18usec and no delay between interrogations. The DTE of sensor 2 has wrapped around because enough time was not given for the echo to die down between interrogations.

This received signal frame has the same signals as in figure 2-16, but the length of the capture window has been reduced from 18usec to 14usec. Since the devices are interrogated multiple times in order to improve the SNR, ideally the interrogations would be made as frequently as possible. In the ideal assumption that the radio can perform the interrogations without any delay in between, the red DTE as seen in the 18usec capture window would wrap around and show up at the beginning of a 14usec capture window as can be seen in figure 2-17. With a system that could operate with close to zero latency between interrogations, waiting for the last DTE to die down would approximately slow down the interrogations by half. Slowing the interrogation by half is approximately a 2.5dB decrease in SNR according to figure 2-13. This would improve the standard deviation of measured temperature spread by roughly 1/3 according to the relationship in figure 2-12. This particular improvement may or may not be significant. It is more of a positive

byproduct of DTE suppression, but nevertheless, it is an artifact that may have to be taken into account when designing the system.

2.6 Chapter 2 Summary

The purpose of this chapter is to give a general introduction to passive wireless SAW sensor embodiments. The main contribution by the author is the method of predicting the precision of a SAW sensor as a function of SNR, and as a function of distance. A summary of the chapter is now given as a list of sub-points for every section, in the order of appearance.

Passive Wireless SAW Sensor Embodiments:

- Two main types of passive wireless SAW sensor topologies are the resonant and delay line type in a reflective 1-port configuration.
- The sensing mechanism for the resonator approach is based on frequency shift.
- The wave velocity changes under the reflectors or the whole propagation path.
- The temperature coefficient of frequency (TCF) determines the velocity change as a function of temperature.
- SiO2 film sputtered on top of the device can temperature compensate.
- In a passive wireless multi-sensor system these types of sensors require their own frequency range of operation.
- The other main type of passive wireless SAW sensor topology is the delay line configuration; usually a wideband IDT and a propagation path delay followed by acoustic reflectors.
- The delay line configuration lends itself to a greater variety of sensing approaches.

- With the delay line type of sensor, one can measure amplitude, time delay, or frequency shift of the reflected wave
- The amplitude approach has been used to make a hydrogen gas sensor, cryogenic liquid level sensor, and a Reed switch closure sensor.
- The delay line measurement approach could also use a sensing film in the middle of the propagation path.
- The presence of a gas or of a pathogen would cause a stiffness change or a mass loading change in the film that would in turn cause a measurable delay.
- The shift in frequency of a whole bandwidth is tracked.

OFC Coded Reflector Devices:

- Consist of a wideband IDT, a propagation path delay, and a set of OFC coded reflectors.
- Each reflector, or chip (a communications term, sequence of chips making up a bit), is a Bragg reflector with a special center frequency.
- An example of OFC basis functions are shown in figure 2-6a, where each basis function is offset by τ to give a stepped chirp signal.
- Several reflectors can be placed back to back and still have significant in-band wave energy reach the farthest Bragg reflector.
- There is some frequency overlap between the reflectors with frequency components deviating from the local center frequency of each reflector.
- An advantage of designing the SAW temperature sensor with reflectors whose response closely resembles that of sequential orthogonal basis functions is coding.

Measurand Extraction:

- SAW devices built on Y-Z lithium niobate are natural temperature sensors.
- A temperature change will change the velocity under the reflector grating and thus the sensor frequency response.
- During the temperature extraction the returned signal is processed and convolved with an ideal rectangle-function-constructed matched filter.
- The simply constructed matched filter does a very good job of capturing the signal for the purpose of correlation.
- The best matched filter is constructed with a given frequency scaling factor α.
- A VNA can be used as a transceiver controlled through GPIB by a Matlab program that also includes a post-processing algorithm to extract temperature.

Passive Wireless SAW Sensor Precision:

- Path loss is a $1/r^4$ relationship when the signal travels to the passive sensor, incurs some sensor insertion loss, and then travels back to the transceiver.
- This relationship has been characterized for a particular OFC design for the measurement of temperature.
- A relationship between extracted temperature precision and sensor signal SNR is established and shown in figure 2-12.
- Integrating (or signal averaging) provides a means to increase the SNR at the expense of extra time required to obtain the measurement.

- The integration or summation of Gaussian noise increases the RMS noise amplitude by $\sqrt{n} \cdot A_{noise}$, where *n* is the number of integrations. Coherent sensor signal integrations increase the amplitude by $n \cdot A_{signal}$ when integrated.
- An SNR increase of a factor of *n* is obtained by coherent integrations.
- Averaging to increase the SNR ideally assumes that the temperature or whatever is being measured remains constant. Studies about effects of rate of change of temperature on temperature precision or accuracy have not been carried out.
- The rate of change of temperature being measured has to be taken into account.

Double Transit Echo Problem:

- When the predominant noise or interference is deterministic, signal integration will not increase the SNR, and there may be an offset to the mean extracted temperature. Such type of interference is inherent in a passive SAW multi-sensor system with reflective delay line devices. Mainly present because of the echoes that arise due to the cavity that is formed between the IDT and the reflectors, resulting in the double transit echo (DTE).
- The reflector response appears for a finite time duration.
- The double transit echo (DTE) with subsequent sensor signals.
- Reflectors have limitations on the shape and length of reflected waveforms that can be generated for use as sensor signals.
- Available working bandwidth also plays an important role in determining the sensor response length.

- Even selective interrogation of passive sensors is a possibility—perhaps with pairing a coded IDT with a specific interrogation signal waveform. Perhaps an RF switch can be used for selective interrogation.
- Because of the convolution-like operation that takes place as the signal arrives at either IDT or reflector, the DTE is about twice as long as the main signal.

.

CHAPTER 3:
DOUBLE TRANSIT ECHO THEORY

3.1 P-Matrix Description of SAW Multi-Transit Echoes

In the ongoing effort of developing and improving wireless SAW sensor systems, a fundamental limitation of the passive sensor approach is the limited time/space available for placement of the reflective structures that re-transmit the modified interrogation signal. In a sensing system that employs passive wireless SAW sensors with the antenna-IDT-reflectors configuration, the interrogation signal that enters the crystal through the antenna-IDT electro-acoustic transformer and is modified as it travels through the crystal and back to the antenna, will usually undergo a reflection at the IDT-antenna port.

The bidirectional IDT is mismatched at the acoustic ports. Therefore, a cavity is formed between the IDT and reflectors and the mismatch at the IDT acoustic port facing the reflectors causes the initial interrogation signal to become partially trapped, causing multiple reflections.

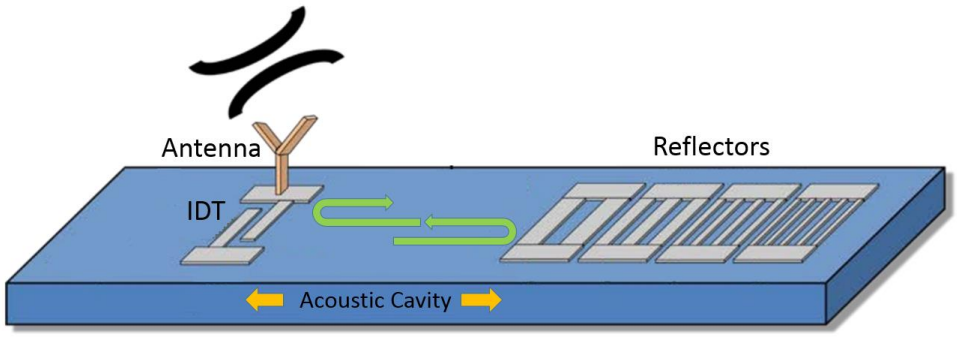

Figure 3-1. Acoustic cavity formed between IDT and reflectors.

The initial interrogation signal that enters the crystal and is reflected and sent back out of the SAW device through the antenna is the signal of interest. Any energy trapped inside the IDT-reflector cavity, that is, all reflections, or echoes, beside the 1st, contaminate the available sensor

signal time space as shown in the previous section—limiting how many or how close the sensors can be placed while maintaining a certain precision or accuracy.

One way of describing the phenomenon of multiple echoes as a result of the mismatched IDT acoustic port is to use a P-Matrix description. The P-Matrix is similar to a scattering matrix used in RF transmission line theory, but it is used for describing acoustic elements. It is a mixed matrix containing 3 ports, 2 acoustic and 1 electrical port. The acoustic ports are described in the scattering parameters form, while the electrical port is described in the admittance parameter form as shown in figure 3-2.

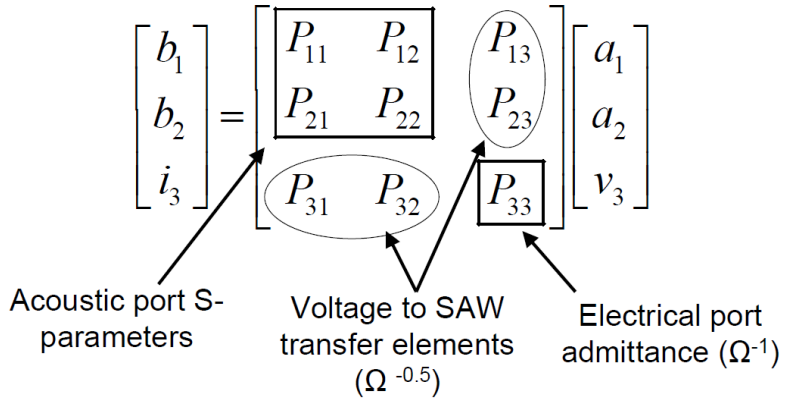

Figure 3-2. The mixed P-Matrix description of 1 dimensional SAW structures with its entries grouped into like units. Image of D. Puccio, from Figure 4-4 of his dissertation [8].

The 3-port P-matrix above is used to describe the IDT. P-matrices used to describe the acoustic delay and the reflector banks without external loading reduce to 2x2 2-port matrix descriptions, or for cascading purposes all of the entries in the last row and column are set to 0. A coupling of modes analysis is used to generate the P-matrix elements [32]. P-matrices are cascaded to obtain an overall P-matrix describing the entire SAW device.

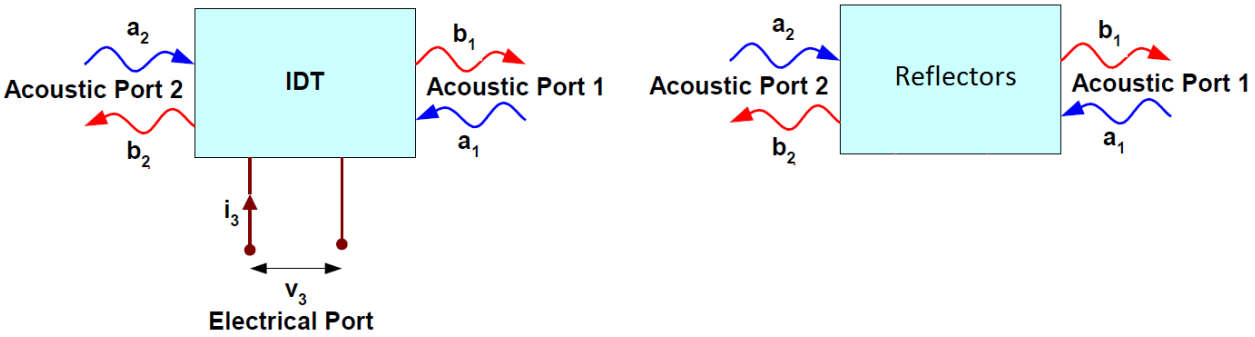

Figure 3-3. P-Matrix block diagram of a reflective delay showing the relationship between corresponding acoustic scattering port wave amplitudes plus the electrical port of the IDT. Modified image of N. Saldanha, from Figure 3-3 of her dissertation [11].

Cascading P-matrices can be accomplished by using signal flow graph theory. Cascading two P-matrices connected electrically in parallel as show in figure 3-4

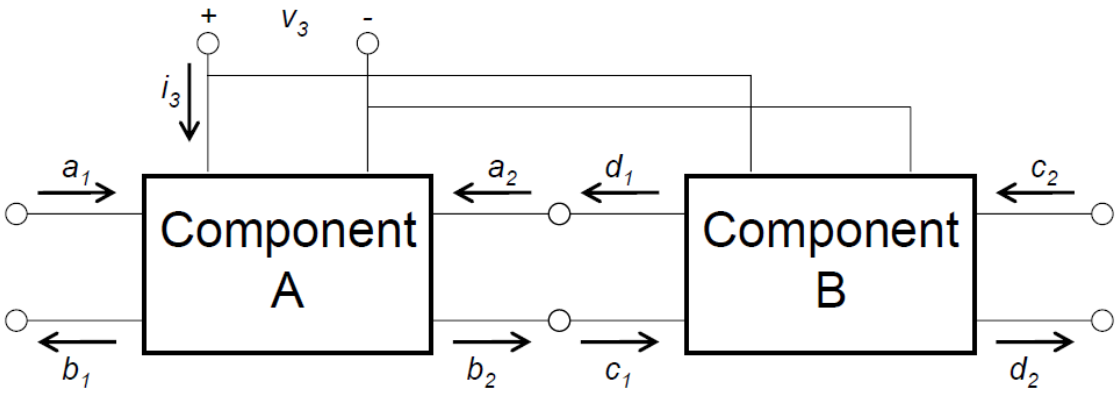

Figure 3-4. P-Matrix cascade with parallel electrical connection. Image from D. Puccio, Figure 4-5 of his dissertation [8].

is accomplished using the following signal flow graph in figure 3-5 [8].

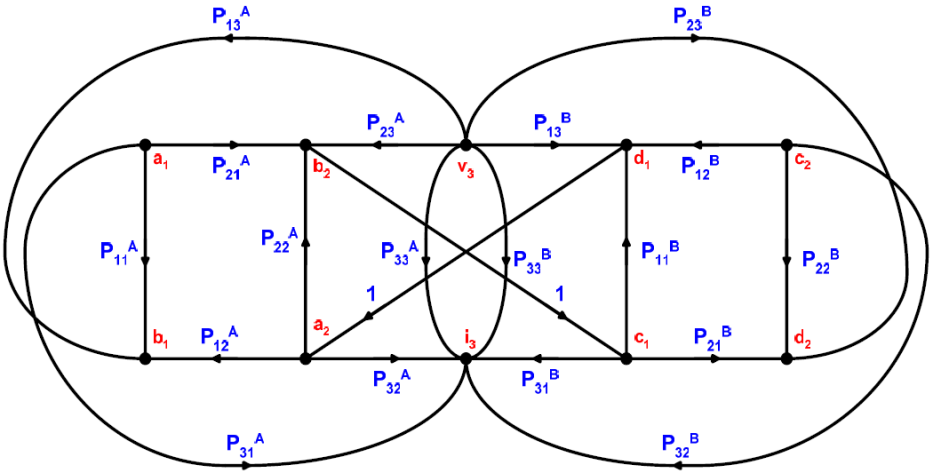

Figure 3-5. Signal flow graph for P-Matrix cascade with parallel electrical connection. Image from D. Puccio, Figure 4-6 of his dissertation [8].

The P-matrix description of the combined elements is found in [8, 32]. The propagation path delay can be absorbed by the P-matrix of the combined reflectors when cascading from right to left. The superscripts in the signal flow graph are changed from "A" and "B" to "T" and "R", to represent the transducer and the reflector P-matrix representation, respectively, in equation 3-1—the admittance of the reflective delay-line device. The admittance of the SAW device in terms of P-parameters becomes

$$Y(\omega) = P_{33}^{T} + \frac{P_{32}^{T} P_{23}^{T} P_{11}^{R} e^{-i\omega 2\tau_D}}{1 - P_{22}^{T} P_{11}^{R} e^{-i\omega 2\tau_D}} = P_{33}^{T} + \frac{b e^{-i\omega 2\tau_D}}{1 - a e^{-i\omega 2\tau_D}} \tag{3-1}$$

where τ_D is the time delay corresponding to the 1-way distance between transducer and reflectors. The impulse response of the SAW devices becomes

$$\Gamma(\omega) = \frac{1 - z0^{*}Y}{1 + z0Y} = \frac{\frac{1 - z0^{*}P_{33}^{T}}{1 + z0P_{33}^{T}} + \frac{P_{33}^{T} az0^{*} - bz0^{*} - a}{1 + z0P_{33}^{T}} e^{-i\omega 2\tau_D}}{1 - \frac{P_{33}^{T} az0 - bz0 + a}{1 + z0P_{33}^{T}} e^{-i\omega 2\tau_D}} \tag{3-2}$$

If the substitution $e^{i\omega 2\tau_D} = z$ is made, the reflection coefficient, gamma has the form of the z-transform of a 1st order infinite impulse response (IIR) filter

$$\Gamma(\omega) = \frac{b_0 + b_1 z^{-1}}{1 - a_1 z^{-1}} \tag{3-3}$$

The representation of $\Gamma(\omega)$ in equation 3-3 has the equivalent power series representation

$$\Gamma(\omega) = b_0 + (b_0 a_1 + b_1) z^{-1} + a_1 (b_0 a_1 + b_1) z^{-2} + {a_1}^2 (b_0 a_1 + b_1) z^{-3} + \cdots \tag{3-4}$$

A similar analysis is done by D. Malocha [33] where $\Gamma(\omega)$ is separated as

$$S_{33} = S_{33}^A + S_{33}^B \tag{3-5}$$

Where S_{33}^A is the IDT response without a reflector, and S_{33}^B is a term containing the echo information. In his derivation S_{33}^B becomes

$$S_{33}^B = \frac{-2 \cdot {q_2}/{(1+q_1)^2}}{1 + {q_2}/{(1+q_1)}} = \frac{-2}{1+q_1} \cdot \{ \frac{q_2}{1+q_1} + \left(\frac{q_2}{1+q_1}\right)^2 + \left(\frac{q_2}{1+q_1}\right)^3 + \cdots \tag{3-6}$$

where

$$q_1 = \frac{P_{33}^T}{Y0}, q_2 = \frac{\frac{P_{32}^T P_{23}^T P_{11}^R e^{-i\omega 2\tau_D}}{1 - P_{22}^T P_{11}^R e^{-i\omega 2\tau_D}}}{Y0} \quad and \; S_{33}^A = \frac{1-q_1}{1+q_1} \tag{3-7}$$

Both derivations of the series expansion of the impulse response to show the multiple echoes are equivalent.

In equation 3-4 the b_0 term corresponds to the IDT response without the reflectors, also referred to as IDT ringing. The reflector contributions from the multiple echoes add to the transducer ringing. The main transit response minus the IDT ringing takes the form $(b_0 a_1 + b_1) z^{-1}$, with the z^{-1} term providing the corresponding time delay when the frequency domain form is transformed to the time domain. Figure 3-6 shows a simulation of an OFC device time

response with superimposed multi-transit echoes crossing underneath the IDT ringing level and all the way down to the computational noise floor.

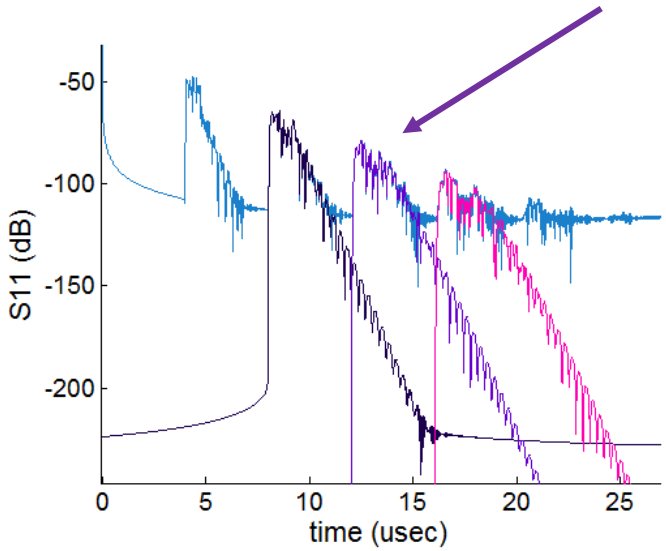

Figure 3-6. Simulation of OFC device to show individual echoes. The 4th term in the expansion corresponds to the 3rd echo shown in purple.

The series representation of the time domain feedback diagram easily shows the recursive relationship between the echoes. Each consecutive echo is multiplied in frequency, or convolved in time, by a_1, the echo transfer function.

Setting $a_1 = 0$ therefore gives the condition for echo suppression.

$$a_1 = \frac{P_{33}^T P_{22}^T P_{11}^R z0 - P_{32}^T P_{23}^T P_{11}^R z0 + P_{22}^T P_{11}^R}{1 + z0 P_{33}^T} = P_{22}^T - \frac{P_{32}^T P_{23}^T}{y0 + P_{33}^T} = 0 \qquad (3\text{-}8)$$

This result can also be obtained by algebraic manipulation of P-matrix equations corresponding to **Error! Reference source not found.**. The equations describing the IDT port-2 scattering waves are placed in the acoustic reflection coefficient form $b_2/a_2 = 0$. However, this relationship is obtained immediately when converting the IDT P-matrix in an electro-acoustic scattering matrix (equation 3-10), as done by B. Abbot in his dissertation "A coupling-of-modes model for SAW transducers with arbitrary reflectivity weighting" [32].

$$\begin{bmatrix} b_1 \\ b_2 \\ b_3 \end{bmatrix} = \begin{bmatrix} S_{11} & S_{12} & S_{13} \\ S_{12} & S_{22} & S_{23} \\ S_{31} & S_{32} & S_{33} \end{bmatrix} \begin{bmatrix} a_1 \\ a_2 \\ a_3 \end{bmatrix} \tag{3-10}$$

This formulation gives the acoustic port reflection coefficient directly.

$$S_{22} = P_{22}^T - \frac{P_{32}^T P_{23}^T}{y0 + P_{33}^T} \tag{3-11}$$

The electric port voltage and current, v_3 and i_3, are replaced by scattering waves, leaving the acoustic port reflection coefficient in terms of the characteristic impedance $1/y0$.

Something to note from the acoustic reflection coefficient equation above, it is composed on one side of an acoustic reflection parameter, P_{22}. On the other side of the equation are electrical and acousto-electrical parameters. Since there is an acoustic reflection component, the other component must be an electrical reflection component. The characteristic impedance feeding the IDT and also the electrical load as the IDT re-radiates as the source, $y0$, has to be chosen so that the two terms in equation 3-11 cancel.

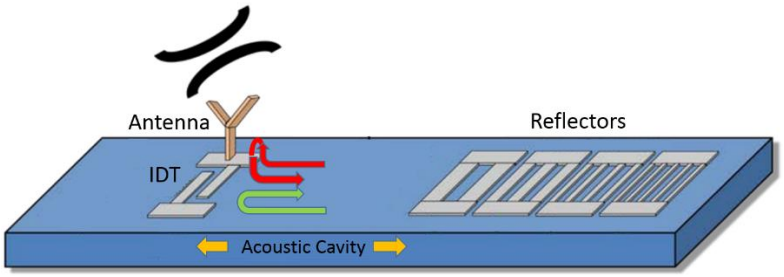

Figure 3-7. The concept of the acoustic and electric component of reflection—the echo off the IDT is a combination of an acoustic reflection component and an electrical mismatch component. Modified image from B. Fisher, Figure 2-19 of his dissertation [12].

By having a model with P-parameters that are able to predict the device response, including DTE, it is theoretically possible to subtract the DTE based on the main transit. It is difficult to match

the echo magnitude and phase with enough accuracy to effectively subtract it out without inadvertently adding to it—the unwanted echo is many decibels below the main transit signal level. It would be difficult, but perhaps worth looking into in the future, especially if computational resources improve. However, this dissertation will employ a physical approach to echo suppression by making use of the acoustic reflection coefficient relationship. An IDT with favorable properties will be used, along with the proper load impedance, in order to efficiently suppress the multi transit echoes in a wireless sensor configuration.

The first discussion of multi transit echoes dates back to Smith et al. in 1969, in the context of filters. The two-port device is mainly concerned with the odd transits; specifically the triple transit echo (TTE). Transits in filters are counted 1 for each 1-way distance between IDTs. In reflective delay lines the round-trip from IDT to reflector and back is counted as 1 transit. For the TTE, the wave is partially reflected off the port 2 IDT, then off the port 1 IDT and finally out through port 2. In the TTE case the wave bounces off an IDT acoustic port twice, and once in the case of the DTE. Different people like Skie, Engan, and Hashimoto [34, 35] have formulated equations to describe the TTE using various approaches. However, the first person to use P-parameters to describe multi transit echoes was B. Abbott while working on his dissertation under the direction of D.C Malocha back in the late 80s [32].

Similar to the matching issue of reciprocal, lossless 3-port networks, bidirectional SAW transducers cannot be matched at all ports simultaneously. The approach taken is to make the transducer as directional as possible. If the IDT were completely directional, and if the electrical port were matched, then the acoustic port of interest would be completely matched, and the other completely mismatched—this would be ideal. This mode of operation is approximately achievable

with a group type unidirectional transducer (GUDT) at center frequency. This type of IDT requires 2 electrical feeds with a specific phase difference between them. Some description of the operation of this device and a method to implement it in a wireless configuration are given in appendix A. However, the main chapters will focus on the goal of suppressing the multi transit echoes by use of a single-phase unidirectional transducer (SPUDT).

When modeling IDTs using the combination of uniform sections through the cascading of P-parameters, an analytical description of a uniform IDT in terms of P-parameters is derived from coupling of modes (COM) equations by Abbott [32]. Similar to the infinite series description of Γ in 1-port reflective delay line devices given in the sections above, an infinite series description of S12 is given by Abbot as

$$S_{12}^{F} = \frac{S_{13}^{2}}{1 - S_{11}^{2}} = S_{13}^{2}[1 + S_{11}^{2} + S_{11}^{4} + \cdots \tag{3-12}$$

The "F" superscript stands for filter and refers to RF 2-port S-parameters, whereas the other "S" parameters in the equation refer to the 3-port acoustic-electric scattering matrix of equation 3-10. A SPUDT is then simulated by assuming ideal phasing between transduction center and reflection center of

$$\Phi_B - 2\Phi_T = 90^0 \tag{3-13}$$

This phase relationship produces unidirectional behavior that is explained in Appendix D. By inserting the above phase relationships into the COM equations describing the uniform transducer, Abbott finds a simple analytic representation for the insertion loss at center frequency. Malocha derives this equation for the 1-port reflective device in [33], and also compares triple and double transit echo levels.

$$S_{13}^2 = -\frac{4G_{33}/G_L}{(1+4G_{33}/G_L)^2(1+e^{-2KL})} \tag{3-14}$$

The TTE suppression level, the level of the TTE with respect to the 1st transit, is similarly found.

$$S_{11}^2 = \tanh(KL) - \frac{4G_{33}/G_L}{(1+4G_{33}/G_L)^2(1+e^{-2KL})} \tag{3-15}$$

The filter is assumed composed of identical transducers, G_{33} being the admittance of a single transducer, and G_L the load admittance being purely real. The capacitive susceptance of the transducers is assumed to resonate with an inductance. The factor KL is a combination of the reflectivity per wavelength, or transduction period, K, and the length of the transducer, L. The plots of the above two equations are reproduced as shown in the original work and given in figure 3-8, as a function of reflectivity KL.

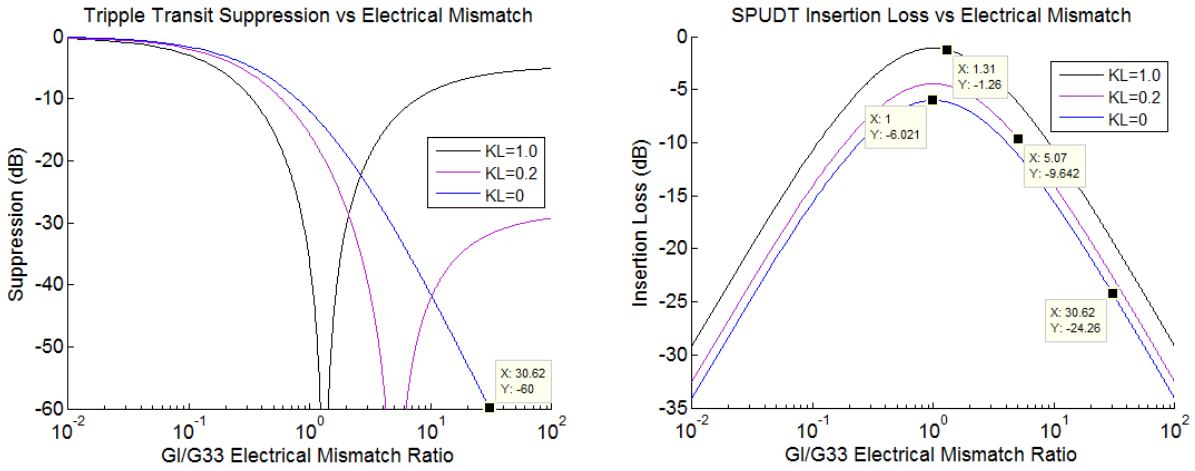

(a) (b)

Figure 3-8. Triple transit suppression and insertion loss vs. electrical mismatch ratio for 3 reflectivity values [32].

The plots show that in order to suppress the echo, the higher the directionality, the better the transducer can be matched and still obtain the same level of echo suppression at a specific frequency. For equal length SPUDTs, increasing the reflectivity per transduction period K increases the directionality—how the reflectivity and transduction mechanisms affect directionality is described in Appendix D. Unfortunately in practical devices the reflectivity can't

be increased arbitrarily. At some point the bulk energy and inelastic losses created by the structures with increasing reflectivity will cancel out the lower insertion loss resulting from the increased directivity. In the original work, the argument is made that a bidirectional IDT corresponds to the case when KL=0. While split finger (4f0 sampled) bidirectional IDTs are reflectionless at center frequency, ¼ wavelength (2f0) IDTs do have reflectivity. However, as far as the TTE suppression vs. mismatch relationship goes, both behave similarly—the echo suppression increases monotonically as the electrical mismatch ratio is increased. For the bidirectional case, perfect center frequency suppression is obtained at an infinite mismatch ratio. The graphs show that 60dB TTE suppression requires approximately 24dB of loss on the main transit. But by introducing directionality the echo suppression profile changes. The perfect suppression is no longer found at an infinite mismatch ratio—the suppression actually converges asymptotically at infinite mismatch. Directionality introduces a dip in the echo suppression curve—perfect suppression is found at a specific value of mismatch relatively near electrically matched conditions. To the left and right of the null, the echo level will rapidly increase as matching changes from optimum. The trace representing KL=.2 maintains the same level of suppression over a wider mismatch range than the KL=1 trace. Using a COM model simulation in Appendix H, the relationship between maximum DTE level over the bandwidth as a function of cells in the transducer is shown for an example SPUDT (using an artificial simulated reflector having only 1 strip for ultra-wide bandwidth). Something to note from the curves in Figure 3-8b is that the bidirectional case gives an insertion loss of 6dB when matched, as expected—3dB is lost at the sending IDT and another 3dB is lost at the receiving IDT. Losses within the IDT or free surface propagation loss are not taken into account.

Even though there will be a tradeoff between directivity and the bandwidth of echo suppression, a high directivity is desired. Also, for matching purposes, a lower device Q is desired so that a better electrical match can be obtained over a wider bandwidth. The discussion has assumed a constant load impedance over frequency; future applications may be able to incorporate a frequency dependent characteristic impedance. Appendix D will deal with the SPUDT transducer—how the directionality comes about and a method used to optimize the SPUDT characteristics.

3.2 Chapter 3 Summary

This chapter provides an analytic description of multi-transit echoes using a P-Matrix description of the reflective-delay-line device and gives the condition for echo suppression. It has previously been shown to involve a cancellation of the mechanical reflection with the electric port reflection. The main contribution by the author is to give an analytic description of the echoes that looks like a discrete time IIR filter, showing the echo transfer function a_1. A summary of the chapter is now given as a list of sub-points, it the order of appearance.

P-Matrix Description of SAW Multi-Transit Echoes:

- In a sensing system that employs passive wireless SAW sensors with the antenna-IDT-reflectors configuration, the interrogation signal enters the crystal through the antenna-IDT electro-acoustic transformer and is modified as it travels through the crystal and back to the antenna.
- The signal will usually undergo a reflection at the IDT-antenna port.

- The bidirectional IDT cannot be matched at both the electrical port and the acoustic port facing the reflectors at the same time.
- A cavity is formed between the IDT and reflectors.
- The mismatch at the IDT acoustic port facing the reflectors causes the initial interrogation signal to become partially trapped, causing multiple reflections.
- The initial interrogation signal that enters the crystal and is reflected and sent back out of the SAW device through the antenna is the signal of interest.
- Any energy trapped inside the IDT-reflector cavity, that is, all reflections, or echoes, beside the 1st, contaminate the available sensor signal time space; limiting how many or how close the sensors can be placed while maintaining a certain precision or accuracy.
- One way of describing the phenomenon of multiple echoes is to use a P-Matrix description of the SAW device.
- P-Matrix is used for describing electrical and acoustic ports.
- The admittance P33 is converted to S11, or Γ, the reflection coefficient, which becomes the simulated sensor response.
- The device S11 response has the form of the z-transform of a 1st order infinite impulse response (IIR) filter.
- Equations describing the IDT port-2 scattering waves are placed in the acoustic reflection coefficient form $b_2/a_2 = 0$, in order to give the condition for echo suppression.
- Three-port acoustic S-matrix formulation gives the acoustic port reflection coefficient directly.

- Acoustic reflection coefficient equation is composed on one side of an acoustic reflection parameter, P_{22}. On the other side of the equation are electrical and acousto-electrical parameters.
- This dissertation will employ a physical approach to echo suppression by making use of the acoustic reflection coefficient relationship.
- The first discussion of multi transit echoes dates back to Smith et al. in 1969, in the context of filters.
- For the bidirectional case, perfect center frequency suppression is obtained at an infinite mismatch ratio.
- Directionality introduces a dip in the echo suppression vs. electrical-port mismatch curve.

CHAPTER 4:
COUPLING OF MODES MODELING OF 1ST AND 3RD HARMONIC SPUDT

In this chapter the coupling of modes (COM) model will be used to model SPUDT devices. In chapter 5 the COM model will be used to design special reflectors for the reflective delay line device. Having a COM model of the SPUDT will help predict echo suppression levels for the reflective delay-line devices presented in chapter 5.

An optimized SPUDT cell layout is presented Appendix E. This design, and EWC, and a 4f0 split-finger transducer will be modeled in the last two sections of this chapter. A technique for extracting the probe pad parasitic is presented in section 4-1. Modeling results of 1st harmonic devices are presented in section 4-2 and 3rd harmonic devices in section 4-3.

The reader is referred to Appendix F for a discussion of the COM parameters and instructions on how to set up the simulation for both 1st and 3rd harmonic devices. The interested reader is also shown how to estimate two important COM parameters, the capacitance and the transduction coefficient, by knowing the static charge distribution. Cheng, Wu and Chang have previously modeled 3rd harmonic bidirectional transducers in a pulse position coded SAW tag embodiment at 2.5GHz using the COM model [36]. The transduction coefficient was calculated from the charge distribution in their simulation, similar to the "calculated αRatio" value shown in Figure 4-5, and discussed in Appendix E, section 3.3. In this chapter, the calculated (estimated) transduction coefficient is also compared to the COM extracted value from the experimental data. The work here shows both COM modeling of 3rd harmonic operating bidirectional as well as unidirectional transducers. With the information contained in appendix F, and making use of the P-Matrix cascade relationships mentioned in chapter 3, the reader will be able to replicate the

device modeling results shown in this chapter and chapter 5. The measured device data will be attached as part of this electronic dissertation.

4.1 Probe pad Parasitic Extraction using SAW Device Circuit Model

The measured data will have some parasitics associated with the RF probe contacts and the device probe pads. The impedance (or conductance) of the SAW device has to be combined with an appropriate electrical network in order to properly match the simulation to the measured data. The circuit model to be used is given in figure 4-1.

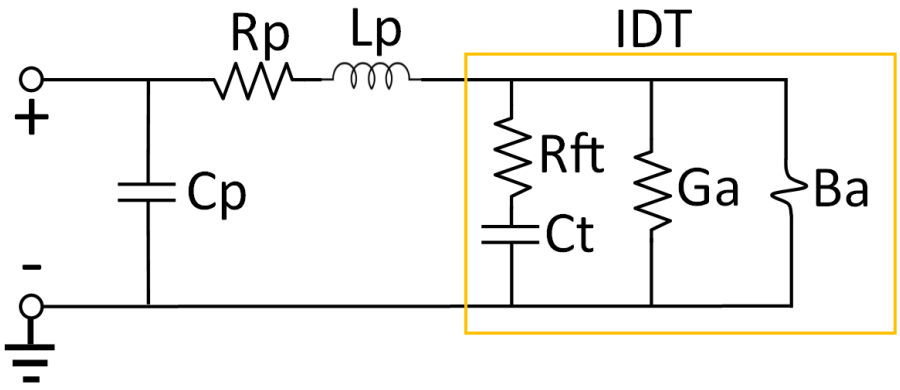

Figure 4-1. Circuit model used to include contact and probe pad parasitics. The IDT portion of the circuit is not used in this chapter.

In this circuit, the lower case "p" subscript refers to the parasitics outside the IDT—Rp includes the effects of the contact resistance and probe pad resistance. Ct is the transducer capacitance, Ga the radiation conductance, and Ba the Hilbert Transform susceptance. Within the IDT there is sheet resistance loss resulting from the thin aluminum film of the device—here denoted as Rft to refer to the entire transducer, instead of the single cell finger resistance, Rf. The IDT portion of the circuit, based on the impulse response (IR) model is not used in this chapter. This version of the IDT model which places Rft inside the 3-leg junction next to Ct is taken from Figure 2-8 of

Fisher's dissertation [12]. Another way to model Rft is to place it outside the 3-leg junction, in series with Rp—this version of the IDT model is found in Figure 7-43 of Puccio's dissertation [8] and also referred to in [33] as the 1st order circuit of choice for the IDT.

At the moment the author is concerned with extracting the parasitics for combination with COM model simulations of the SPUDTs, so that the combined simulation can be compared against measured data. The measured device response (S-parameters or any other mapping of S-parameters like admittance or impedance) gives us two equations, a real part and an imaginary part, for a range of frequencies—therefore two knowns for each frequency point. The two unknowns can be solved by minimizing the difference between predicted and measured, over a wide range of frequencies. In the circuit of figure 4-1 if Ct and Rft are known, and Lp assumed to be zero which is a good approximation, the two unknowns Cp and Rp can be calculated—Ga and Ba really just occur at near center frequency and can be approximately smoothed or interpolated out, so that basically two lines remain so having the shape Ga or Ba is not necessary. Figure 4-2 is an impulse response fit of measured data from a 30cell EWC device at 1st harmonic. The bottom trace is the conductance and top trace the susceptance. Blue corresponds to the measured device and red to the impulse response fit. The top straight blue line is a smoothed susceptance and bottom straight blue line is an interpolated plus smoothed conductance, of the measured data.

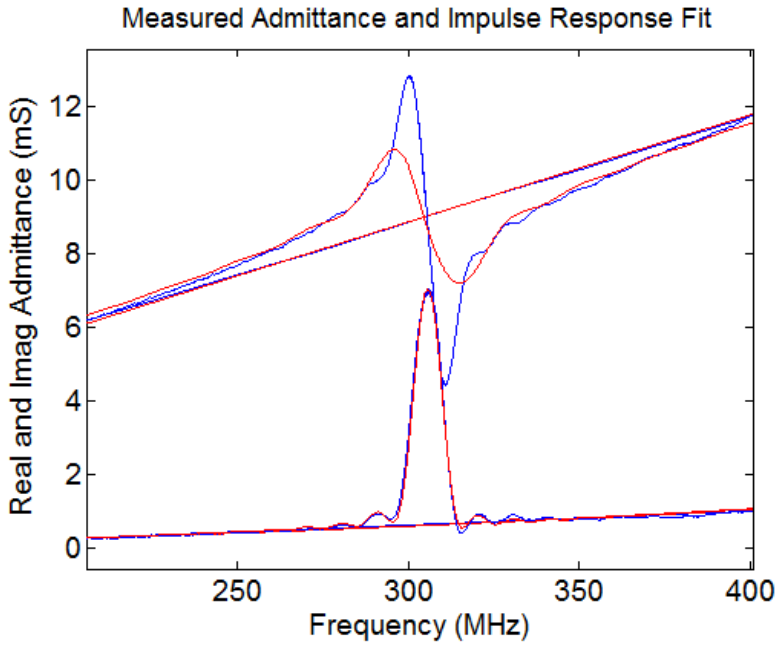

Figure 4-2. Impulse Response fit of measured data form a 30cell EWC device at 1st harmonic. The bottom trace is the conductance and top trace the susceptance. Blue corresponds to the measured device and red to the Impulse Response fit. The top straight blue line is a smoothed susceptance and bottom straight blue line is an interpolated plus smoothed conductance, of the measured data.

To generate the straight red lines, Ga=0 is set in the impulse response model; predicting shape can help with the extraction of unknown parameters, but not used here.

In the Nelder-Mead optimization that was run to obtain the fit data shown in figure 4-2, parasitic parameters were already known. The scaling factor of the coupling coefficient in the impulse response definition of Ga was adjusted to match the level of the conductance. The straight lines were used by the optimization to find Rft and Ct. There were two equations and two unknowns. Perhaps the shape could help solve for more unknowns, but have to be careful because I've tried to solve for a 3rd parameter and it seems to have solved for 3 parameters with 2 unknowns, but after some time the optimization began to diverge in a straight line—so it basically found multiple solutions, it found a ratio between parameters that solved but could not give specific

solutions. With this said, trying to extract all the above parasitics from only the device of interest may be possible, but we'll make use of two dedicated structures to do this.

The approach that is taken to extract the parasitics is to build two test structures—an open probe pad and a shorted probe pad (approximate short since the film has resistance). These are shown in Figure 4-3.

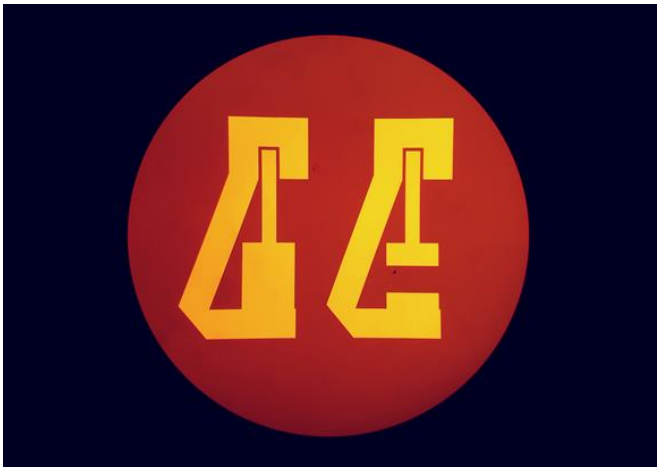

Figure 4-3. Open (right) and approximately shorted (left) probe pad structures used for parasitic extraction.

The probe pads for all of the devices have been kept the same so that the parasitics extraction doesn't have to be done multiple times—especially since the film thickness is about the same, so reusing the same values for Cp, Rp, and Lp is reasonably valid.

Using the two separate probe pad structures, good approximations can be obtained for the three parasitic parameters in our circuit model. First the open structure is used to obtain a value for Cp. According to our circuit model, an open IDT would give no current through the inductor or resistor. Well, this is not a perfect model, in reality the whole probe pad is really a distributed capacitor (a bunch of them all along the probe pad between hot and ground), and there is resistance throughout. Perhaps it's a better idea to change our circuit by placing the parallel capacitor between the resistor and inductor, or perhaps use two capacitors, one before and one after, but

we'll just leave it how it is, but that's the kind of rationale used in brainstorming how to model things with lumped elements—try to capture the most pronounced phenomenological effects with as few lumped elements as possible.

The dual objective optimization uses the Z-parameters so that Cp and some series resistance Rpp (not show in circuit model) will nicely decouple into an imaginary part that is only influenced by Cp and the real part is only influenced by Rpp, approximately. Two equations and two unknowns are solved for, Cp and Rpp, but Rpp is discarded and and Cp kept to use in the shorted structure simulation. The shorted probe pad structure is used on a second optimization of the full parasitic part of the circuit with the IDT shorted—the value of Cp is known, and Rp and Lp are solved using another dual objective optimization, again minimizing the difference between measured and circuit model, real and imaginary parts over the whole frequency band.

The extraction program is run for these two probe pad structures at both a 300MHz and a 900MHz center frequency, each over a 300MHz frequency span. The results are consistent, giving the following values at the 150-450MHz range: $Cp = 6.91 \cdot 10^{-13}F$, $Rp = 5.25\Omega$, and $Lp = 1.13 \cdot 10^{-9}H$. At the 750-1050MHz range the calculated values are: $Cp = 6.54 \cdot 10^{-13}F$, $Rp = 5.39\Omega$, and $Lp = 1.12 \cdot 10^{-9}H$. The results are consistent. The measured and circuit-modeled real and imaginary parts of the impedance and conductance are shown in figure 4-4 .

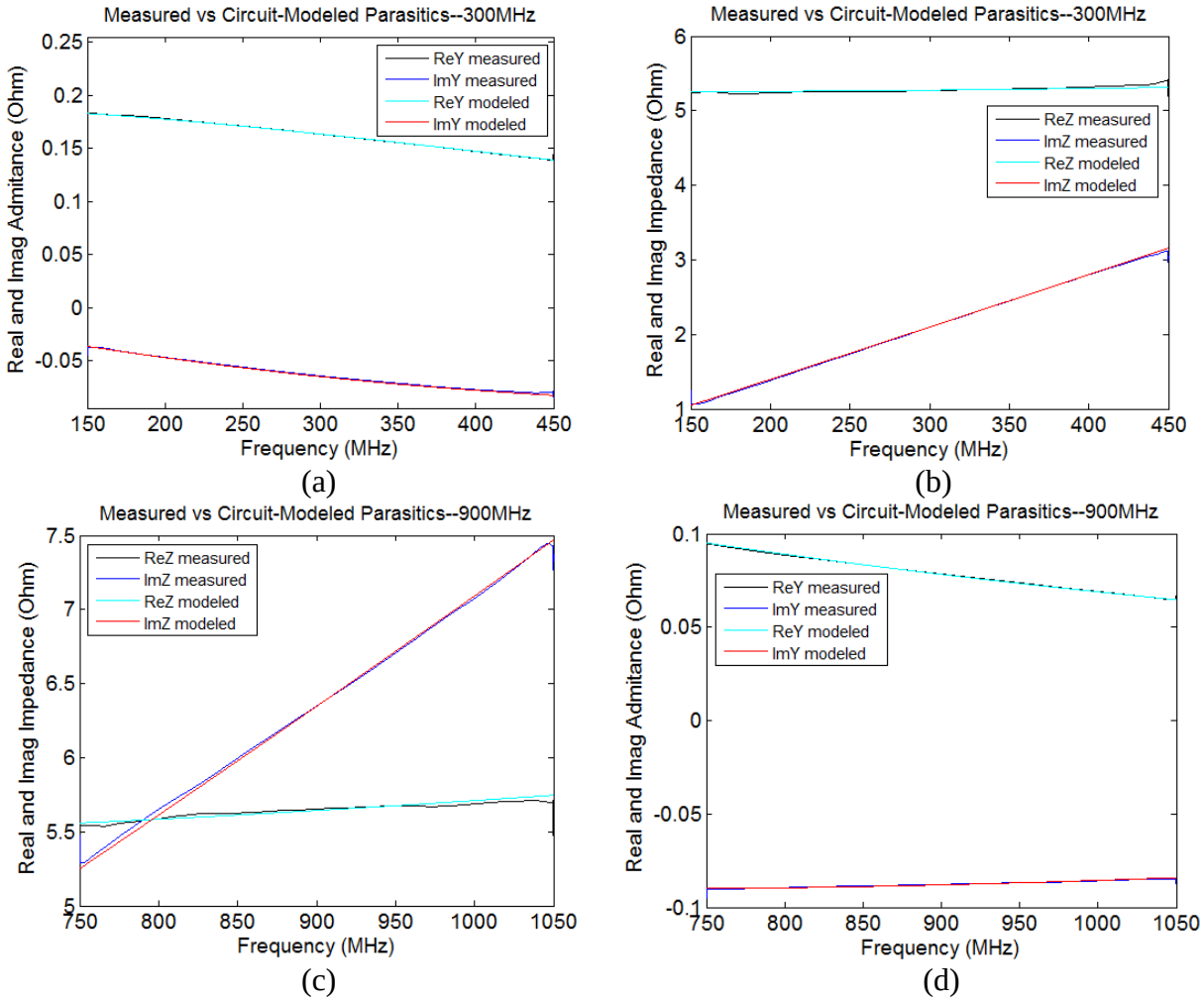

Figure 4-4. The figures show the measured vs. circuit-modeled parasitics over frequency span of 300MHz. Figures (a) and (b) correspond to the frequency span centered at 300MHz and figures (c) and (d) correspond to the frequency span centered at 900MHz. Admittances are on the left (a)(c) and impedances are on the right (b)(d).

There is good agreement over both frequency ranges. The parasitic elements obtained can now be used in conjunction with the coupling-of-modes model. The parasitics circuit is placed in ABCD matrix form, as well as the COM modeled SPUDT filters. These are cascaded and converted back to the desired parameters. The COM model fit of selected devices at the 1st harmonic of operation is presented in the following section.

4.2 1st Harmonic COM Matching of Experimental Results

The COM model fit of selected devices is now presented, 4 filters with operation at 1st and 3rd harmonic.

Two of the filters are 2hot4f0 bidirectional, the other 2 filters each have one SPUDT and one wideband (8pair) 2hot4. All of the parameters needed to replicate the coupling-of-modes simulation for each filter are given in Figure 4-5. Also included are the theoretical calculations of the transduction coefficient, the α_{Ratio} from equations F-37 and F-42 in Appendix F. Both the 1st harmonic and 3rd harmonic simulation parameters are given in Figure 4-5. It can be seen that the predicted transduction coefficient magnitudes are somewhat in the ballpark—the 2hot4f0 device(s) of filter 1 is used as the reference so it's given an α_{Ratio} of 1. From the boldface fonts in the table, EWC and optimized SPUDT parameters can easily be found—the calculated α_{Ratio} is a little high but it's consistent in that both model inputs are slightly lower than the calculated values. For a proper comparison the fabrication would need to be accurate and testing should first be done at lower frequency and over a wide range of metal thickness. Something to note is that the input values for Cf are about three times lower at 3rd harmonic. This is expected since our input for number of wavelengths increases by 3 from 1st to 3rd harmonic but the number of cells stayed the same. Another value that should approximately increase by 3 is the transduction coefficient since the number transduction sources stayed the same but the number of wavelengths tripled. What is seen from the red fonts in Figure 4-5 is that for the 2hot4f0 transducer, α_{SF} at 1st harmonic is not 3 times the 3rd harmonic value, but only scaled by 1.75—for this transducer, the coupling coefficient is supposed to be almost the same at both the 1st and 3rd harmonic, so that is one discrepancy that will remain unanswered for now. Perhaps using a crystal cut with very little 3rd

harmonic bulk mode generation might be a place to start investigating, if it were of interest to do so. Something else to note are the 3rd harmonic sheet resistance (Rs) values. If the 1st harmonic value is tripled, there still seems to be significant sheet resistance that is unaccounted for. It seems like increasing the sheet resistance, Rs, artificially helps to model non-Rayleigh radiation from the 3rd harmonic devices. It may not be an ideal way to do this since the slope of the out-of-band 1-port parameters (shown as admittance) still deviate from the COM prediction (which is excellent at 1st harmonic). However, the responses, including multiple transits are sufficiently well modeled. This helps to show areas where non-Rayleigh mode radiation is present in the S21 time domain plots. With these clarifications made, this section ends with Figure 4-5, followed by plots of the measured responses overlaid with the coupling-of-modes simulation fit. The forward and reverse SPUDT responses use the same COM parameters, except that the TC-RC angle is flipped 180^0.

Table 4-1. List showing the COM parameters needed to generate the device response figures that follow.

Filter Number	Transducer Type	Harmonic	αSF	αRatio	Calculated αRatio	Cf	Rs	γLoss	|R|	ϕTCRC	Vidt
1	2hot4f0 40pair	1	1.4	1 (reference)	1 (reference)	1.346x10^-13	2	100	0	0	3414
	2hot4f0 40pair		1.4	1 (reference)	1 (reference)	1.346x10^-13	2	100	0	0	3414
2	2hot4f0 8pair	1	1.4	1	1	1.346x10^-13	2	100	0	0	3414
	2hot4f0 40pair		1.4	1	1	1.346x10^-13	2	100	0	0	3414
3	2hot4f0 8pair	1	1.4	1	1	1.399x10^-13	3	100	0	0	3414
	EWC 40pair		1.03	**0.74**	**0.83**	1.090x10^-13	1.8	100	-0.0081	103	3419
4	2hot4f0 8pair	1	1.4	1	1	1.399x10^-13	2	100	0	0	3414
	Optimized 40pair		0.88	**0.63**	**0.72**	1.195x10^-13	1.8	100	-0.0126	114	3422
1	2hot4f0 40pair	3	0.8	1 (reference)	1 (reference)	3.857x10^-14	2x3+9	2400	0	0	3410
	2hot4f0 40pair		0.8	1 (reference)	1 (reference)	3.857x10^-14	2x3+9	2400	0	0	3410
2	2hot4f0 8pair	3	0.7667	1.02	1	4.194x10^-14	2x3+12	2400	0	0	3408
	2hot4f0 40pair		0.8133	0.96	1	4.194x10^-14	2x3+6	2400	0	0	3408
3	2hot4f0 8pair	3	0.7933	0.99	1	4.194x10^-14	3x3+9	2400	0	0	3413
	EWC 40pair		0.32	**0.4**	**0.53**	3.274x10^-14	1.8x3+9.1	800	-0.0044	70	3421
4	2hot4f0 8pair	3	0.7667	0.96	1	4.194x10^-14	2x3+12	2400	0	0	3408
	Optimized 40pair		0.53	**0.66**	**0.83**	3.812x10^-14	1.8x3+2.6	1100	-0.005	93	3421
5	2hot4f0 8pair	3rev	0.73			3.736x10^-14	2x3+12	2400	0	0	3415
	Optimized2 40pair		0.5466			3.812x10^-14	1.8x3+2.6	1400	-0.0074	102.5	3421

It should not go unnoticed that the optimized SPUDT is also an improvement over the EWC at 1st harmonic—the reflection magnitude is increased by 1.56 over the 1st harmonic EWC, with the TC-RC angle not too far from optimum. Notice the more flattened forward passband in figure 4-8b. It does have slightly lower coupling than the EWC at the 1st harmonic.

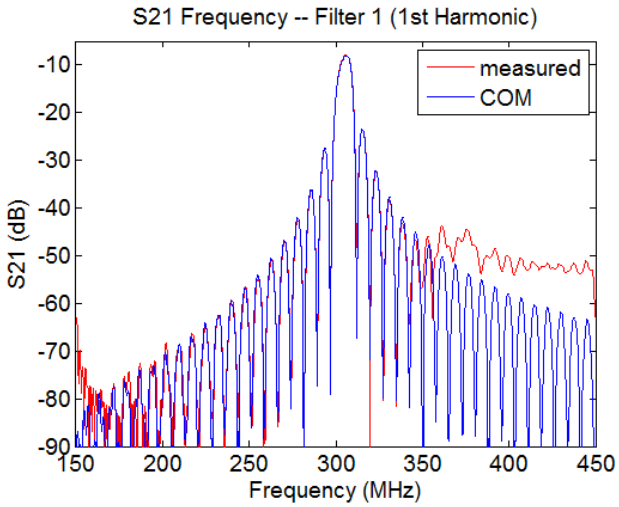
S21 Frequency -- Filter 1 (1st Harmonic)
measured
COM
S21 (dB)
Frequency (MHz)

(a)

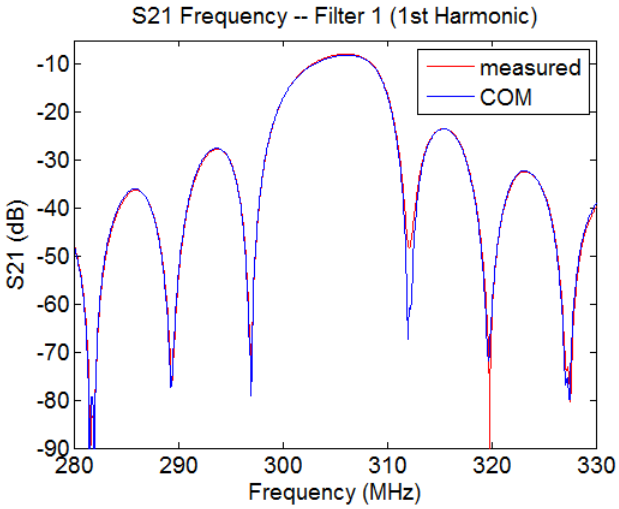
S21 Frequency -- Filter 1 (1st Harmonic)
measured
COM
S21 (dB)
Frequency (MHz)

(b)

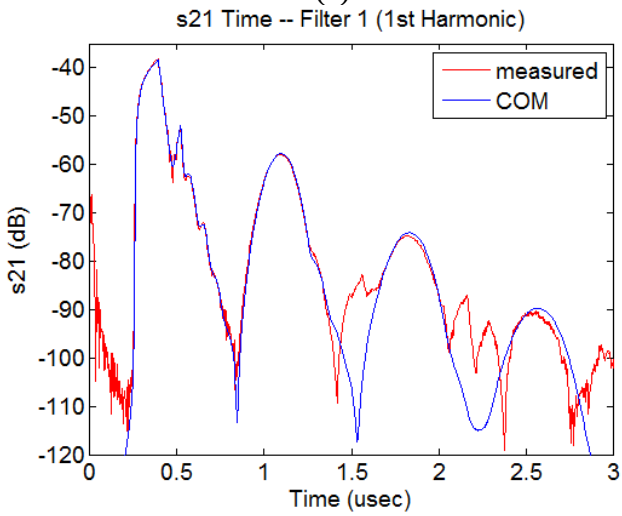
s21 Time -- Filter 1 (1st Harmonic)
measured
COM
s21 (dB)
Time (usec)

(c)

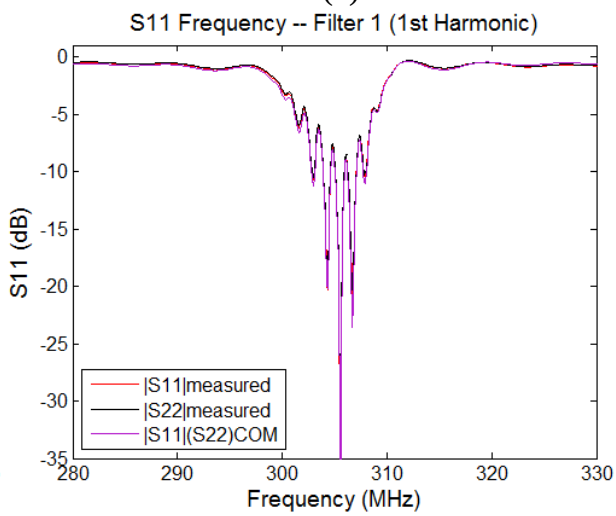
S11 Frequency -- Filter 1 (1st Harmonic)
|S11|measured
|S22|measured
|S11|(S22)COM
S11 (dB)
Frequency (MHz)

(d)

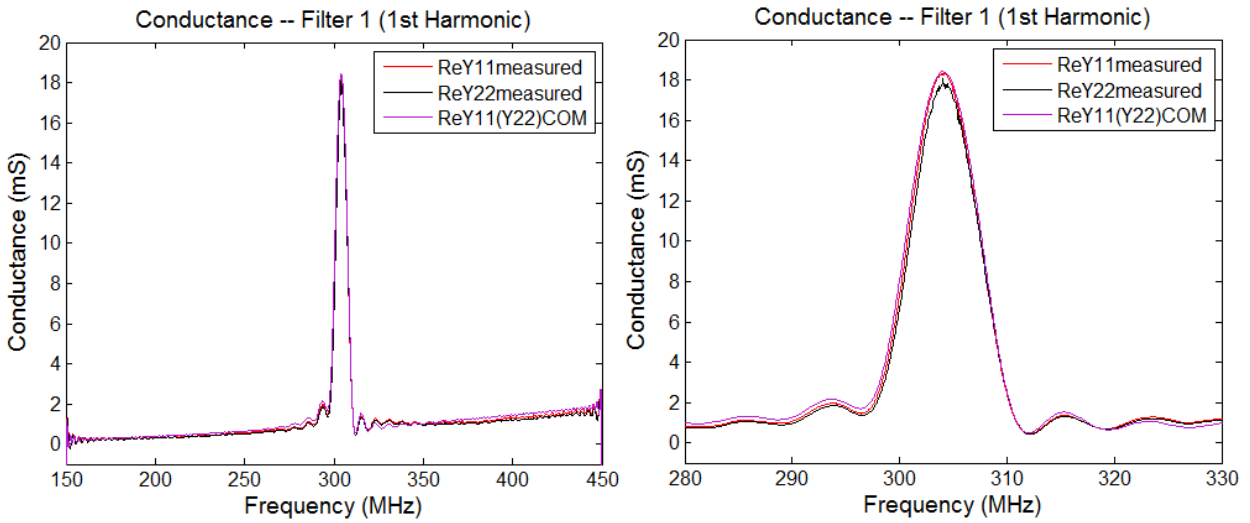

(e)

(f)

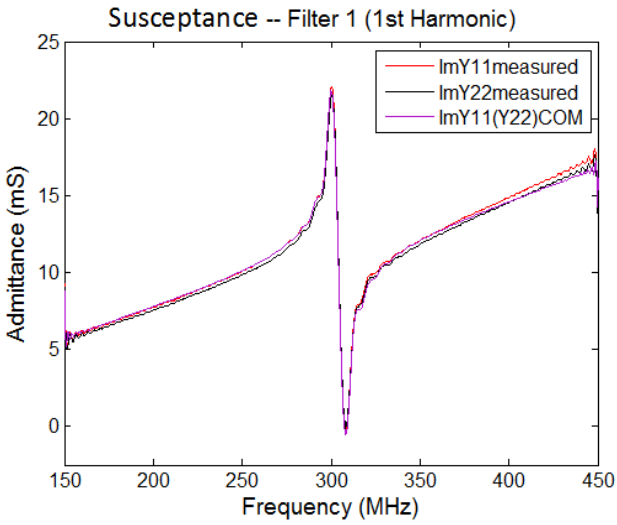

(g)

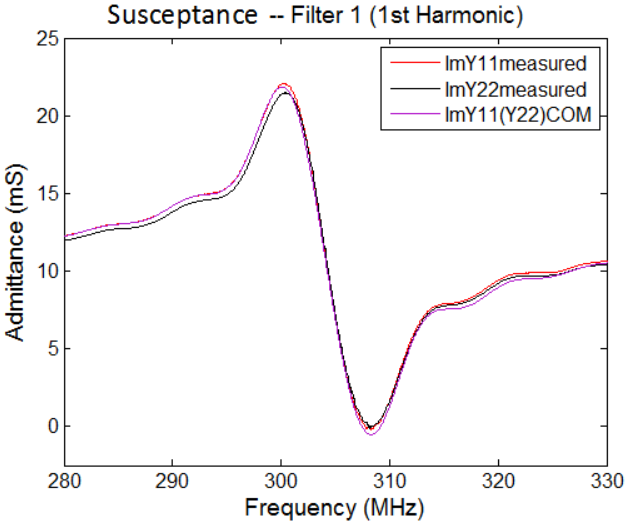

(h)

Figure 4-5. The figures (a) through (h) show the measured and COM fit of responses of filter 1 which is composed of 2 bidirectional 2hot4f0 transducers, 40pair each, operating at 1st harmonic. (a) and (b) S21 frequency, (c) S21 time, (d) S11 frequency with echoes, (e) and (f) conductance, (g) and (h) admittance.

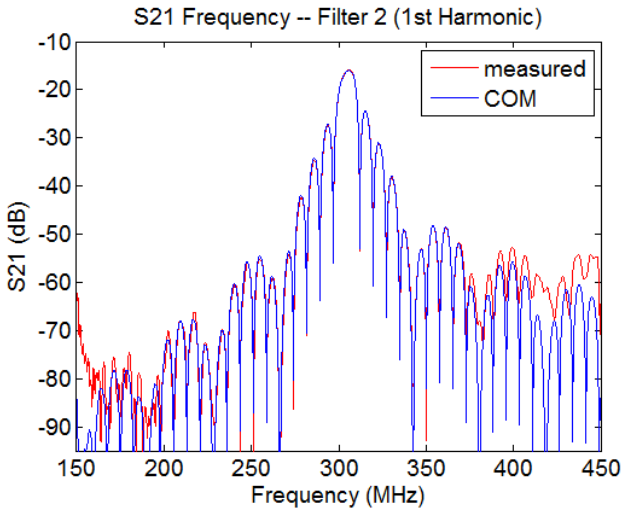
S21 Frequency -- Filter 2 (1st Harmonic)
measured
COM
S21 (dB)
Frequency (MHz)

(a)

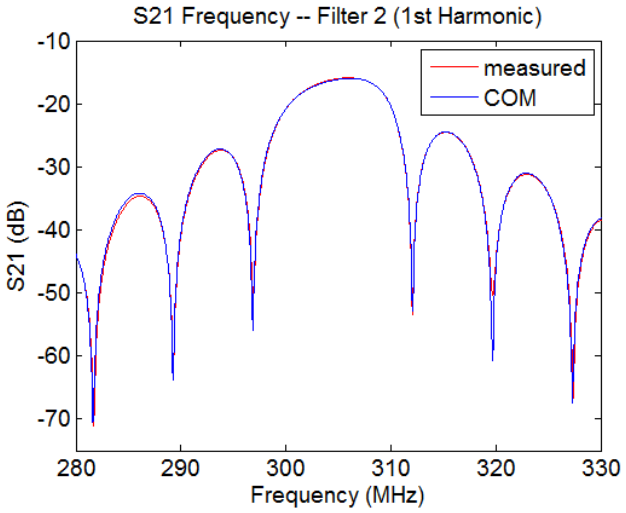
S21 Frequency -- Filter 2 (1st Harmonic)
measured
COM
S21 (dB)
Frequency (MHz)

(b)

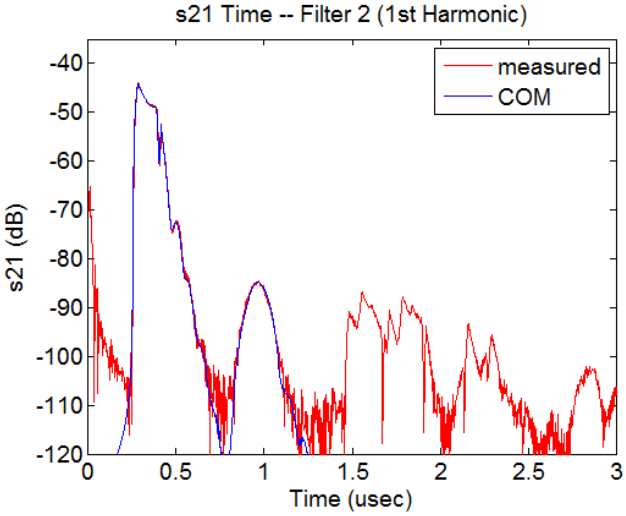
s21 Time -- Filter 2 (1st Harmonic)
measured
COM
s21 (dB)
Time (usec)

(c)

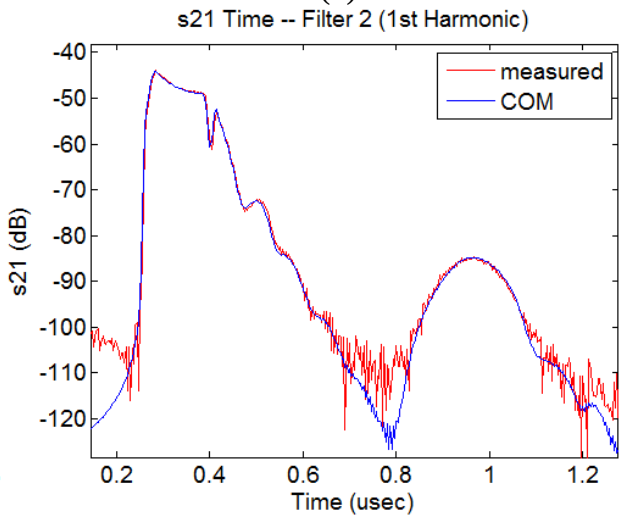
s21 Time -- Filter 2 (1st Harmonic)
measured
COM
s21 (dB)
Time (usec)

(d)

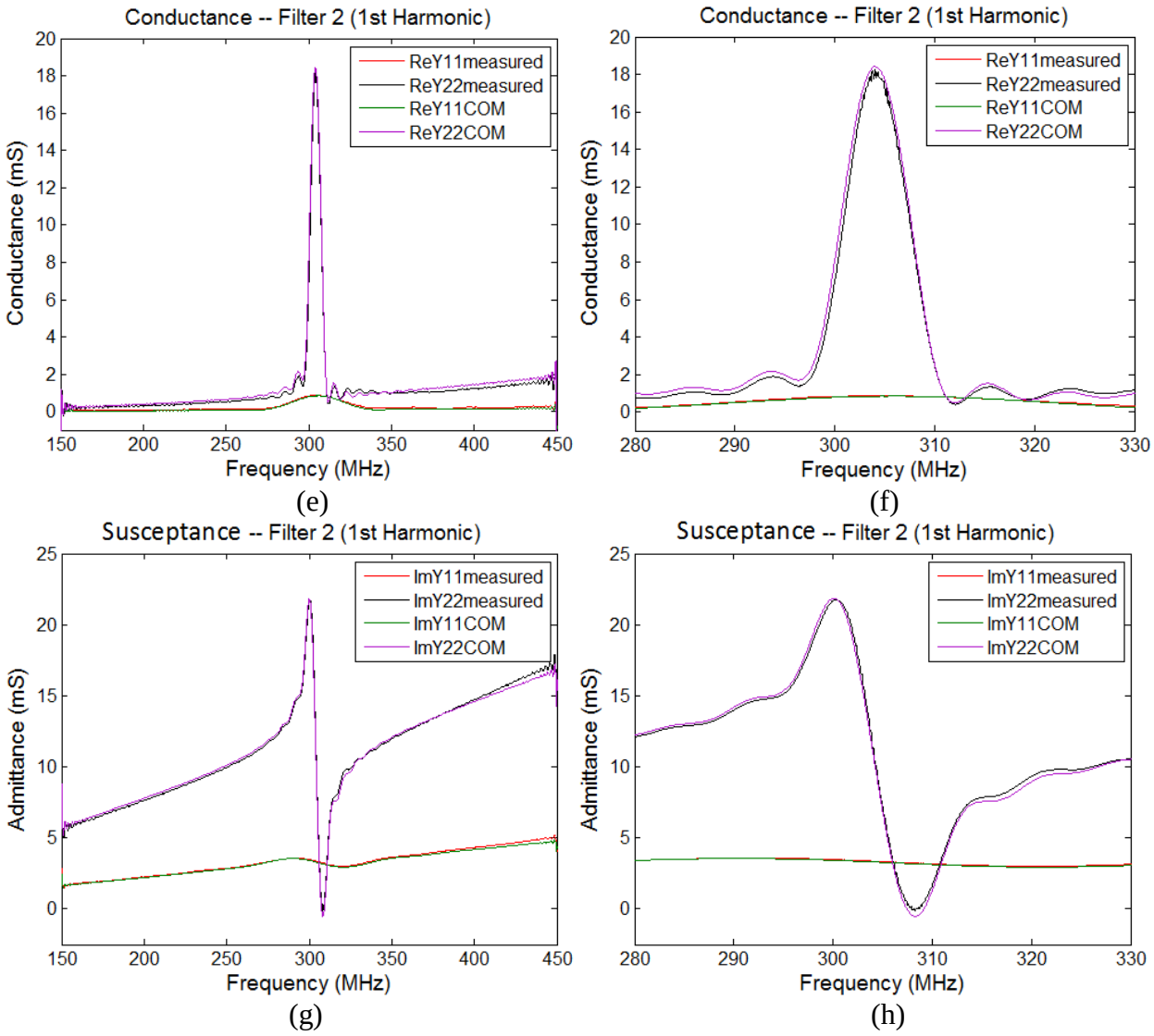

Figure 4-6. The Figures (a) through (h) show the measured and COM fit of responses of filter 2 which is composed of 2 bidirectional 2hot4f0 transducers, 8pair 2hot4f0 on port 1 and a 40pair on 2, operating at 1st harmonic. (a) and (b) S21 frequency, (c) and (d) S21 time, (e) and (f) conductance, (g) and (h) admittance.

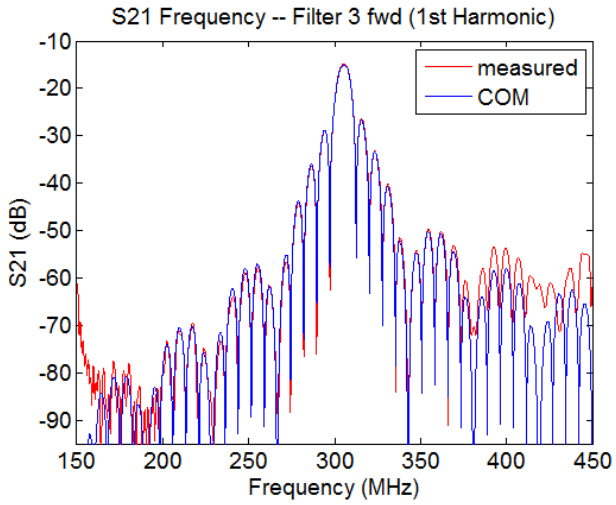
S21 Frequency -- Filter 3 fwd (1st Harmonic)
measured
COM
S21 (dB)
Frequency (MHz)

(a)

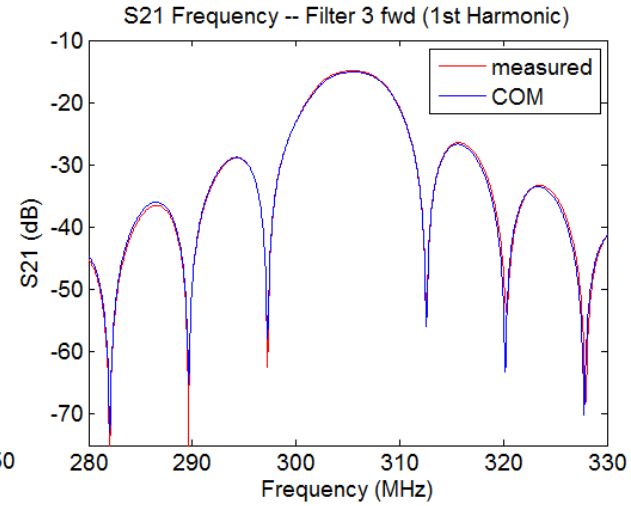
S21 Frequency -- Filter 3 fwd (1st Harmonic)
measured
COM
S21 (dB)
Frequency (MHz)

(b)

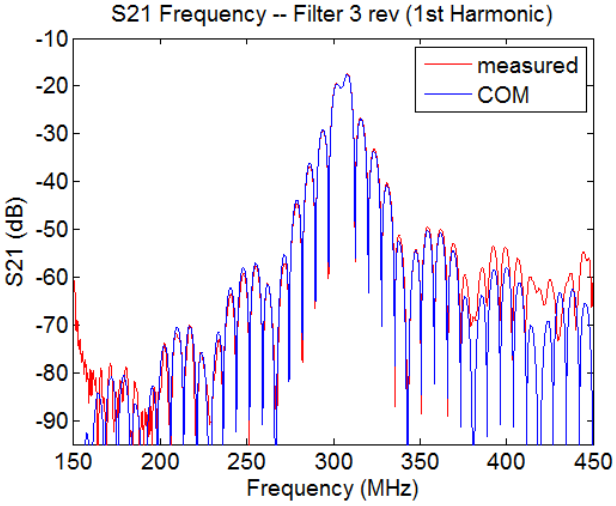
S21 Frequency -- Filter 3 rev (1st Harmonic)
measured
COM
S21 (dB)
Frequency (MHz)

(c)

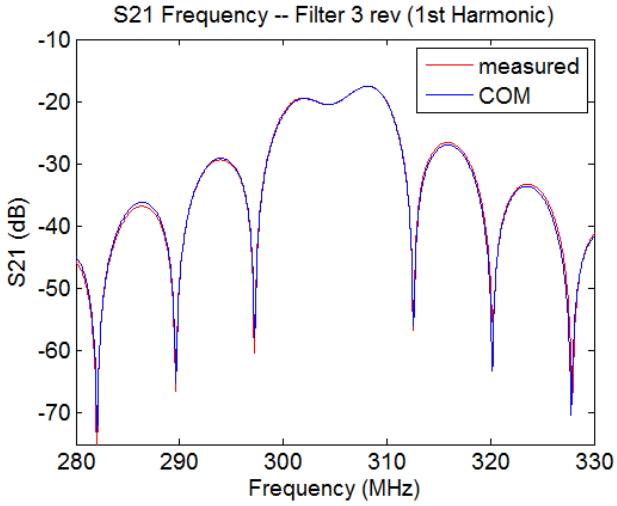
S21 Frequency -- Filter 3 rev (1st Harmonic)
measured
COM
S21 (dB)
Frequency (MHz)

(d)

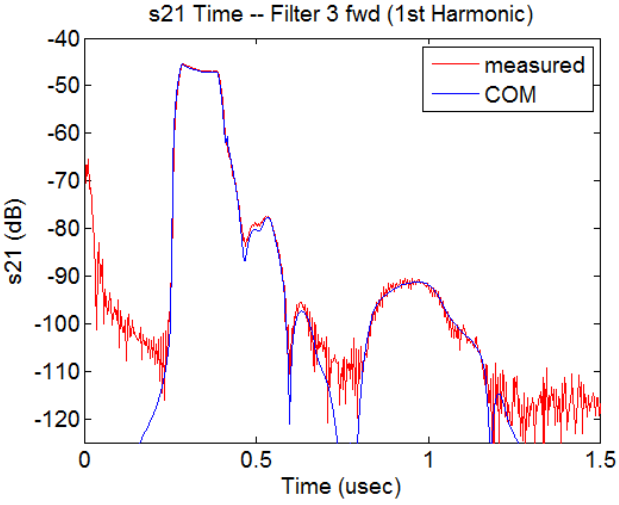
s21 Time -- Filter 3 fwd (1st Harmonic)
measured
COM
s21 (dB)
Time (usec)

(e)

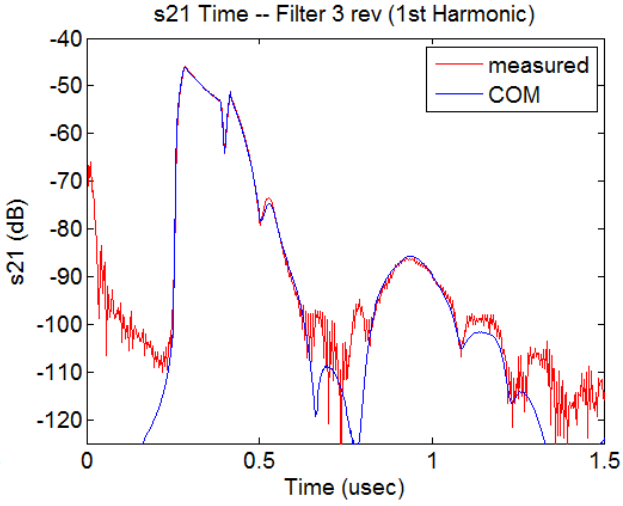
s21 Time -- Filter 3 rev (1st Harmonic)
measured
COM
s21 (dB)
Time (usec)

(f)

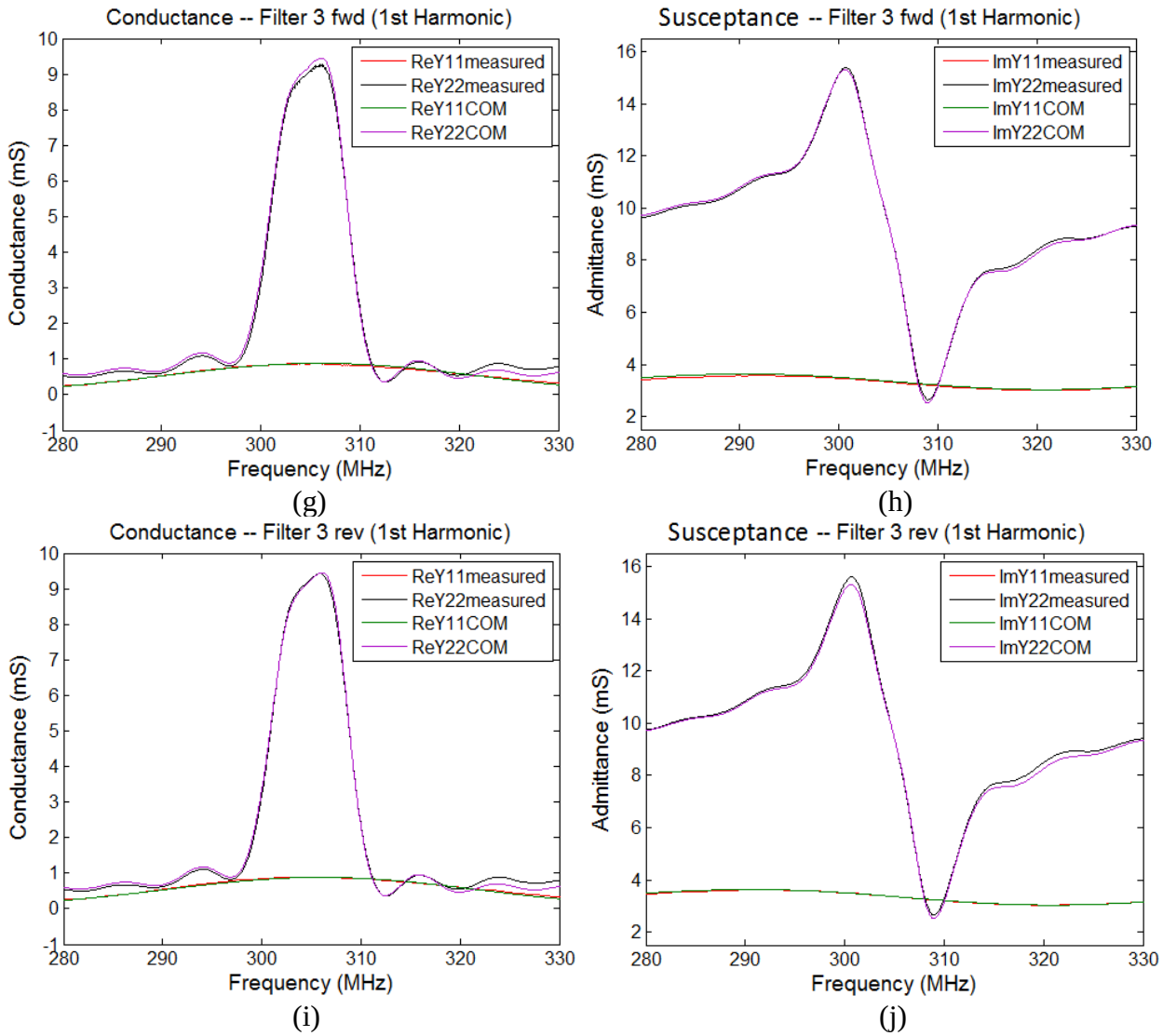

Figure 4-7. The figures (a) through (j) show the measured and COM fit of responses of filter 3 which is composed of an 8pair 2hot4f0 bidirectional on port 1 and a 40pair EWC SPUDT on 2, operating at 1st harmonic. (a) and (b) fwd S21 frequency, (c) and (d) rev S21 frequency, (e) fwd S21 time, (f) rev S21 time, (g) and (h) conductance, (i) and (j) admittance.

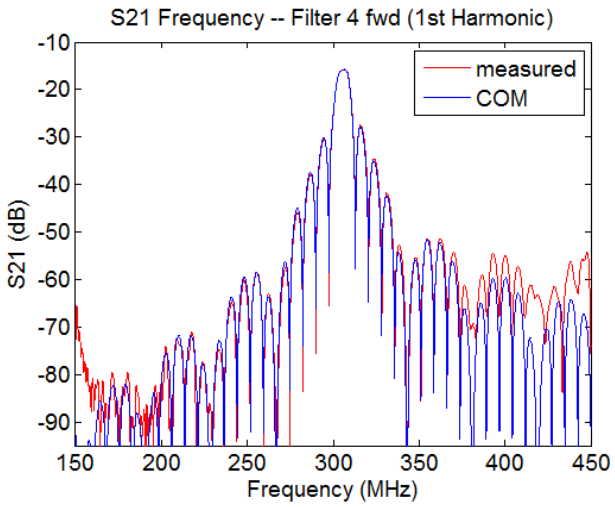
S21 Frequency -- Filter 4 fwd (1st Harmonic)
measured
COM
S21 (dB)
Frequency (MHz)

(a)

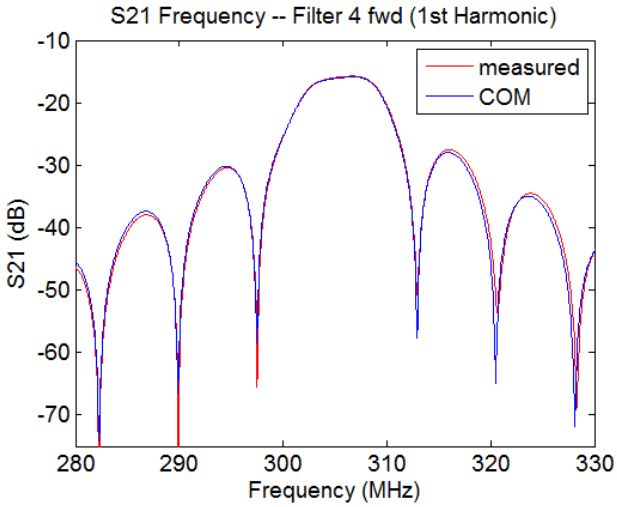
S21 Frequency -- Filter 4 fwd (1st Harmonic)
measured
COM
S21 (dB)
Frequency (MHz)

(b)

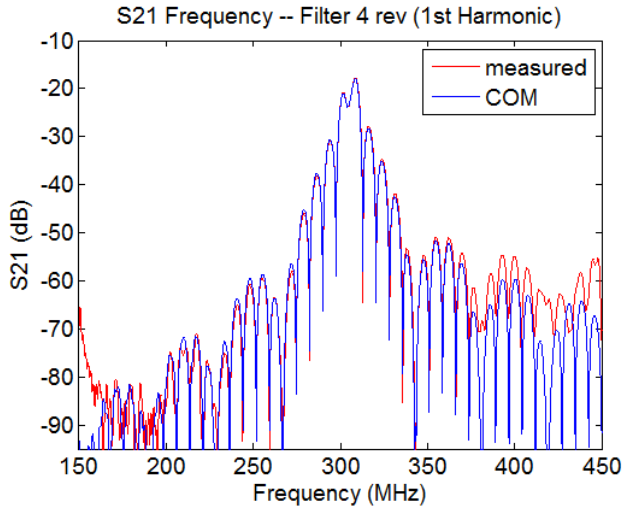
S21 Frequency -- Filter 4 rev (1st Harmonic)
measured
COM
S21 (dB)
Frequency (MHz)

(c)

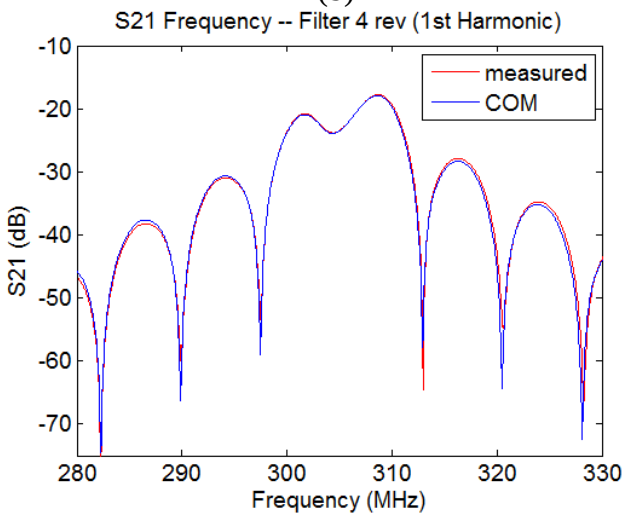
S21 Frequency -- Filter 4 rev (1st Harmonic)
measured
COM
S21 (dB)
Frequency (MHz)

(d)

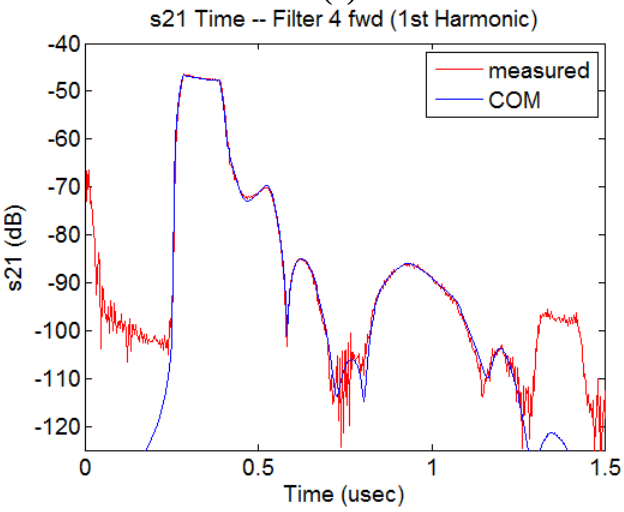
s21 Time -- Filter 4 fwd (1st Harmonic)
measured
COM
s21 (dB)
Time (usec)

(e)

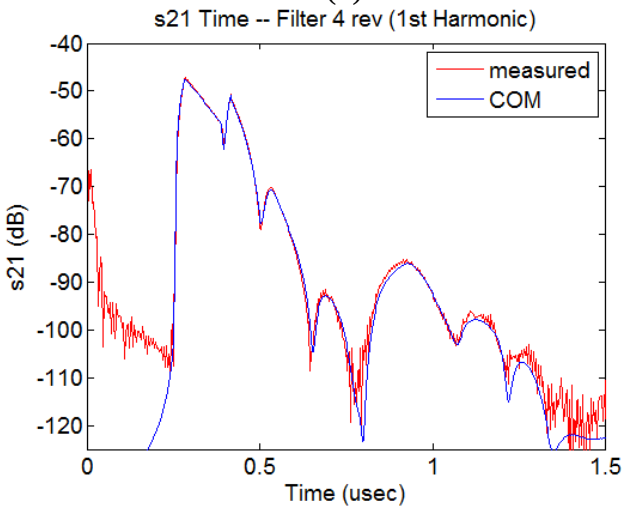
s21 Time -- Filter 4 rev (1st Harmonic)
measured
COM
s21 (dB)
Time (usec)

(f)

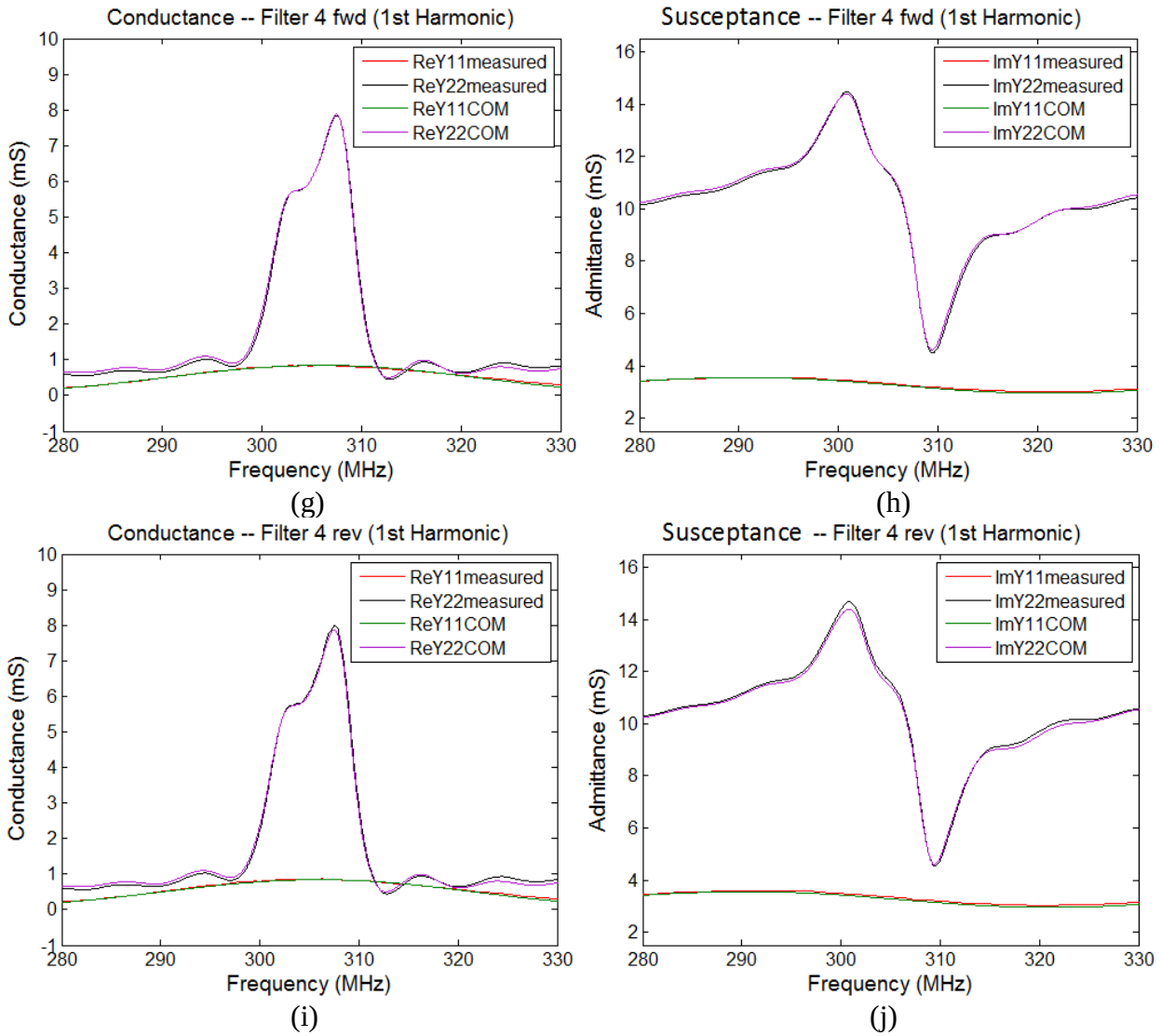

Figure 4-8. The figures (a) through (j) show the measured and COM fit of responses of filter 4 which is composed of an 8pair 2hot4f0 bidirectional on port 1 and a 40pair optimized SPUDT on 2, operating at 1st harmonic. The optimized SPUDT is also an improvement at 1st harmonic—the reflection magnitude is increased by 1.56 over the 1st harmonic EWC. (a) and (b) fwd S21 frequency, (c) and (d) rev S21 frequency, (e) fwd S21 time, (f) rev S21 time, (g) and (h) conductance, (i) and (j) admittance.

4.3 3rd Harmonic COM Matching of Experimental Results

This section continues from the previous section, but the COM model is used now to match the 3rd harmonic operating devices. The Raleigh mode that the COM model simulates is not as clean as at the 1st harmonic operation. Also, the port 1 and port 2 responses that seemed almost indistinguishable at 1st harmonic, will show distinct differences at 3rd harmonic. The measured responses with overlapped simulation are given in Figure 4-9 through Figure 4-12. The COM modeling parameters are given in the bottom half of Figure 4-5 in previous section.

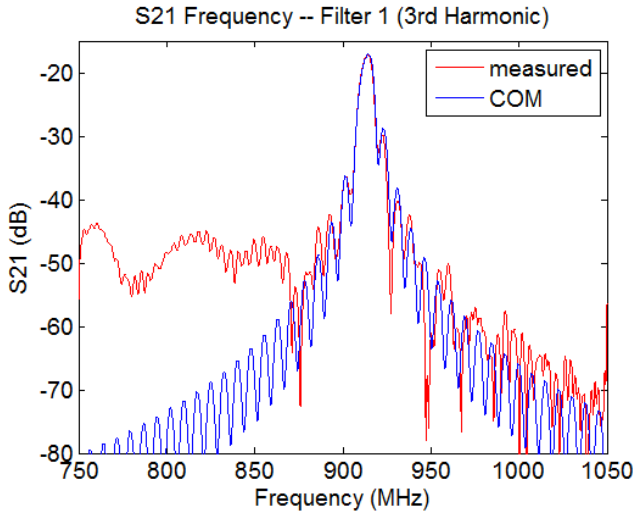

(a)

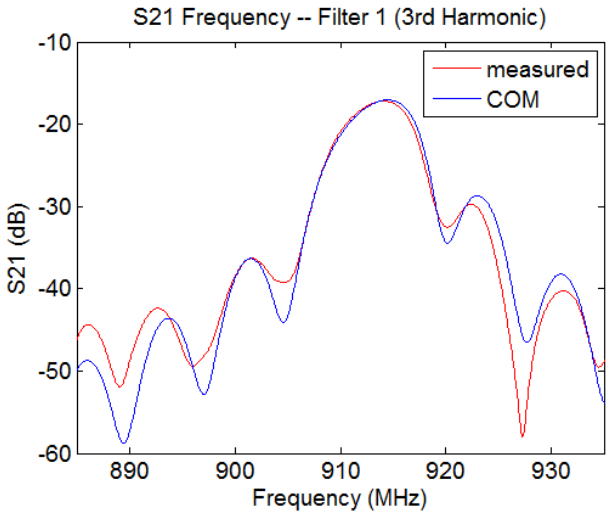

(b)

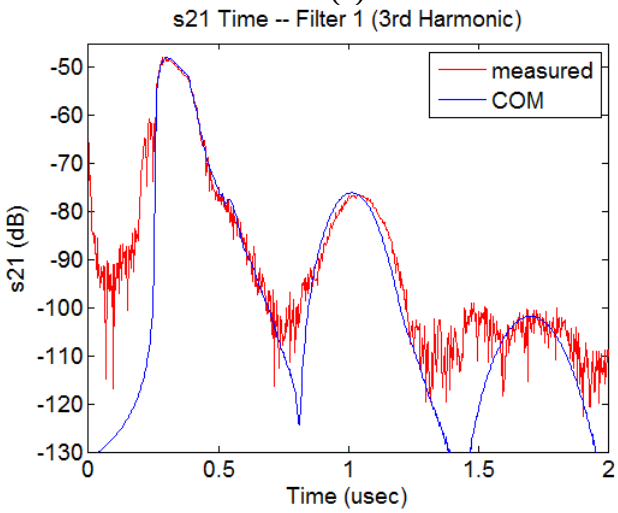

(c)

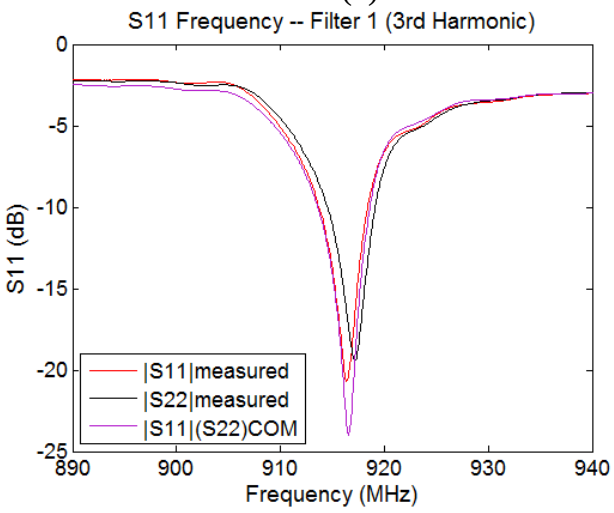

(d)

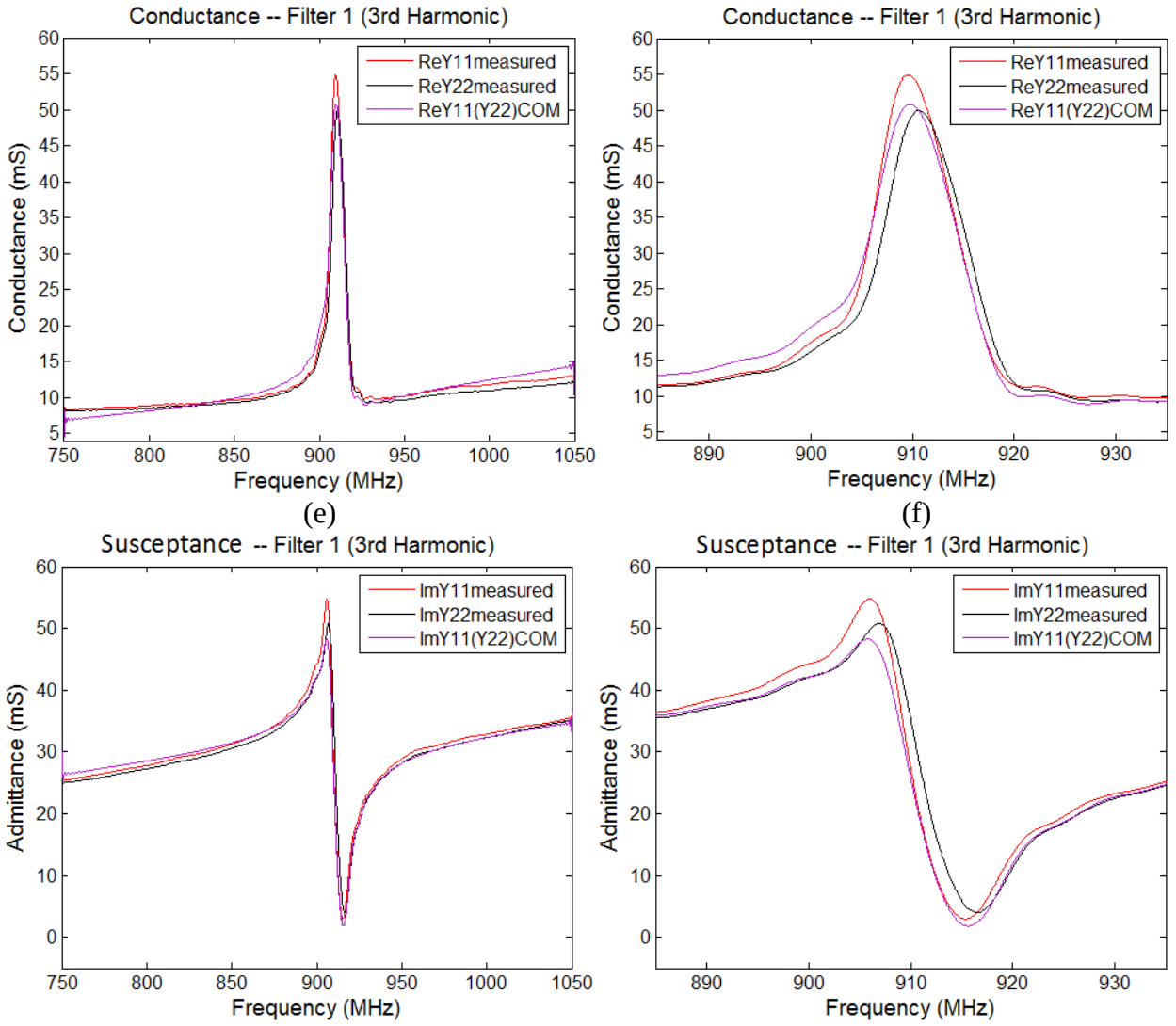

Figure 4-9. The figures (a) through (h) show the measured and COM fit of responses of filter 1 which is composed of 2 bidirectional 2hot4f0 transducers, 40pair each, operating at 3rd harmonic. (a) and (b) S21 frequency, (c) S21 time, (d) S11 frequency, (e) and (f) conductance, (g) and (h) susceptance.

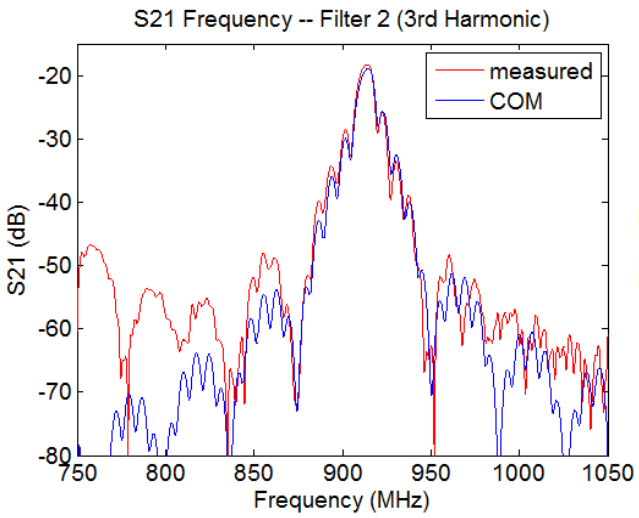
S21 Frequency -- Filter 2 (3rd Harmonic)
measured
COM
S21 (dB)
Frequency (MHz)

(a)

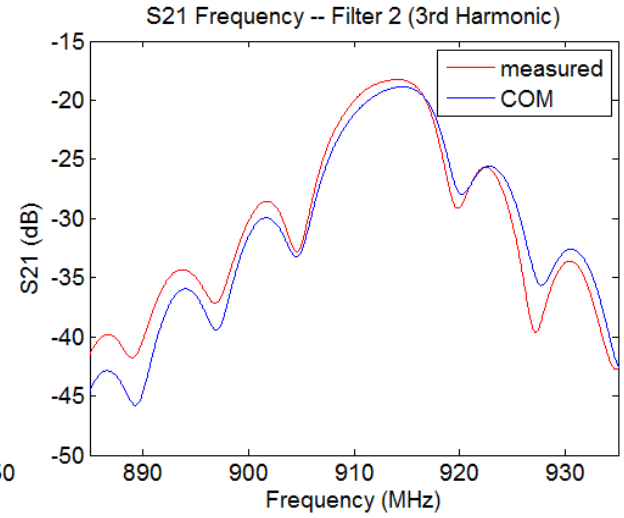
S21 Frequency -- Filter 2 (3rd Harmonic)
measured
COM
S21 (dB)
Frequency (MHz)

(b)

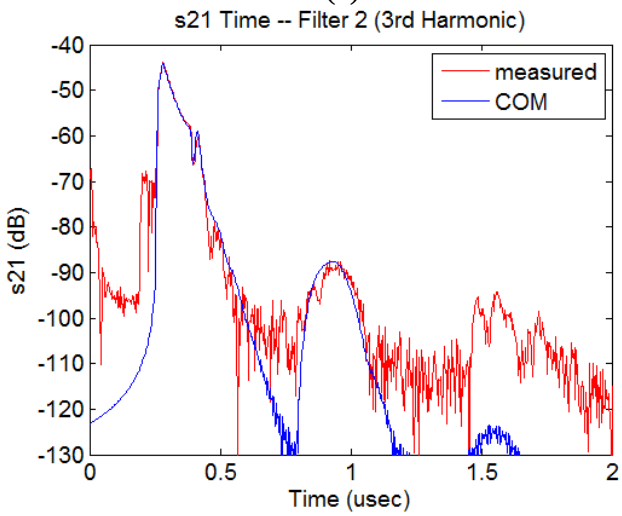
s21 Time -- Filter 2 (3rd Harmonic)
measured
COM
s21 (dB)
Time (usec)

(c)

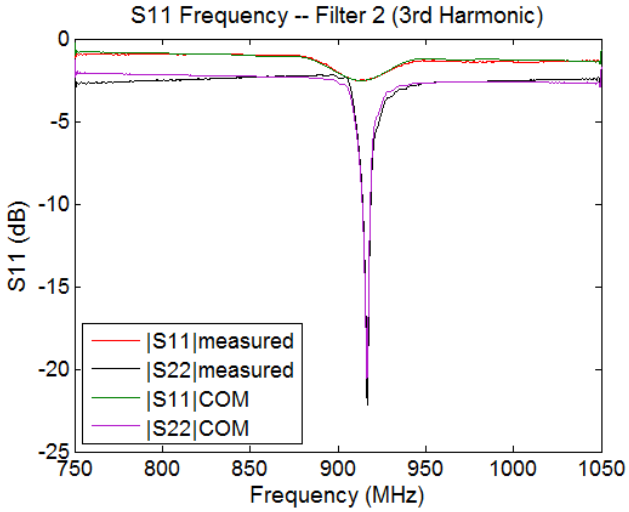
S11 Frequency -- Filter 2 (3rd Harmonic)
|S11|measured
|S22|measured
|S11|COM
|S22|COM
S11 (dB)
Frequency (MHz)

(d)

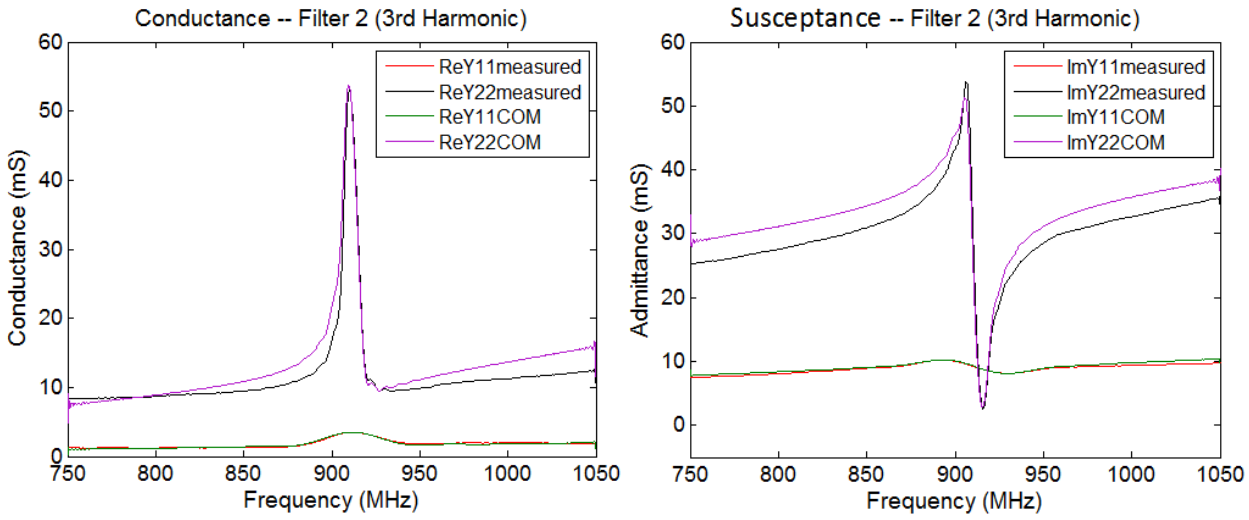

(e) (f)

Figure 4-10. The figures (a) through (f) show the measured and COM fit of responses of filter 2 which is composed of 2 bidirectional 2hot4f0 transducers, 8pair 2hot4f0 on port 1 and a 40pair on 2, operating at 3rd harmonic. (a) and (b) S21 frequency, (c) S21 time, (d) S11 frequency, (e) conductance, (f) susceptance.

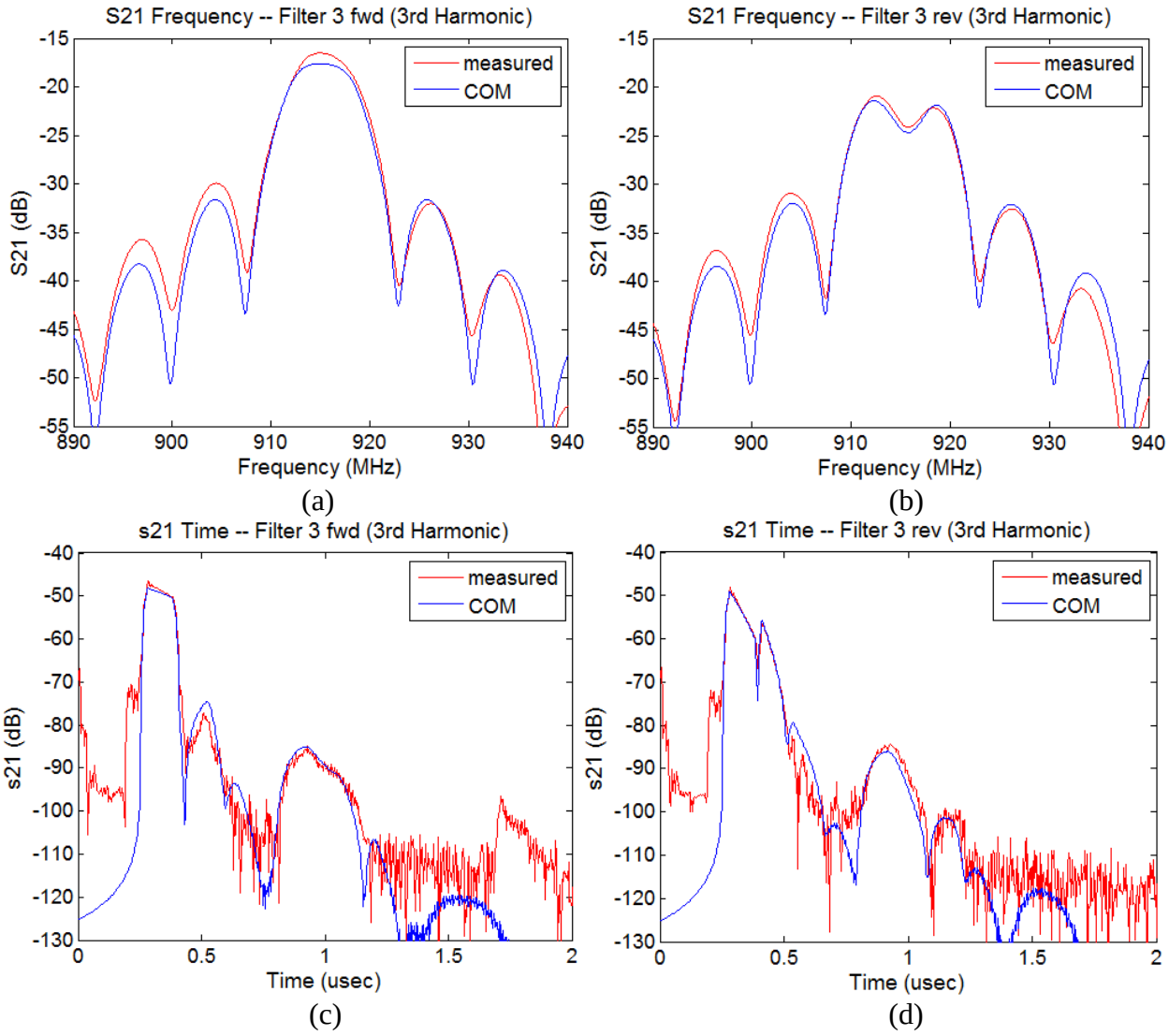
S21 Frequency -- Filter 3 fwd (3rd Harmonic)
measured
COM
S21 (dB)
Frequency (MHz)
(a)
S21 Frequency -- Filter 3 rev (3rd Harmonic)
measured
COM
S21 (dB)
Frequency (MHz)
(b)
s21 Time -- Filter 3 fwd (3rd Harmonic)
measured
COM
s21 (dB)
Time (usec)
(c)
s21 Time -- Filter 3 rev (3rd Harmonic)
measured
COM
s21 (dB)
Time (usec)
(d)

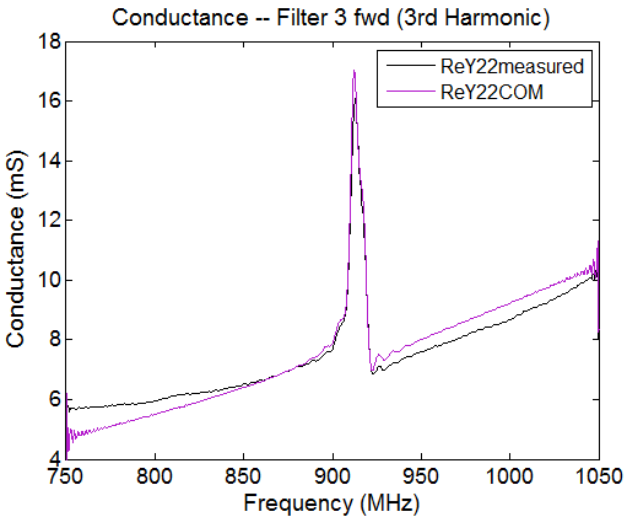
Conductance -- Filter 3 fwd (3rd Harmonic)
ReY22measured
ReY22COM
Conductance (mS)
Frequency (MHz)

(e)

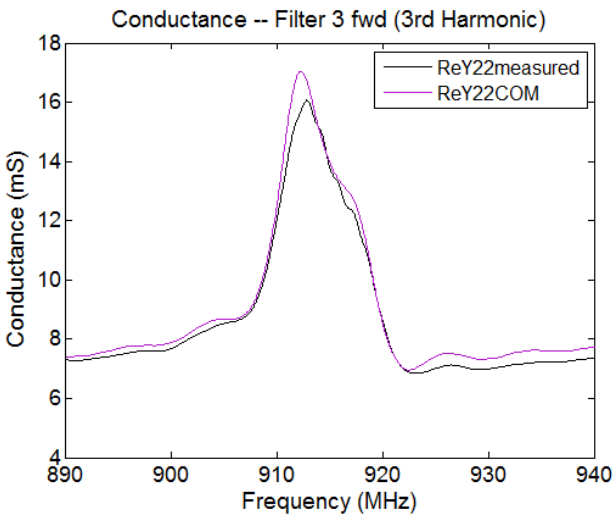
Conductance -- Filter 3 fwd (3rd Harmonic)
ReY22measured
ReY22COM
Conductance (mS)
Frequency (MHz)

(f)

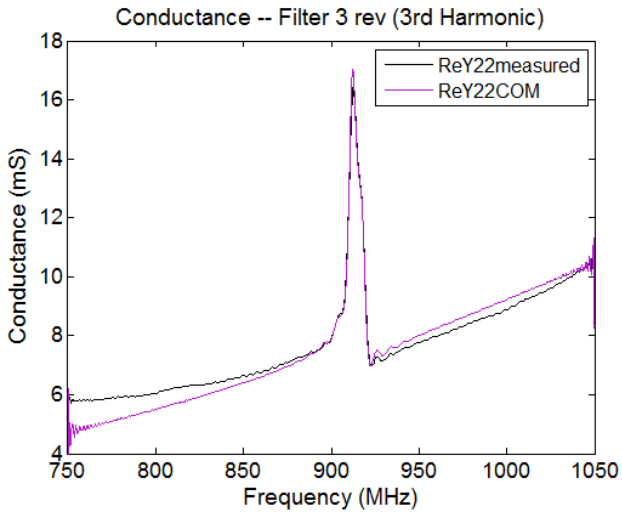
Conductance -- Filter 3 rev (3rd Harmonic)
ReY22measured
ReY22COM
Conductance (mS)
Frequency (MHz)

(g)

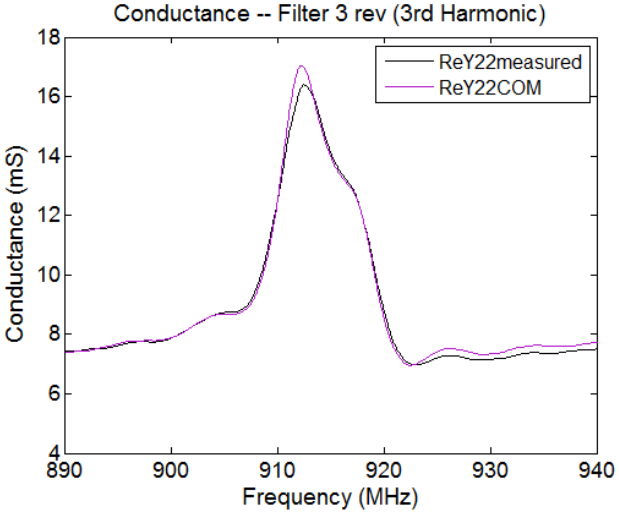
Conductance -- Filter 3 rev (3rd Harmonic)
ReY22measured
ReY22COM
Conductance (mS)
Frequency (MHz)

(h)

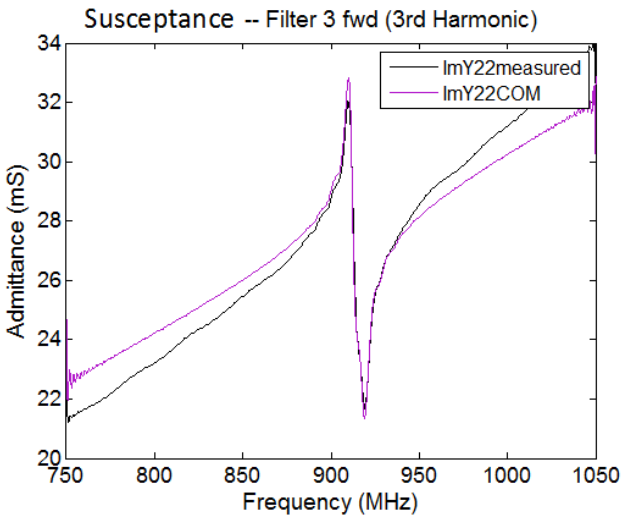
Susceptance -- Filter 3 fwd (3rd Harmonic)
ImY22measured
ImY22COM
Admittance (mS)
Frequency (MHz)

(i)

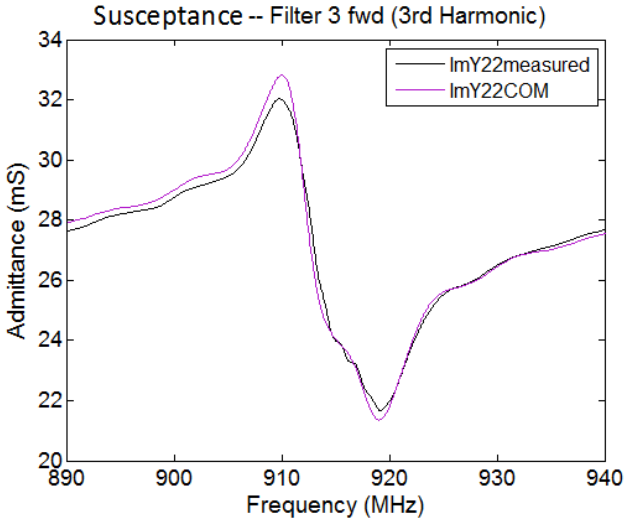
Susceptance -- Filter 3 fwd (3rd Harmonic)
ImY22measured
ImY22COM
Admittance (mS)
Frequency (MHz)

(j)

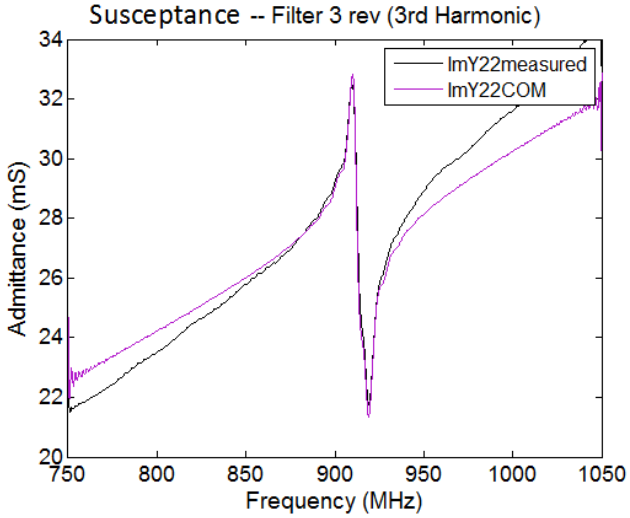
Susceptance -- Filter 3 rev (3rd Harmonic)
ImY22measured
ImY22COM
Admittance (mS)
Frequency (MHz)

(k)

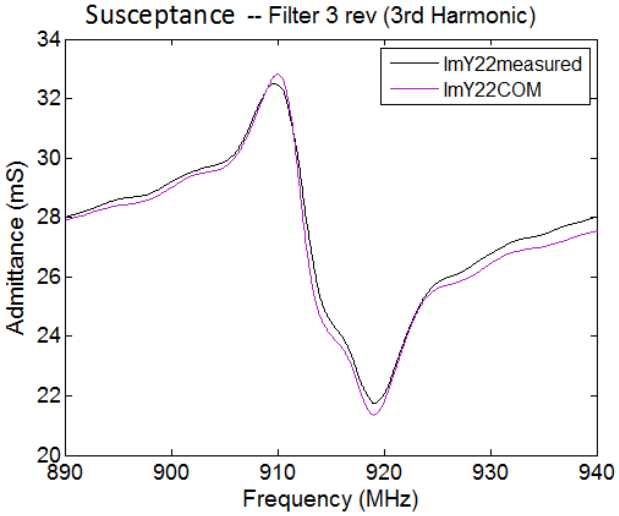
Susceptance -- Filter 3 rev (3rd Harmonic)
ImY22measured
ImY22COM
Admittance (mS)
Frequency (MHz)

(l)

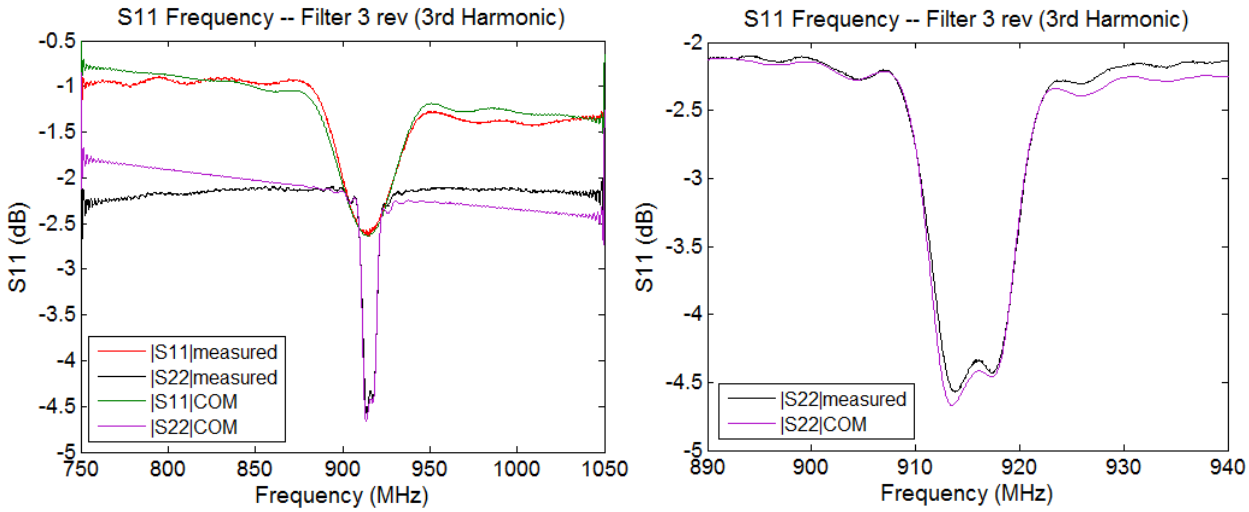

(m) (n)

Figure 4-11. The figures (a) through (l) show the measured and COM fit of responses of filter 3 which is composed of an 8pair 2hot4f0 bidirectional on port 1 and a 40pair EWC SPUDT on 2, operating at 3rd harmonic. (a) S21 fwd frequency, (b) S21 rev frequency, (c) S21 fwd time, (d) S21 rev time, (e) and (f) conductance fwd, (g) and (h) conductance reverse, (i) and (j) susceptance fwd, (k) and (l) susceptance reverse, (m) and (n) S11 frequency reverse.

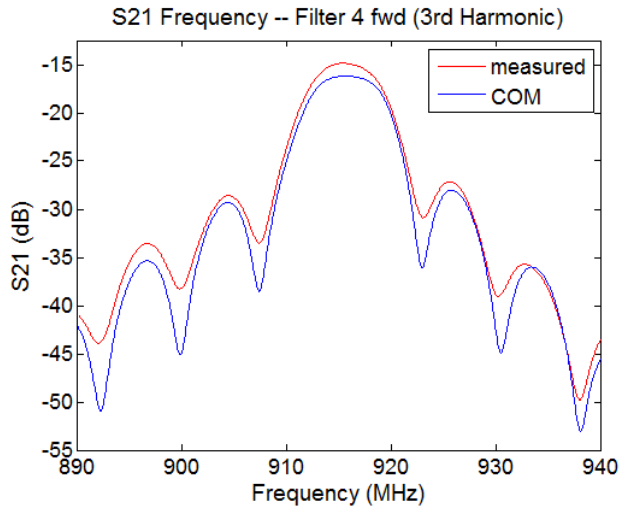
S21 Frequency -- Filter 4 fwd (3rd Harmonic)
measured
COM
S21 (dB)
Frequency (MHz)
-15
-20
-25
-30
-35
-40
-45
-50
-55
890
900
910
920
930
940

(a)

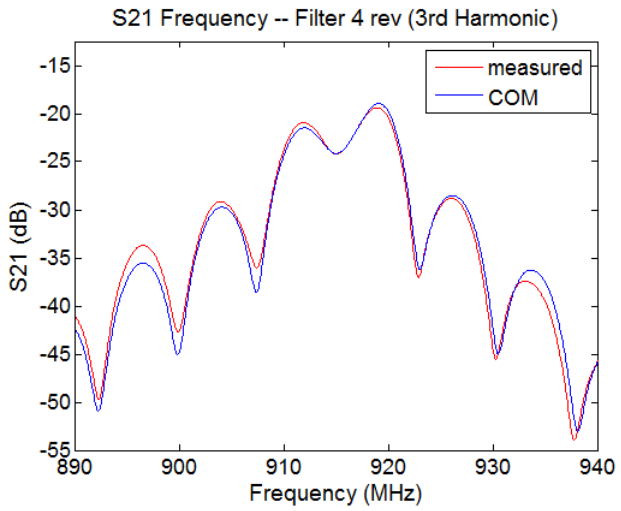
S21 Frequency -- Filter 4 rev (3rd Harmonic)
measured
COM
S21 (dB)
Frequency (MHz)
-15
-20
-25
-30
-35
-40
-45
-50
-55
890
900
910
920
930
940

(b)

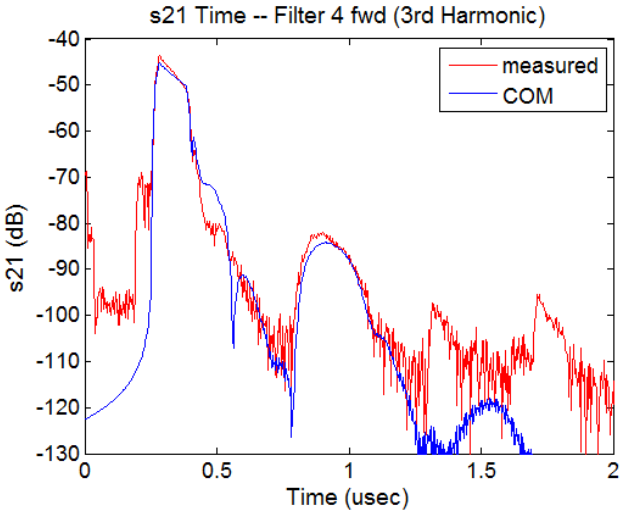
s21 Time -- Filter 4 fwd (3rd Harmonic)
measured
COM
s21 (dB)
Time (usec)
-40
-50
-60
-70
-80
-90
-100
-110
-120
-130
0
0.5
1
1.5
2

(c)

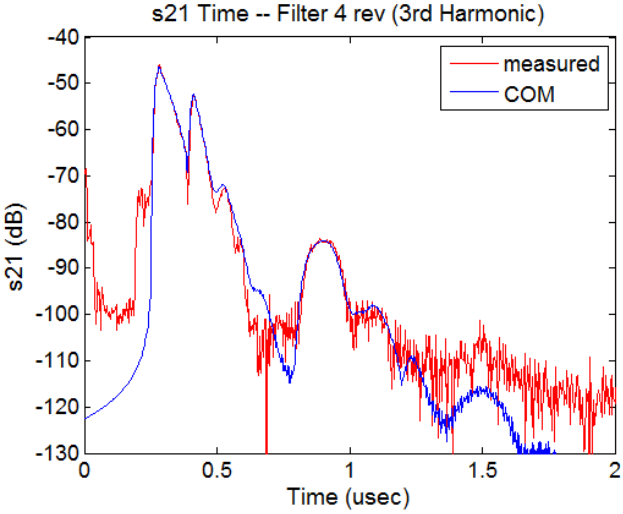
s21 Time -- Filter 4 rev (3rd Harmonic)
measured
COM
s21 (dB)
Time (usec)
-40
-50
-60
-70
-80
-90
-100
-110
-120
-130
0
0.5
1
1.5
2

(d)

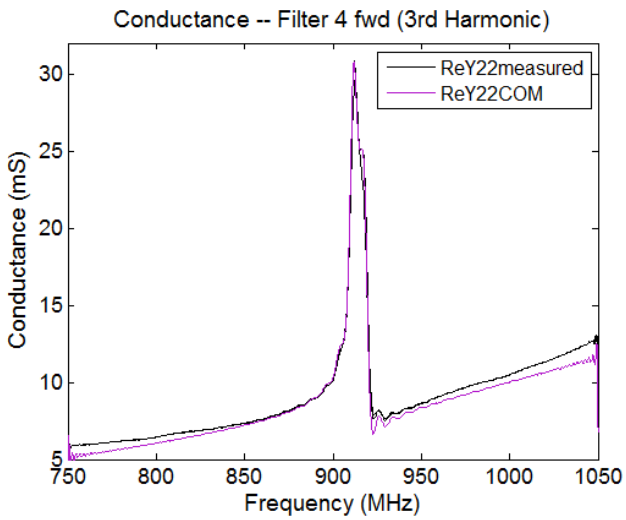
Conductance -- Filter 4 fwd (3rd Harmonic)
ReY22measured
ReY22COM
Conductance (mS)
Frequency (MHz)
30
25
20
15
10
5
750
800
850
900
950
1000
1050

(e)

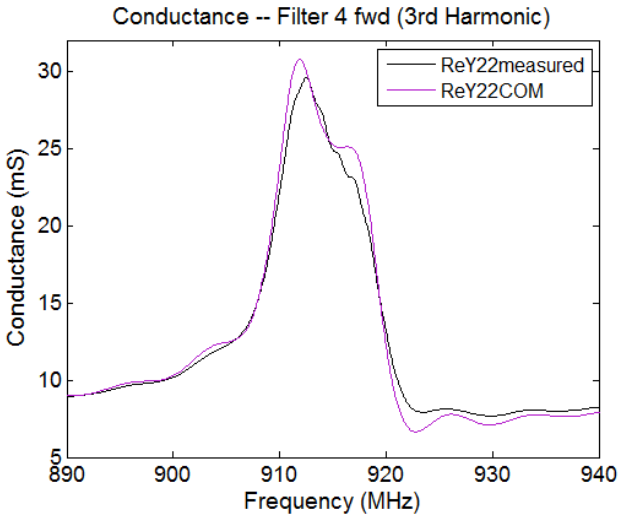
Conductance -- Filter 4 fwd (3rd Harmonic)
ReY22measured
ReY22COM
Conductance (mS)
Frequency (MHz)
30
25
20
15
10
5
890
900
910
920
930
940

(f)

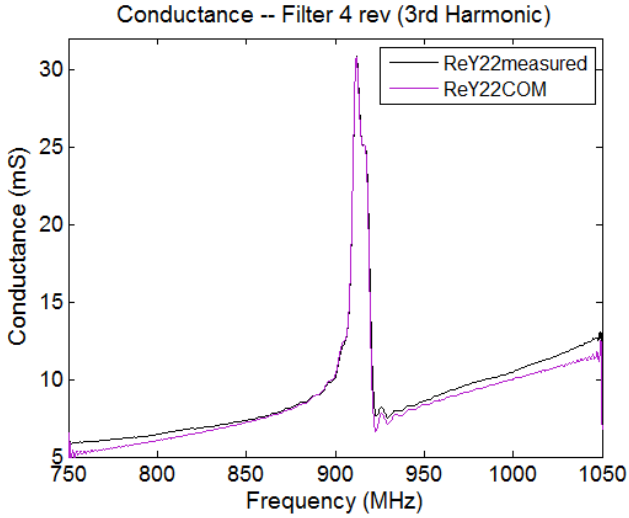
Conductance -- Filter 4 rev (3rd Harmonic)
ReY22measured
ReY22COM
Conductance (mS)
Frequency (MHz)
30
25
20
15
10
5
750
800
850
900
950
1000
1050

(g)

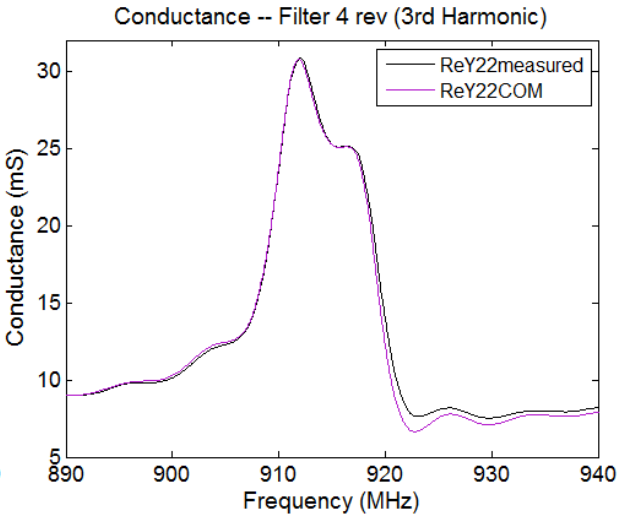
Conductance -- Filter 4 rev (3rd Harmonic)
ReY22measured
ReY22COM
Conductance (mS)
Frequency (MHz)
30
25
20
15
10
5
890
900
910
920
930
940

(h)

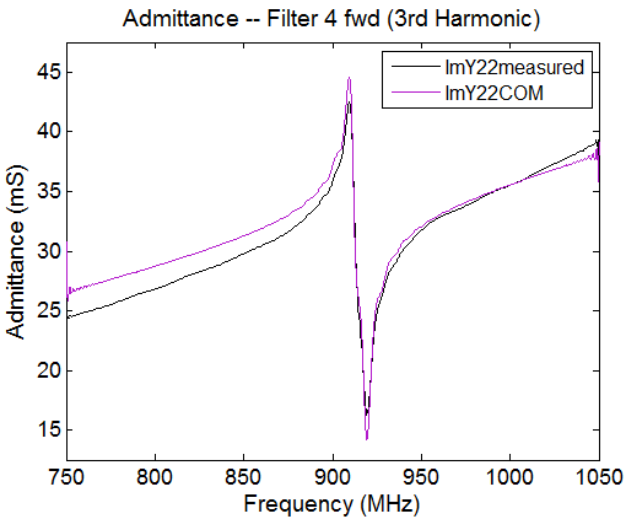
Admittance -- Filter 4 fwd (3rd Harmonic)
ImY22measured
ImY22COM
Admittance (mS)
Frequency (MHz)
45
40
35
30
25
20
15
750
800
850
900
950
1000
1050

(i)

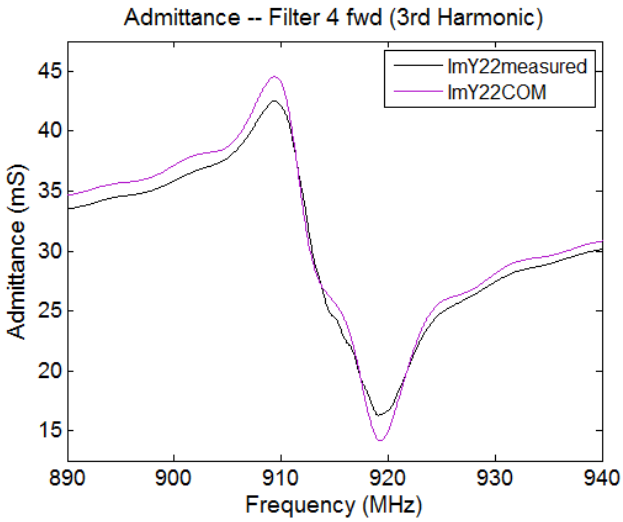
Admittance -- Filter 4 fwd (3rd Harmonic)
ImY22measured
ImY22COM
Admittance (mS)
Frequency (MHz)
45
40
35
30
25
20
15
890
900
910
920
930
940

(j)

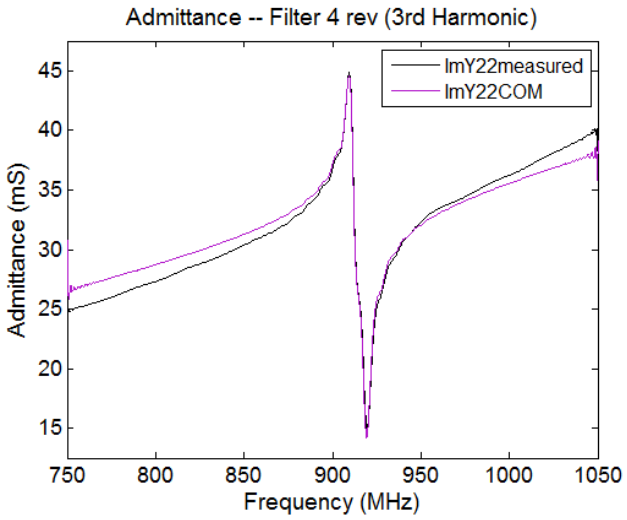
Admittance -- Filter 4 rev (3rd Harmonic)
ImY22measured
ImY22COM
Admittance (mS)
Frequency (MHz)
45
40
35
30
25
20
15
750
800
850
900
950
1000
1050

(k)

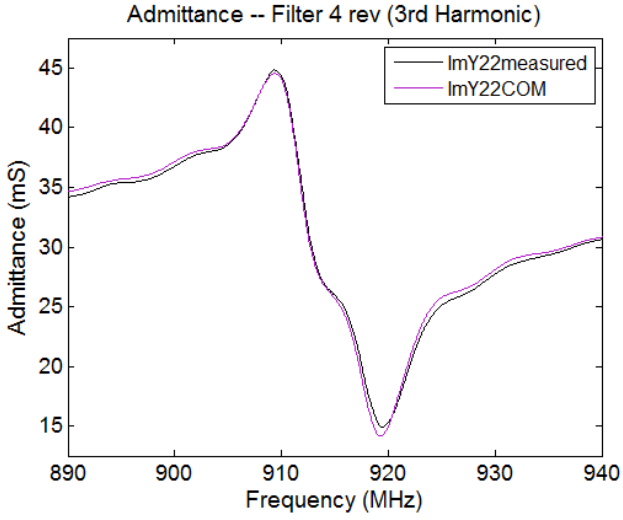
Admittance -- Filter 4 rev (3rd Harmonic)
ImY22measured
ImY22COM
Admittance (mS)
Frequency (MHz)
45
40
35
30
25
20
15
890
900
910
920
930
940

(l)

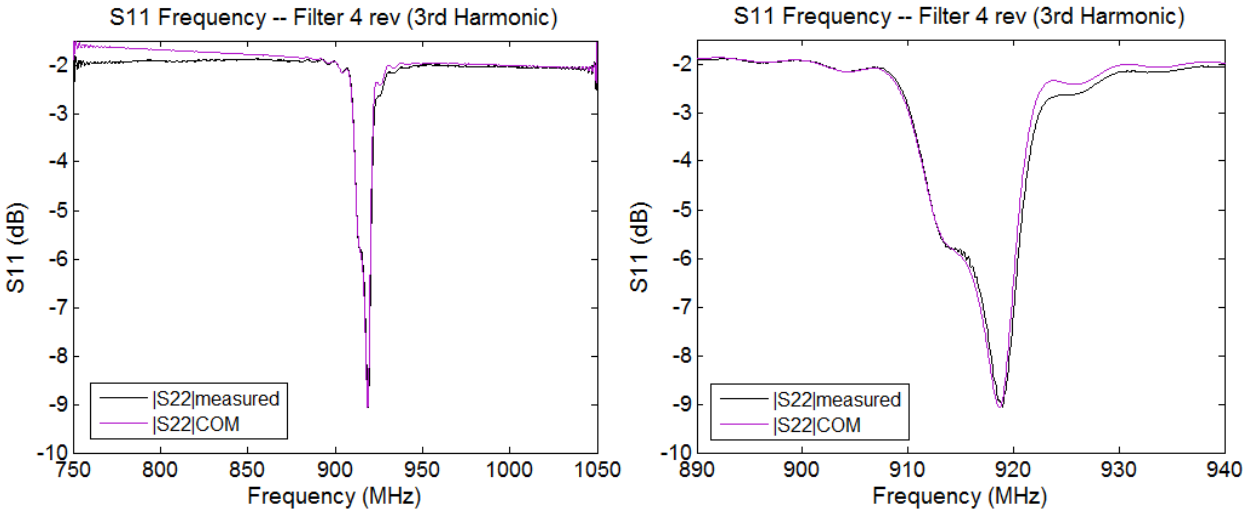

(m) (n)

Figure 4-12. The figures (a) through (j) show the measured and COM fit of responses of filter 4 which is composed of an 8pair 2hot4f0 bidirectional on port 1 and a 40pair optimized SPUDT on 2, operating at 3rd harmonic. (a) S21 fwd frequency, (b) S21 rev frequency, (c) S21 fwd time, (d) S21 rev time, (e) and (f) conductance fwd, (g) and (h) conductance reverse, (i) and (j) admittance fwd, (k) and (l) admittance reverse, (m) and (n) S11 frequency reverse.

The 3rd harmonic devices can be modeled. A distinct difference between the 3rd harmonic modeling as compared to 1st is the deviation of the out-of-band levels. This suggests that non-Rayleigh radiation, probably bulk radiation, is present. Also consider the sheet resistance modeling parameter in Figure 4-5, Rs. Because there are 3 wavelengths per transduction period at 3rd harmonic, the sheet resistance should increase by approximately a factor of 3. However, the 3rd harmonic devices are modeled as having excess sheet resistance in comparison to 1st harmonic, suggesting that this may be compensating for bulk mode radiation.

Something else to notice from the modeling results of the 3rd harmonic devices is the prediction of the forward S21. The EWC forward simulation predicted an insertion loss that was 1.1dB lower than measured, and 1.35dB lower than measured for the optimized SPUDT. The model predicts a forward response with less insertion loss than the actual measured device. This happens for both SPUDT filter sets. These devices were modeled by 1st matching to the reverse

response. Then when comparing the forward S21 response, the same modeling parameters were used as those used for the reverse response, only making a sign change on the TC-RC phase. Why the forward response is not accurately modeled is something that is a bit puzzling, and won't be investigated further as part of this effort.

Before ending the discussion and presentation of the COM modeling of 3rd harmonic devices, the best device found during this effort is now presented—at least in regards to directionality. The best device response is actually found in a slightly different optimized SPUDT. With respect to the optimized SPUDT, the thick ground is moved right, closer to the hot electrode by 20^0 at 3rd harmonic (20/360*lambda0_3rdH)—this device layout is referred to as optimized2, thus the device layout of filter 4 is renamed optimized1. The thickness of this optimized2 device is 2150 angstroms. The microscope picture is shown in Figure 4-13.

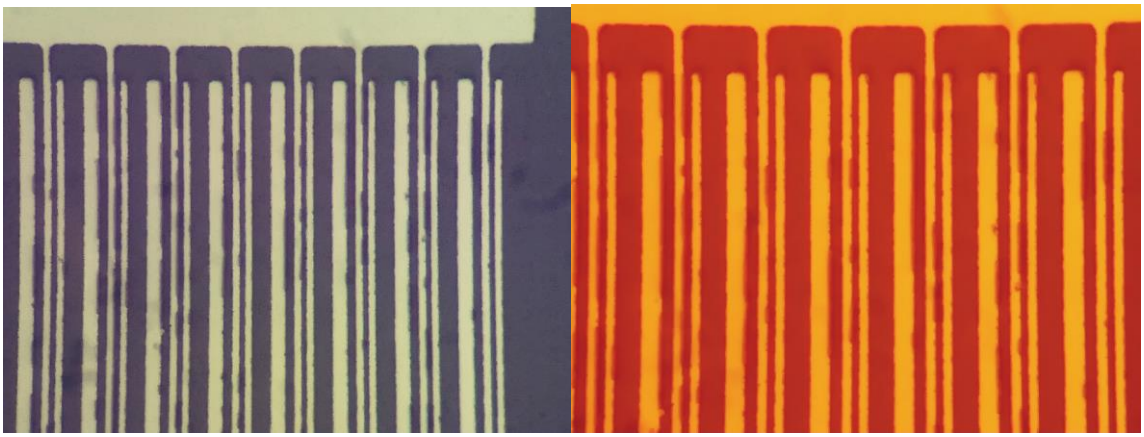

Figure 4-13. Microscope picture of optimized2 SPUDT. The jagged edges are the result of relatively high film thickness for the line width. This results even after increasing the photoresist thickness by spinning at 1.48 krpm.

Unfortunately the measured forward response is not available, only the reverse characteristics. And the COM model does not give an accurate forward S21 insertion loss level when changing the sign of the TC-RC angle, as is the case for 1st harmonic SPUDT modeling. A brief exercise of how the forward S21 for this device can be estimated is now presented. The COM parameters will

be adjusted to match the forward S21 response of SPUDT filters 3 and 4. Based on the adjustment factor for filters 3 and 4, the forward response of this optimized2 device, SPUDT filter 5, is estimated. Two parameters are changed, the propagation loss within the transducer (γ_{loss}) and the delay path propagation loss. The interesting thing is that the free-surface propagation loss has to be made into a gain for the best matching of the forward response. Of course, this is artificial, but it does make one wonder what is actually occurring. With this said, the adjustment in propagation loss parameters are now given.

The compensation values for γ_{loss} are as follows: increase of 1.5 times for the EWC and an increase of 1.64 times for the optimized SPUDT. The compensation factor is similar for EWC and optimized1, so it's not expected that the optimized2 compensation should be much different. Since optimized2 and optimized1 are more alike, the compensation factor for optimized2 is chosen to be the same as optimized1. $\gamma_{loss} = 1100$ for the reverse optimized1 and 1800 for the forward compensation. For the reverse optimized2 $\gamma_{loss} = 1400$, so it's multiplied by 1.64 to give a forward $\gamma_{loss} = 2290$. The EWC freespace propagation loss is changed from 180 to -50, for the optimized1 it's changed to -100, so it's also changed to -100 for the optimized2. The rest of the modeling parameters are given in Figure 4-5, filter 5, and are the same for both forward and reverse. Figure 4-14 and Figure 4-15 show the compensated forward S21 response for filters 3 and 4, respectively.

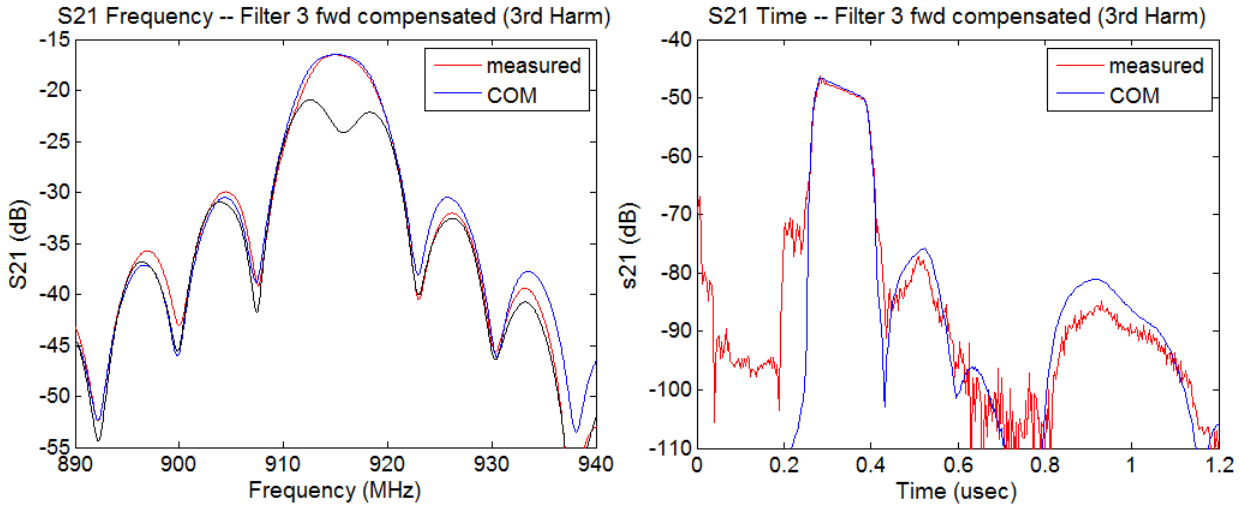

(a) (b)

Figure 4-14. Figure (a) and (b) show the measured and artificially forward compensated S21 COM fit for filter 3. This is done mainly to obtain some confidence in the forward S21 prediction of filter 5, for which there is no measured data. Compare these figures with figure 4-11 (a)(c).

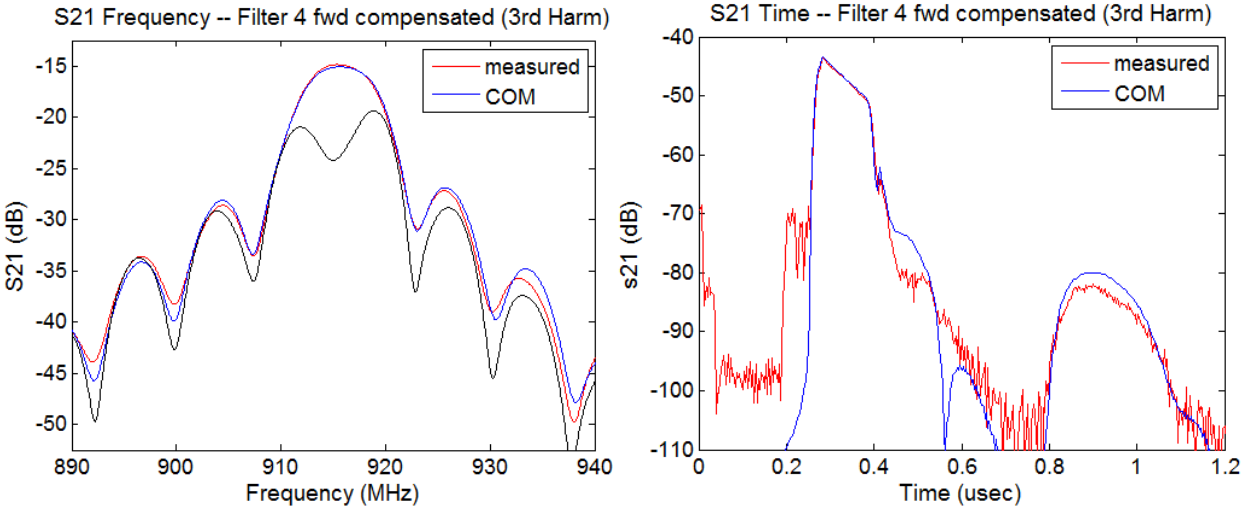

(a) (b)

Figure 4-15. Figure (a) and (b) show the measured and artificially forward compensated S21 COM fit for filter 4. This is done mainly to obtain some confidence in the forward S21 prediction of filter 5, for which there is no measured data. Compare these figures with figure 4-12(a)(c).

As can be seen in the compensated S21 frequency and time responses of the EWC and optimized1 response, the insertion loss levels agree. Although not a perfect agreement, the S21 time response

is well matched where most of the energy lies. Now the optimized2 device response is shown, the reverse response in Figure 4-16(b,c) and the compensated S21 frequency response in Figure 4-16a.

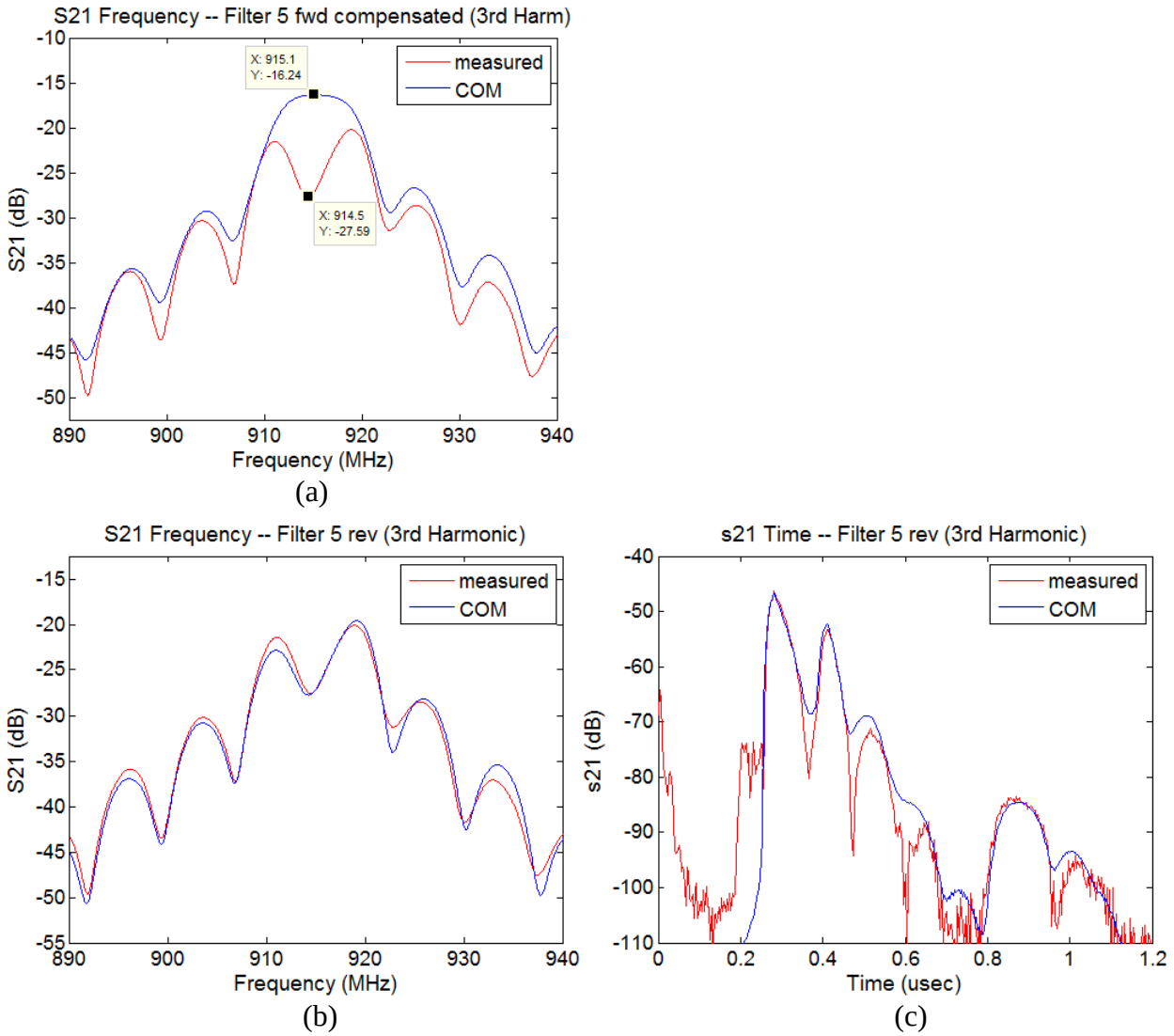

Figure 4-16. S21 frequency and time for optimized2 SPUDT device of filter 5. (a) shows the COM modeled compensated forward S21, estimated from the reverse S21 because the forward filter was not available. (b) shows the COM matching of the reverse S21 in frequency and (b) in time. The directivity is approximately 11.35dB. In comparison, the EWC and optimized1 devices, filter 3 and 4, have a directivity of approximately 7.5 and 8.71dB, respectively.

To have confidence that the compensated forward response is accurate, the offset between the forward and reverse side-lobe peaks can be compared to that of the EWC and optimized1 in Figure 4-14a and Figure 4-15a, respectively. The forward and reverse S21 side-lobe levels of the optimized2 response in Figure 4-16a are consistent with those of the EWC and optimized1 devices—there is high confidence that the forward S21 estimate is accurate. Plots of the electrical parameters, both measured and COM simulation, are shown in Figure 4-17.

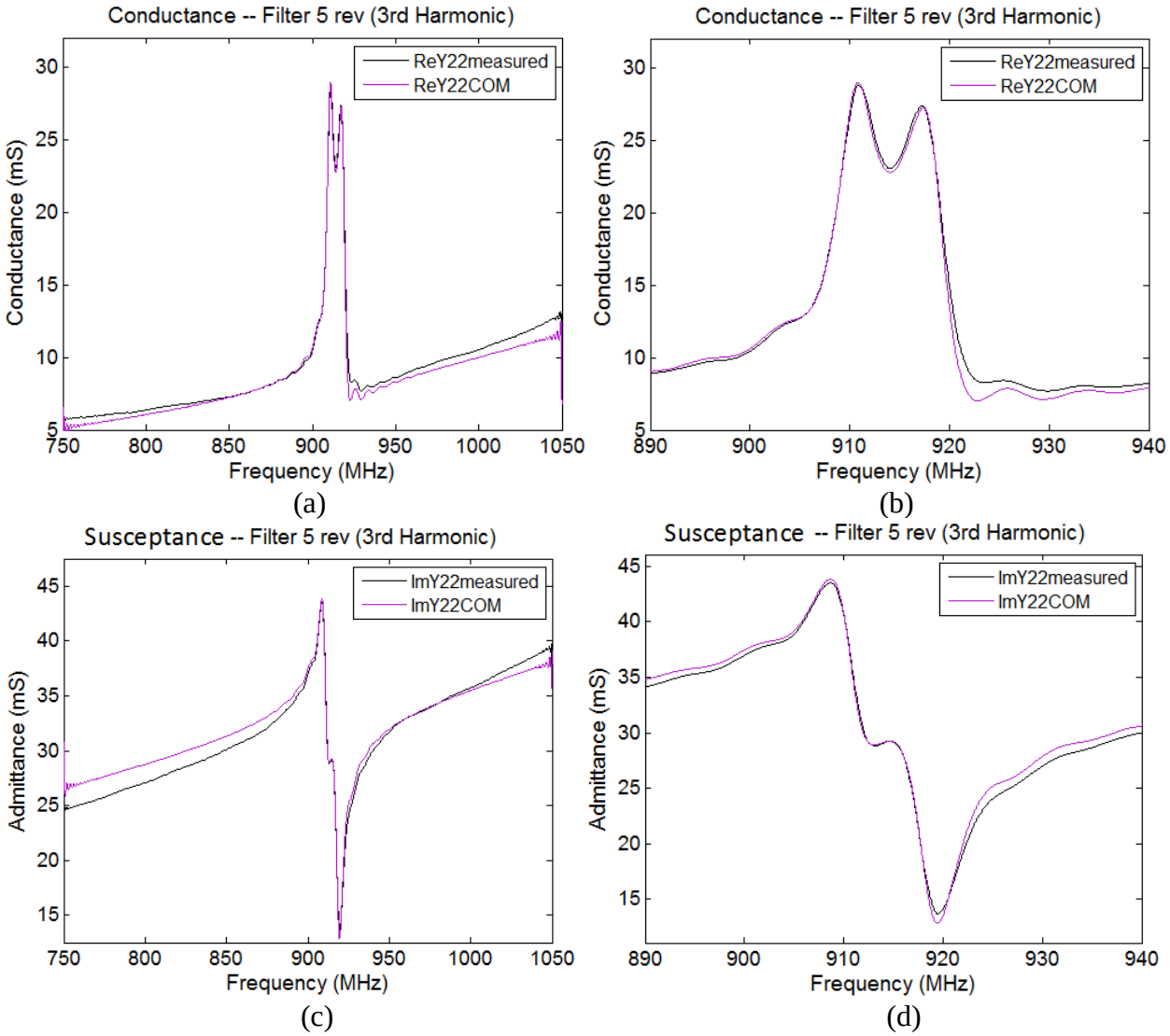

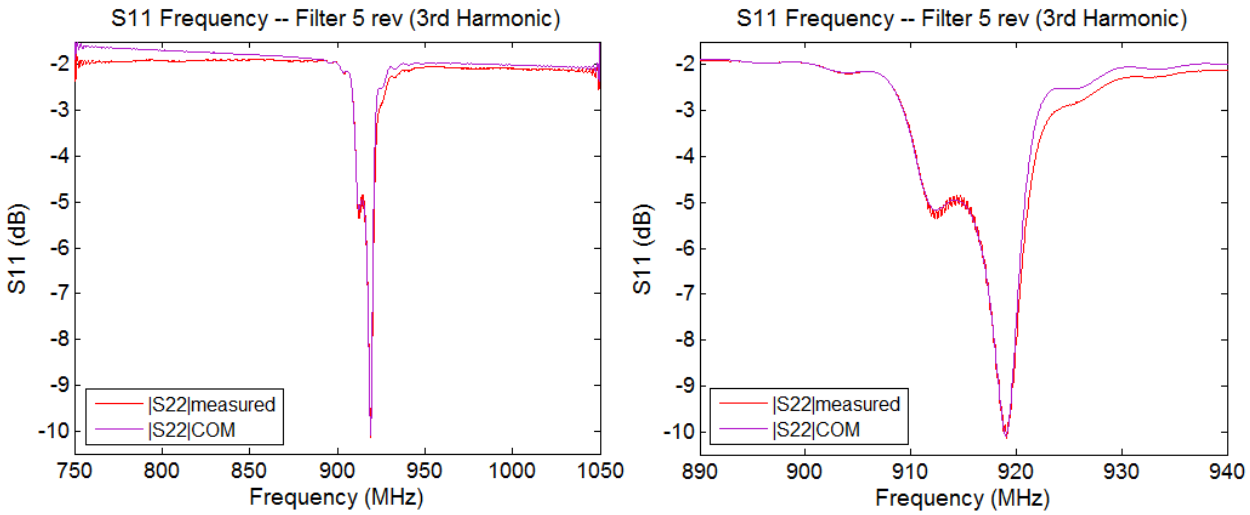

Figure 4-17. Electrical parameters of optimized2 SPUDT. (a) and (b) are conductance, (c) and (d) are susceptance, and (f) and (g) are S11 frequency.

The optimized2 device has a reflection magnitude that is approximately .0074 per wavelength, and thus approximately 1.68 times greater than the EWC reflection magnitude of .0044. The TC-RC angle is not far from optimum at 102.5deg. The directivity is approximately 11.35dB. The EWC and optimized1 devices, filter 3 and 4, have a directivity of approximately 7.5 and 8.71dB, respectively. The directivity of the best optimized1 found is approximately 10.7dB, this device is shown in Appendix E, Figure E-5.

4.4 Chapter 4 Summary

This chapter has shown successful COM modeling of SPUDT devices. It has shown that 3rd harmonic devices can be modeled with certain modifications to the sheet resistance in order to compensate for what appears to be non-Rayleigh radiation. There is a discrepancy in the forward to reverse modeling by only changing the sign of the transduction center / reflection center phase (TC-RC). While the forward response of the 1st harmonic devices was accurately obtained by

knowing the reverse response parameters, for 3rd harmonic, the forward prediction has slightly more insertion loss than the measured devices. The main contribution by the author in this section is to show that the 3rd harmonic optimized SPUDT of Appendix E was successfully modeled and shown to have higher coupling and higher directionality than the EWC SPUDT at metal thickness of approximately 2200Ang. It was also shown that the optimized SPUDT had higher directionality than the EWC at 1st harmonic also, with only a slight decrease in coupling. The optimized SPUDT layout has minimum linewidth of lambda0/8 (1st harmonic). The 3rd harmonic modeling parameters obtained in this chapter are used in the next chapter to model reflective delay line devices. The interested reader can replicate all of the results of this chapter by building up a COM model with the information given in Appendix F and COM parameters in Figure 4-5. The measured device files are attached as part of this electronic dissertation submission.

CHAPTER 5:
WALSH-HADAMARD-LIKE CODED REFLECTORS

The effort for enhanced DTE suppression by using 3rd harmonic unidirectional transducers has resulted in the bandwidth of the transducer being reduced by a factor of 3, as compared to a fundamental operating device having the same number of transduction periods. It was decided to use 10cell SPUDTs in the design that would be mounted on an antenna, especially for comparison with previously designed and antenna-mounted 3rd harmonic group types (GUDTs) having 10cells and 20λ0 aperture, shown in Appendix A. The transducer used in the 1-port devices all throughout this chapter will be a 10pair optimized2 SPUDT. The 3dB bandwidth of this device is determined from the COM model simulation of a 1port reflective delay line having a 1-strip reflector so that the reflector response (meaning P11) is almost constant over frequency. The 1st transit of the reflected signal is extracted from S11 by subtracting the transducer response in time (or dividing it out in frequency), thus indirectly showing an analog of S21 corresponding to a filter using two of these transducers. Thus the 6dB bandwidth of this signal is measured, which is the same as the 3dB bandwidth of the single transducer—calculated at just under 26MHz, the bandwidth of the ISM band at 915MHz. In order to design a reflective SAW sensor using this transducer, the reflector design has to be designed such that it fits within these bandwidth constraints. An OFC design to do this shown in section 6-2, first considering an alternate approach to correlations in the next section.

5.1 Matched Filter Generation and Inverse Domain Correlations

It is of interest to use a coded reflector design, at least for identification. Perhaps future work will improve upon code collisions, especially if a passive RF switch (or equivalent) can be implemented. It's known that orthogonal frequency coded (OFC) devices provide sensor identification. The sensor identification process involves a correlation. In the current implementation of the sensor acquisition algorithm, a bank of scaled ideal sensor signals are generated and stored in an array, and then the cycle of interrogations begins to find the best match. This bank of matched filters is called ideal because each are constructed from ideally generated cosines.

An actual OFC sensor signal deviates from this ideal waveform as mentioned in chapter 2. It is necessary to state that the bank of matched filters could be generated by obtaining the sensor signal for an arbitrary scaling factor of 1, and then generating a piecewise polynomial fit. This polynomial fit can be scaled and the bank of matched filters generated from a single signal. In the case of a reflector signal that highly deviates from the truncated cosine approach, the polynomial fit approach can be used, only adding computational time to the initialization of the acquisition algorithm. If using the polynomial fit approach, or similar, a COM generated signal or baseline measurement of the sensor signal can be used.

At this moment a different approach to signal correlation is presented, that may or may not be useful for the implementation of the current sensor acquisition algorithm. It may actually be more relevant for an application such as the correlator-receiver communication system developed by D. Gallagher [37], where each bit is encoded as an OFC waveform that is correlated with a matching receiver. A different receiver or a different channel has its own corresponding OFC

waveform—so that a cross-correlation produces little energy (ideally zero) where the peak of the auto-correlation occurs when synchronized (see Figure 7.6 in D. Gallagher's dissertation [37] for a good illustration) . In this kind of receiver the OFC signal is generated by a coded transducer, not coded reflectors—but similar issues like stored energy, as in reflectors, have to be dealt with. If the SAW transducer can generate orthogonal waveforms, OFC or any other, then the correlator-receiver approach can be used.

In the following sections of this chapter, orthogonal waveforms generated by reflectors will be looked at—OFC and two other approaches which are better suited for the bandwidth restrictions of the 10cell 3rd harmonic operating transducers used here. The other two orthogonal signal sets are based on the +/- phase coding used by the Walsh-Hadamard set of orthogonal functions. The codes are synthetized here with SAW reflectors, but it is highly probable that a SAW transducer can also synthetize them. The measure of orthogonality is defined here as the difference between the auto-correlation peak magnitude and the cross-correlation null, in decibels. Two correlation approaches will be presented, the standard time-domain correlation (STC) uses the following definition:

$$StandardTimeCorrelation = ifft\big(\, H(f)_1 \cdot conj(H(f)_2)\big) \tag{6-1}$$

where $H(f)$ is given as the FFT of the time domain signal $h(t)$ —if $H(f)_1 = H(f)_2$ it's an auto-correlation, when different it's a cross-correlation. A different way to perform the correlation is now proposed. Let's call it an inverse domain correlation (IDC) and define it as follows:

$$InverseDomainCorrelation = fft\Big(ifft(\, H(f)_1) \cdot conj\big(ifft(H(f)_2)\big)\Big) \tag{6-2}$$

where the frequency domain representation of the signal is being considered as the original signal being correlated—so it first starts with an inverse FFT and then an FFT. At the moment it is

unclear what the benefits of performing the correlation this way may be. Both forms of the correlation will be given for the reflector signals considered in the next three sections, so the reader is referred to the many plots shown there for a comparison. What has been noticed is that at times, and for many of our examples, the difference between the auto-correlation peak and the cross-correlation null can be greater for the inverse domain correlation. Also, the width of the null can be wider in the inverse domain correlation at times. This suggests that, for example, the correlation-receiver application [37] may have better cross-correlation rejection using the IDC—at least in the absence of noise and RF feedthrough. It is beyond the scope of this dissertation to investigate this further.

5.2 Single Track OFC Coded Reflectors

Our reflector design has to be single track. Separating the reflectors into more than 1 track is done to keep closer reflectors from partially blocking those behind them, since the Bragg reflector bandwidths overlap. Using multiple acoustic tracks with a single transducer has the issue of apodization loss in a time slot where part of the beamwidth doesn't receive wave energy. Avoiding 2-track apodization loss gains approximately 3dB, with all else equal. One can also use separate transducers for each Bragg reflector, each a separate track, 1 per Bragg reflector, tailoring each transducer center frequency to match that of the reflector for better efficiency. Unfortunately, the transducers are capacitively coupled. Unless one is willing to make a very long OFC transducer for each OFC reflector and possibly skip every other OFC frequency, there is going to be significant energy interchange between tracks—such energy interchange ruins the echo suppression ability (as seen from some preliminary simulations not shown here). Also, the echo

suppression ability over the whole bandwidth decreases with increasing transducer length (at least for uniform transducers, shown in Appendix H)—so that takes away from the echo suppression help that OFC transducers might offer multiple track devices. At least for the moment it seems that the design is restricted to single track devices if good echo suppression characteristics are to be achieved.

Consider the frequency domain representation of a single frequency Bragg reflector bank as used for OFC chips. Figure 5-1 compares the frequency response of a single frequency reflector bank for 80 wavelengths (160 strips at fundamental) vs. 20 wavelengths, using reflectivity per strip of .015 (a good value for 1st harmonic aluminum reflectors at 915MHz and approximately 750Ang thickness, please refer to [38]). P11 is shown, so the bandwidth of the IDT has no effect on the response.

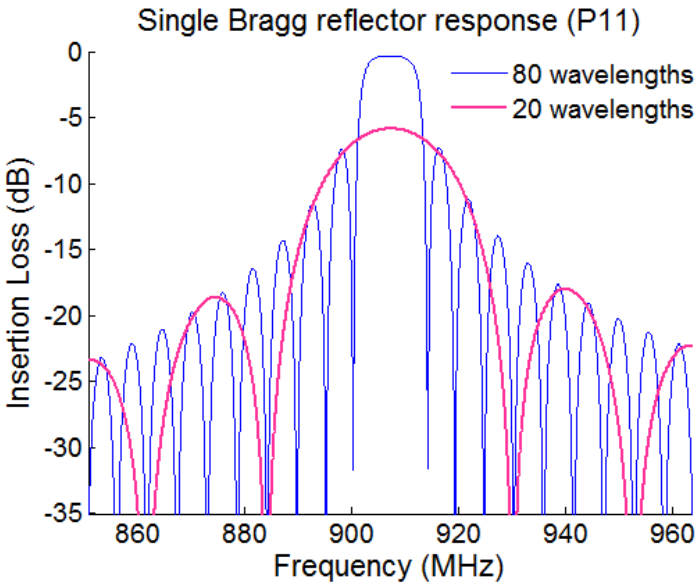

Figure 5-1. Effect of increasing chip length for a single frequency reflector on P11. The stored energy causes more deviation from the sin(x)/x frequency response as the length increases.

As can be seen from Figure 5-1, the sin(x)/x shape is lost as the reflector gets longer. This design tries to fit 4 OFC chips in the ISM band. 80 wavelengths are not enough to narrow the bandwidth sufficiently, and already the stored energy is distorting the stand alone OFC chip. One thing that can be done is to lower the reflectivity. The OFC reflectors are first designed with lowered reflectivity and simulated using the COM model.

For modeling the following OFC devices in this section, the transducer uses the same COM parameters as the transducer in the first line of Figure 5-14 (section 5.4.3). The reflectors are modeled as 1st harmonic reflectors, with |R|=.015 (~750Ang Al height, ~50a/p). The correlation characteristics are better when using 1st harmonic over 2nd harmonic, a result of the loss increasing for 2nd harmonic reflectors. The propagation loss parameter being approximately γ_{Loss}=100 for 1st harmonic. For the 2nd harmonic reflectors used in the next sections γ_{Loss}=400. The reflectivity per strip for 2nd harmonic is |R|=.031 (~500Ang Al height, ~50a/p), but it's almost equivalent (per length) to 1st harmonic because it gets divided by two since there are half the number of strips per wavelength. The OFC codes are labeled 1 through 4, with 1 being the lowest center frequency chip and 4 the highest. Bragg reflectors corresponding to these frequencies are shuffled in space/time in order to generate the OFC signal. For example, the stepped chirp OFC from low to high frequency is labeled as OFC[1 2 3 4]. The center frequencies used are 907.2, 912.4, 917.6, and 922.8MHz. The grating velocity is vg=3441m/s, so the wavelength of the Bragg reflector equals vg divided by its center frequency. The number of 1st harmonic reflector strips is 2x[89.5 90 90.5 91] for the corresponding frequencies of OFC[1 2 3 4]. In each sub-figure of Figure 5-2 the same OFC reflector layout is simulated, first with the reflectivity reduced by 10% and then normal value. This is done for two OFC codes.

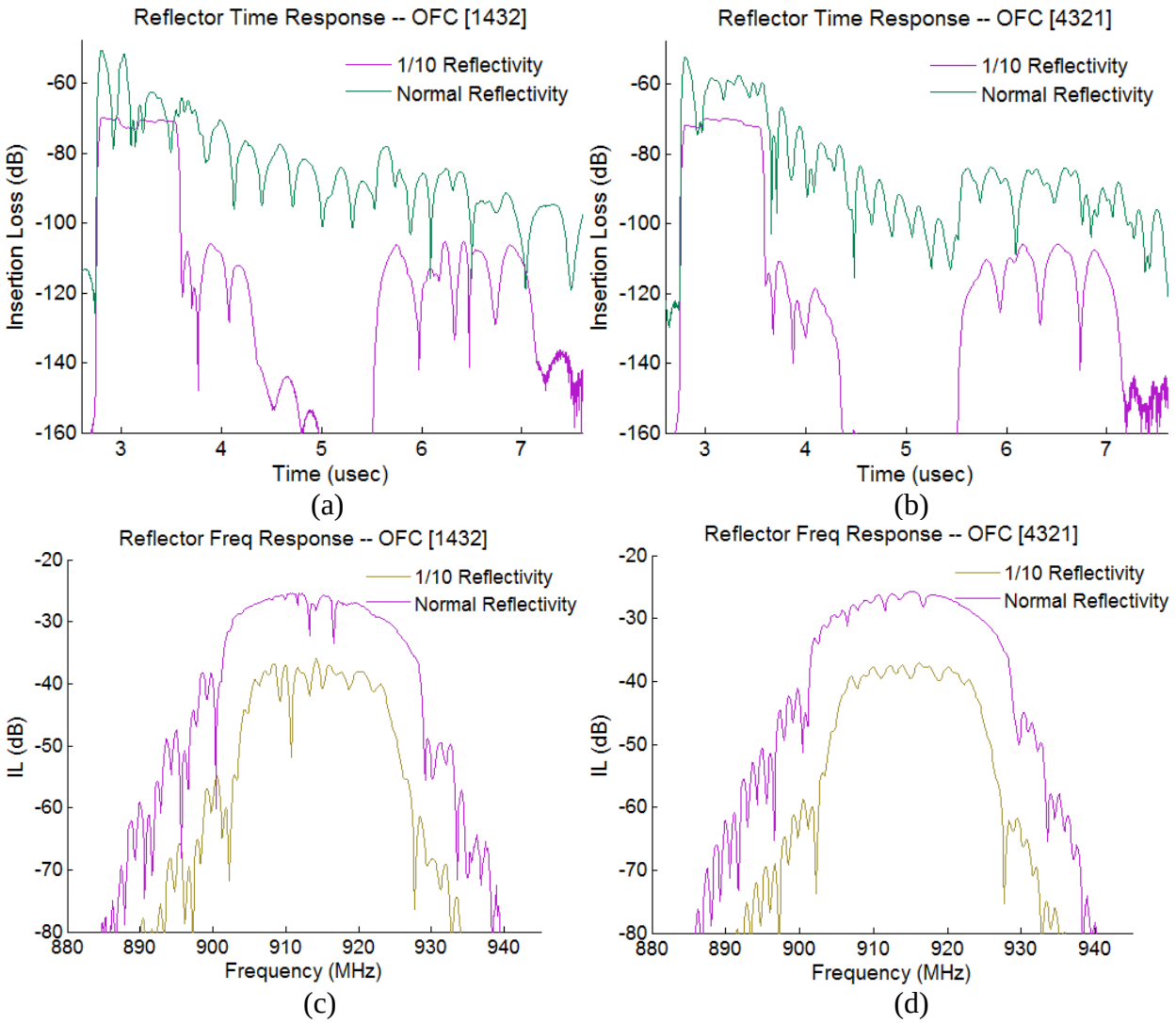

Figure 5-2. These figures show the simulated response of two OFC devices, codes (a) [1432] and (b) [4321]. In each subplot, one trace is modeled at 1/10 reflectivity and the other at normal reflectivity (values are given above). The increase in reflectivity shows a deviation from the ideal response, showing the blocking in time of adjacent chip frequencies and causing roll-off in frequency—making a narrow bandwidth design difficult.

When the reflectivity is kept small, the time response can be seen as separate rect functions, with very little amplitude modulation; mainly caused by the transducer. The frequency response is also quite flat. With high reflectivity the first reflector considerably blocks those behind it, especially if the OFC frequencies are adjacent in frequency. Increasingly shrinking the bandwidth becomes increasingly difficult as reflectivity increases, as well as causing lots of time domain ringing.

Notice that the side lobes of the reduced reflectivity response are lower than that of the higher reflectivity reflectors. Notice how the bandwidth also increases (Figure 5-2(c,d)). The only way to make OFC reflectors that work well with our 10cell SPUDT devices is to decrease reflectivity by using withdrawal weighting and possibly changing the a/p ratio as well. Sufficiently lowering the reflectivity will most likely introduce significant insertion loss. There may be some advantage to using withdrawal weighting over change a/p because of the decreased use of metal that has more insertion loss than free surface (perhaps an advantage over bulk mode conversion loss). In this effort it was chosen to only fabricate devices with the in-house mask pattern generator, without use of the image repeater. This restricted the reflectors to 2^{nd} harmonic operation. Trying to make these OFC reflectors with the 2^{nd} harmonic reflectors is even more problematic. The increased attenuation makes the insertion loss even worse for the reflectors further back in time, further deteriorating the orthogonality. This was seen in simulation results not shown here, but can be verified by the interested reader (Appendix F has the information necessary for replicating the COM model used here). For this reason it was decided not to use OFC reflectors—a Walsh-Hadamard-like approach was used instead, shown in the next two sections. This section is ended by showing plots of the auto and cross-correlations for a couple of selected pairs of OFC devices—that is, with OFC reflectors. Plots are first shown for the 1/10 reflectivity COM simulation and then full reflectivity. The cross-correlation graphs show a black circle corresponding to the location where a null would be ideal for orthogonal signals. The cross-correlations are normalized to the higher peak of the two corresponding auto-correlations.

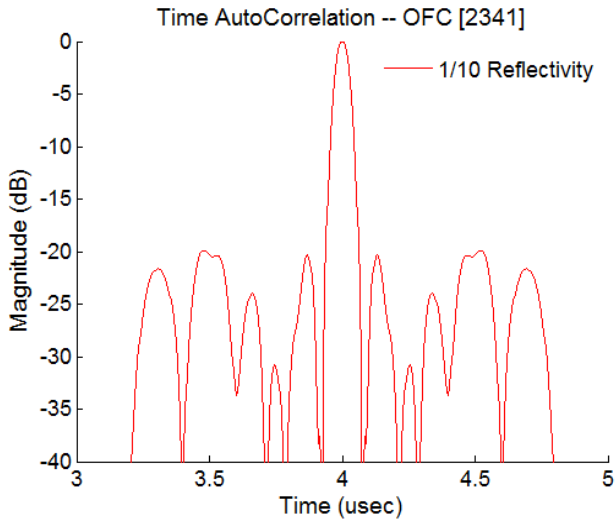
Time AutoCorrelation -- OFC [2341]
1/10 Reflectivity
Magnitude (dB)
Time (usec)
0
-5
-10
-15
-20
-25
-30
-35
-40
3
3.5
4
4.5
5

(a)

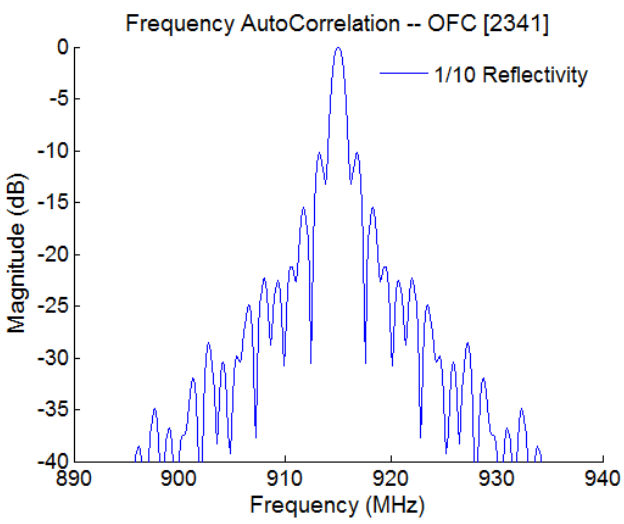
Frequency AutoCorrelation -- OFC [2341]
1/10 Reflectivity
Magnitude (dB)
Frequency (MHz)
0
-5
-10
-15
-20
-25
-30
-35
-40
890
900
910
920
930
940

(b)

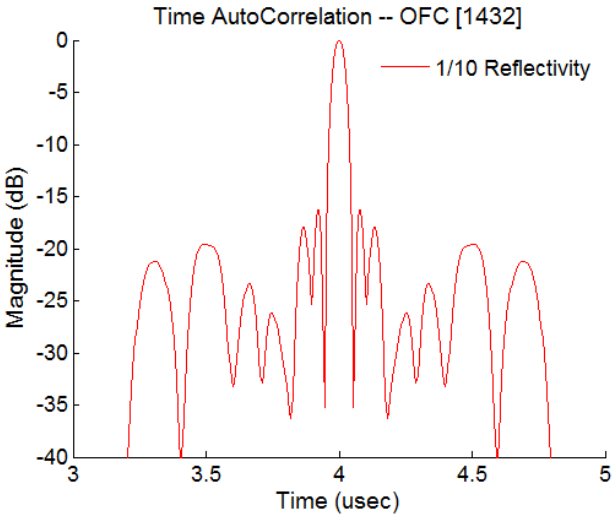
Time AutoCorrelation -- OFC [1432]
1/10 Reflectivity
Magnitude (dB)
Time (usec)
0
-5
-10
-15
-20
-25
-30
-35
-40
3
3.5
4
4.5
5

(c)

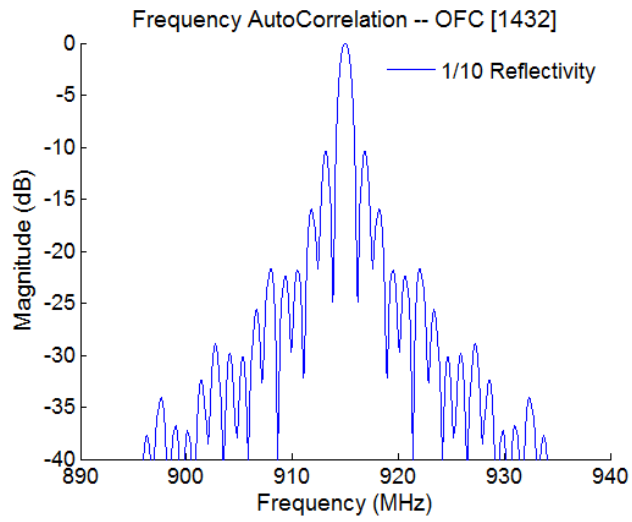
Frequency AutoCorrelation -- OFC [1432]
1/10 Reflectivity
Magnitude (dB)
Frequency (MHz)
0
-5
-10
-15
-20
-25
-30
-35
-40
890
900
910
920
930
940

(d)

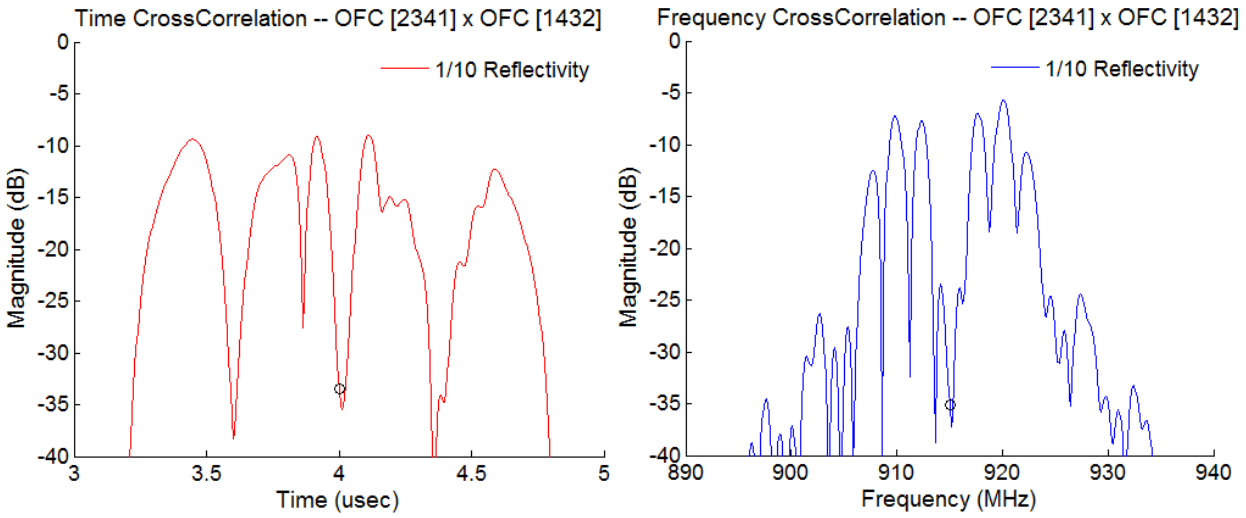

(f) (g)

Figure 5-3. Auto and cross-correlation of reduced reflectivity simulations, for both time and frequency domain waveforms, for OFC codes [2341] and [1432]. The circle gives the location where ideally the null of the cross-correlation should occur in order to correspond to the auto-correlation peak location. The cross-correlation is normalized to the peak of the auto-correlation peak (highest of the 2). The high out of ban levels of the cross-correlation in comparison to the auto-correlation may be due to the relatively narrow bandwidth of the OFC design, but this aspect has not been looked into, except verifying that the relative levels shown here are correct by comparing with un-normalized plots.

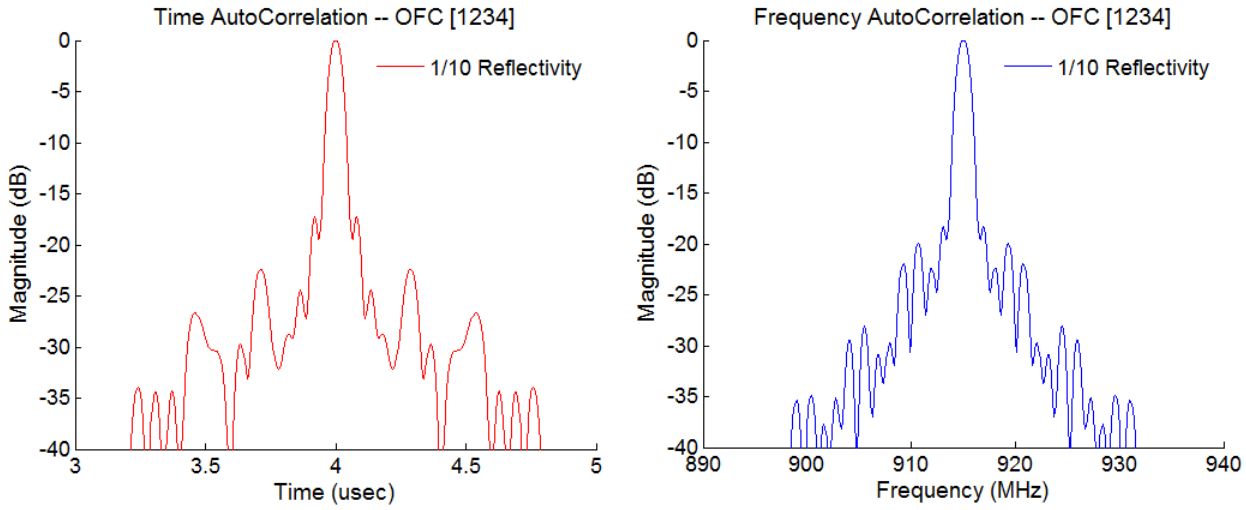

(a) (b)

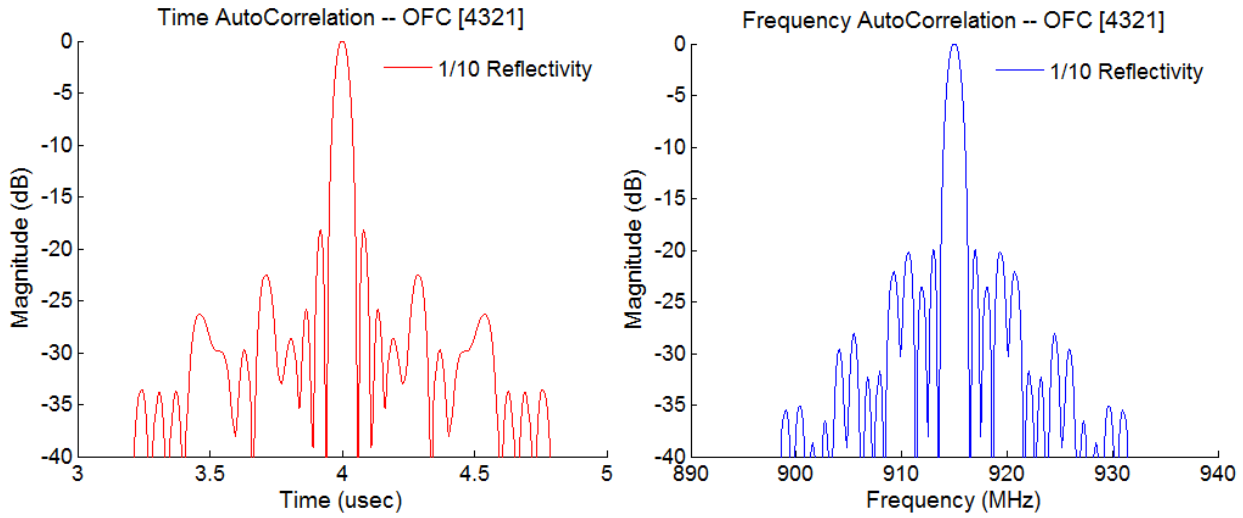

(c) (d)

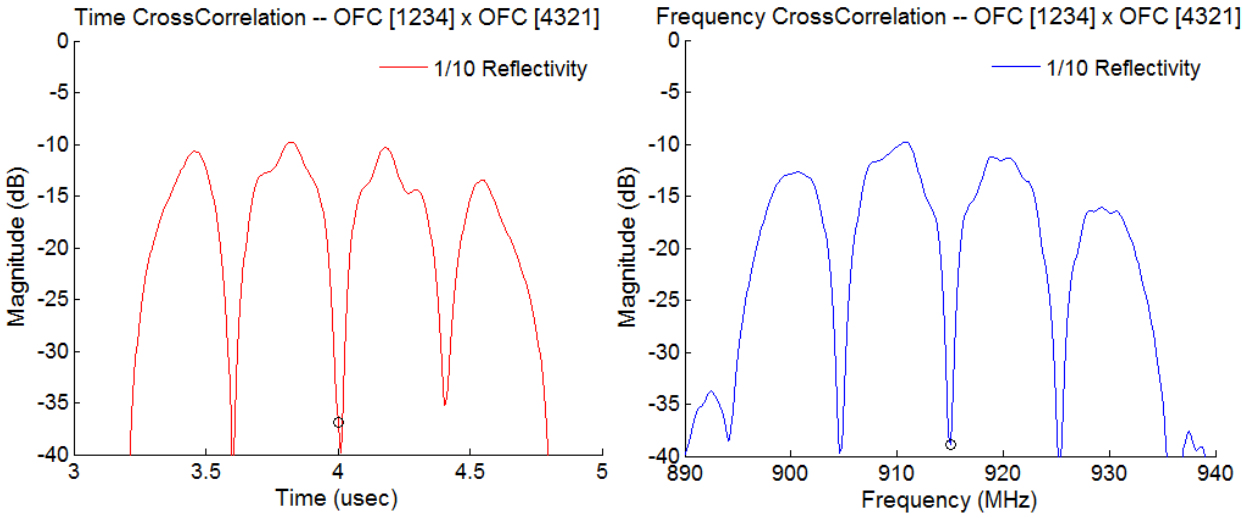

(f) (g)

Figure 5-4. Auto and cross-correlation of reduced reflectivity simulations, for both time and frequency domain waveforms, for OFC codes [1234] and [4321]. The circle gives the location where ideally the null of the cross-correlation should occur in order to correspond to the auto-correlation peak location.

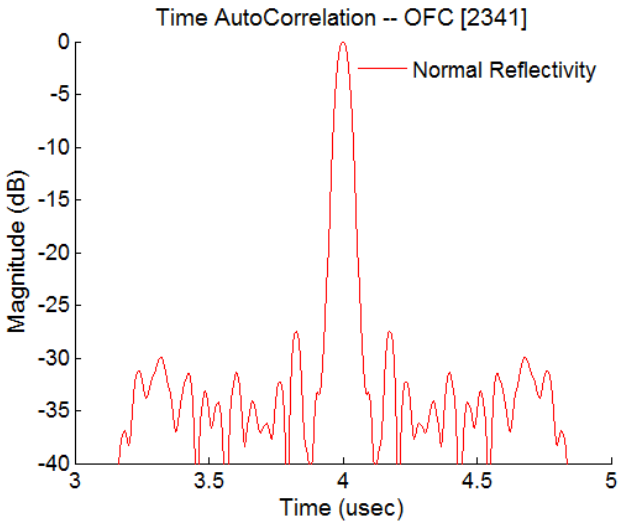
Time AutoCorrelation -- OFC [2341]
Normal Reflectivity
Magnitude (dB)
Time (usec)
0
-5
-10
-15
-20
-25
-30
-35
-40
3
3.5
4
4.5
5

(a)

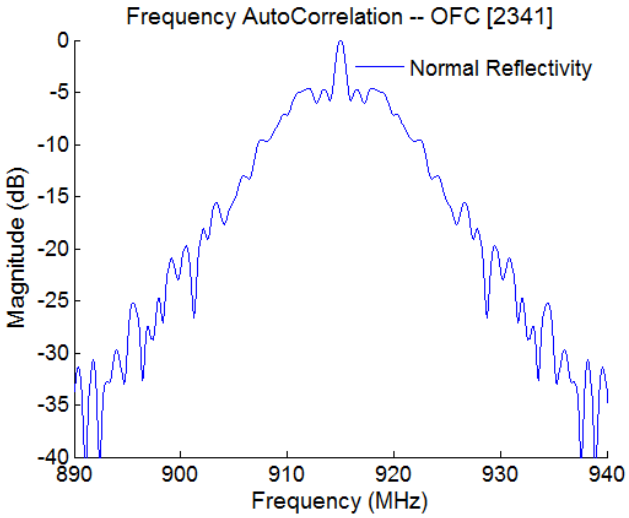
Frequency AutoCorrelation -- OFC [2341]
Normal Reflectivity
Magnitude (dB)
Frequency (MHz)
0
-5
-10
-15
-20
-25
-30
-35
-40
890
900
910
920
930
940

(b)

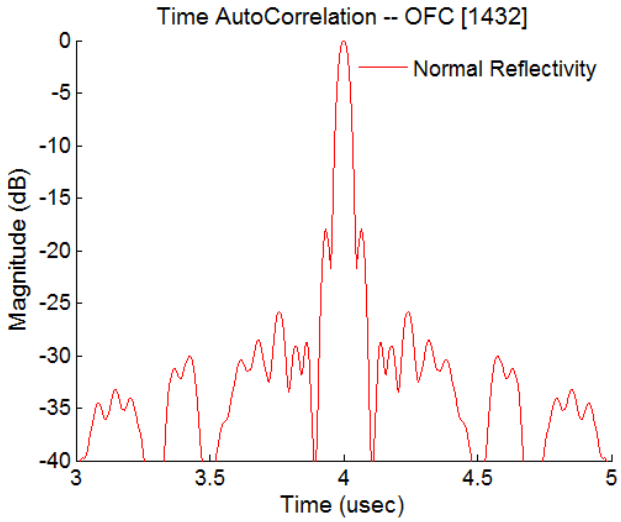
Time AutoCorrelation -- OFC [1432]
Normal Reflectivity
Magnitude (dB)
Time (usec)
0
-5
-10
-15
-20
-25
-30
-35
-40
3
3.5
4
4.5
5

(c)

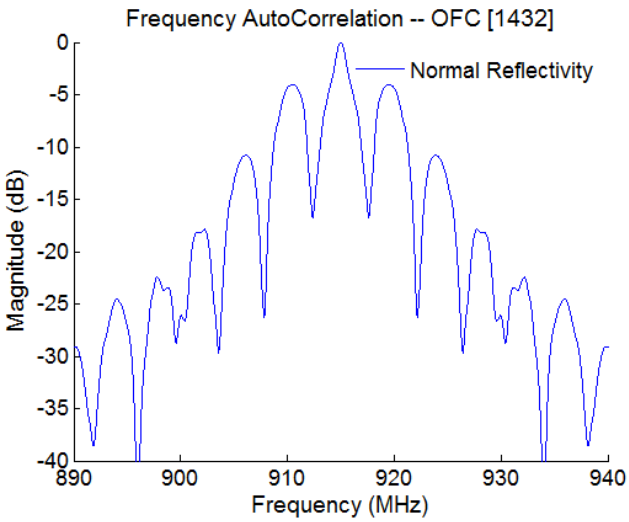
Frequency AutoCorrelation -- OFC [1432]
Normal Reflectivity
Magnitude (dB)
Frequency (MHz)
0
-5
-10
-15
-20
-25
-30
-35
-40
890
900
910
920
930
940

(d)

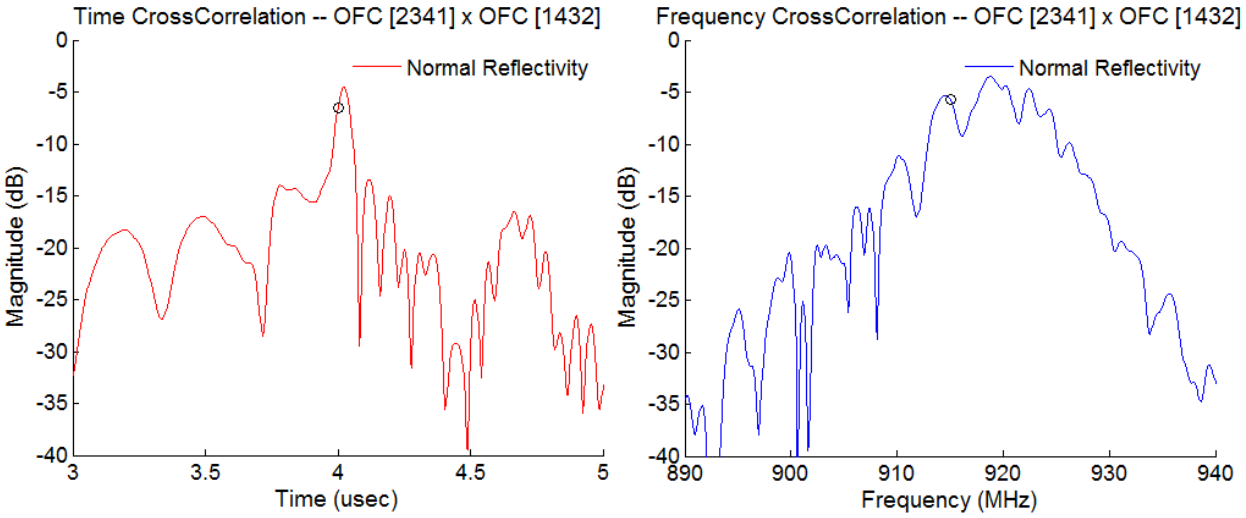

(f) (g)

Figure 5-5. Auto and cross-correlation of normal reflectivity simulations, for both time and frequency domain waveforms, for OFC codes [2341] and [1432]. The circle gives the location where ideally the null of the cross-correlation should occur in order to correspond to the auto-correlation peak location. Devices with such bad correlation properties would never be designed by the CAAT group at UCF.

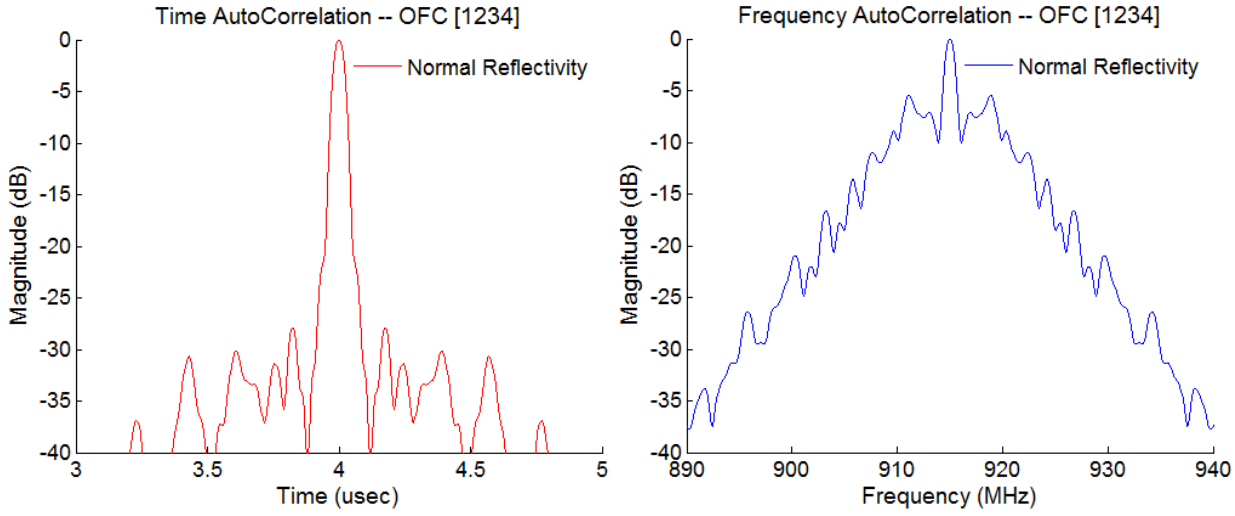

(a) (b)

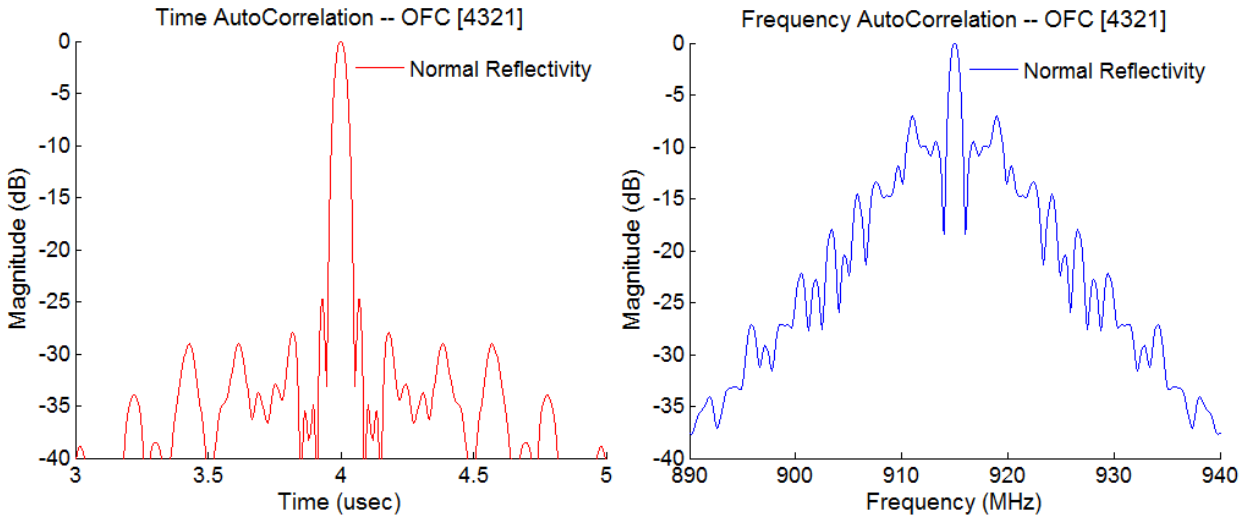

(c) (d)

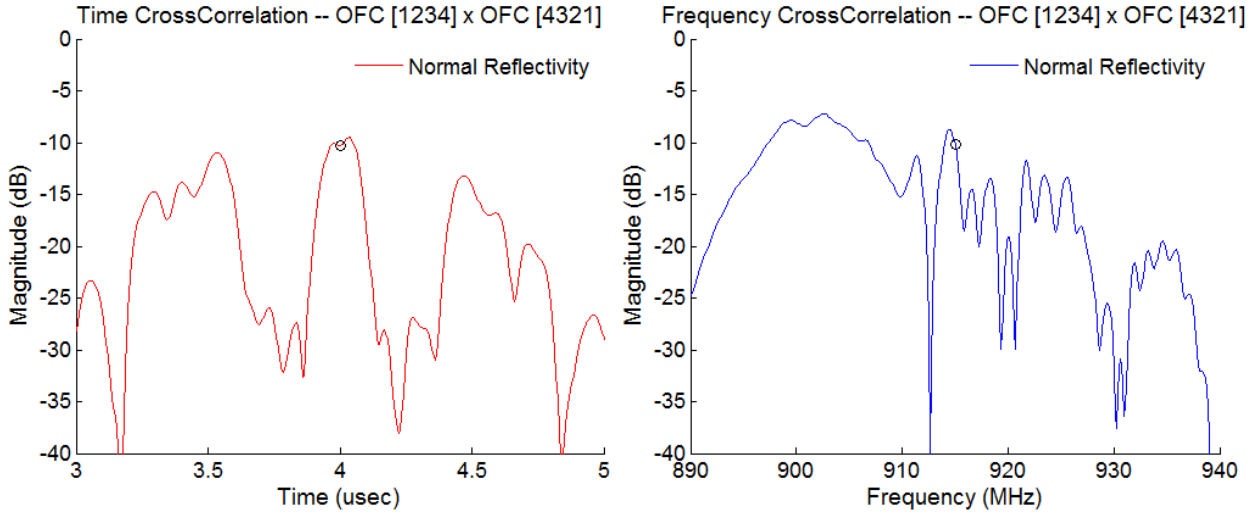

(f) (g)

Figure 5-6. Auto and cross-correlation of normal reflectivity simulations, for both time and frequency domain waveforms, for OFC codes [1234] and [4321]. The circle gives the location where ideally the null of the cross-correlation should occur in order to correspond to the auto-correlation peak location. Devices with such bad correlation properties would never be designed by the CAAT group at UCF.

5.3 Walsh-Hadamard-like Coded Reflectors for Pulse Shaping and Orthogonality

5.3.1 Motivation and Introduction to Walsh-Hadamard-like Reflectors

In trying to avoid the problems associated with a relatively narrow bandwidth for OFC reflectors, as discussed in the previous section, it was decided to try another coding approach—using single frequency reflectors with +/- phase shifts. The +/- sequences resemble the Walsh-Hadamard codes which use a sequence of +/-1s and come in sets that are powers of 2 long. Our implementation deviates from this in that the length of the code is actually 5. The resemblance is mainly in the use of +/-1 phase shifts as if it were binary phase shift keying. Chen Fu et al. have used BPSK coded reflectors for a SAW temperature sensor at 2.5 GHz previously [39]. The number of electrodes per chip were increased gradually to obtain amplitude compensation, however, it used withdraw weighted reflectors at approximately 10% density, so the reflectivity is low. One of the goals here is to use high reflectivity for lower loss, and not just amplitude compensate for time domain amplitude but also for the purpose of finding orthogonal or semi-orthogonal coded reflectors and devices.

The original motivation was not so much orthogonality as it was being able to better distribute the sensor signal energy over the passband, use the highest reflectivity possible to minimize insertion loss, and still keep the bandwidth narrow enough for use with our 10cell 3rd harmonic SPUDT in the near-ISM band. Before introducing the new reflector types, it should be noted that pulse shaping of the reflector response has been accomplished with apodized reflectors [27, 40], but that would not work well for echo suppression. Another alternative for electrodes with narrower bandwidth than OFC for the same length are noise-like reflectors, see Figure 3 of [41]. The discussion on the new BPSK based reflectors continues.

This is being called a Walsh-Hadamard-like (WHL) reflector, but can also be called a WHLMW (short for Walsh-Hadamard-Luis-Malocha-Weeks), thanks to Prof. Don Malocha for the SAW device platform for orthogonal reflectors and thanks to Prof. Art Weeks for the idea to apply the WH coding scheme.

The first approach to using the +/- phase shifted chips is to use equal length chips with varied reflectivity (referred to as WHL1). These may be categorized as amplitude modulated BPSK (AM-BPSK). The code sequence representation uses a 1 for a phase shift between adjacent chips, and 0 for no phase shift. A 5-chip WHL1 code is represented as WHL1[x x x x] , x=1 or 0. For example, WHL[1 1 0 0] has a 180^0 phase shift between chips 1&2 and 2&3, but no phase shift between chips 3&4 and 4&5—so the 1's indicate a phase shift between adjacent chips. The BPSK modulation on the carrier allows for greater penetration of the wave energy into the SAW reflector as compared to an equal length Bragg reflector. The +/- phase shifts spread the bandwidth, so the Fourier transform no longer looks like a sin(x)/x.

Unfortunately stored energy is still a problem and restricts the length of the reflectors. The stored energy effect is mitigated by lowering the reflectivity for the closest reflectors and gradually increasing the reflectivity for the reflectors further away. After the initial design which used a +/- phase shift between every chip, it was then noticed that by randomly changing the phases between chips (the code sequence), it resulted in interesting return bands. Not only was the necessary bandwidth achieved, but it turns out that some codes are mutually orthogonal to some degree. The codes can also be further optimized for better orthogonality. The WHL1 reflectors use equal chip length and variable reflectivity.

5.3.2 Walsh-Hadamard-like Reflector Implementation Using 2nd Harmonic Reflectors

To begin with, only 3 reflectivity values are used, .015 per strip for the first 3 chips, .02 for the 4th chip, and .031 for the 5th chip. These are implemented here with 2nd harmonic reflectors. If the COM algorithm P-matrix equations are set up for 1st harmonic reflectors, the 2nd harmonic reflectors are modeled by doubling the number of strips and then dividing reflectivity per strip by 2. These values were adjusted by hand and only 3 were chosen for proof of concept and because of plans to fabricate the device. Also to keep in mind is that the transducer plays a part in the synthesis of these functions. Further tuning using an optimization routine should be performed for best results.

Each chip is constructed of equal frequency Bragg reflectors consisting of 30 strips of 2nd harmonic reflectors, so 30 fundamental wavelengths (at ~457MHz). 2nd harmonic aluminum reflectors have more loss but are easier to work with for controlling reflectivity (loss values given in section 6-2). The reflectivity From [38] or chapter 4 of N. Saldanha's dissertation [11] the reflectivity values for 2nd harmonic reflectors can be obtained. It's interesting that for 2nd harmonic reflectors, the reflectivity increases with decreasing metal thickness, at least in a practical thickness range. The reflectivity profile is approximately Gaussian with changing a/p ratio, slightly less abrupt than the fundamental reflectors—also favorable that the highest reflectivity is obtained at 50% a/p ratio.

Since 2nd harmonic reflectors are nominally twice as wide as fundamental, it's not unreasonable to attempt fabricating the WHL1 devices at UCF without an extensive experimental characterization effort—although achieving correct linewidths for 3 different widths simultaneously can be tricky. On an initial 2nd harmonic reflector measurement, the reflectivity

measurement of .031per strip for shorted Al reflectors at ~1.5%h/λ (~550Ang) confirmed the value given by Saldanha in [11, 38]. When designing the reflectors it was chosen to increase the a/p ratio to decrease the reflectivity. This decision was made to help the fabrication tolerance, but a better choice would probably be to decrease the a/p ratio in order to avoid propagation loss under metal—this has not been characterized. Changing the a/p ratio changes the velocity, which is also characterized by Saldanha. From these velocity values the reflector wavelengths were adjusted for the 3 a/p ratios in order to give the same center frequency on each chip.

An initial WH1 mask was fabricated with different 3 codes. Initial bad results and time constraints led to the initial wrong assumption that the design parameters were not achieved by the fabrication. This led to the design of variable chip-length length, same reflectivity, Walsh-Hadamard-like 2 reflectors (WHL2) which are presented in the next section.

After the initial WHL2 devices showed what closely resembled a single frequency Bragg reflector response similar to the WHL1 devices, it was understood that the WHL1 devices had the incorrect chip spacing. The fundamental spacing of 1/4λ used to achieve a 180^0 phase shift turns into a full wavelength at 2^{nd} harmonic, so the WHL2 devices in the next section were successfully corrected. With this said, a second fabrication of WHL1 reflectors was never attempted because of time constraints and having already successfully made WHL2 devices. Only coupling-of-modes simulations will be shown for the WHL1 reflector devices. However, the accuracy of the COM matching of measured WHL2 reflectors gives confidence that the simulations presented in this section are accurate representations of what fabricated device measurements would give.

5.3.3 Definition of Orthogonality Measure

Some of these WHL device responses have good degree of orthogonality. There's a relatively large difference between the auto-correlation peak and the cross-correlation null corresponding to the auto-correlation peak location. This is defined here as the orthogonality level (OL), for the time or frequency domain waveform correlation, TOL and FOL, respectively. If OL is mentioned, it means the smaller of the 2, min(TOL, FOL). Many codes have a TOL or FOL of 5 to 10db, only those with about 10db or more are chosen—the higher this value the better the orthogonality between codes. Improvement should be possible after optimizing some of the parameters (specially the reflectivity values). Of the codes with good orthogonality, most of them are only orthogonal on sets of pairs. However, 3-code sets have been found being all mutually orthogonal—about 17sets (probably more) having minimum orthogonality level of ~10dB, and 3 sets found with a minimum OL of 20dB. One 4-code set was found having a TOL of 12.4dB and FOL of 13.3dB. By changing the number of chips, length, and further adjustments to reflectivity values, more and better 4-code sets may be obtained.

5.3.4 WHL1 Simulation Results

First shown are a series of plots of selected WHL1 device responses and correlation plots—the COM simulation of these devices uses a 50Ohm characteristic impedance and COM parameters as given in the first line of Figure 5-14 (section 5.4.3), except for the reflector reflectivity which is varied as specified above. In the simulation results, notice how the frequency domain cross-correlation is almost perfectly symmetric and the null naturally tends to fall on the location corresponding to the auto-correlation peak.

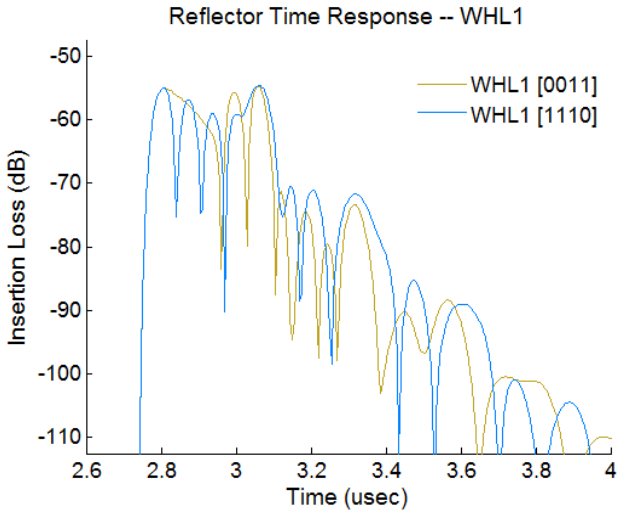
Reflector Time Response -- WHL1
WHL1 [0011]
WHL1 [1110]
Insertion Loss (dB)
Time (usec)

(a)

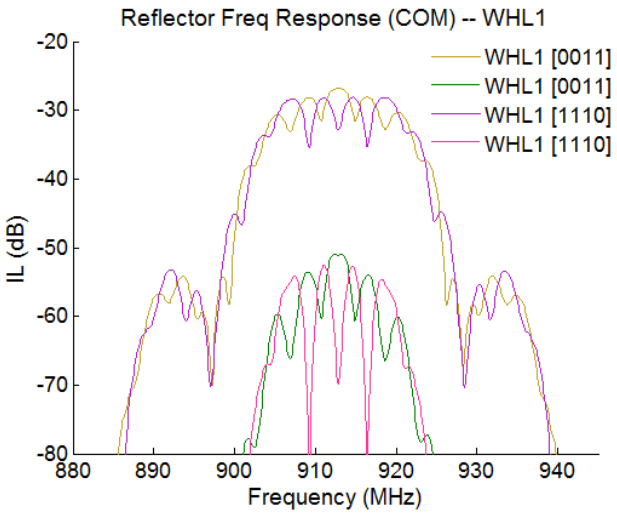
Reflector Freq Response (COM) -- WHL1
WHL1 [0011]
WHL1 [0011]
WHL1 [1110]
WHL1 [1110]
IL (dB)
Frequency (MHz)

(b)

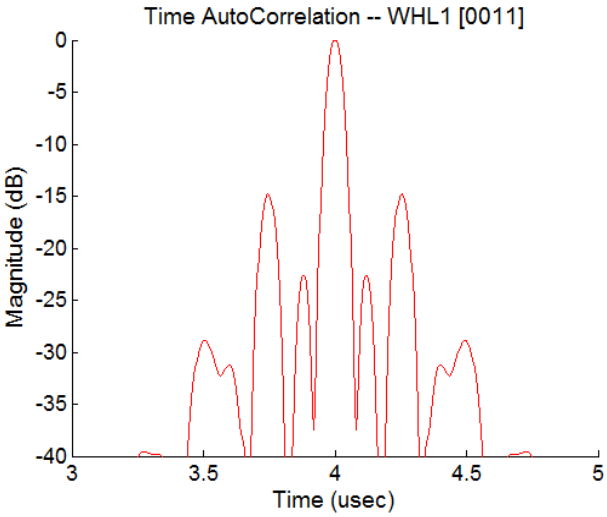
Time AutoCorrelation -- WHL1 [0011]
Magnitude (dB)
Time (usec)

(c)

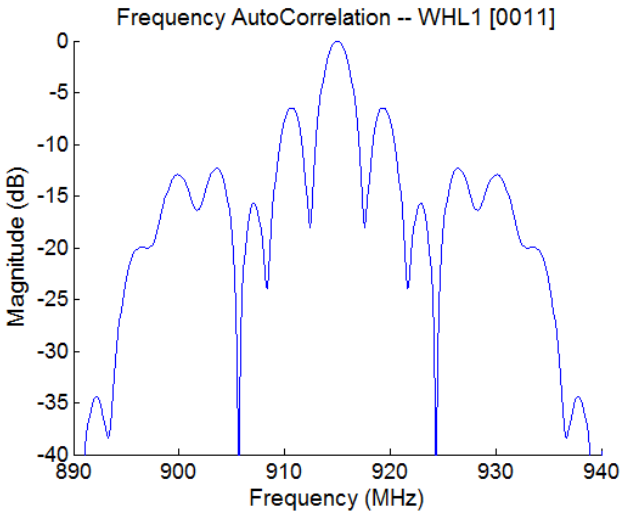
Frequency AutoCorrelation -- WHL1 [0011]
Magnitude (dB)
Frequency (MHz)

(d)

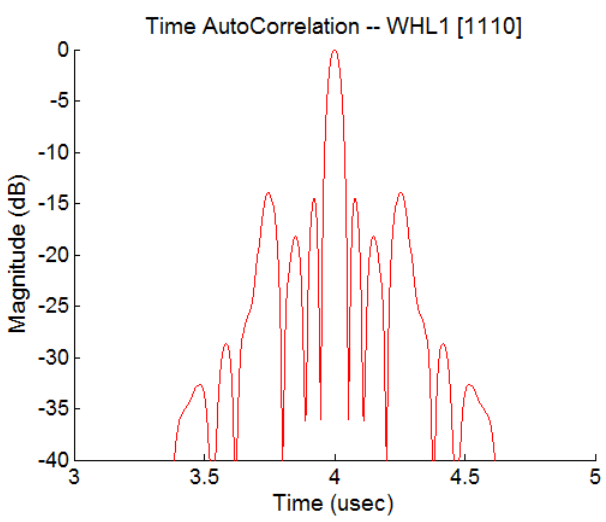

(f)

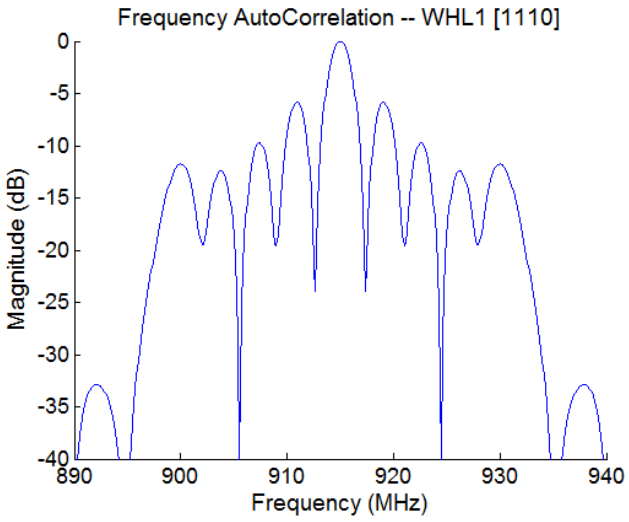

(g)

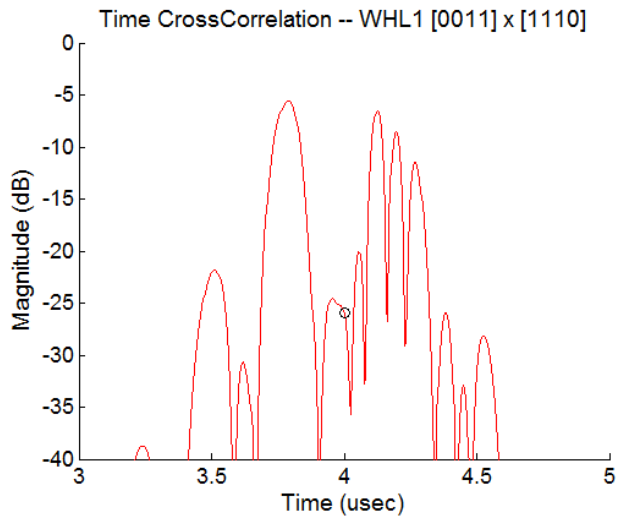

(h)

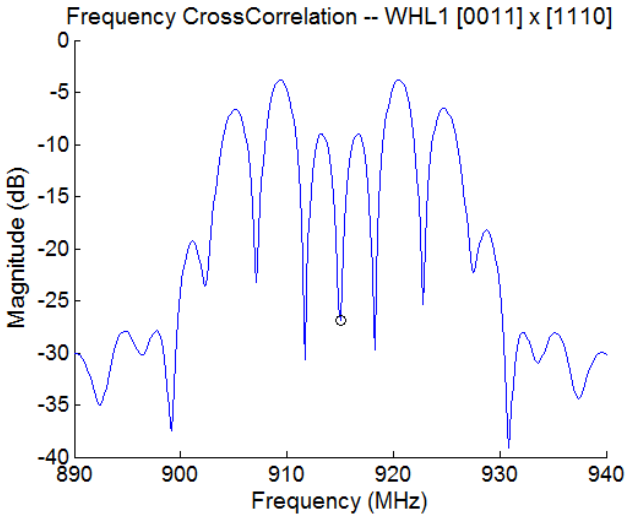

(i)

Figure 5-7. Simulation of WHL1[0011] and [1110] time and frequency domain waveforms, and auto and cross-correlations for both time and frequency domain waveforms. The circle gives the location where ideally the null of the cross-correlation should occur in order to correspond to the auto-correlation peak location.

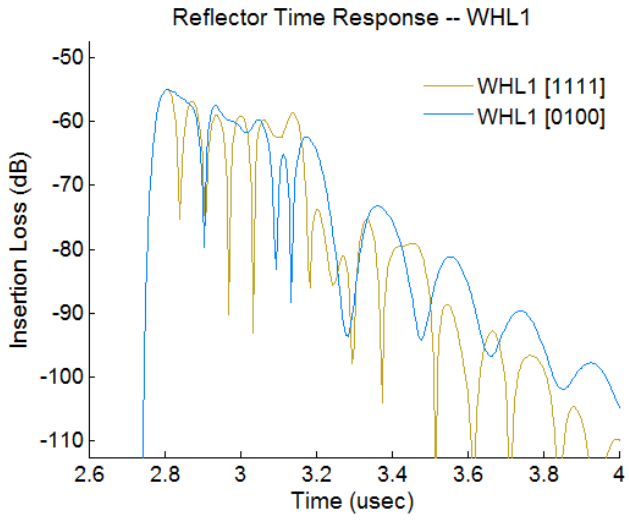
Reflector Time Response -- WHL1
WHL1 [1111]
WHL1 [0100]
Insertion Loss (dB)
-50
-60
-70
-80
-90
-100
-110
2.6
2.8
3
3.2
3.4
3.6
3.8
4
Time (usec)

(a)

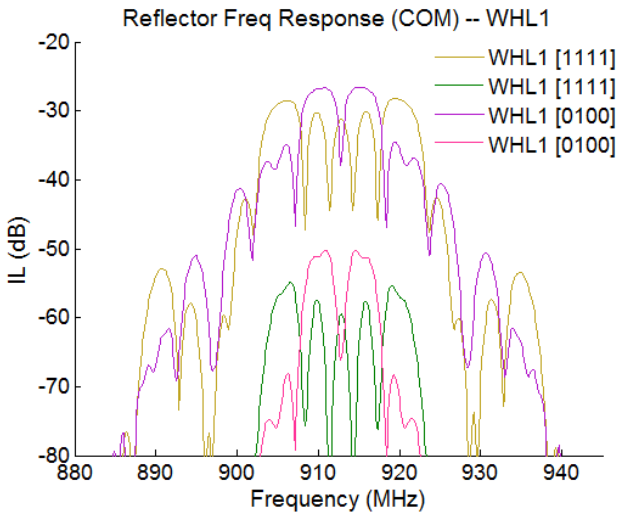
Reflector Freq Response (COM) -- WHL1
WHL1 [1111]
WHL1 [1111]
WHL1 [0100]
WHL1 [0100]
IL (dB)
-20
-30
-40
-50
-60
-70
-80
880
890
900
910
920
930
940
Frequency (MHz)

(b)

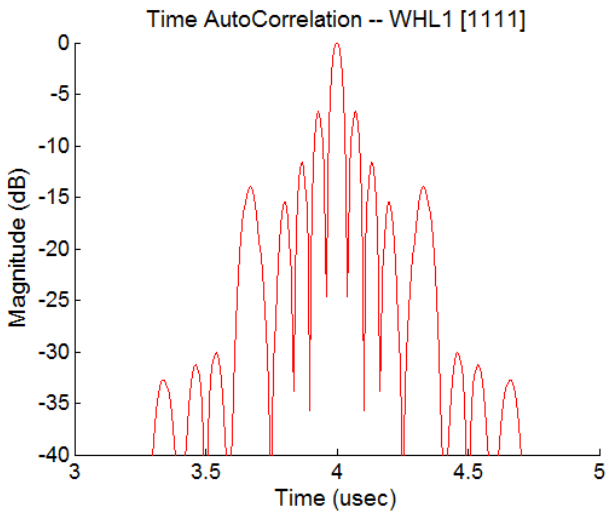
Time AutoCorrelation -- WHL1 [1111]
Magnitude (dB)
0
-5
-10
-15
-20
-25
-30
-35
-40
3
3.5
4
4.5
5
Time (usec)

(c)

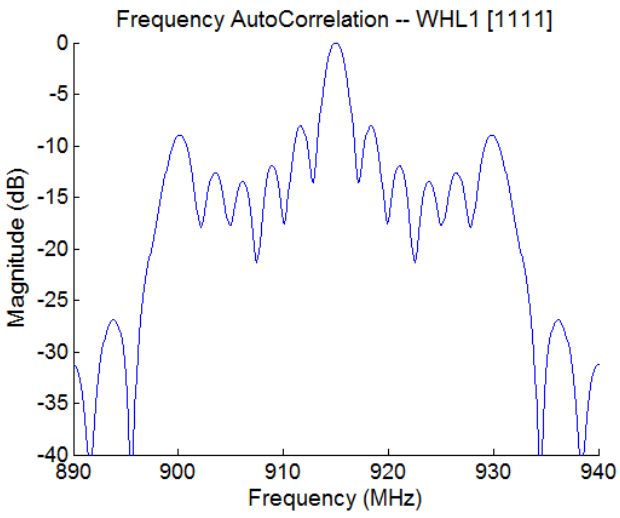
Frequency AutoCorrelation -- WHL1 [1111]
Magnitude (dB)
0
-5
-10
-15
-20
-25
-30
-35
-40
890
900
910
920
930
940
Frequency (MHz)

(d)

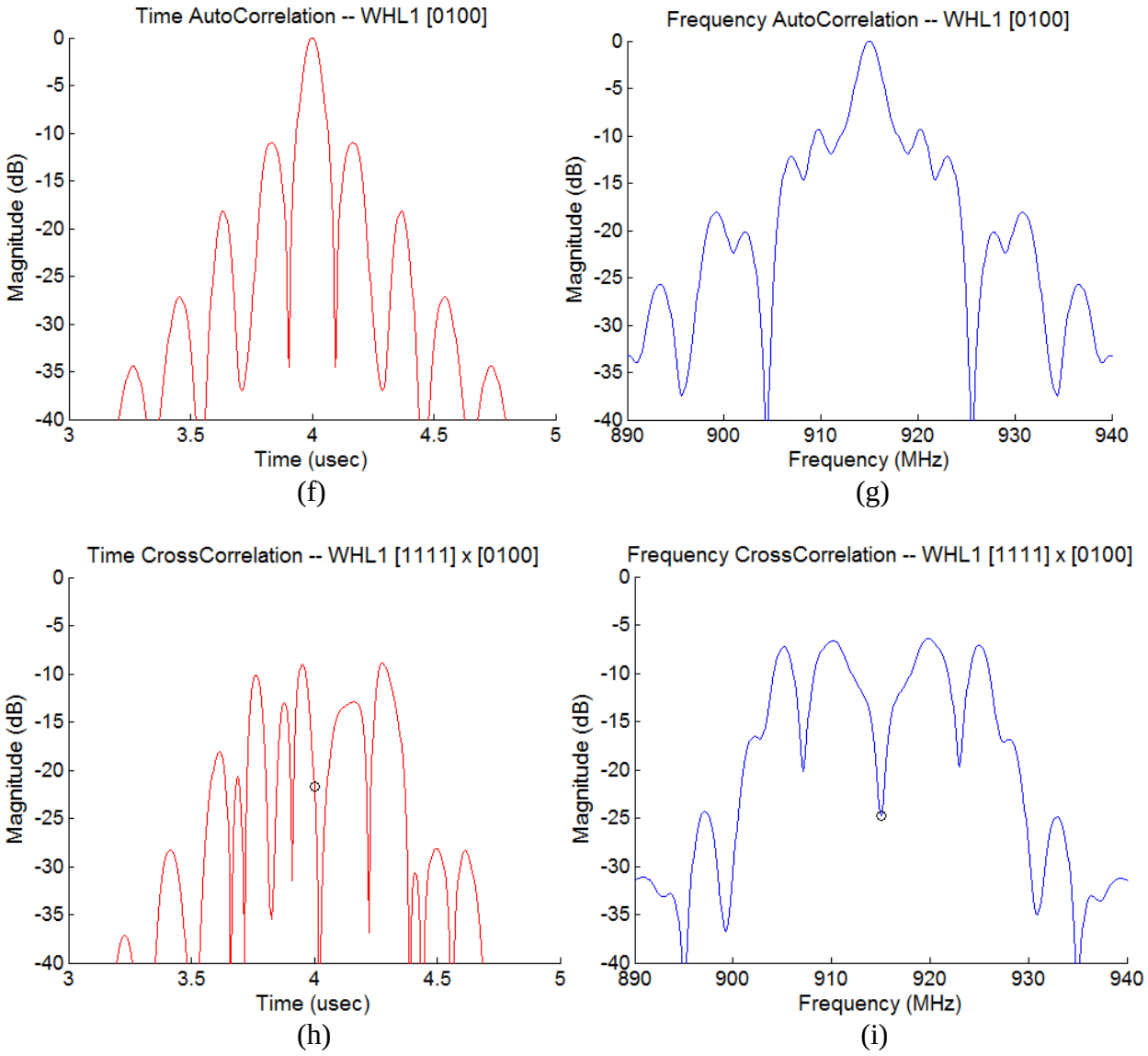

Figure 5-8. Simulation of WHL1[1111] and [0100] time and frequency domain waveforms, and auto and cross-correlations for both time and frequency domain waveforms. The circle gives the location where ideally the null of the cross-correlation should occur in order to correspond to the auto-correlation peak location.

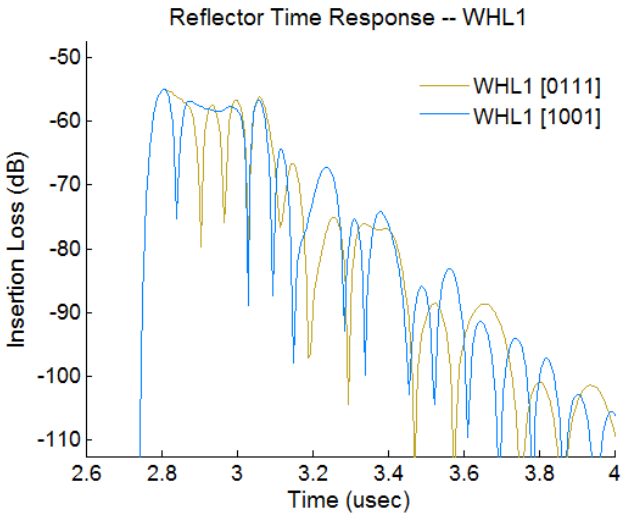
Reflector Time Response -- WHL1
WHL1 [0111]
WHL1 [1001]
Insertion Loss (dB)
-50
-60
-70
-80
-90
-100
-110
2.6
2.8
3
3.2
3.4
3.6
3.8
4
Time (usec)

(a)

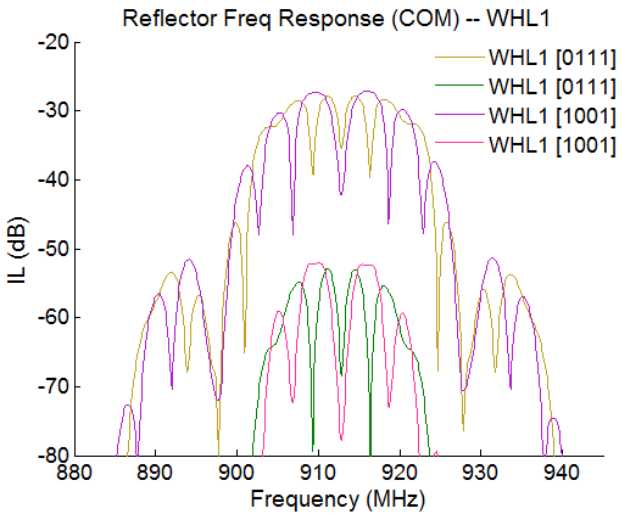
Reflector Freq Response (COM) -- WHL1
WHL1 [0111]
WHL1 [0111]
WHL1 [1001]
WHL1 [1001]
IL (dB)
-20
-30
-40
-50
-60
-70
-80
880
890
900
910
920
930
940
Frequency (MHz)

(b)

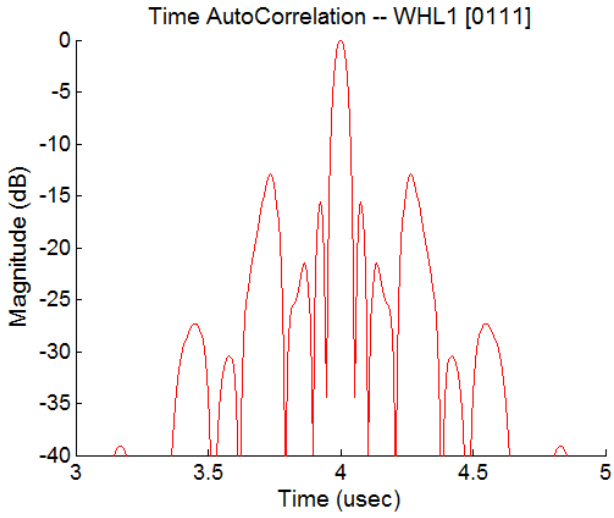
Time AutoCorrelation -- WHL1 [0111]
Magnitude (dB)
0
-5
-10
-15
-20
-25
-30
-35
-40
3
3.5
4
4.5
5
Time (usec)

(c)

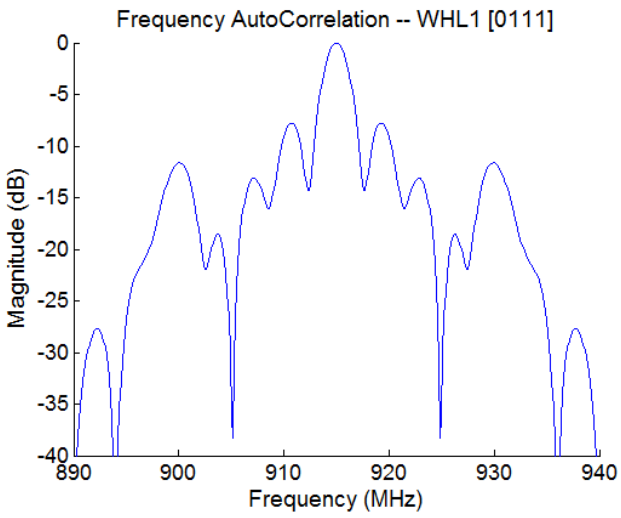
Frequency AutoCorrelation -- WHL1 [0111]
Magnitude (dB)
0
-5
-10
-15
-20
-25
-30
-35
-40
890
900
910
920
930
940
Frequency (MHz)

(d)

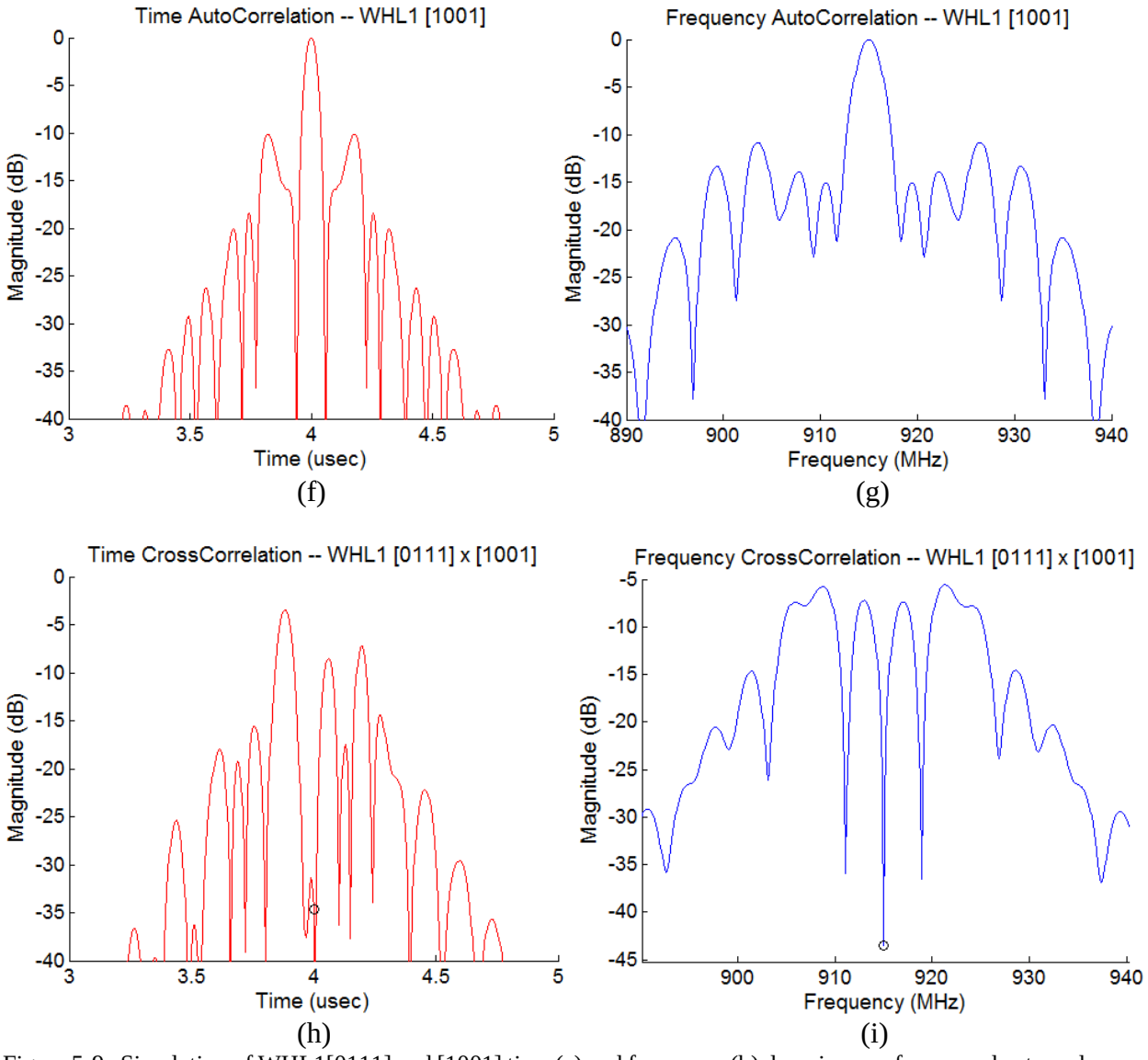

Figure 5-9. Simulation of WHL1[0111] and [1001] time (a) and frequency (b) domain waveforms, and auto and cross-correlations for both time and frequency domain waveforms (c through i).

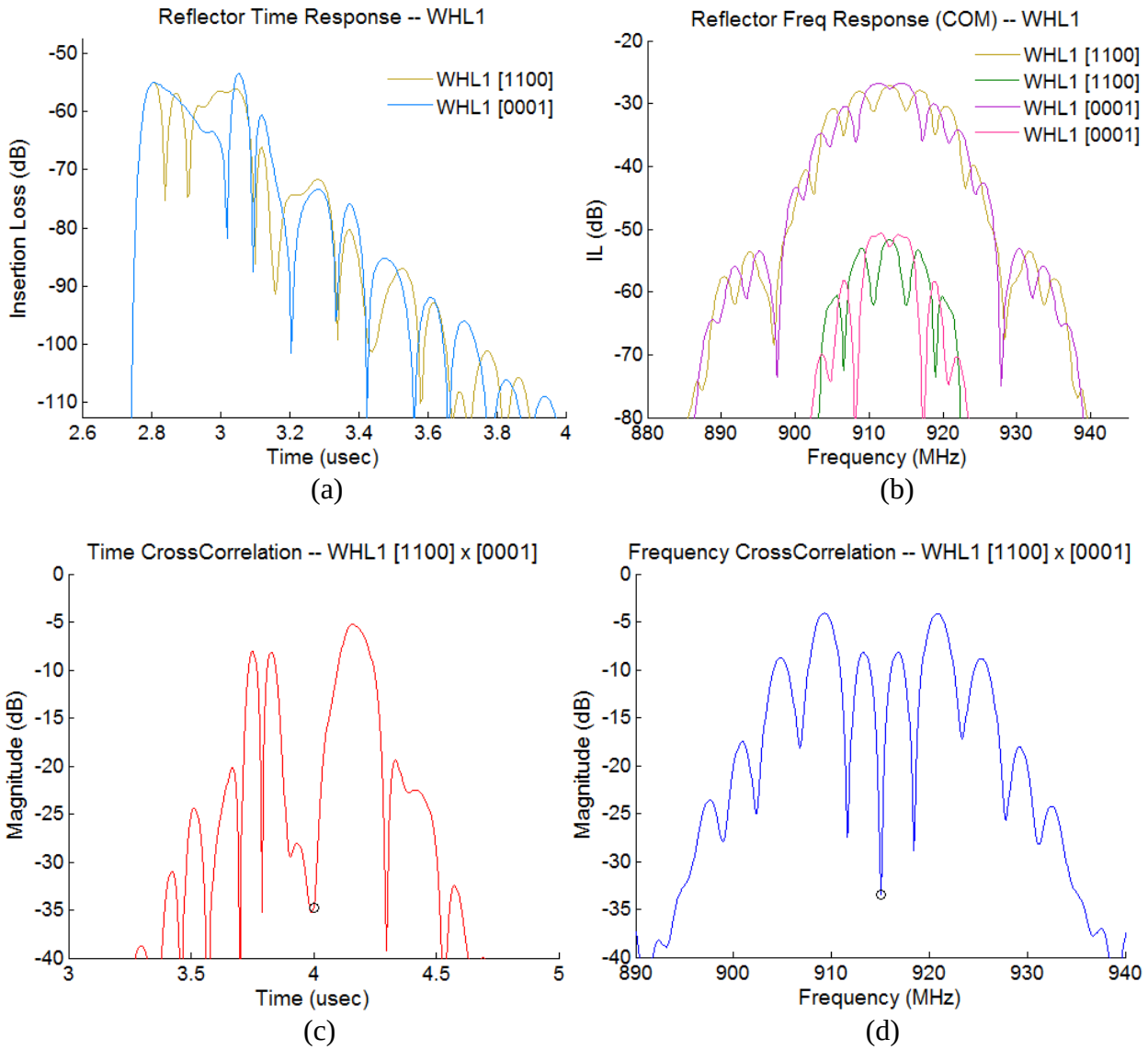

Figure 5-10. Simulation of WHL1[1100] and [0001] time (a) and frequency (b) domain waveforms, and cross-correlations for both time (c) and frequency (d) domain waveforms.

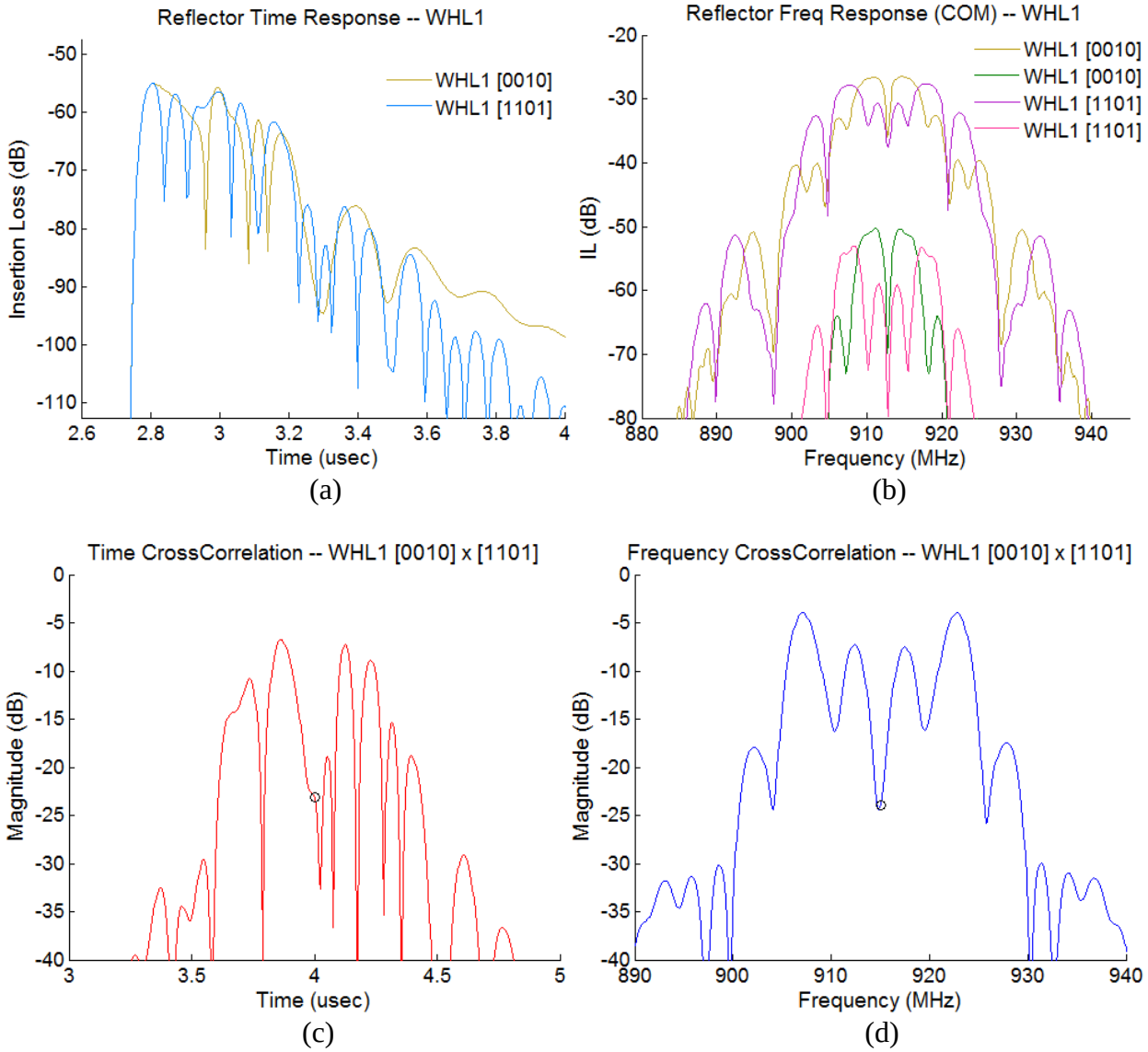

Figure 5-11. Simulation of WHL1[0010] and [1101] time (a) and frequency (b) domain waveforms, and cross-correlations for both time (c) and frequency (d) domain waveforms.

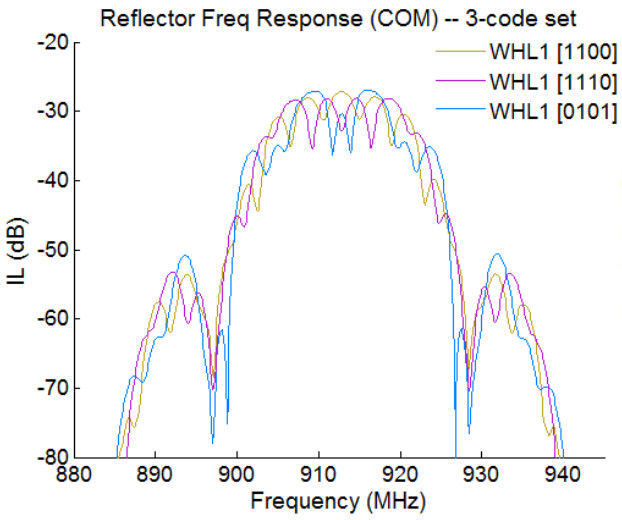
Reflector Freq Response (COM) -- 3-code set
WHL1 [1100]
WHL1 [1110]
WHL1 [0101]
IL (dB)
Frequency (MHz)

(a)

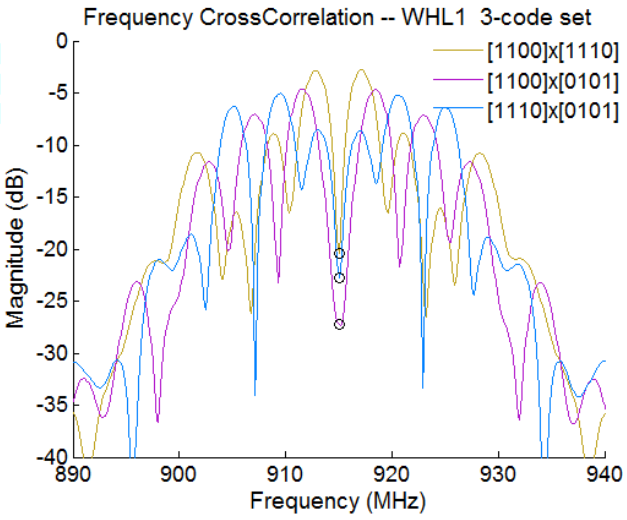
Frequency CrossCorrelation -- WHL1 3-code set
[1100]x[1110]
[1100]x[0101]
[1110]x[0101]
Magnitude (dB)
Frequency (MHz)

(b)

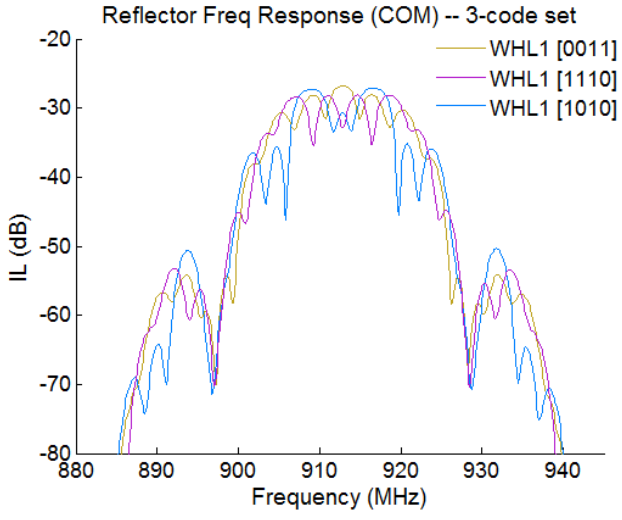
Reflector Freq Response (COM) -- 3-code set
WHL1 [0011]
WHL1 [1110]
WHL1 [1010]
IL (dB)
Frequency (MHz)

(c)

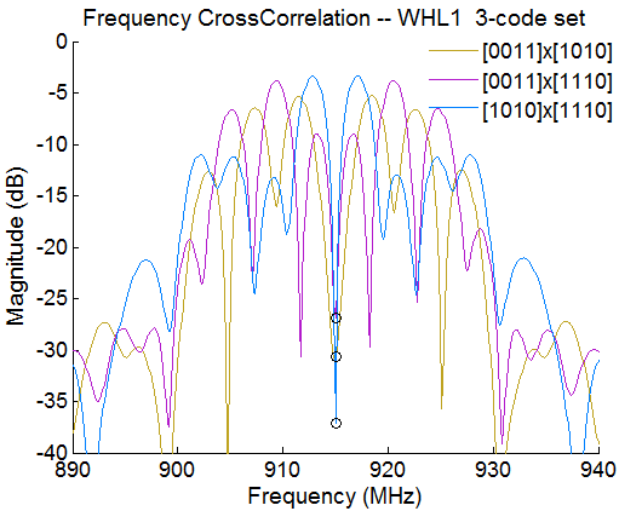
Frequency CrossCorrelation -- WHL1 3-code set
[0011]x[1010]
[0011]x[1110]
[1010]x[1110]
Magnitude (dB)
Frequency (MHz)

(d)

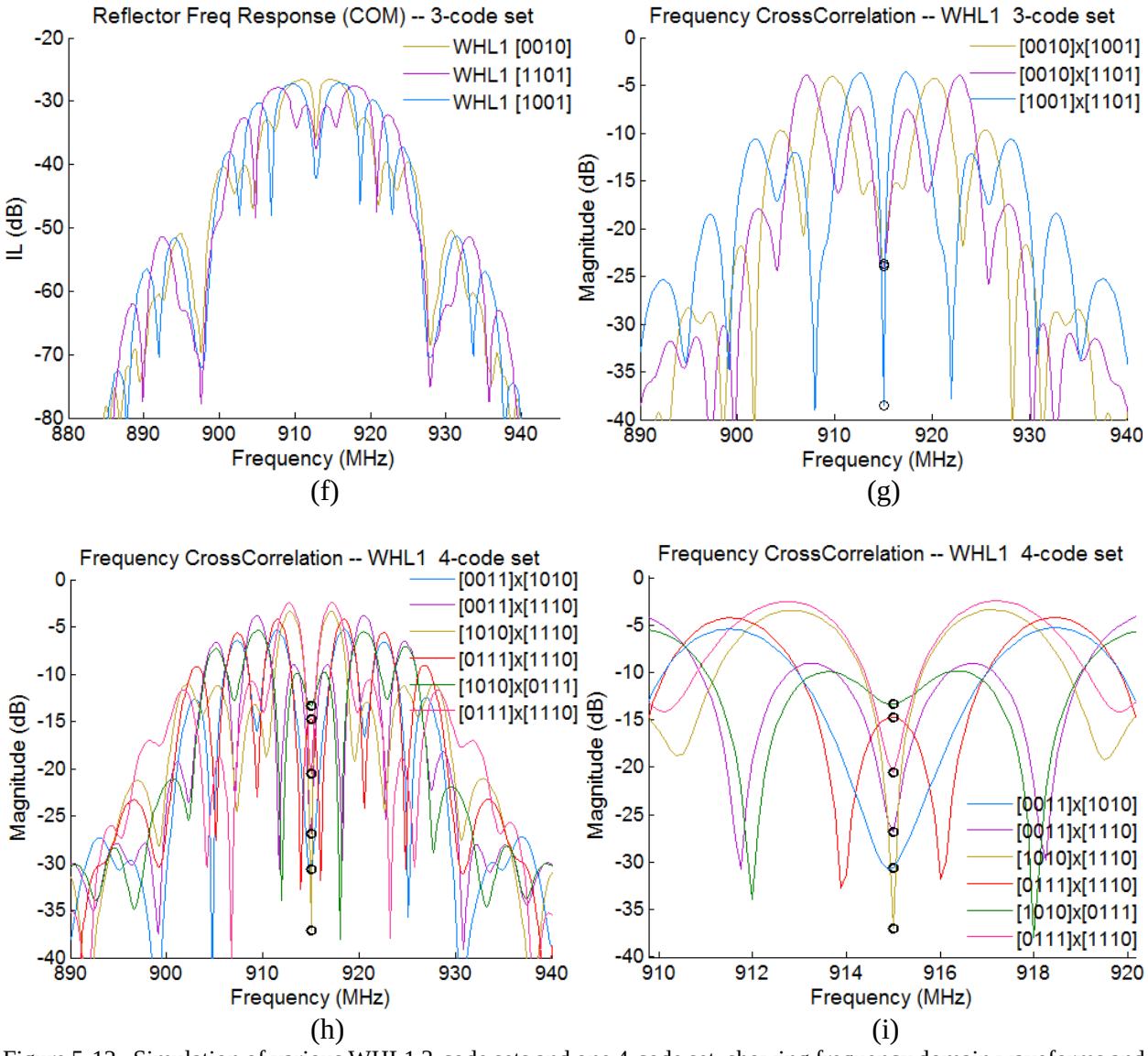

Figure 5-12. Simulation of various WHL1 3-code sets and one 4-code set, showing frequency domain waveforms and frequency domain cross-correlation. (a) and (b) show frequency response and frequency cross-correlation for set [1100], [1110], [0101]. (c) and (d) show frequency response and frequency cross-correlation for set [0011], [1110], [1010]. (f) and (g) show frequency response and frequency cross-correlation for set [0010], [1101], [1001].

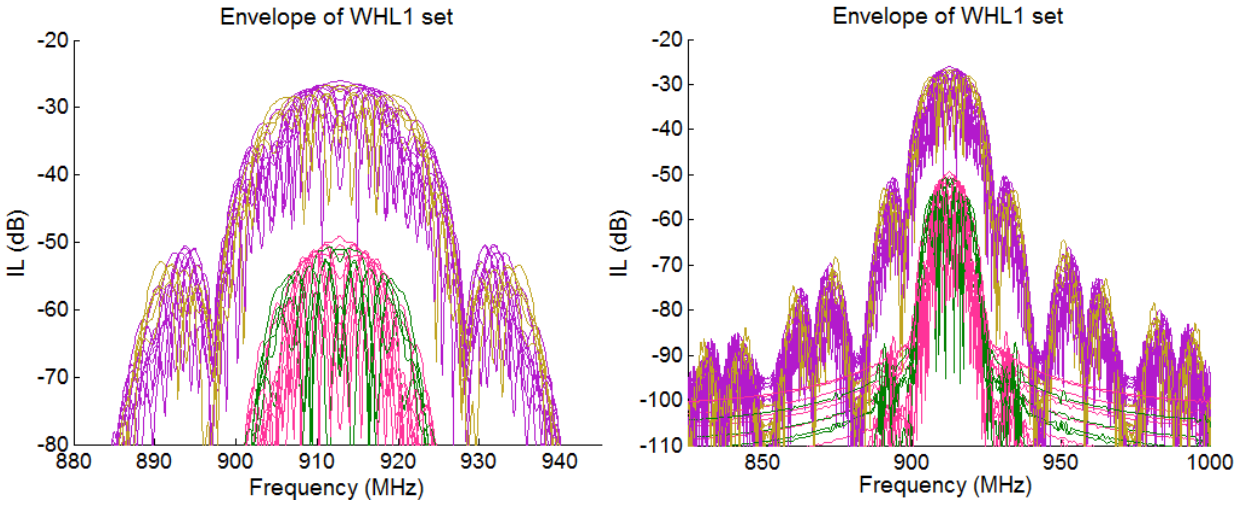

(a) (b)

Figure 5-13. Frequency response envelope of the WHL1 set presented here. (a) zoomed in, (b) zoomed out.

5.4 Varied Length Equal Reflectivity WH-like Coded Reflectors

5.4.1 Introduction to Walsh-Hadamard-like-2 Reflectors

This section presents the Walsh-Hadamard-like 2 (WHL2) codes, which have varied length reflectors (chips) and same reflectivity throughout—therefore identical electrodes. This is not to be confused with pulse width modulation, because the widths are very specific and can't just be modulated randomly. What this is fundamentally doing is compensating for the stored energy effect of electrodes and shaping the frequency domain function, so a simple analytic representation is not appropriate. OFC is defined using ideal truncated cosines. Section 6-2 shows that the SAW reflectors give appropriate approximations with low reflectivity, but not so with high reflectivity—noting from Figure 5-6f that the OFC cross-correlation actually gives a peak instead of a null. The WHL designs here are defined directly with high reflectivity, so a simple truncated cosine model

is not appropriate, and needs to make use of the COM model (instructions on setting up a COM model can be found in Appendix F).

Even though WHL2s are not equal length like a true WH sequence, the name is appropriate because it is very similar to WHL1 in the frequency domain. The fabricated WHL2 devices have chip lengths of [14 4 22 24 30] wavelengths at ~457MHz—also equal to the number of 2nd harmonic reflector strips as implemented here. With the WHL2 design, if the a/p ratio changes the device is probably going to keep similar characteristics and mainly just be scaled in frequency, with second order effects being small. With the WHL1 devices, if all the electrode widths change by the same amount or percentage, it will make the frequency asynchronous between the chips, and probably more sensitive to fabrication issues. The WHL2 devices have a shorter time response. In the initial design process of shaping the bandwidth, 5 chip-length combinations were stumbled upon which gave good results—these combinations are [14 2 16 30 X], [14 6 26 30 X], [14 8 24 36 X], [14 4 22 26 X], and [14 4 22 24 X], with the last reflector possibly having lengths of 0, 30 or 60. Code mining for good cross-correlation properties was done for only 3 chip-length combinations, which are still called WHL2, the distinction between them is denoted by placing the chip-length sequence before the letters. The 3 chip-length sequences analyzed for cross-correlation properties and searched for 3-code sets having frequency orthogonality level (FOL) greater than 10dB are: [14 4 22 24 30]WHL2, [14 2 16 30 30]WHL2, and [14 2 16 30 0]WHL2, this last one having 4 chips instead of 5.

5.4.2 Summary of Results for Walsh-Hadamard-like 1 and 2 Reflectors

The bandwidth between these 3 WHL2 sequences and also the WHL1 set is compared by looking at the 10dB bandwidth of the set envelope since the 3dB BW varies from code to code. The envelope plots are given at the end of this section, the 10dB BW values are as follows: WHL1=22.6MHz, [14 4 22 24 30]WHL2=27.6MHz, [14 2 16 30 20]WHL2=27.5MHz, [14 2 16 30 0]WHL2=27.3MHz. The WHL1 BW is a little flatter and narrower. Leaving out the last chip on the last WHL2 sequence didn't change the bandwidth much, but does change response characteristics and significantly changes the OL of many of the similar codes. The best frequency cross-correlation, or FOL values, obtained for 3-code sets of the WHL2 sequences are 18.3dB, 14.2dB, and 12.2dB, respectively for the order stated a few lines back. The number of 3-set codes found with FOL values over 10 for the WHL2 sequences in the order stated above are 3, 10, and 5. It's difficult to make conclusions as to what sequence is better without having application specifications to guide the design. Also, further optimization and mining of these type of codes would probably benefit from changing chip reflectivity as well and running a systematic search algorithm over several days, and then running a narrower optimization search over several days based on results from the coarser systematic search. The orthogonality level seems to be better on average for the WHL1 devices. Although all the combinations have not been tried, there seems to be more pairwise orthogonal WHL1 codes than WHL2. The WHL2 time domain null is generally narrower and the frequency domain null generally about the same or wider.

5.4.3 Summary of Results for Walsh-Hadamard-like 1 and 2 Reflectors

The fabricated WHL2 devices are bonded using silver-infused conductive epoxy to ~5.5mm leads of wire that are used in a differential antenna measurement method presented in the

next chapter. The differential measurement method uses two coaxial cables that are united through the grounds in order to measure a differential 1-port device. A 2-port S-parameter measurement is taken and converted to a 1-port impedance. The measurement results are shown using this technique rather than using ground-signal probes since the GS probe measurement gave a jagged looking out-of-band response. The differential measurement gives a clean measurement, unfortunately the lack of control in the epoxy application and curing process seems to introduce substantial variations in probepad parasitics. Also, the parasitics circuit model used (shown in previous chapter) may need adjustment if lumped element parasitic values are to be estimated by using the procedure shown in the previous chapter. In order to match the COM model to measured WHL2 devices shown below, Cp, Rp, and Lp were manually adjusted for each device. Three [14 4 22 24 30]WHL2 codes were built; WHL2[1 1 1 1], WHL2[0 0 1 1], and WHL2[1 1 0 0], and a fourth device having a 35wavelength (at 3rd harmonic) single frequency Bragg reflector—having a 3dB bandwidth of 12MHz. Since the Bragg reflector device has less insertion loss, this is the device that is 1st epoxy-bonded to the differential probe leads and antenna and the only device used to physically suppress the DTE (shown next chapter)—the least amount of reflector insertion loss was desired in order to have as much of the echo out of the noise as possible. The experimental WHL2 devices were all bonded on a different date than the single-reflector device—these have much different parasitic values than the single-reflector device. The parasitic values used for all 4 devices are now given (Cp, Rp, Lp): WHL2[1 1 1 1]=>(1.0e-12, 10, 6.0e-9), WHL2[0 0 1 1]=> (1.05e-12, 10, 7.6e-9), WHL2[1 1 0 0]=> (1.0e-12, 10, 6.8e-9), and single reflector(8.4e-13 F, 1 Ohm, 6.1e-9 H). Fortunately the device that is used to demonstrate wireless echo suppression has much less parasitic resistance—the epoxy bonding procedure that day worked best.

After the differential impedance measurements were taken, the device response of the 4 devices were matched to COM simulations. It's difficult to say exactly what the magnitude and phase of the 10cell SPUDTs are, since a nearby 40cell or so SPUDT was not included in the mask. Bad planning and no follow through Also, in order to make sure not to break off the epoxy-bonded leads during the measurements of WHL2 fabricated devices, the 2-cable probe (shown next chapter) was separated and then its grounds rewound (shown next chapter) after inserting the leads into the coax—possibly throwing off the calibration. So the accuracy of the S-parameters for the 3 measured WHL2 devices is questionable. This is said because level of the echo is highly dependent on the load impedance as seen by the transducer. In the initial simulations below, used to match the COM simulation to the experimental results, a constant 50ohm load impedance is assumed and an attempt to match the echo level is done by changing the magnitude of the transducer reflectivity—the interest is not simulating the IDT, but showing that the reflector simulation closely matches the measured reflector response. A set of COM simulations is then shown starting in Figure 5-18, where the real and imaginary parts of the load impedance are changed in order to simulate an optimized echo suppression for each device—in this case the same reflectivity is kept for all devices since the optimized echo level is highly dependent on SPUDT reflectivity magnitude and phase, not caring about the characteristic impedance values used to optimize the echo suppression. The echo suppression optimization is also run for the measured devices and compared against the COM simulated results. It was noticed that the true physical characteristic impedance value used for actual physical echo suppression (Z0(915MHz))=71+j18Ohm, given next chapter) was closest to the calculated value of (Z0=58+j40Ohm) which was extracted from the differential impedance measurement, and

deviated more for the GS probe measurements. As stated before, the impedance values obtained from the COM simulation need to be taken with a grain of salt since it does not properly take into account the "4th" port which generates non-Rayleigh waves—it's uncertain how it currently may affect the optimized load impedance value. Figure 5-14 gives the transducer parameters used to match the reflector response to the measured data. For the echo suppression optimization all of the parameters are kept the same as in Figure 5-14, the only thing changed is that |R| is set to -.006 for all devices.

Table 5-1. COM parameters of the transducers used to match the simulated WHL2 reflector response to the response of the experimental devices.

To match experimental devices										
Device	Transducer Type	αSF	Cf	Rs	γLossIDT	|R|IDT	Vidt	γLossRef	|R|ref	Vref
WHL2[1111]	Optimized2 10pair	0.5466	3.812x10^-14	8	1400	-0.006	3410	400	.031/2	3441
WHL2[0011]	Optimized2 10pair	0.5466	3.812x10^-14	8	1400	-0.005	3412.5	400	.031/2	3444
WHL2[1100]	Optimized2 10pair	0.5466	3.812x10^-14	8	1400	-0.004	3412.5	400	.030/2	3444
Single Ref	Optimized2 10pair	0.5466	3.812x10^-14	8	1400	-0.004	3416	400	.031/2	3448

The transducer electrical characteristics are shown only for the single reflector device and the WHL2[1111] device. The COM simulation matching of experimental devices is 1st shown, Figure 5-14 through Figure 5-17. Then the echo suppression of experimental data and COM simulations is shown starting in Figure 5-18 through Figure 5-22—the echo suppression of experimental data is done by converting the measured response to admittance and regenerating S11 parameters with an optimized impedance (constant over frequency). The maximum value for both DTE and 1st Transit over a frequency range is used in the optimization—this tends to flatten out the DTE response, as opposed to putting a notch at center frequency if only the center frequency value of the DTE is optimized. Then a few selected WHL2 auto and cross-correlations are shown starting in Figure 5-23. Finally concluding this chapter with plots of the envelopes for the 3 WHL2 sequences discussed.

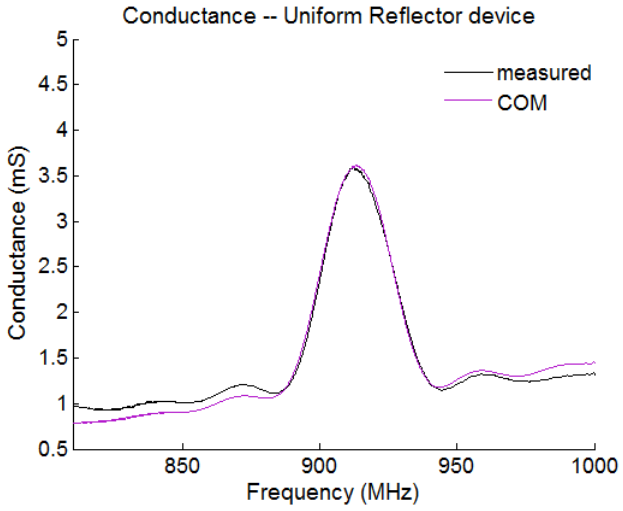
Conductance -- Uniform Reflector device
measured
COM
Conductance (mS)
Frequency (MHz)
5
4.5
4
3.5
3
2.5
2
1.5
1
0.5
850
900
950
1000

(a)

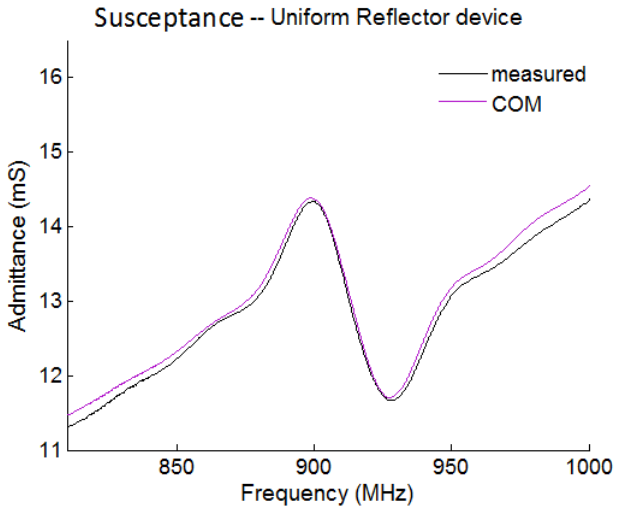
Susceptance -- Uniform Reflector device
measured
COM
Admittance (mS)
Frequency (MHz)
16
15
14
13
12
11
850
900
950
1000

(b)

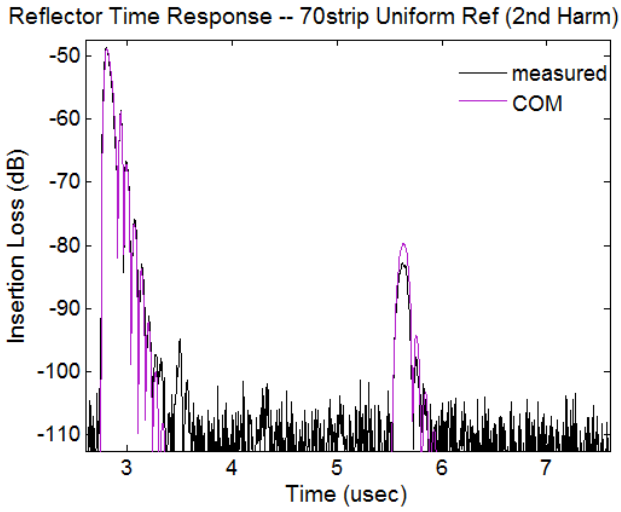
Reflector Time Response -- 70strip Uniform Ref (2nd Harm)
measured
COM
Insertion Loss (dB)
Time (usec)
-50
-60
-70
-80
-90
-100
-110
3
4
5
6
7

(c)

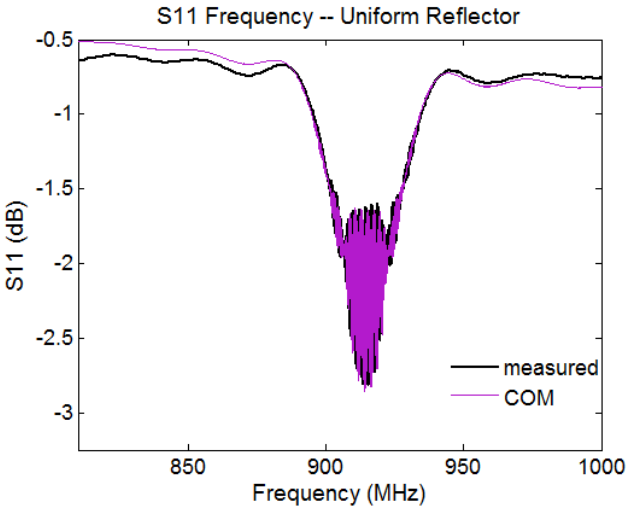
S11 Frequency -- Uniform Reflector
measured
COM
S11 (dB)
Frequency (MHz)
-0.5
-1
-1.5
-2
-2.5
-3
850
900
950
1000

(d)

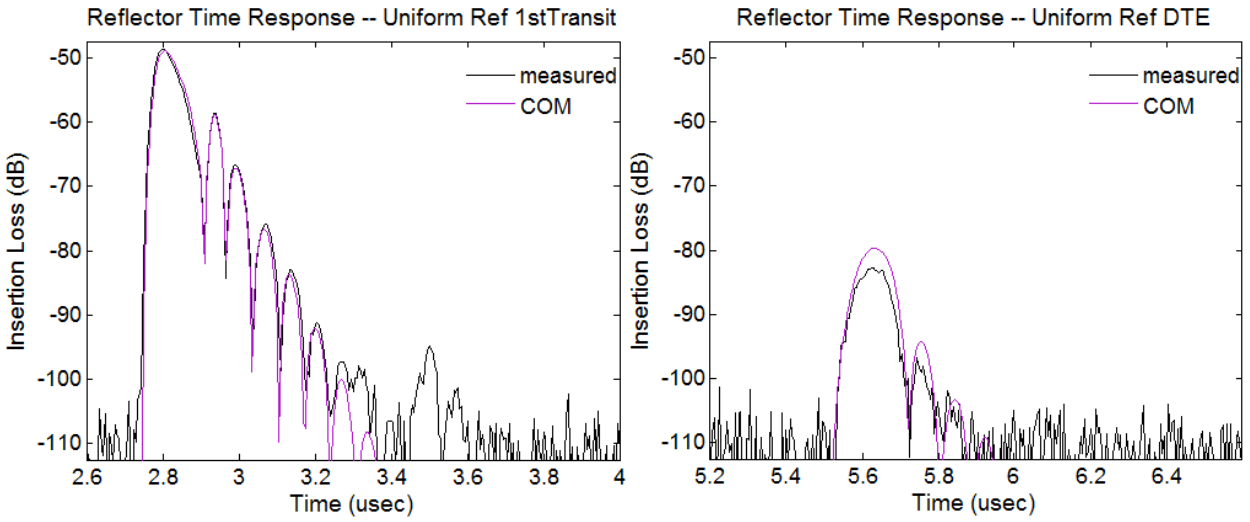

(e) (f)

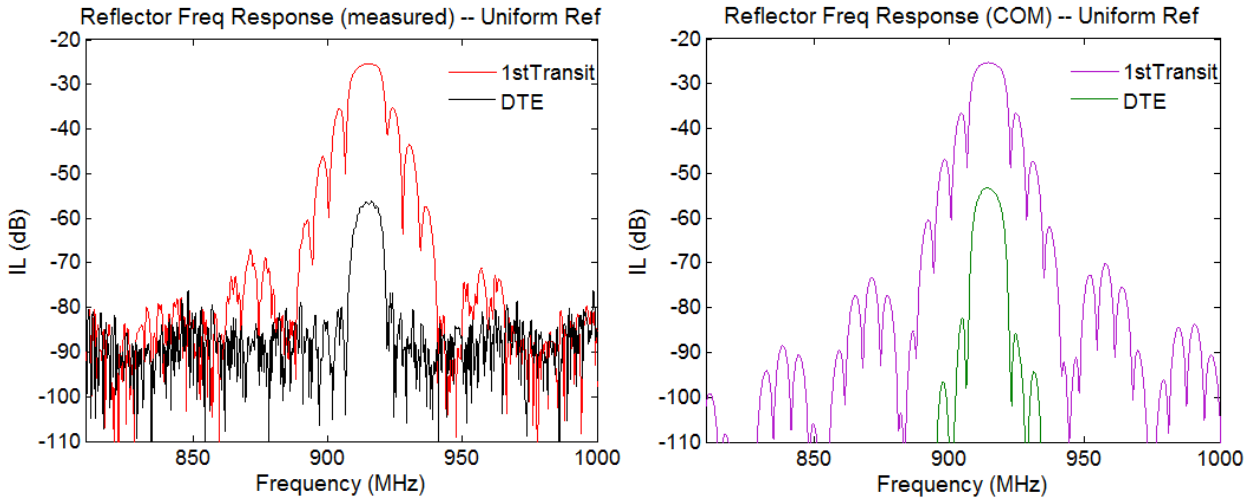

(g) (h)

Figure 5-14. Measured response of uniform reflector device and COM simulation to match measured response. (a) conductance, (b) susceptance, (c) S11 time, (d) S11 frequency, (e) main transit in time (f) DTE in time, (g) frequency response of gated 1st transit and DTE measured, (h) frequency response of gated 1st transit and DTE simulation.

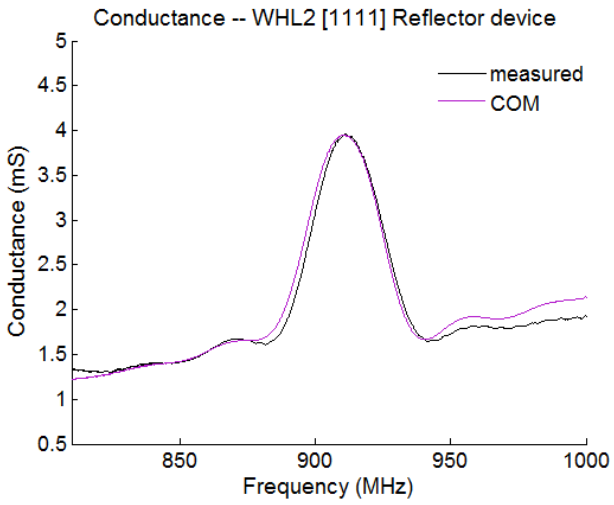
Conductance -- WHL2 [1111] Reflector device
measured
COM
Conductance (mS)
Frequency (MHz)
5
4.5
4
3.5
3
2.5
2
1.5
1
0.5
850
900
950
1000

(a)

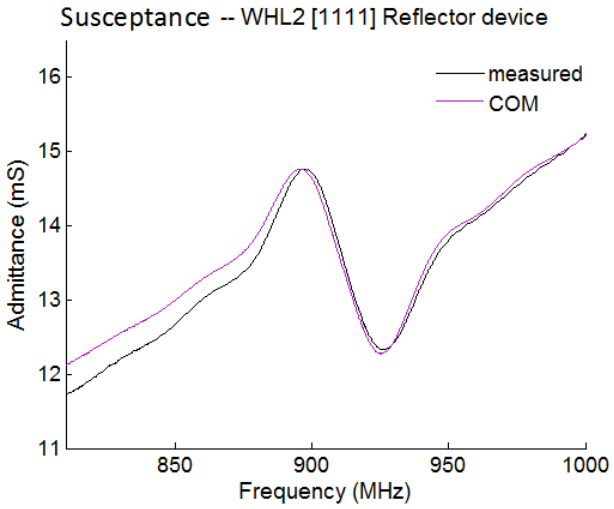
Susceptance -- WHL2 [1111] Reflector device
measured
COM
Admittance (mS)
Frequency (MHz)
16
15
14
13
12
11
850
900
950
1000

(b)

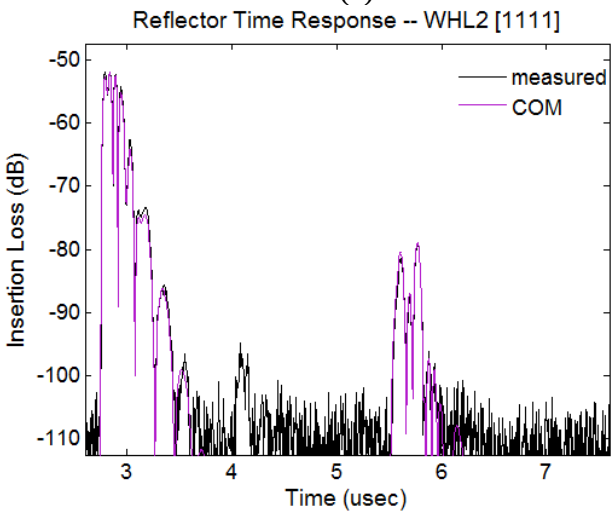
Reflector Time Response -- WHL2 [1111]
measured
COM
Insertion Loss (dB)
Time (usec)
-50
-60
-70
-80
-90
-100
-110
3
4
5
6
7

(c)

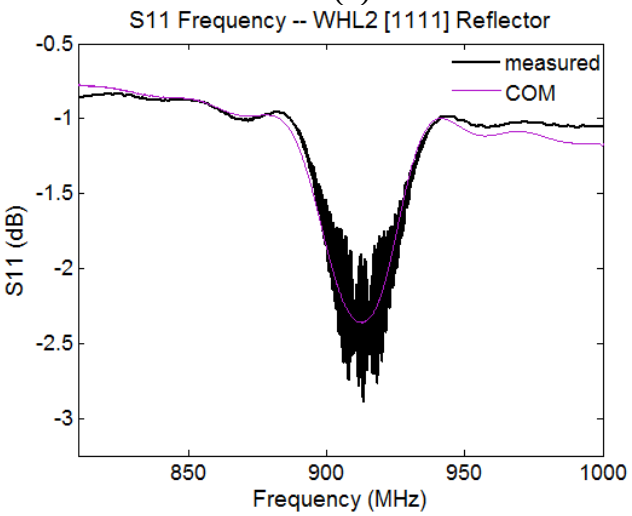
S11 Frequency -- WHL2 [1111] Reflector
measured
COM
S11 (dB)
Frequency (MHz)
-0.5
-1
-1.5
-2
-2.5
-3
850
900
950
1000

(d)

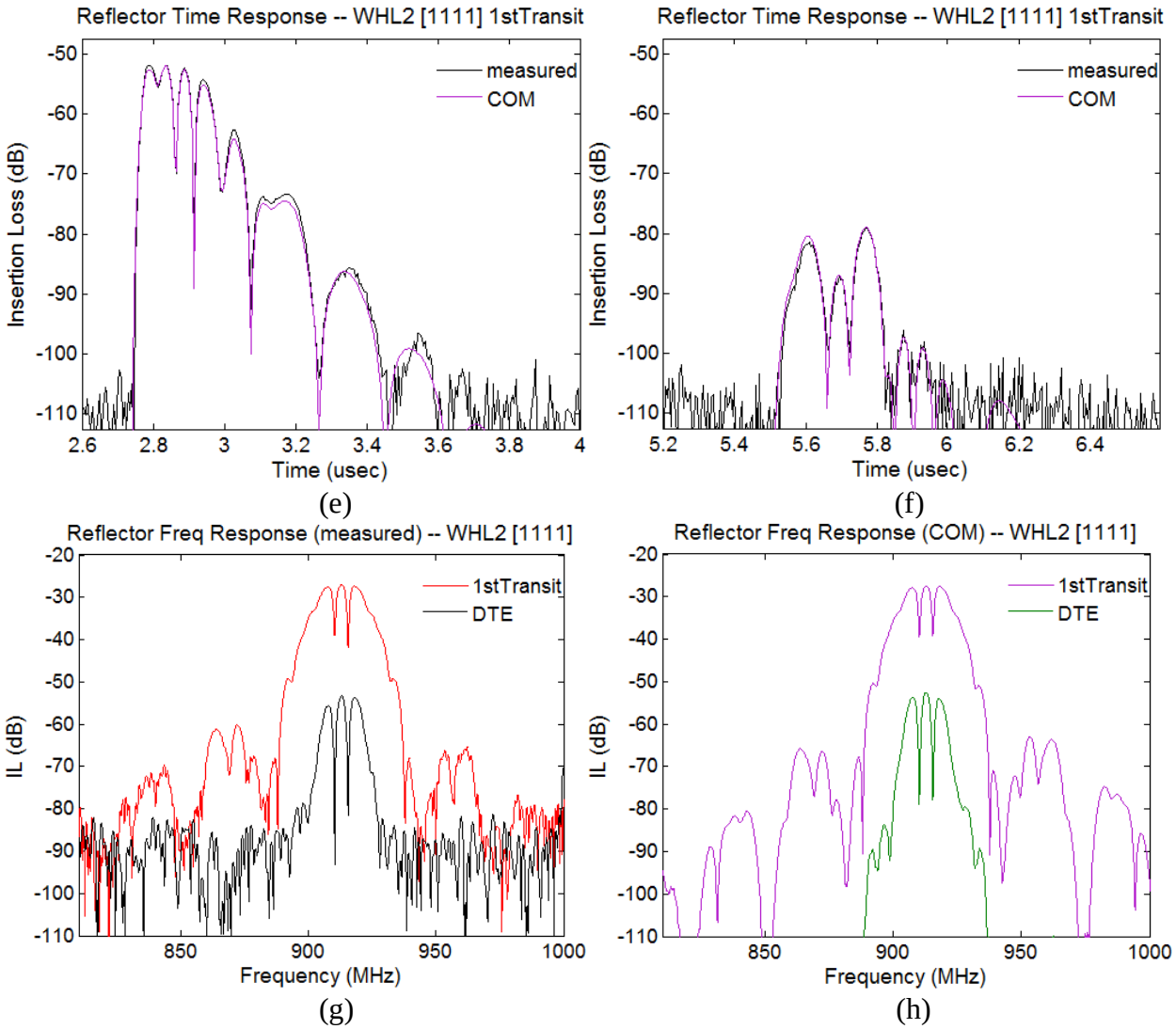

Figure 5-15. Measured response of WHL2[1111] device and COM simulation to match measured response. (a) conductance, (b) susceptance, (c) S11 time, (d) S11 frequency, (e) main transit in time (f) DTE in time, (g) frequency response of gated 1st transit and DTE measured, (h) frequency response of gated 1st transit and DTE simulation.

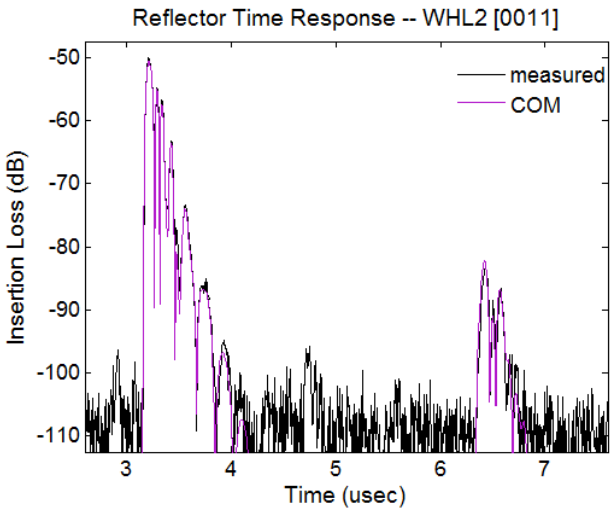
Reflector Time Response -- WHL2 [0011]
Insertion Loss (dB)
Time (usec)
measured
COM

(a)

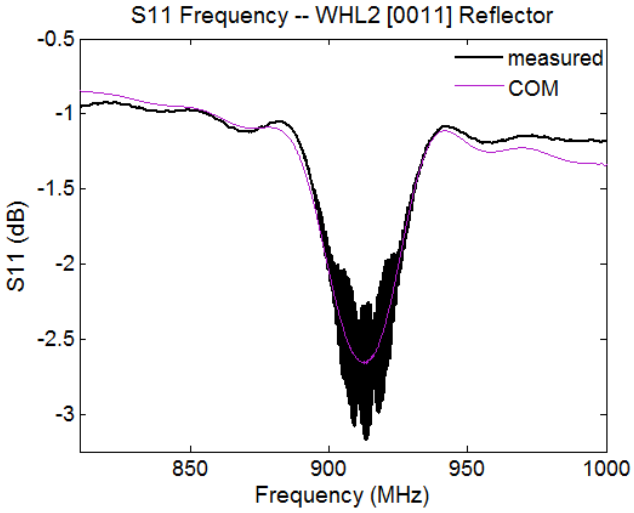
S11 Frequency -- WHL2 [0011] Reflector
S11 (dB)
Frequency (MHz)
measured
COM

(b)

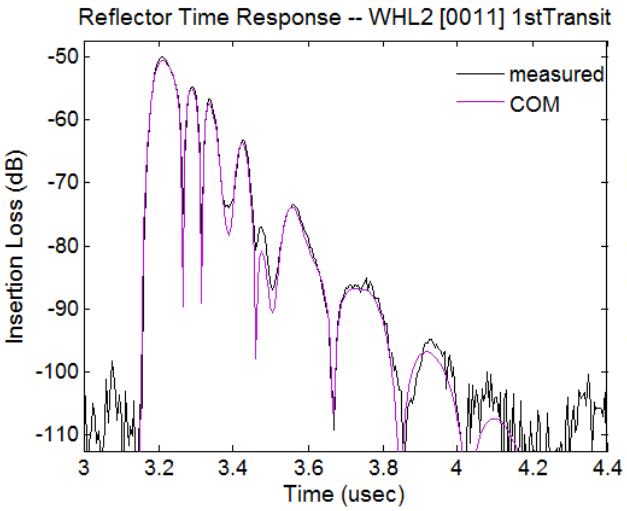
Reflector Time Response -- WHL2 [0011] 1stTransit
Insertion Loss (dB)
Time (usec)
measured
COM

(c)

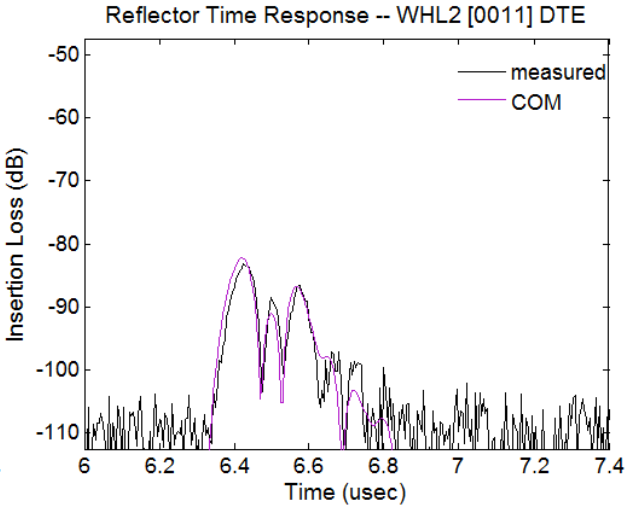
Reflector Time Response -- WHL2 [0011] DTE
Insertion Loss (dB)
Time (usec)
measured
COM

(d)

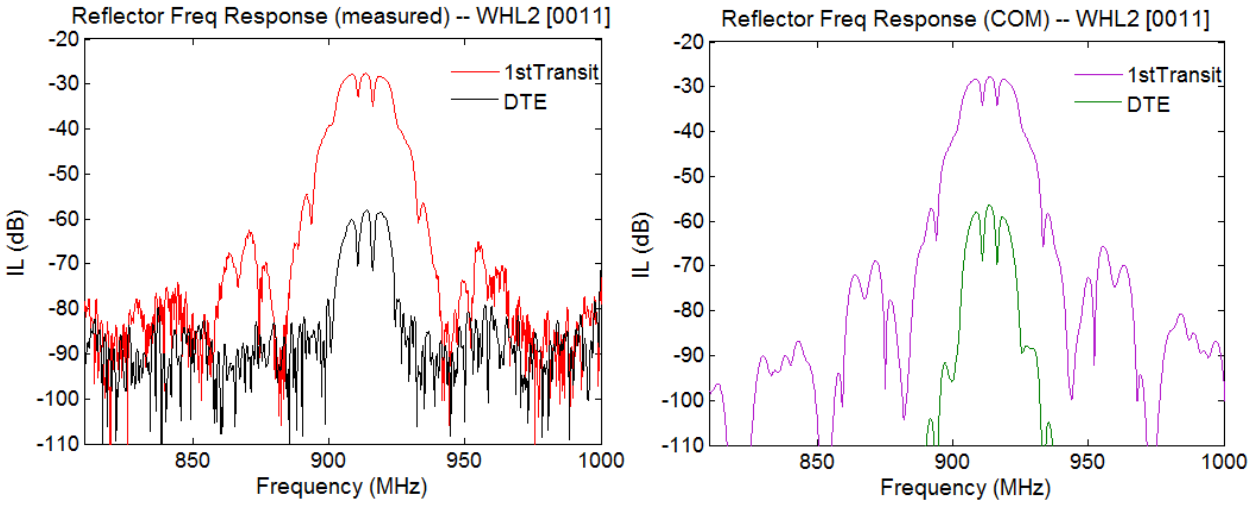

(e) (f)

Figure 5-16. Measured response of WHL2[0011] device and COM simulation to match measured response. (a) conductance, (b) susceptance, (c) S11 time, (d) S11 frequency, (e) main transit in time (f) DTE in time, (g) frequency response of gated 1st transit and DTE measured, (h) frequency response of gated 1st transit and DTE simulation.

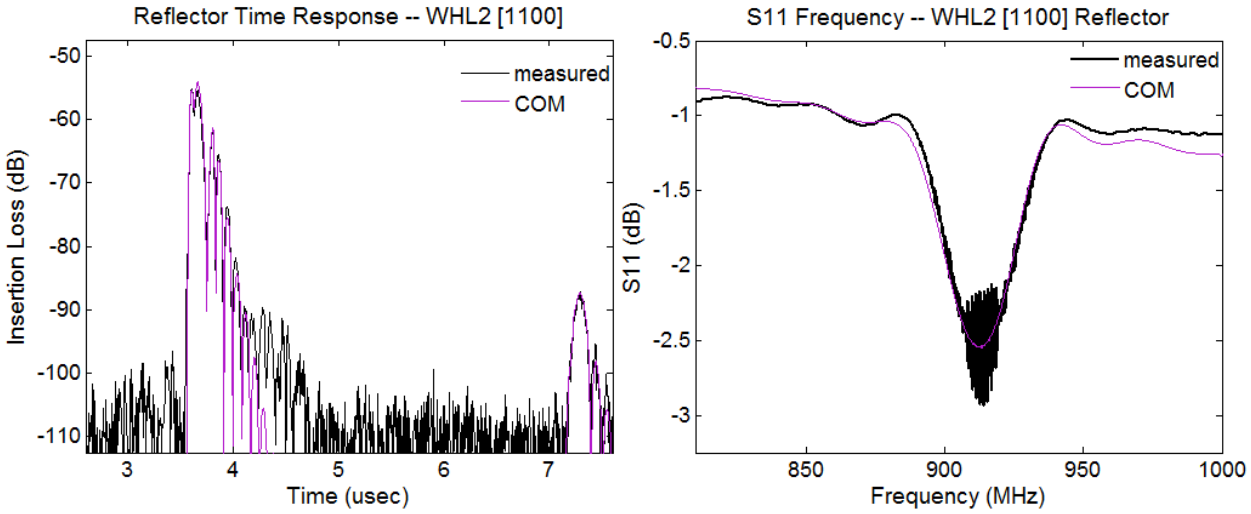

(a) (b)

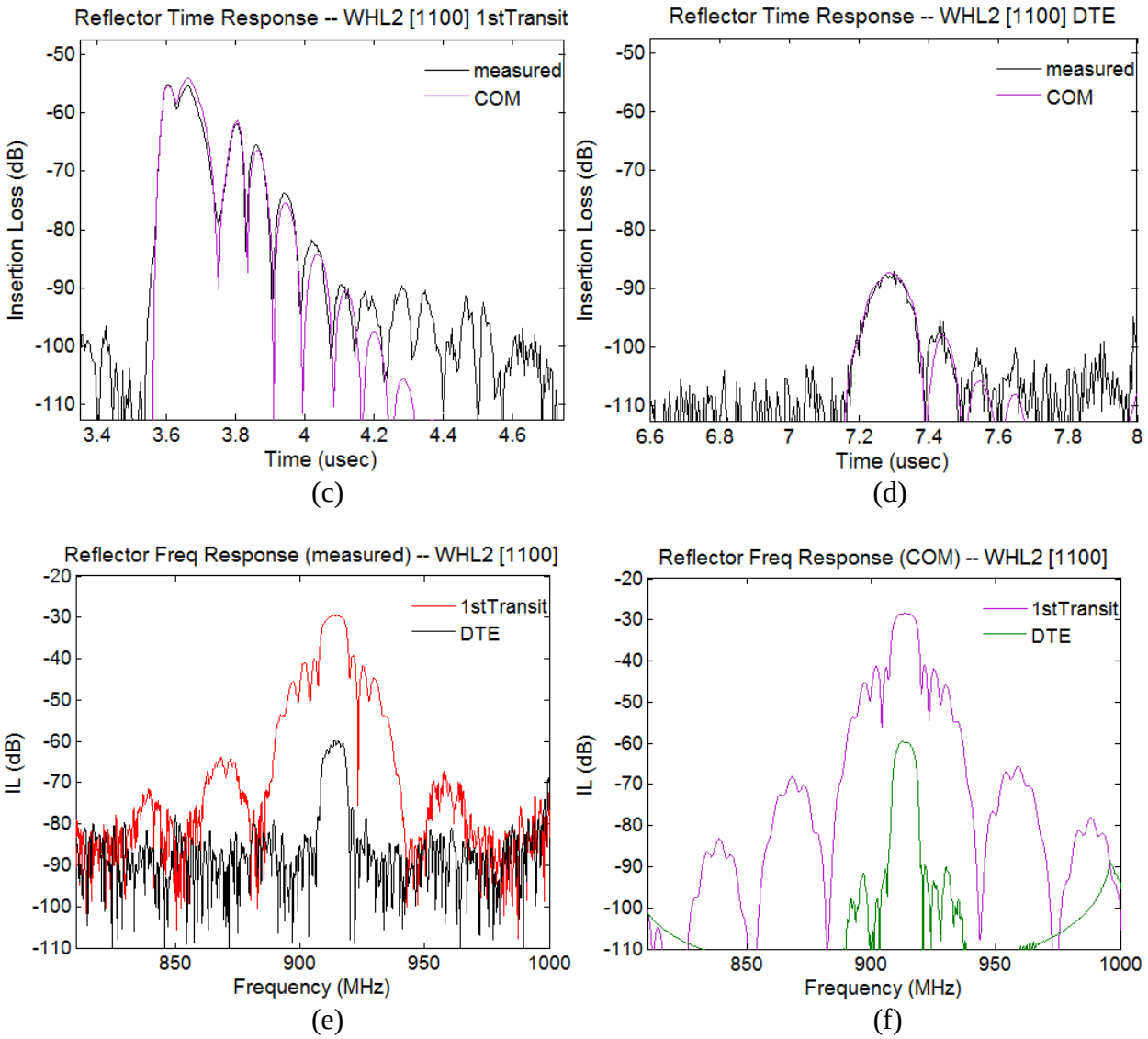

Figure 5-17. Measured response of WHL2[1100] device and COM simulation to match measured response. (a) conductance, (b) susceptance, (c) S11 time, (d) S11 frequency, (e) main transit in time (f) DTE in time, (g) frequency response of gated 1st transit and DTE measured, (h) frequency response of gated 1st transit and DTE simulation.

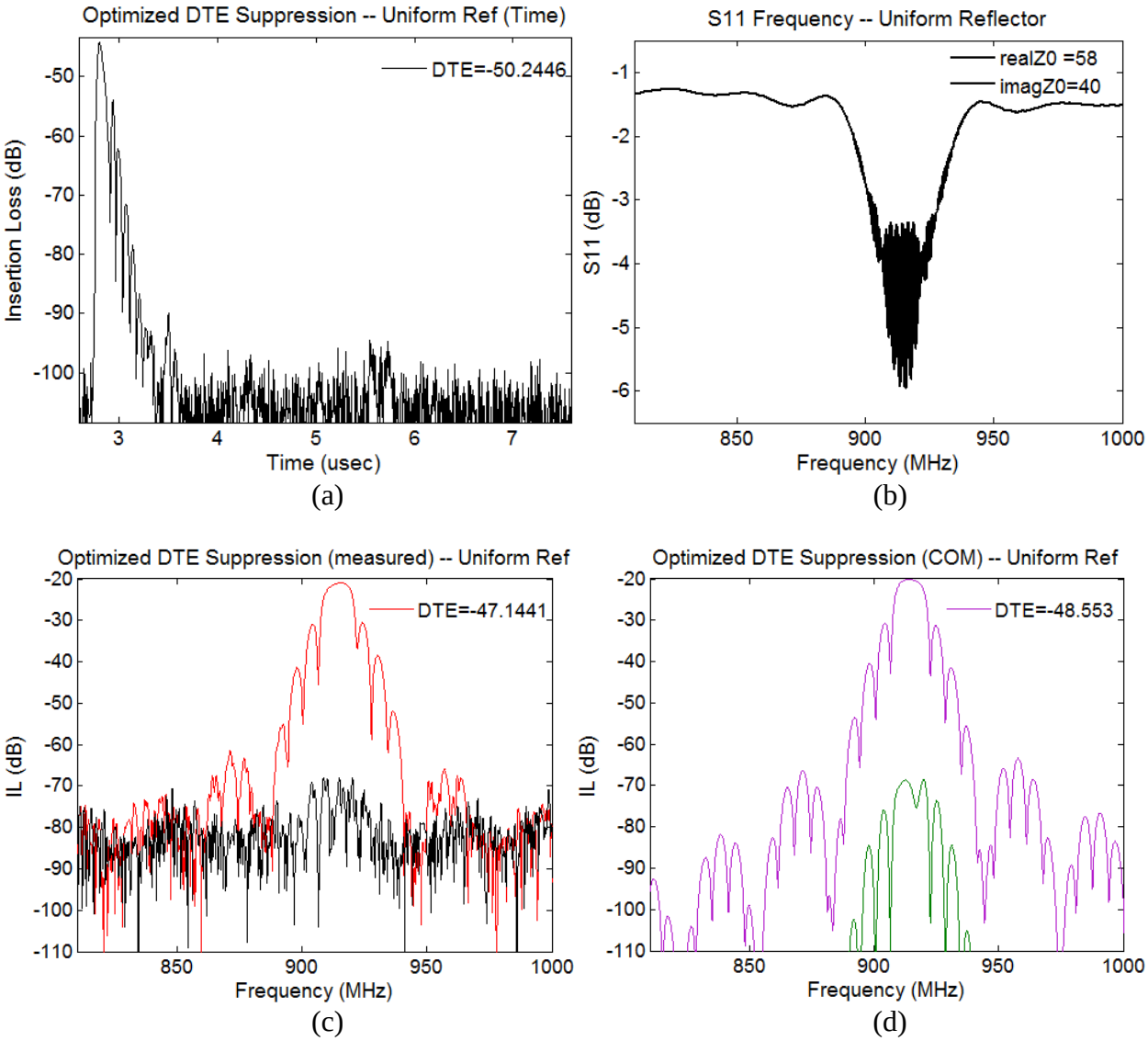

Figure 5-18. Measured uniform reflector device with post-processed optimized DTE suppression. The corresponding COM simulation is also optimized for DTE suppression (d). Plot (b) legend gives the impedance used for the measured device DTE suppression, the impedance used to suppress the echo in the COM simulation is 39+j43Ohm. (a) S11 time, (b) S11 frequency, (c) frequency response of gated 1st transit and DTE measured, (d) frequency response of gated 1st transit and DTE simulation.

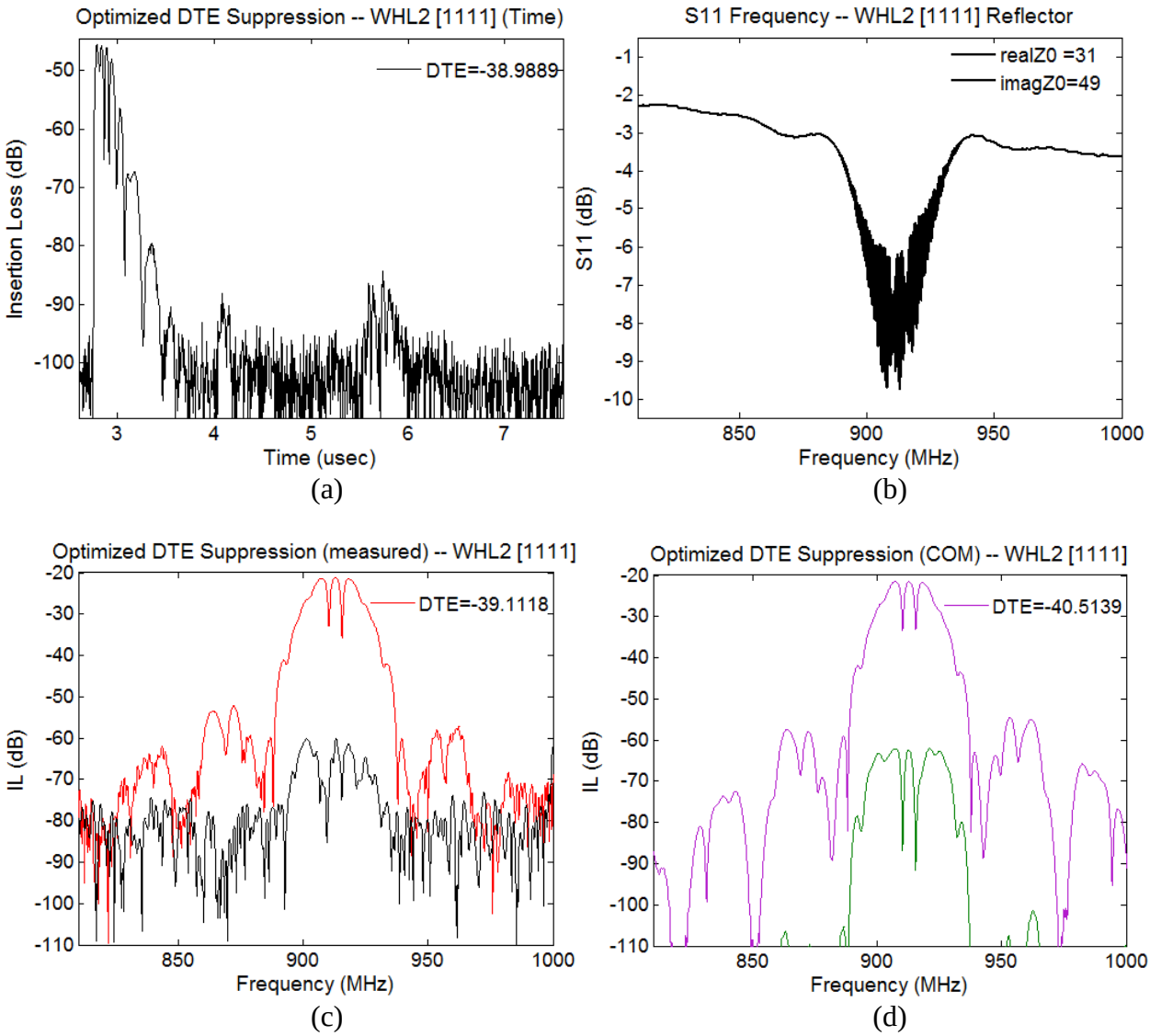

Figure 5-19. Measured WHL2[1111] device with post-processed optimized DTE suppression. The corresponding COM simulation is also optimized for DTE suppression (d). Plot (b) legend gives the impedance used for the measured device DTE suppression, the impedance used to suppress the echo in the COM simulation is 24+j50Ohm. a) S11 time, (b) S11 frequency, (c) frequency response of gated 1st transit and DTE measured, (d) frequency response of gated 1st transit and DTE simulation.

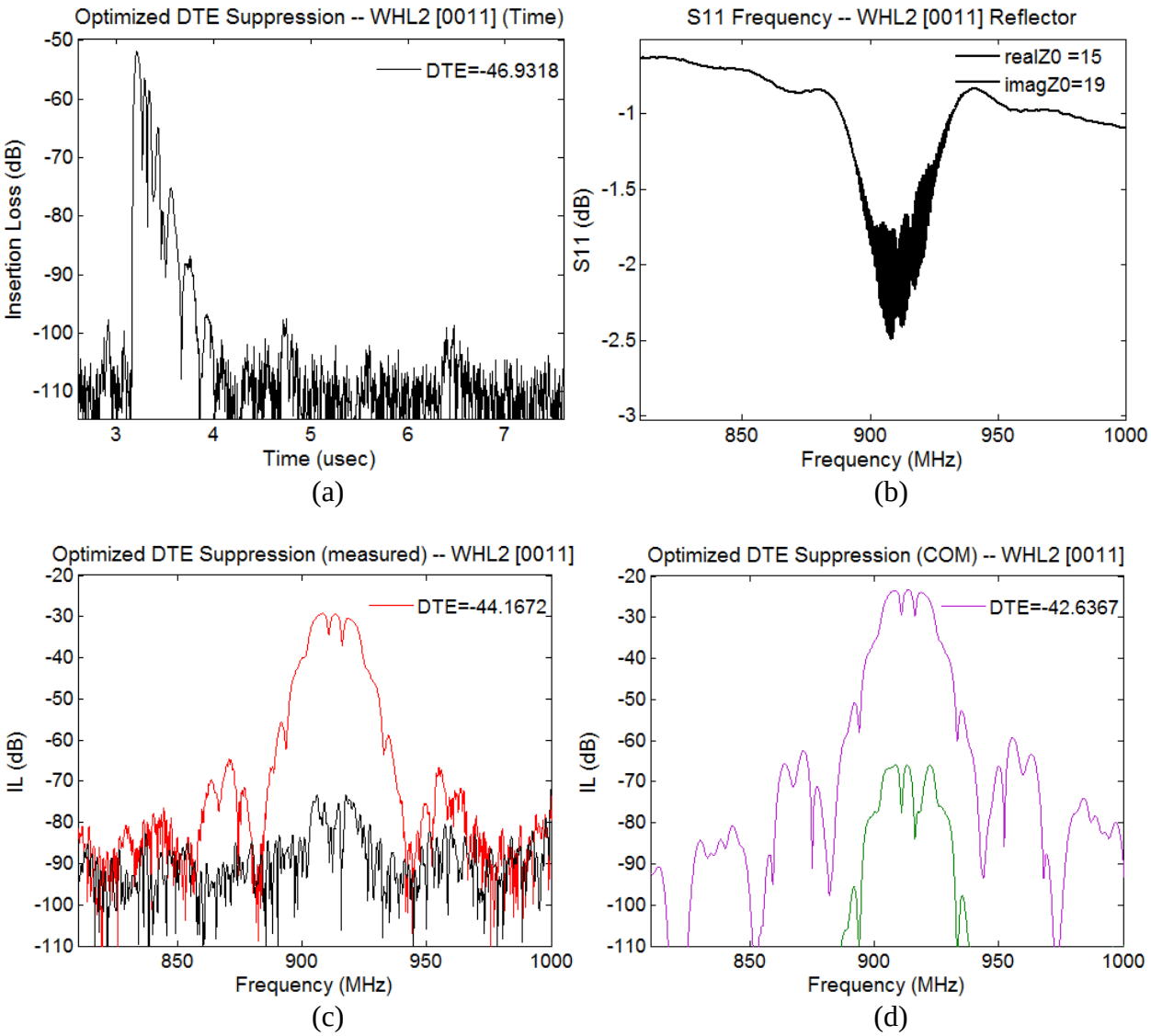

Figure 5-20. Measured WHL2[0011] device with post-processed optimized DTE suppression. The corresponding COM simulation is also optimized for DTE suppression (d). Plot (b) legend gives the impedance used for the measured device DTE suppression, the impedance used to suppress the echo in the COM simulation is 28+j39Ohm. a) S11 time, (b) S11 frequency, (c) frequency response of gated 1st transit and DTE measured, (d) frequency response of gated 1st transit and DTE simulation.

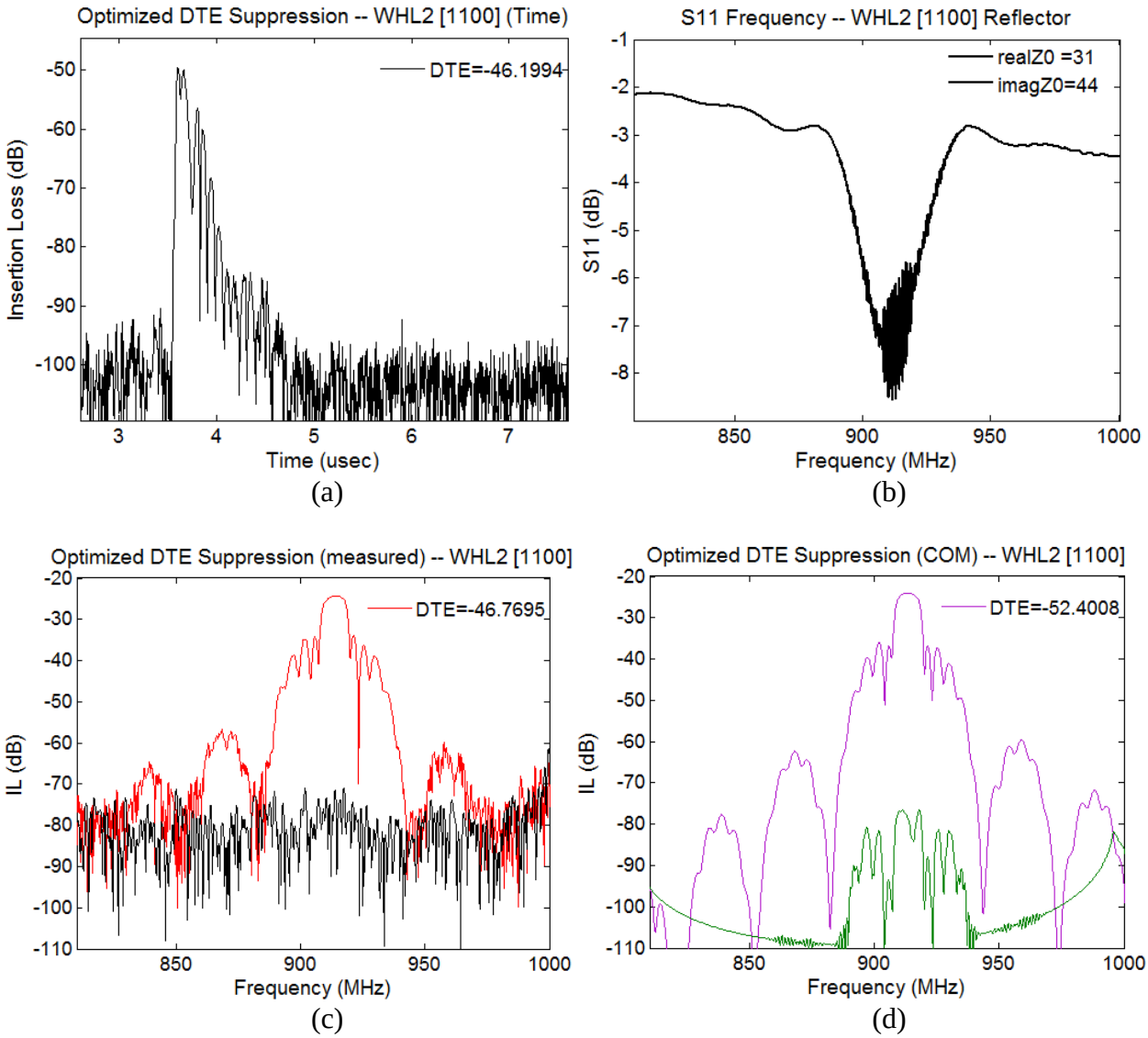

Figure 5-21. Measured WHL2[1100] device with post-processed optimized DTE suppression. The corresponding COM simulation is also optimized for DTE suppression (d). Plot (b) legend gives the impedance used for the measured device DTE suppression, the impedance used to suppress the echo in the COM simulation is 32+j38Ohm. The DTE suppression of the measured device is probably lower that the values shown since it seems to be below the noise floor. a) S11 time, (b) S11 frequency, (c) frequency response of gated 1st transit and DTE measured, (d) frequency response of gated 1st transit and DTE simulation.

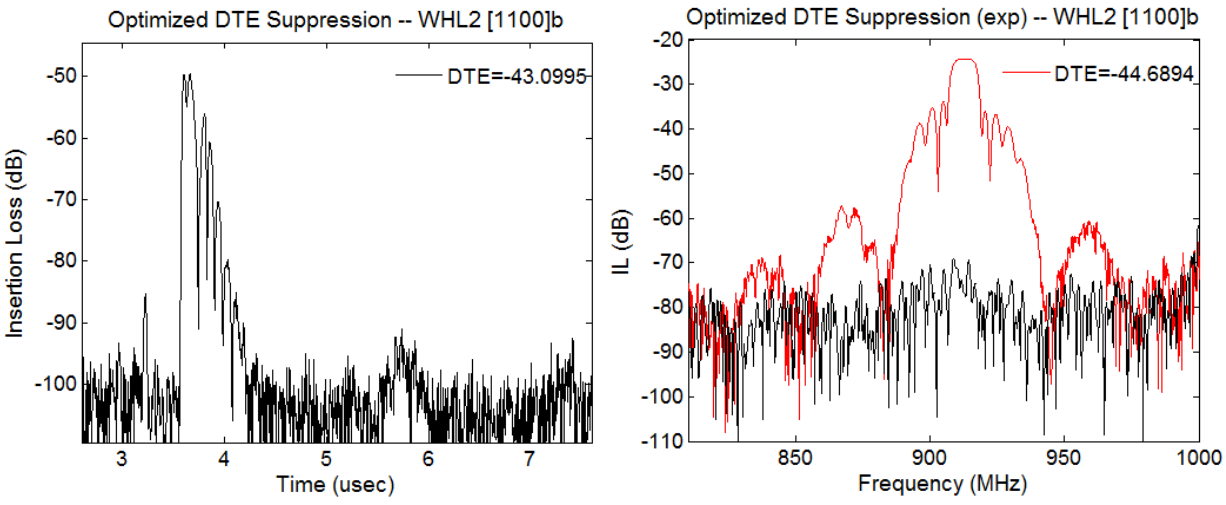

(a)

(b)

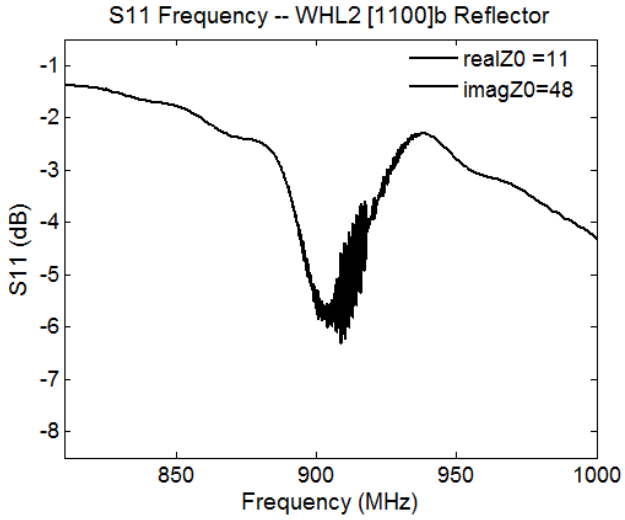

(c)

Figure 5-22. Measured WHL2[1100]b device with post-processed optimized DTE suppression. Plot (c) legend gives the impedance used for the measured device DTE suppression. This device has a flatter passband than the [1100] device above. The reflector response is also higher in frequency relative to the transducer passband than the [1100] device above—this seems to have resulted in an optimized characteristic impedance with a smaller real part and a larger imaginary part, as compared to the similar device above.

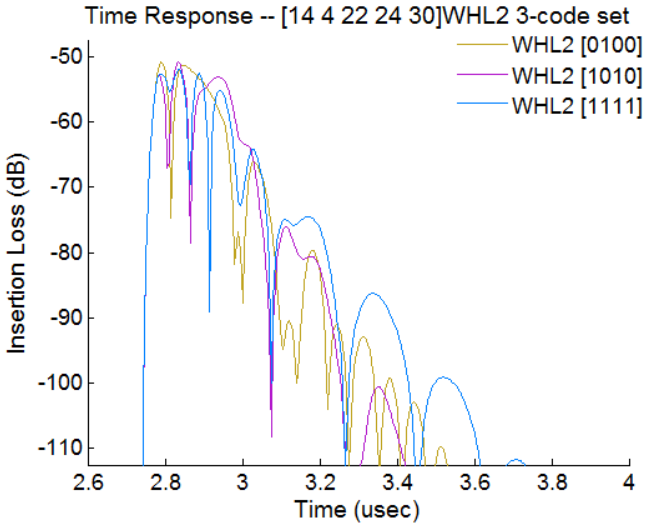
Time Response -- [14 4 22 24 30]WHL2 3-code set
WHL2 [0100]
WHL2 [1010]
WHL2 [1111]
Insertion Loss (dB)
-50
-60
-70
-80
-90
-100
-110
2.6
2.8
3
3.2
3.4
3.6
3.8
4
Time (usec)

(a)

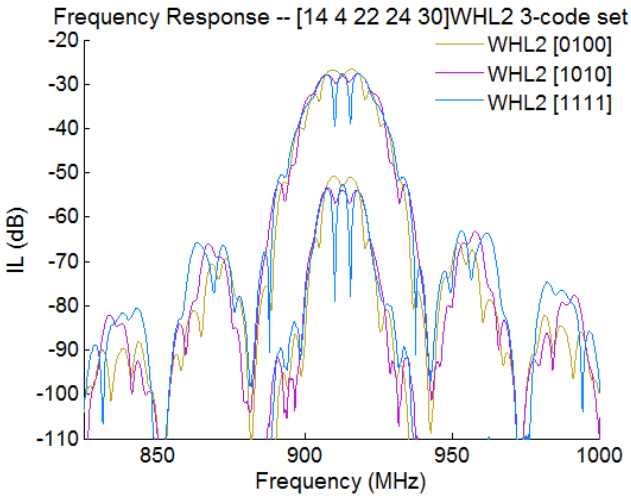
Frequency Response -- [14 4 22 24 30]WHL2 3-code set
WHL2 [0100]
WHL2 [1010]
WHL2 [1111]
IL (dB)
-20
-30
-40
-50
-60
-70
-80
-90
-100
-110
850
900
950
1000
Frequency (MHz)

(b)

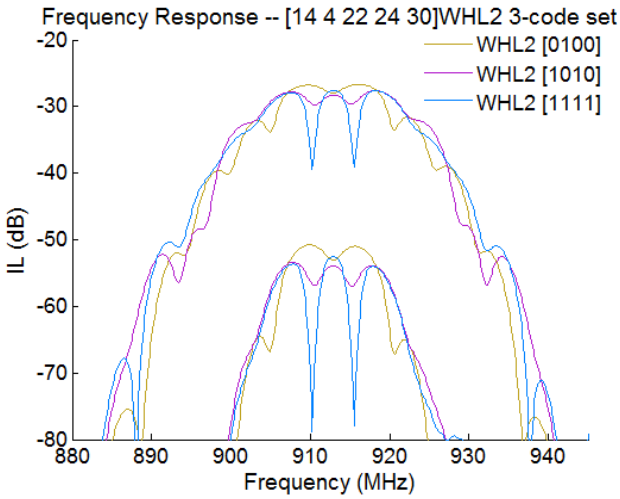
Frequency Response -- [14 4 22 24 30]WHL2 3-code set
WHL2 [0100]
WHL2 [1010]
WHL2 [1111]
IL (dB)
-20
-30
-40
-50
-60
-70
-80
880
890
900
910
920
930
940
Frequency (MHz)

(c)

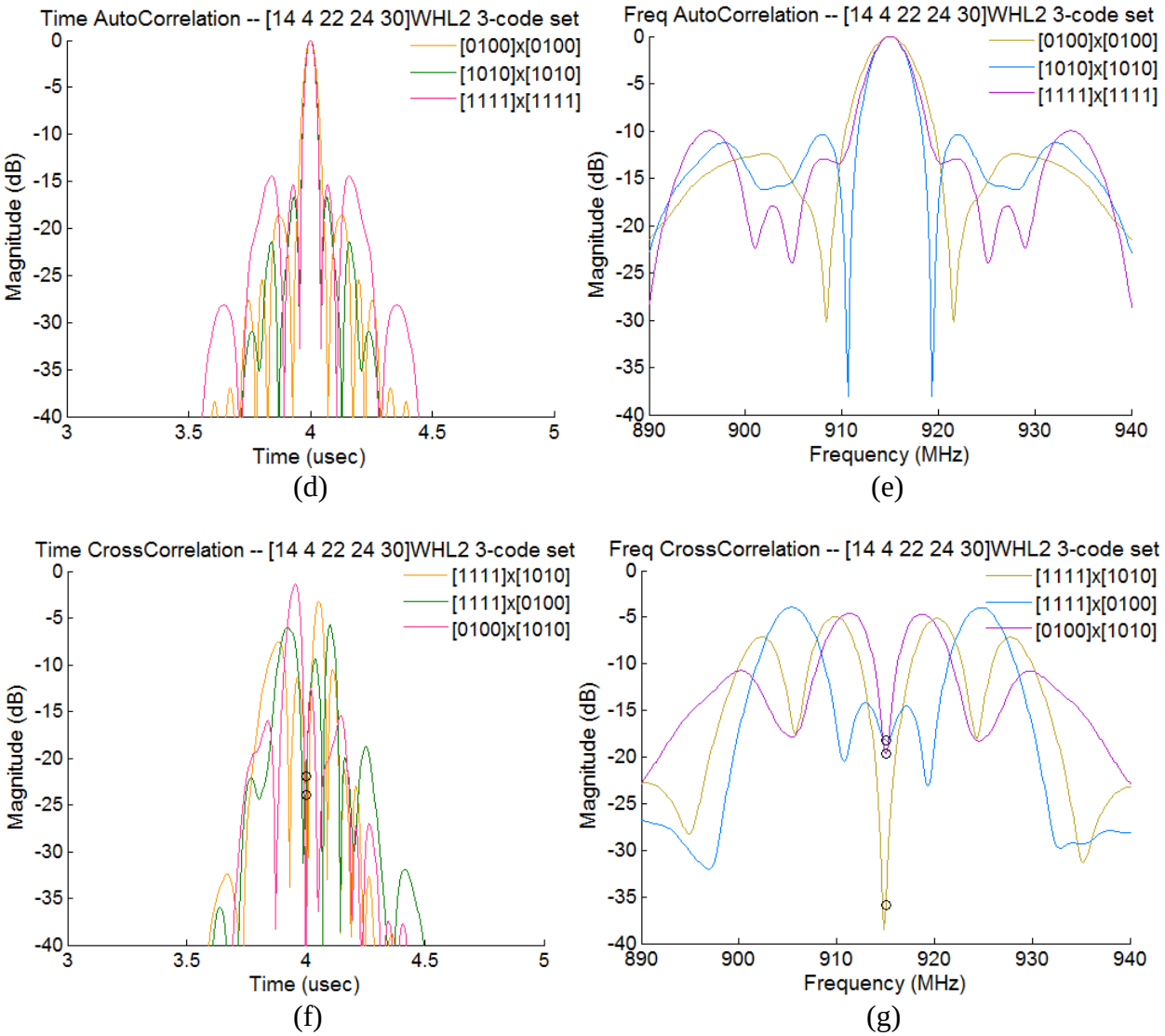

Figure 5-23. Simulation of [14 4 22 24 30]WHL2 3-code set, [0100] [1010] [1111], time and frequency domain waveforms, and auto and cross-correlations for both time and frequency domain waveforms. The circle gives the location where ideally the null of the cross-correlation should occur in order to correspond to the auto-correlation peak location.

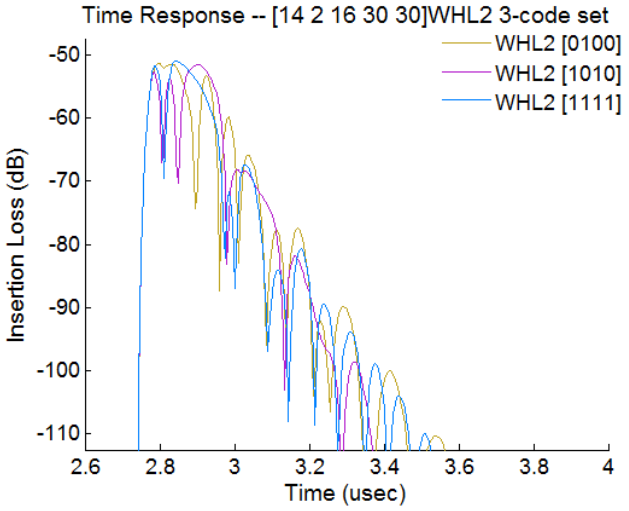
Time Response -- [14 2 16 30 30]WHL2 3-code set
WHL2 [0100]
WHL2 [1010]
WHL2 [1111]
Insertion Loss (dB)
-50
-60
-70
-80
-90
-100
-110
2.6
2.8
3
3.2
3.4
3.6
3.8
4
Time (usec)

(a)

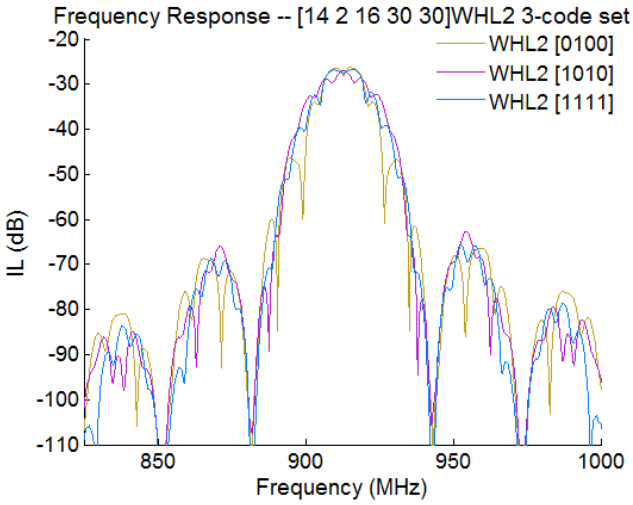
Frequency Response -- [14 2 16 30 30]WHL2 3-code set
WHL2 [0100]
WHL2 [1010]
WHL2 [1111]
IL (dB)
-20
-30
-40
-50
-60
-70
-80
-90
-100
-110
850
900
950
1000
Frequency (MHz)

(b)

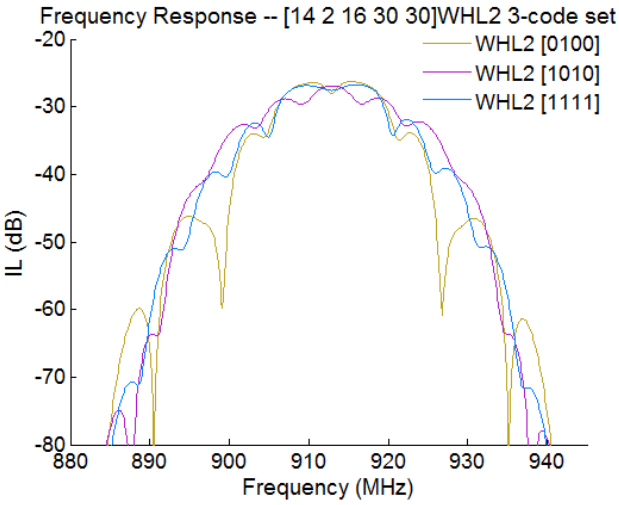
Frequency Response -- [14 2 16 30 30]WHL2 3-code set
WHL2 [0100]
WHL2 [1010]
WHL2 [1111]
IL (dB)
-20
-30
-40
-50
-60
-70
-80
880
890
900
910
920
930
940
Frequency (MHz)

(c)

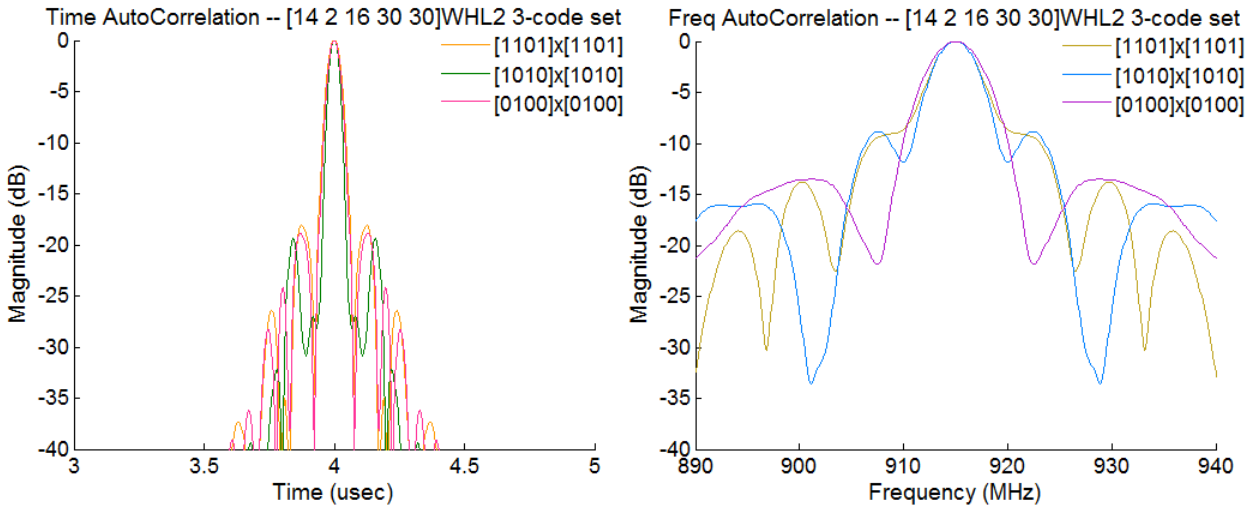

Figure 5-24. Simulation of [14 2 16 30 30]WHL2 3-code set, [1101] [1010] [0100], time and frequency domain waveforms, and auto and cross-correlations for both time and frequency domain waveforms.

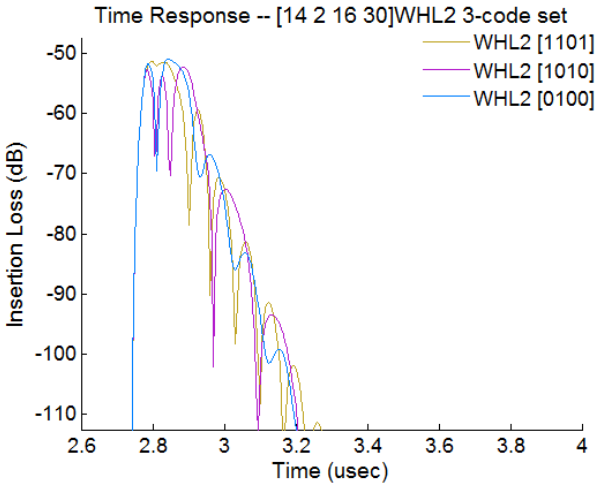
Time Response -- [14 2 16 30]WHL2 3-code set
WHL2 [1101]
WHL2 [1010]
WHL2 [0100]
Insertion Loss (dB)
-50
-60
-70
-80
-90
-100
-110
2.6
2.8
3
3.2
3.4
3.6
3.8
4
Time (usec)

(a)

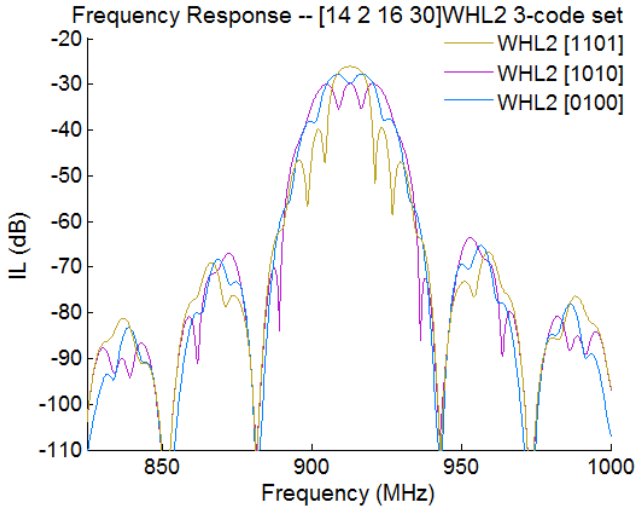
Frequency Response -- [14 2 16 30]WHL2 3-code set
WHL2 [1101]
WHL2 [1010]
WHL2 [0100]
IL (dB)
-20
-30
-40
-50
-60
-70
-80
-90
-100
-110
850
900
950
1000
Frequency (MHz)

(b)

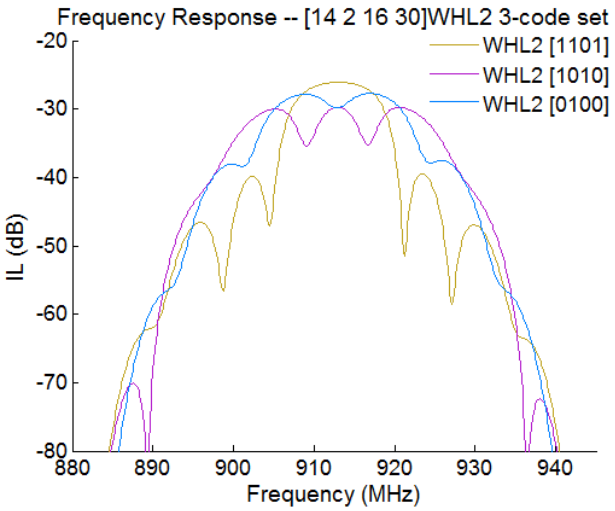
Frequency Response -- [14 2 16 30]WHL2 3-code set
WHL2 [1101]
WHL2 [1010]
WHL2 [0100]
IL (dB)
-20
-30
-40
-50
-60
-70
-80
880
890
900
910
920
930
940
Frequency (MHz)

(c)

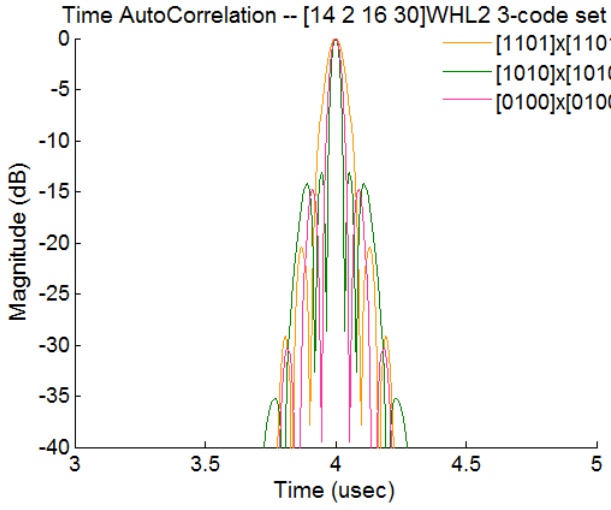
Time AutoCorrelation -- [14 2 16 30]WHL2 3-code set
[1101]x[1101]
[1010]x[1010]
[0100]x[0100]
Magnitude (dB)
0
-5
-10
-15
-20
-25
-30
-35
-40
3
3.5
4
4.5
5
Time (usec)

(d)

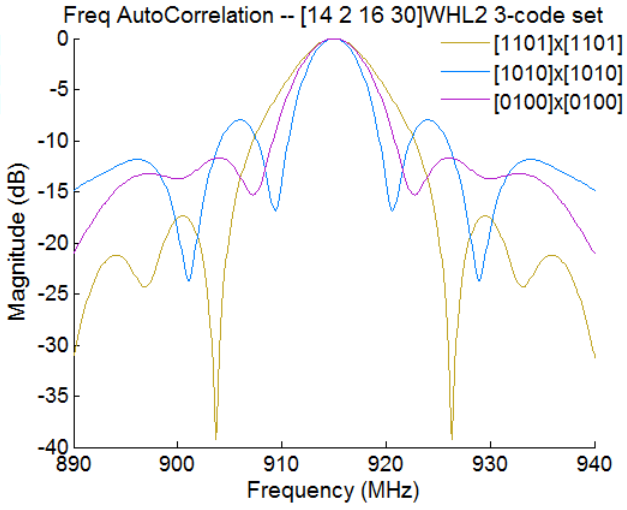
Freq AutoCorrelation -- [14 2 16 30]WHL2 3-code set
[1101]x[1101]
[1010]x[1010]
[0100]x[0100]
Magnitude (dB)
0
-5
-10
-15
-20
-25
-30
-35
-40
890
900
910
920
930
940
Frequency (MHz)

(e)

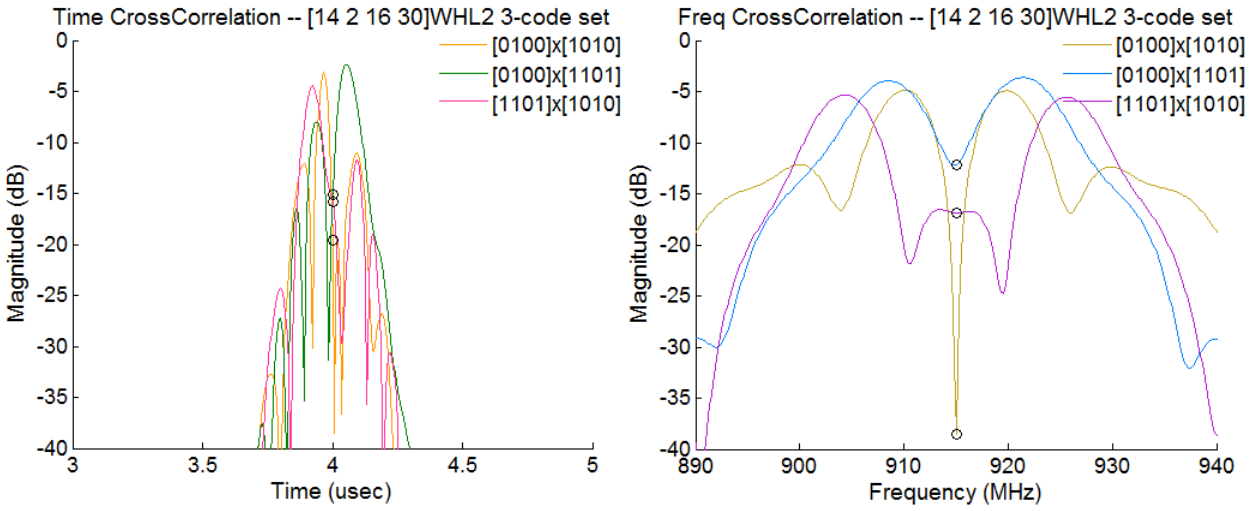

(f) (g)

Figure 5-25. Simulation of [14 2 16 30 0]WHL2 3-code set, [1101] [1010] [0100], time and frequency domain waveforms, and auto and cross-correlations for both time and frequency domain waveforms.

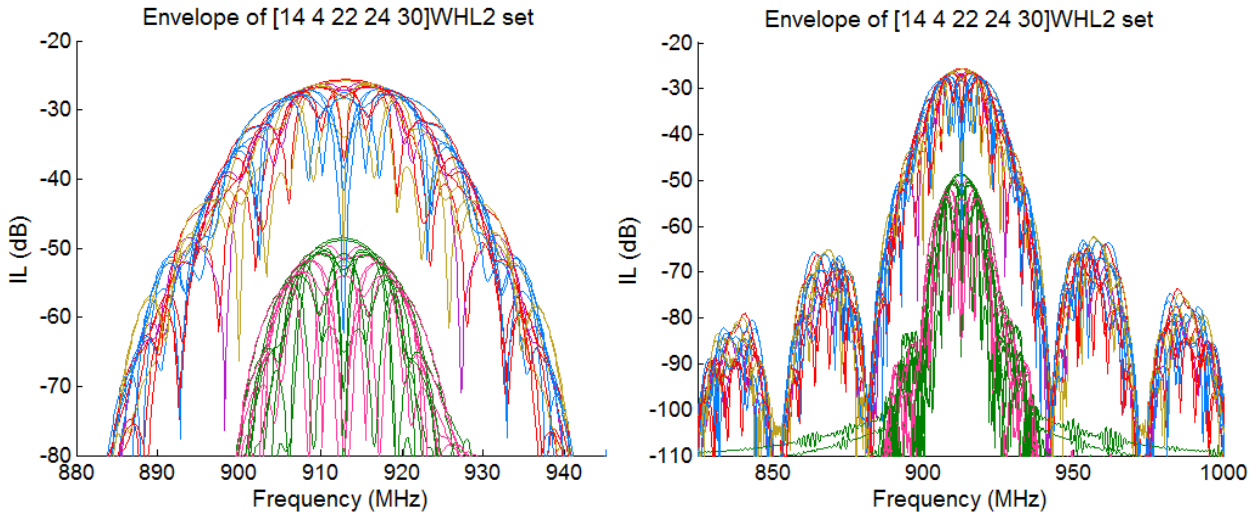

(a) (b)

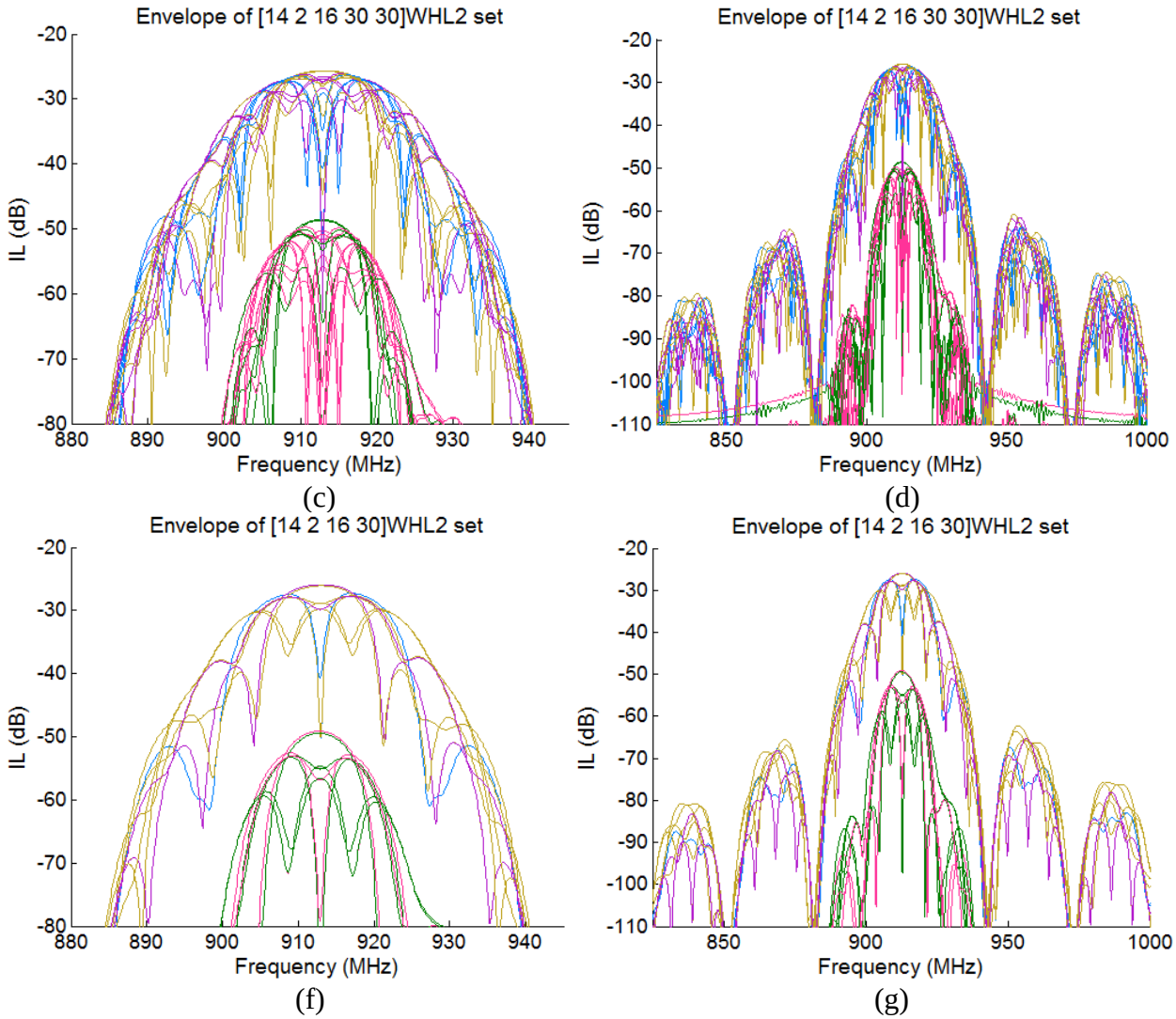

Figure 5-26. Envelope of [14 4 22 24 30]WHL2, [14 2 16 30 30]WHL2, and [14 2 16 30]WHL2 sets.

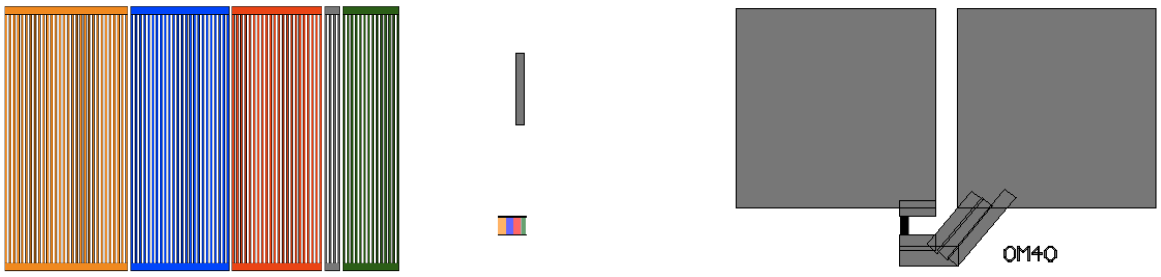

Figure 5-27. Mask layout of (a) the [14 4 22 24 30]WHL2 [1111] reflector and (b) complete reflective delay line device with large bond pads used for antenna integration using silver epoxy.

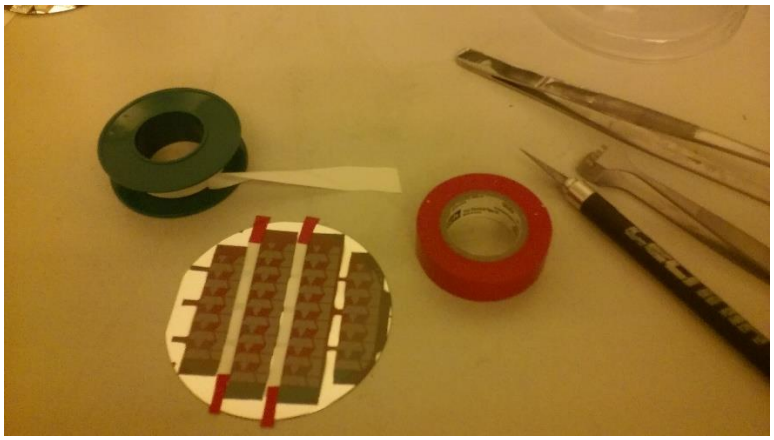

(a)

(b)

Figure 5-28. Illustration of masking method and tools used for a 2-step metal deposition since the reflectors require a different metal thickness than the transducer. (a) shows the teflon tape with electrical tape used to mask the reflectors (these are actually GUDT devices shown). (b) shows the comparison of using paper on the right wafer and teflon tape on the left wafer—the slight gap between the paper edge and the wafer produced a smearing of the deposited aluminum that didn't follow the expected straight line trajectory of the spray of aluminum atoms, almost as if some turbulence at the edges caused the aluminum be deposited unevenly. The teflon tape fixed this problem.

5.5 Optimized Walsh-Hadamad-like Reflectors

To show how WHL coding can benefit from an optimization routine, this section starts by showing a 4 code Walsh-Hadamard (WH) coded reflector response (P11), no transducer, synthesized with 1st harmonic reflectors having a reflectivity of .1%. It is then increased to 1% to show how the orthogonality is lost. Then the reflectivity of each chip is adjusted to show how the orthogonality is regained, to some degree. The propagation loss in the 1st harmonic grating is modeled as constant even when the reflectivity is changed per chip, γ_{Loss}=100. Figure 5-29 shows the time and frequency domain impulse response waveforms, and also the time and frequency auto and cross-correlations of the 4 WH codes.

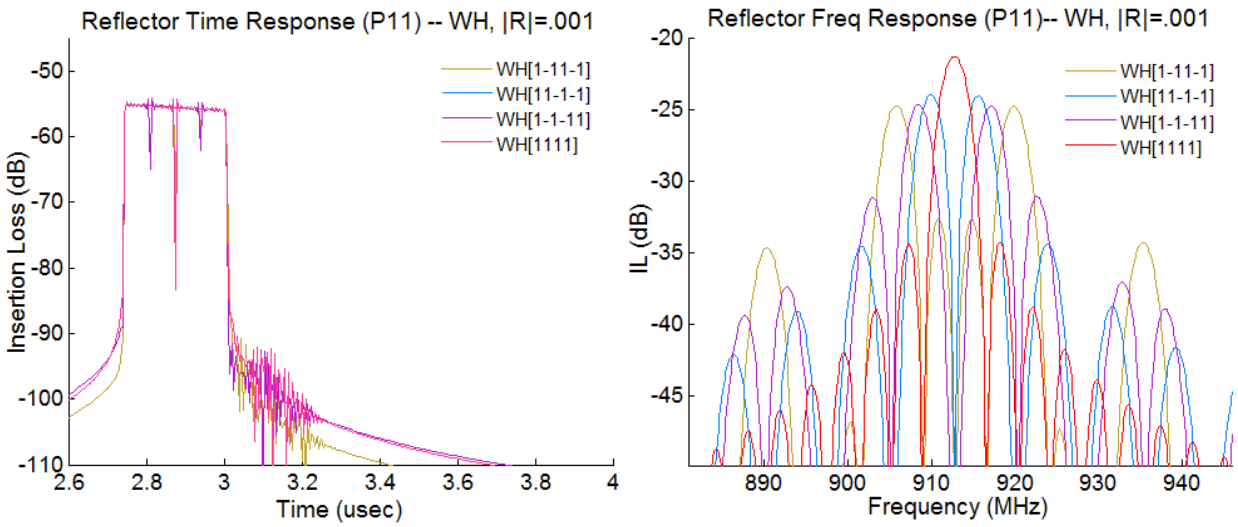

(a) (b)

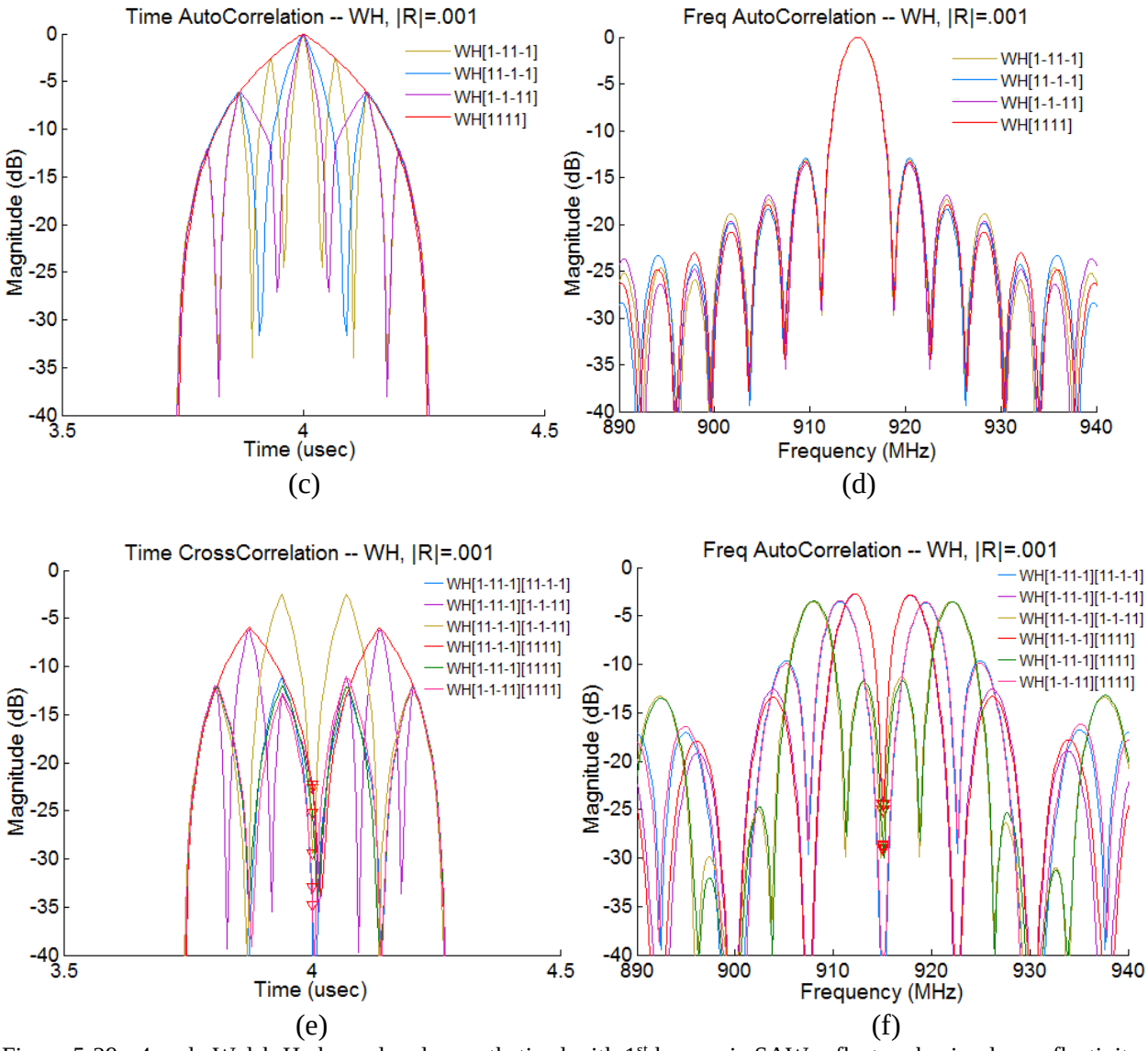

Figure 5-29. 4-code Walsh-Hadamard codes synthetized with 1st harmonic SAW reflectors having low reflectivity, .1% per strip. P11 is shown, so the transducer is not included, only the impulse response of the reflectors. (a) Time response, (b) frequency response, (c) time auto-correlation, (d) frequency auto-correlation, (e) time cross-correlation, (f) frequency cross-correlation. It shows a good level of orthogonality.

The low reflectivity reflectors show good orthogonality, in both time and frequency domain correlations (with frequency being slightly better). Now Figure 5-30 shows similar plots with the reflectivity increased to 1%.

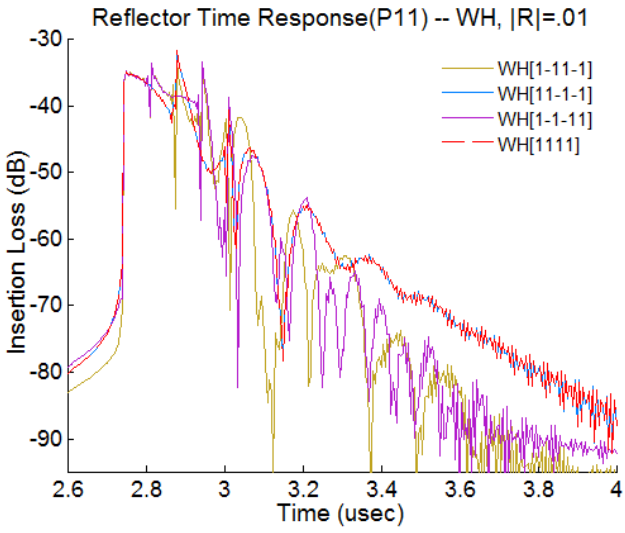
Reflector Time Response(P11) -- WH, |R|=.01
Insertion Loss (dB)
Time (usec)
WH[1-11-1]
WH[11-1-1]
WH[1-1-11]
WH[1111]

(a)

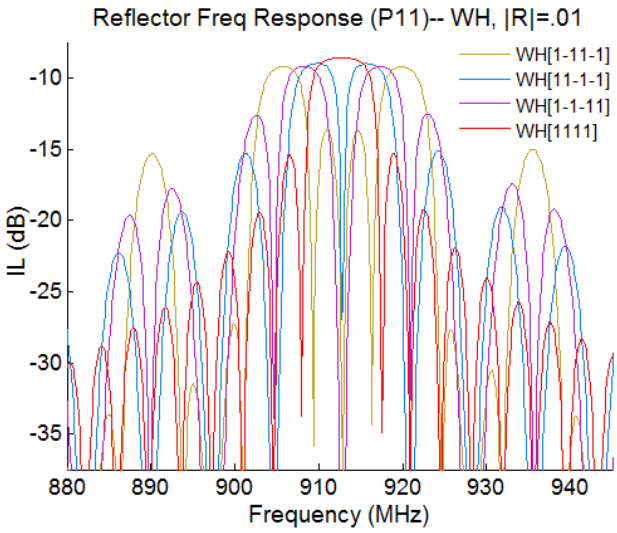
Reflector Freq Response (P11)-- WH, |R|=.01
IL (dB)
Frequency (MHz)
WH[1-11-1]
WH[11-1-1]
WH[1-1-11]
WH[1111]

(b)

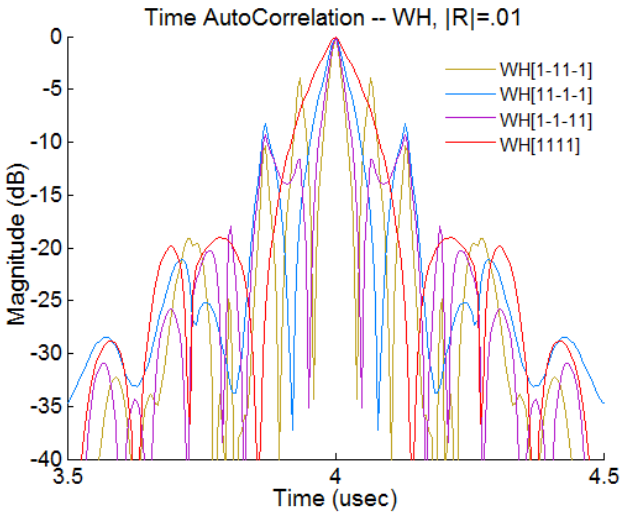
Time AutoCorrelation -- WH, |R|=.01
Magnitude (dB)
Time (usec)
WH[1-11-1]
WH[11-1-1]
WH[1-1-11]
WH[1111]

(c)

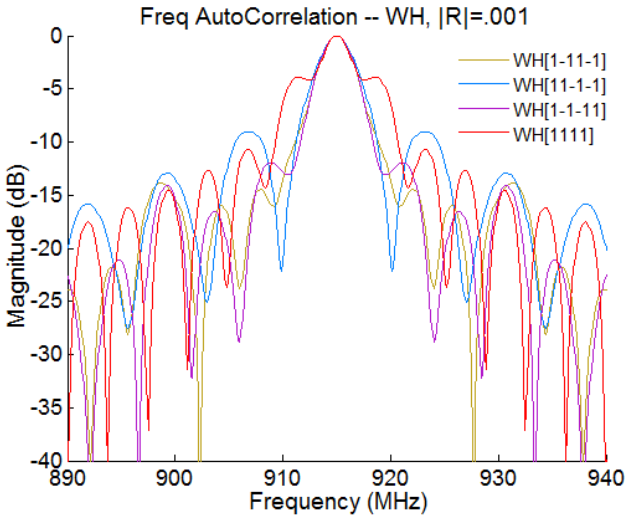
Freq AutoCorrelation -- WH, |R|=.001
Magnitude (dB)
Frequency (MHz)
WH[1-11-1]
WH[11-1-1]
WH[1-1-11]
WH[1111]

(d)

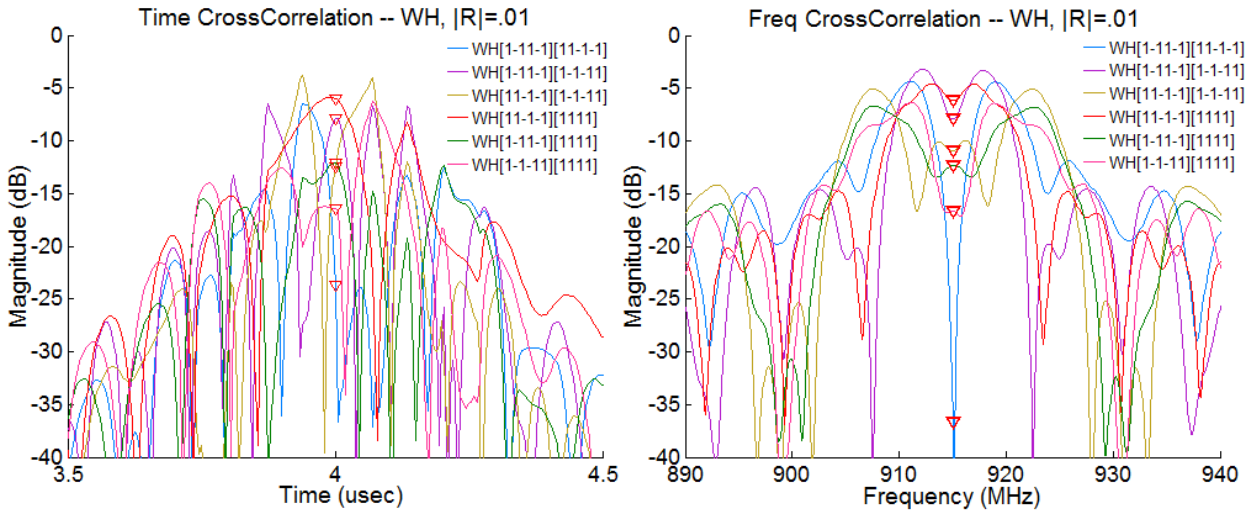

(e) (f)

Figure 5-30. 4-code Walsh-Hadamard coded reflectors synthetized with 1st harmonic SAW reflectors having moderate reflectivity, 1% per strip. P11 is shown, so the transducer is not included, only the impulse response of the reflectors. (a) Time response, (b) frequency response, (c) time auto-correlation, (d) frequency auto-correlation, (e) time cross-correlation, (f) frequency cross-correlation. The orthogonality is level has been reduced to approximately 6 dB.

As can be seen, there is lots of ringing in the time domain, and the orthogonality is basically lost with some of the cross-correlations nulls being only about 6 dB below the auto-correlation peaks. Now the reflectivity of the first 3 chips is varied using a 3-dimention Nelder-Mead optimization. The goal is to bring down the cross-correlation null as much as possible for the 6 correlations of the 4-code WHL1 set. The notation is changed to 1's and 0's to indicate that these are now WHL1 codes and not Walsh-Hadamard since amplitude modulation is now introduced. Figure 5-31 shows the resulting 4-code set of orthogonal reflectors.

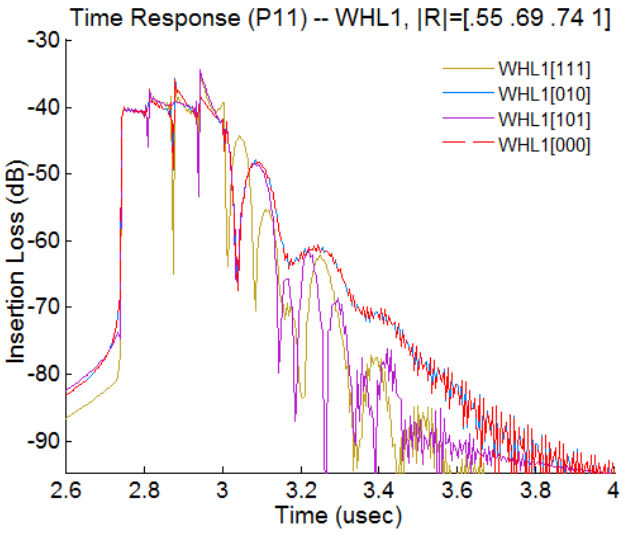
Time Response (P11) -- WHL1, |R|=[.55 .69 .74 1]
Insertion Loss (dB)
Time (usec)
WHL1[111]
WHL1[010]
WHL1[101]
WHL1[000]

(a)

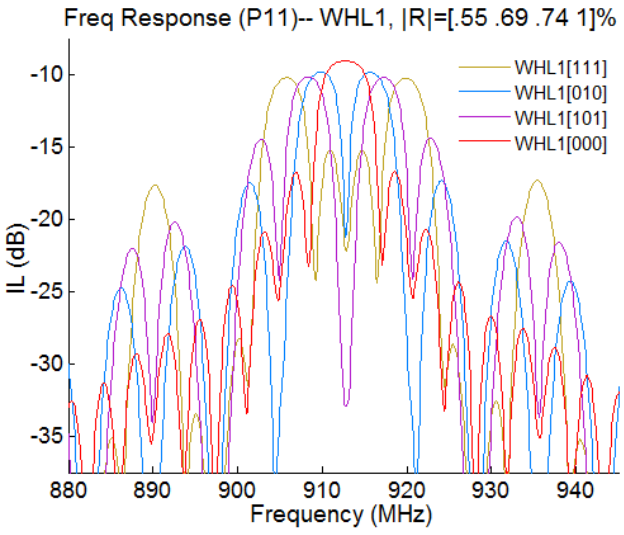
Freq Response (P11)-- WHL1, |R|=[.55 .69 .74 1]%
IL (dB)
Frequency (MHz)
WHL1[111]
WHL1[010]
WHL1[101]
WHL1[000]

(b)

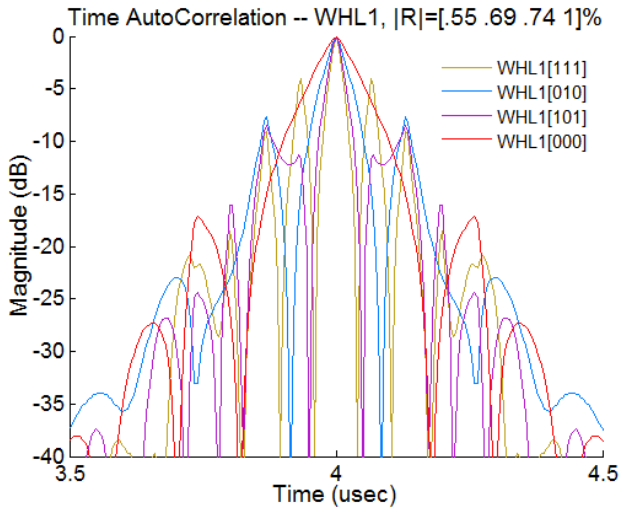
Time AutoCorrelation -- WHL1, |R|=[.55 .69 .74 1]%
Magnitude (dB)
Time (usec)
WHL1[111]
WHL1[010]
WHL1[101]
WHL1[000]

(c)

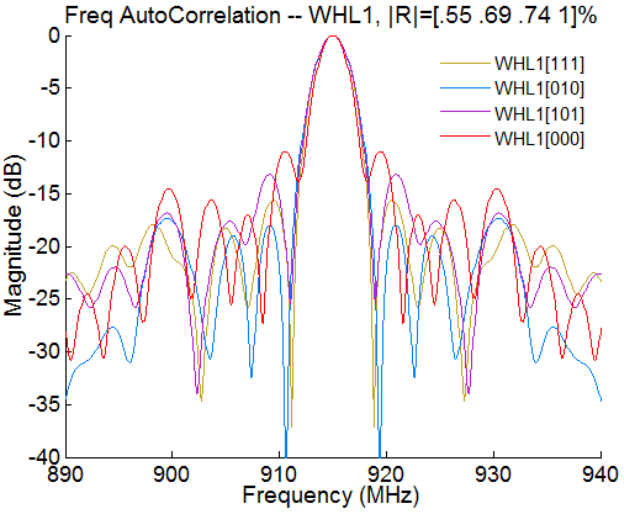
Freq AutoCorrelation -- WHL1, |R|=[.55 .69 .74 1]%
Magnitude (dB)
Frequency (MHz)
WHL1[111]
WHL1[010]
WHL1[101]
WHL1[000]

(d)

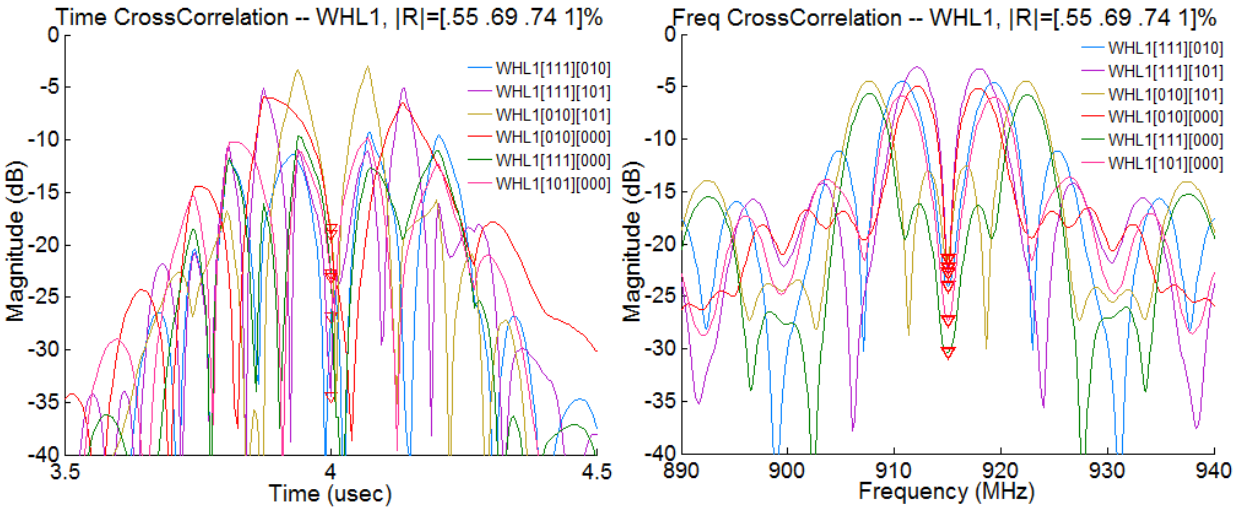

(e) (f)

Figure 5-31. 4-code Walsh-Hadamard-like codes synthetized with 1st harmonic SAW reflectors having moderate reflectivity, 1% per strip. P11 is shown, so the transducer is not included, only the impulse response of the reflectors. (a) Time response, (b) frequency response, (c) time auto-correlation, (d) frequency auto-correlation, (e) time cross-correlation, (f) frequency cross-correlation. The orthogonality level is significantly improved by optimizing the variable chip reflectivity. The frequency auto-correlation looks similar to the ideal WH auto-correlation. The chip reflectivities are [.55 .69 .74 1]%.

By optimizing the chip reflectivity values the orthogonality is regained to a level 21.5 dB below the auto-correlation.

It is now shown that codes with a high orthogonality level also exists for true AM-BPSK, where the chips are ideal truncated cosines, with negligible propagation loss and negligible stored energy effect. The COM simulation approximates the ideal truncated cosine impulse response by multiplying the reflectivity by a factor of .001. Two of these orthogonal codes are shown in Figure 5-32. The time domain waveforms re shown in linear amplitude.

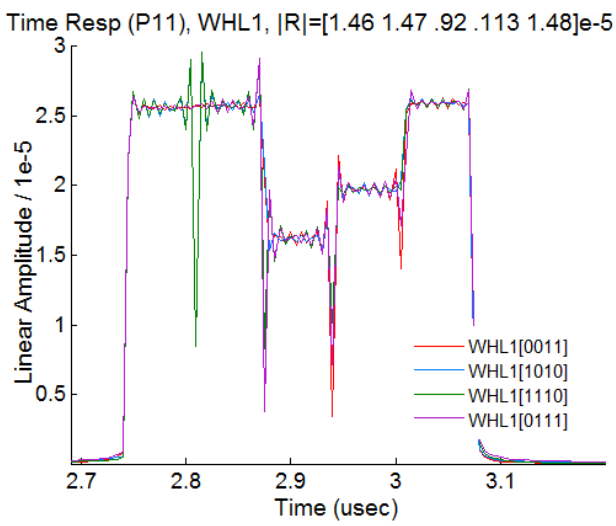
Time Resp (P11), WHL1, |R|=[1.46 1.47 .92 .113 1.48]e-5
Linear Amplitude / 1e-5
Time (usec)
WHL1[0011]
WHL1[1010]
WHL1[1110]
WHL1[0111]

(a)

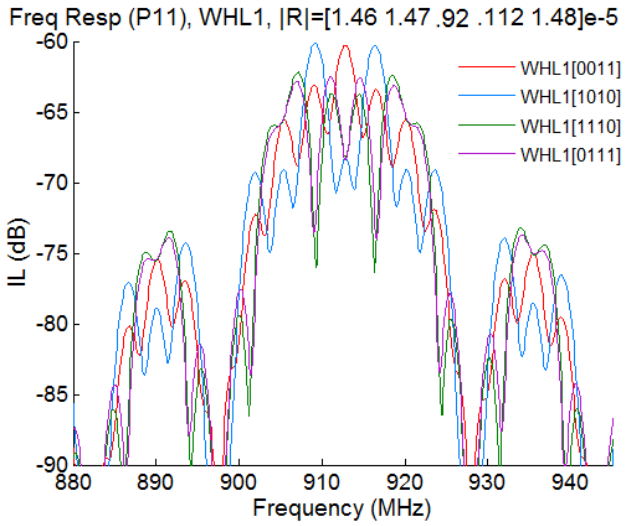
Freq Resp (P11), WHL1, |R|=[1.46 1.47 .92 .112 1.48]e-5
IL (dB)
Frequency (MHz)
WHL1[0011]
WHL1[1010]
WHL1[1110]
WHL1[0111]

(b)

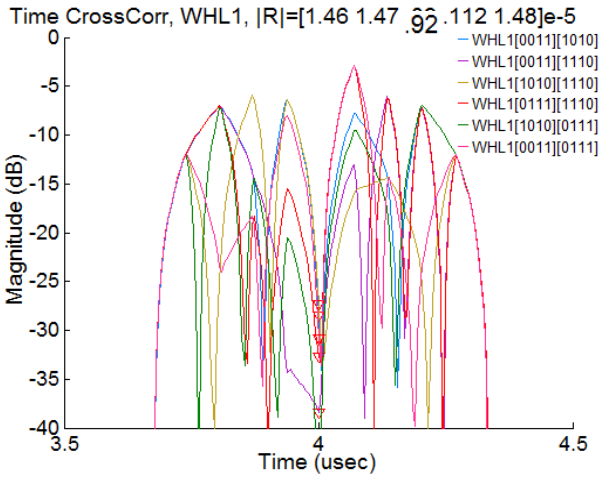
Time CrossCorr, WHL1, |R|=[1.46 1.47 .92 .112 1.48]e-5
Magnitude (dB)
Time (usec)
WHL1[0011][1010]
WHL1[0011][1110]
WHL1[1010][1110]
WHL1[0111][1110]
WHL1[1010][0111]
WHL1[0011][0111]

(c)

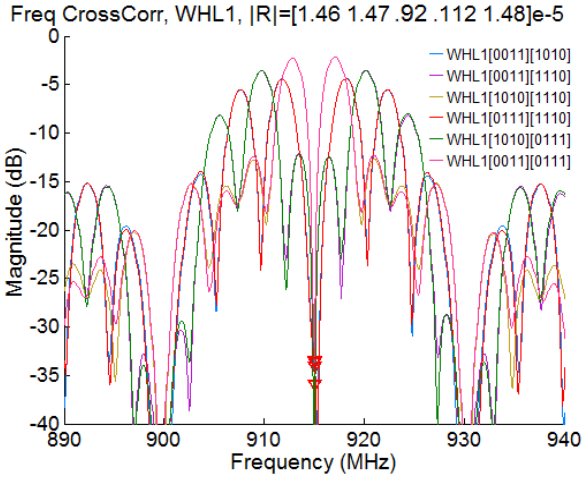
Freq CrossCorr, WHL1, |R|=[1.46 1.47 .92 .112 1.48]e-5
Magnitude (dB)
Frequency (MHz)
WHL1[0011][1010]
WHL1[0011][1110]
WHL1[1010][1110]
WHL1[0111][1110]
WHL1[1010][0111]
WHL1[0011][0111]

(d)

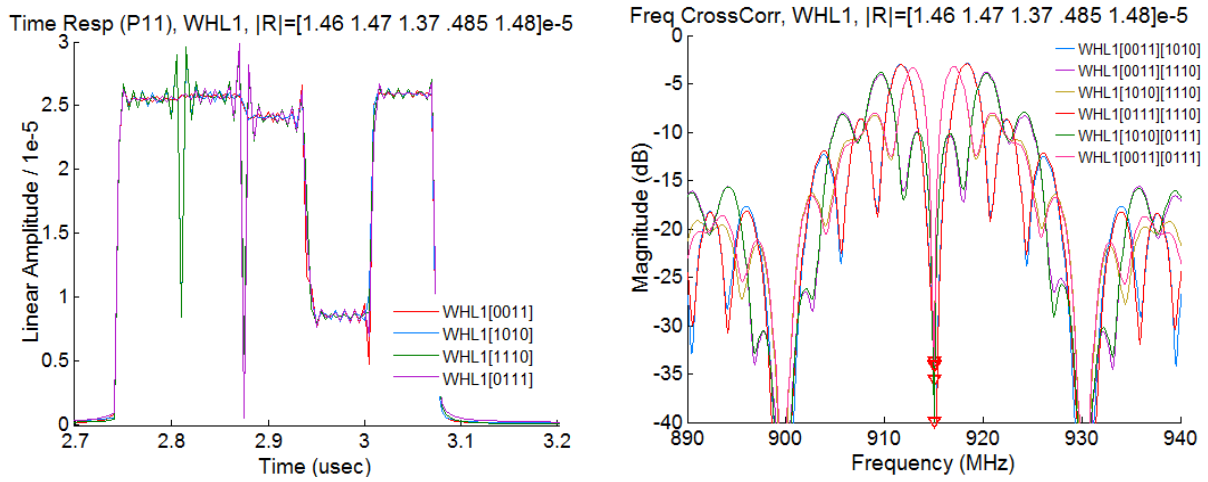

Figure 5-32. Two WHL1 4-set codes synthetized with near ideal truncated cosines. (a) and (b) are the time and frequency domain waveforms for code set 1. (c) and (d) are the time and frequency cross-correlations for code set 1. (e) is the time waveform for code set 2 and (f) is the frequency cross-correlation for code set 2. The chip reflectivity values are [1.46 1.47 .92 .112 1.48]e-5 for code set 1 and [1.46 1.47 1.37 .485 1.48]e-5 for code set 2.

The two 4-code 5-chip WHL1 codes composed of ideal rect functions show that ideal AM-BPSK codes exist—if not perfectly orthogonal, at the moment at least a 33 dB frequency orthogonality level is shown. An optimization algorithm has been utilized in order to find the values. When performing such optimizations it is recommended that seed values be randomized for a better chance of finding clodes. To find these codes the Nelder-Mead optimization was run overnight on a laptop computer running Matlab. 100 iterations were used for each set of starting seed values for reflectivity. About 15 of these runs were performed over approximately an 8 hour period and each run generated different values for reflectivity (amplitude)—about 1/3 having an orthogonality level in the 20 dB range and the other 2/3 in the low 30 dB range.

Now a 5-chip WHL1 device is optimized in a similar fashion. The reflectivity is increased to a maximum of 1.5% for the last electrode and the same 10cell SPUDT transducer used throughout this chapter is used. Figure 5-33 shows the time and frequency domain waveforms and the time and frequency cross-corelations.

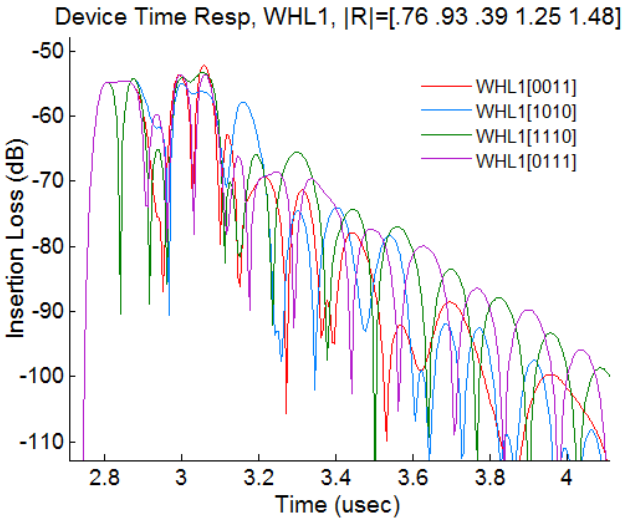
Device Time Resp, WHL1, |R|=[.76 .93 .39 1.25 1.48]
Insertion Loss (dB)
Time (usec)
WHL1[0011]
WHL1[1010]
WHL1[1110]
WHL1[0111]

(a)

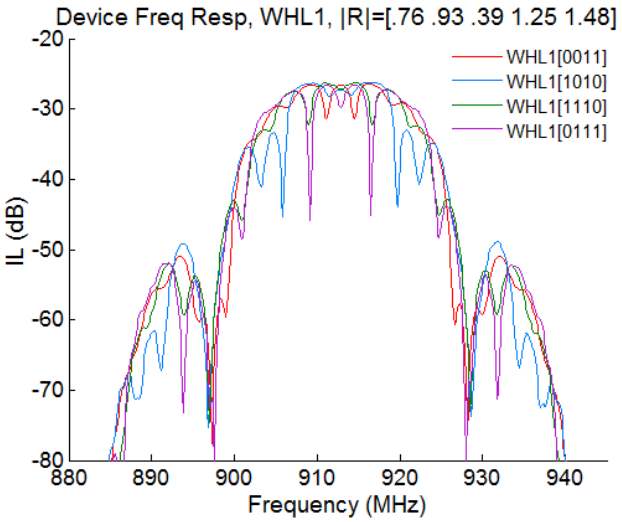
Device Freq Resp, WHL1, |R|=[.76 .93 .39 1.25 1.48]
IL (dB)
Frequency (MHz)
WHL1[0011]
WHL1[1010]
WHL1[1110]
WHL1[0111]

(b)

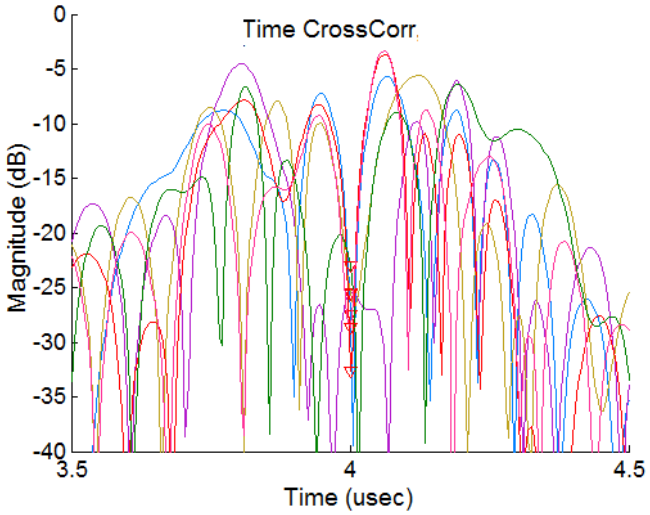
Time CrossCorr
Magnitude (dB)
Time (usec)

(c)

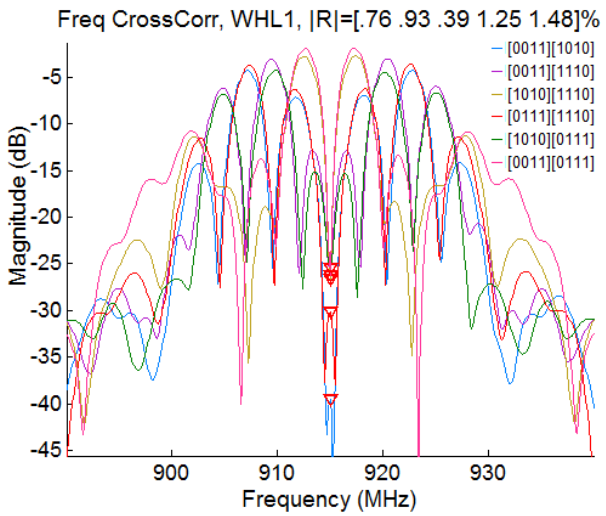
Freq CrossCorr, WHL1, |R|=[.76 .93 .39 1.25 1.48]%
Magnitude (dB)
Frequency (MHz)
[0011][1010]
[0011][1110]
[1010][1110]
[0111][1110]
[1010][0111]
[0011][0111]

(d)

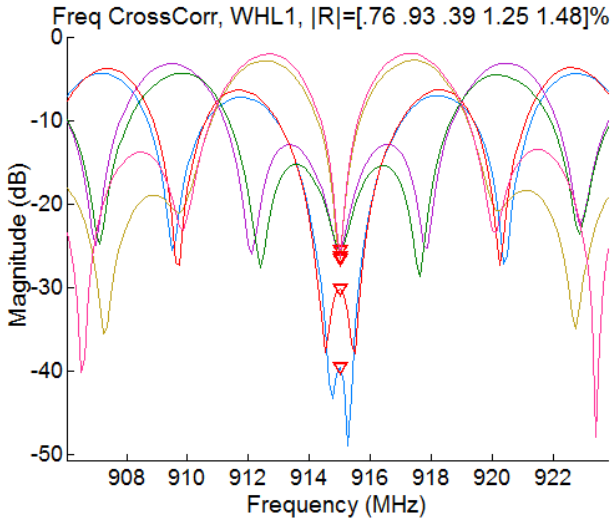

(e)

Figure 5-33. WHL1 4-code set implemented with a reflective delay-line device having maximum reflectivity of 1.48% per strip and 1st harmonic reflectors. (a) is the time response, (b) the frequency response, (c) the time cross-correlation, (d) the frequency cross-correlation, and (e) a close up of the frequency cross correlation. The reflectivity values are [.76 .93 .39 1.25 1.48]%.

Orthogonality levels of 23 dB and 25.5 dB are achieved for the time and frequency domain cross-correlations, respectively. This 4-code 5-chip set shows the energy more evenly distributed over the bandwidth than in the 4-code 4-chip Walsh Haddamard and WHL1 sets shown in Figure 5-29 and Figure 5-31, respectively.

Similarly to the approximately true AM-BPSK 4-code sets synthetized above, now a 4-code pulse width modulated (PWM)-BPSK code is shown. The propagation loss is set to zero in the grating and the reflectivity is multiplied by factor of .001 in order to approximate ideal truncated cosine waveforms. P11 is again used to generate waveform. The chip lengths are adjusted to increase the orthogonality level. First an integer number of electrodes is modeled, then a non-integer number of electrodes. The COM model equations are of a continuous variable, so a non-integer number of electrodes just means that the length of the chip is not restricted to a multiple of the grating period. The chip lengths in number of wavelengths are [29 29 7 23 30] for the

integer lengths and [29.379 29.482 6.885 22.765 30] for the non-integer lengths. The frequency domain waveforms and selected correlations are show in Figure 5-34 and Figure 5-35.

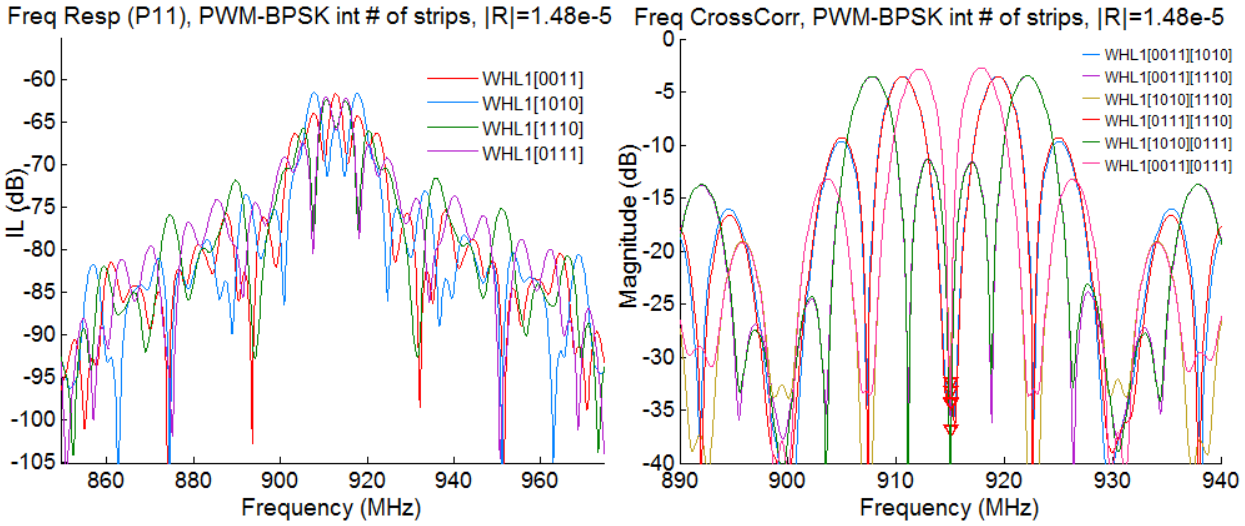

(a) (b)

Figure 5-34. WHL2 4-code set with integer number of electrodes, synthetized with near ideal truncated cosines. (a) Frequency domain waveforms and (b) frequency cross-correlations. The chip lengths in number of wavelengths are [29 29 7 23 30].

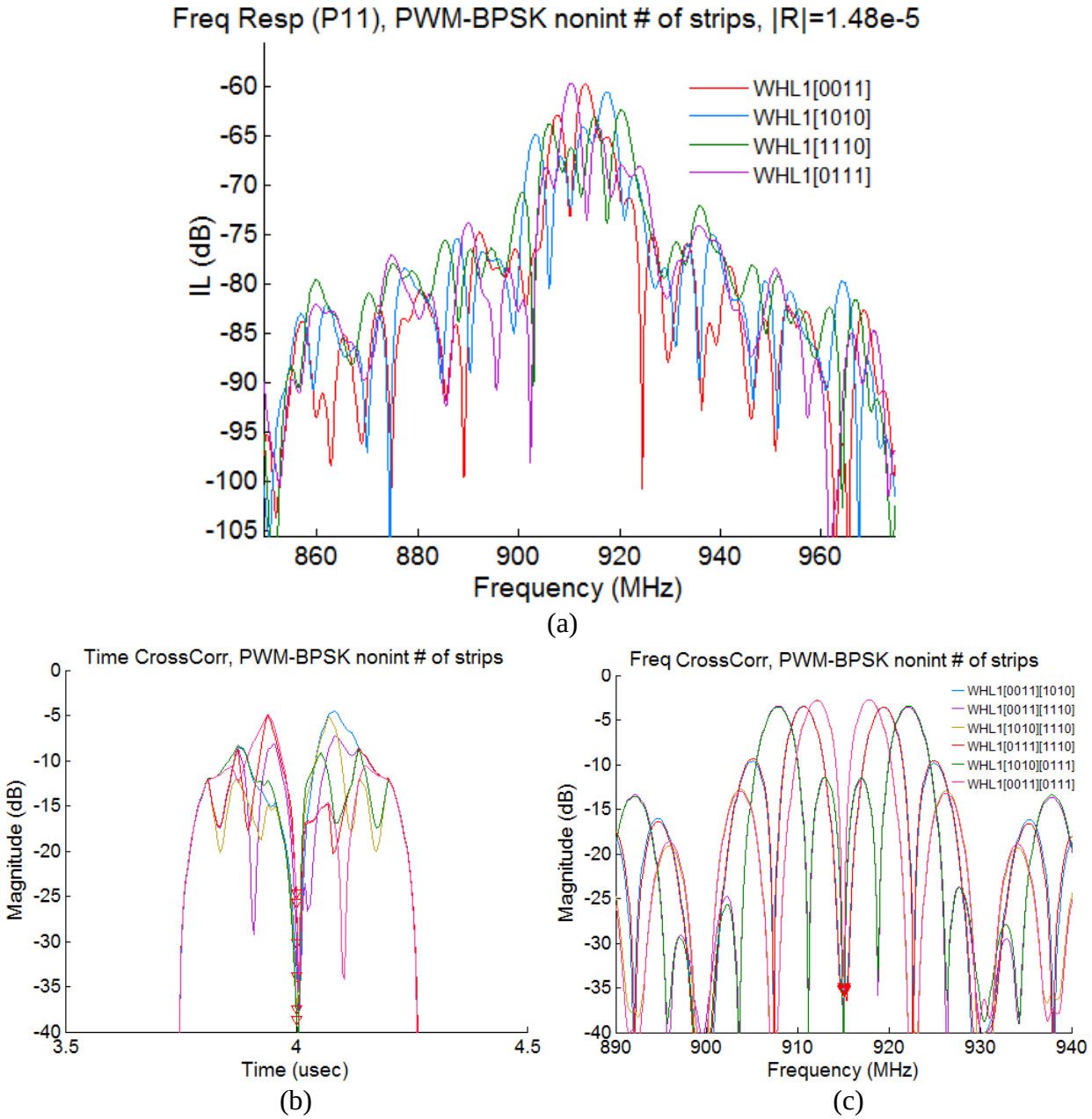

Figure 5-35. WHL2 4-code set with non-integer number of electrodes, synthetized with near ideal truncated cosines. (a) Frequency domain waveforms, (b) time cross-correlation and (c) frequency cross-correlation. The chip lengths in number of wavelengths are [29.379 29.482 6.885 22.765 30].

The PWM-BPSK (WHL2) codes show a frequency domain orthogonality level of 35 dB. Finally a device is simulated with the 10 cell 3rd harmonic SPUDT transducer and 1st harmonic reflectors. The chip lengths are [13 11 20 22 27] wavelengths and the chip reflectivities are [1.0601 .8488

.8814 1.1162 1]*1.48%. The time and frequency response, and frequency auto and cross-correlations are shown in Figure 5-36.

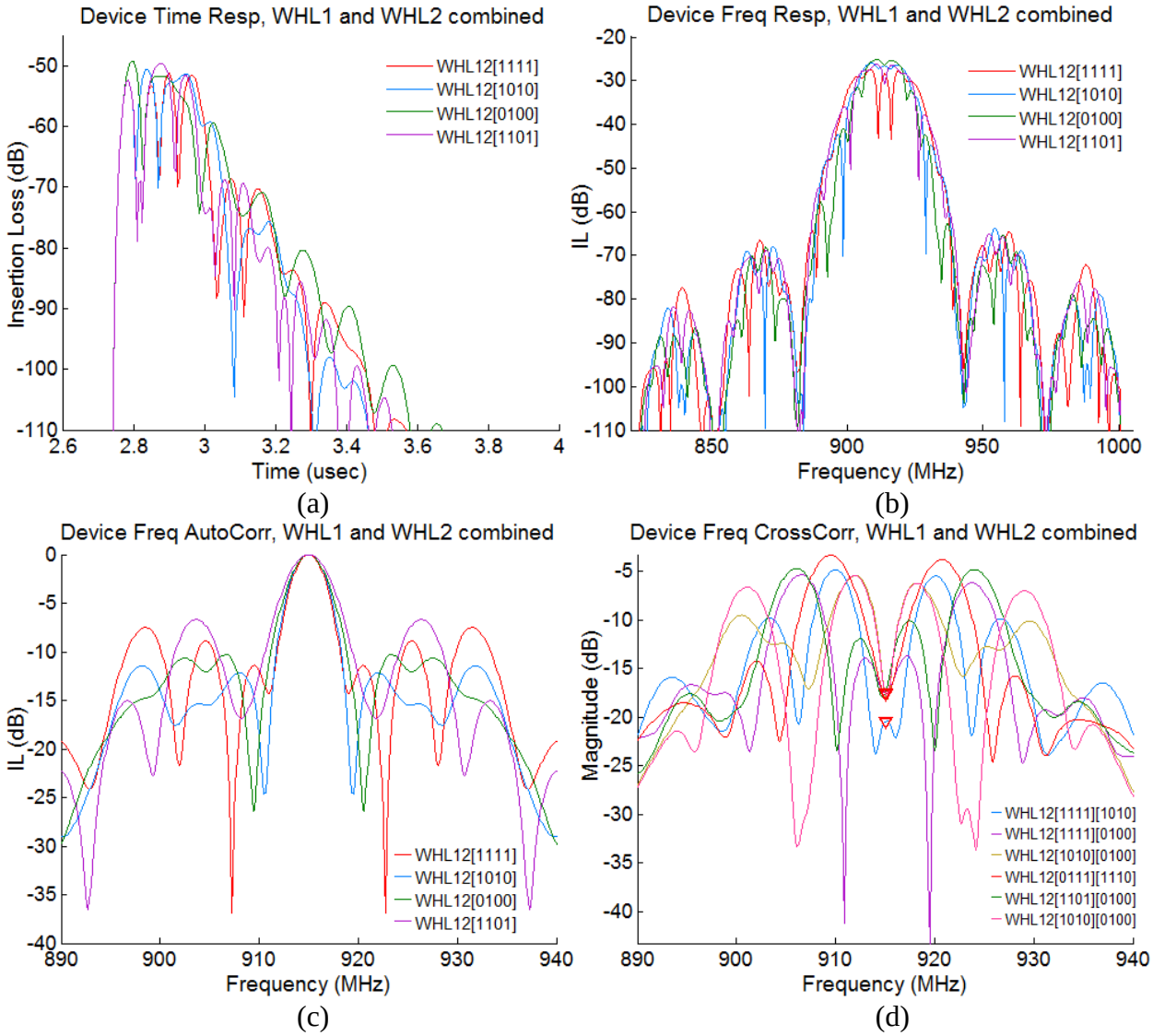

Figure 5-36. Combination of AM and PWM, BPSK coded SAW reflectors operating at 1st harmonic (COM simulation). The chip lengths in number of wavelengths are [13 11 20 22 27]. The reflectivity of the chips are [1.0601 .8488 .8814 1.1162 1]*1.48%. (a) Time domain waveforms, (b) frequency domain waveforms, (c) frequency auto-correlations and (d) frequency cross-correlations.

The simulated hybrid device 4-code set, having both WHL1 and WHL2 type compensation (amplitude and chip width), gives a simulated frequency orthogonality level of approximately 18dB. The time domain ringing is reduced in comparison with the simulated WHL1 4-code set

shown in Figure 5-33. The optimization routine used has helped design these devices. How propagation loss changes as a function of reflectivity has not been considered here.

5.6 Chapter 5 Summary

This chapter presented reflective delay line devices that can be used for antenna integration. The transducer design was restricted to a 10cell 3rd harmonic optimized SPUDT with bandwidth similar to that of ISM band. It was shown that it is difficult to make 4-chip OFC reflectors having that bandwidth and using relatively high reflectivity. For this reason, a new type of reflector is made, called Walsh-Hadamard-like (WHL) reflectors since single frequency chips having +/- phase offsets between chips are used. However, the number of chips don't need to powers of 2. These SAW reflectors are designed directly with high reflectivity and were able to give reflection bands that are highly symmetric and narrow-band enough to work in the ISM band. Many highly orthogonal sets of 3 were found, and even some sets of 4 codes with a high orthogonality level. The designs presented is all but the previous section were synthetized by hand only for shape of bandwidth, the orthogonal properties were found later—therefore further optimization of the designs is necessary in order to achieve better orthogonal characteristics. Some example optimizations were carried out. The optimization helped show also that true AM and PWM BPSK waveforms can be found with very high orthogonality level. As reflectivity is increased the orthogonality level tends to decrease, all else equal. The best simulated 4-code WHL1 device set had a frequency orthogonality level of 25dB, the best simulated 4-code combined-WHL1&2 device set had a frequency orthogonality level of approximately 18dB. These new type of coded SAW reflectors are the main contribution by the author. An orthogonality measure was defined

by looking at the difference between the auto-correlation peak and the cross-correlation null, in dB. It was also proposed to perform the correlation with the frequency domain waveform, showing that at times, and most times, it gives a greater orthogonality measure, and keeps the cross-correlation shape very symmetric. Another main contribution by the author was to show that the 3rd harmonic COM modeled 1-port devices predicted approximately the same level of optimized echo suppression as the post-processed measured devices. There were two types of WHL reflectors presented, WHL1 having same length chips and variable reflectivity (AM-BPSK), and WHL2 having varied length chips and equal reflectivity (PWM-BPSK). The WHL2 reflectors were successfully fabricated, showing very low side lobes and very interesting return bands.

CHAPTER 6:
DTE SUPPRESSION EXPERIMENTAL METHODS AND RESULTS

6.1 Differential Antenna Measurement and Tunable Antenna Design

In order to integrate the reflective delay line 3rd harmonic optimized SPUDT device with an antenna, it helps to be able to measure the impedance of both the device and antenna at the point of union. Even if a ground-signal (GS) probe measurement of the device were trustworthy, the relatively large silver epoxy contact area and size, as in fig 7-1, will change the electrical characteristics and necessary antenna impedance. A modified dipole antenna will be used.

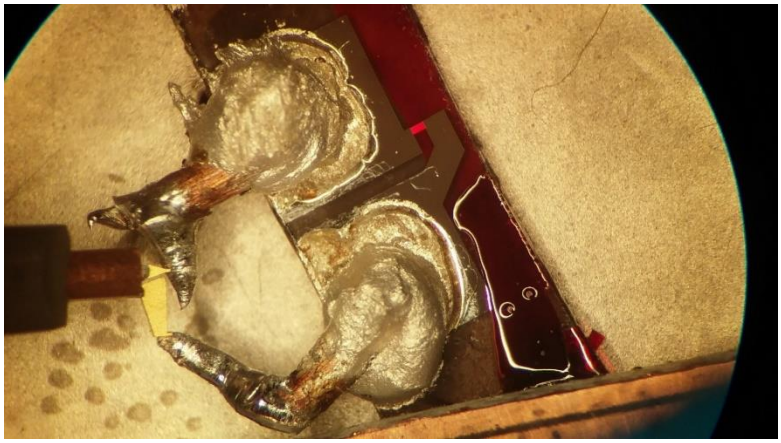

Figure 6-1. Device showing the electrical connection to the bond pads using conductive epoxy to copper wire leads.

Also, measuring the differential dipole antenna with the single ended coax cable will not give a good ballpark measurement. Currently lacking a VNA with differential measurement capabilities, it was resorted to a differential measurement scheme that employs a 2-port S-parameter measurement and requires a measuring jig that combines the two cables into 1. Measurement of differential antennas [42-48] is of interest in the RFID community since having a ground plane may not be practical. Sasamori et al. [47] show that the input impedance of a differential antenna

can be obtained from a 2-port S-parameter measurement where the grounds of the 2 terminals are shorted, and the input impedance across the inner conductors is measured. The differential impedance is given by Sasamori et al. [47] as:

$$Z_{in} = Z_{11} - Z_{11} - Z_{21} + Z_{22} = 2Z_0 \frac{(1 - S_{12})(1 - S_{21}) - S_{11}S_{22}}{(1 - S_{11})(1 - S_{22}) - S_{12}S_{21}} \quad (7\text{-}1)$$

In order to make this measurement, the jig usually has to be de-embedded. It was decided to bypass the de-embedding by combining the coax cables in a modified version of the "jig" shown in Figure 1b of [43], and shown here in Figure 6-2b.

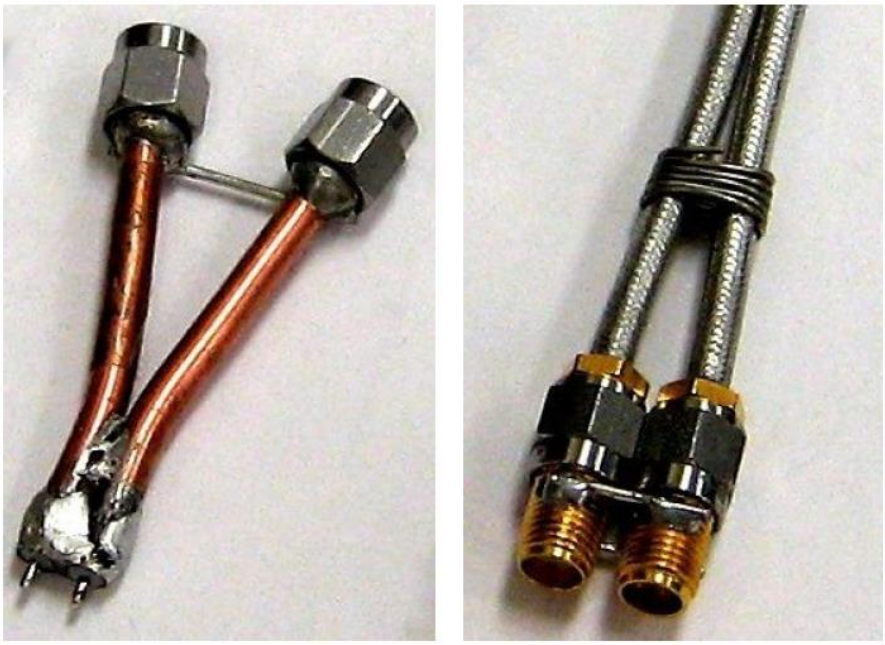

Figure 6-2. Differential measurement jigs, Koskinen et al. use the right jig to measure differential antennas, including unbalanced. Picture from Koskinen et al. [43].

The main difference being that the jig used here is not soldered in place, but can be disassembled in order to perform a S-O-L-T calibration. Homemade calibration standards are made by using coax barrels with the appropriate termination. The through is a "C", with a length of wire about

the same length as the probe leads. When the calibration is done, then the 2 coax cables are united by wrapping a wire around the grounds.

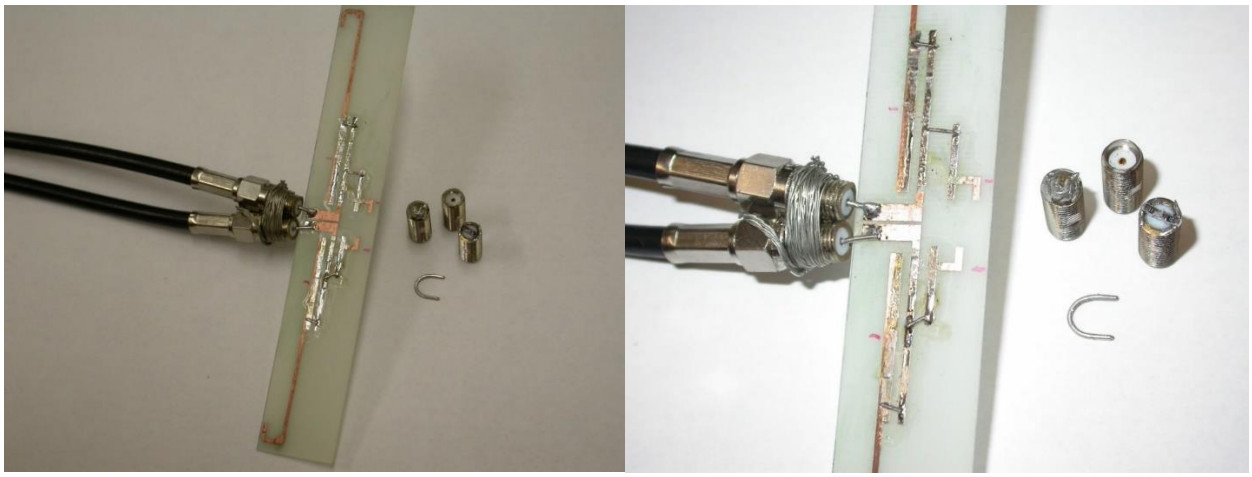

Figure 6-3. Port 1 and Port 2 coax cables combined into a differential probe, with the ability to disassemble for SOLT calibration without having to de-embed a separate probe. Prototype calibration standards are made using 3 barrels and a C-shaped wire as a through standard. This antenna is tuned for 50 Ohm.

The impedance measurement of this approach was tested with a few resistors and the real part was very close to the DC resistance (within 4%). Measuring the same resistor by soldering to an SMA and using an impedance analyzer actually gave real parts that had higher error. Chip capacitors were also measured, and the differential impedance measurement gave imaginary components that were closer to spec than when mounted on an SMA. The length of the "C" through standard that remained outside after it was inserted into the differential probe was also doubled and tripled and its impedance measured. Such measurements gave negligible (1 or 2ohm, less than 5) real part change, but the imaginary part changed from 3ohm to 37ohm and 71ohm—an almost linear change in imaginary part with increased wire length. The j3ohm reading corresponds to the "C" through standard, depending on the inserting pressure applied it can change by approximately +/-2 ohms imaginary. Since the effect of test leads is somewhat understood or predicted by the tests above, and also seeing from the resistor and capacitor measurements that the readings seem reasonable

(lacking proper test standards), some confidence is gained that this measurement approach can make sufficiently accurate measurements for both the epoxy-bonded device and the differential antenna. If an antenna with some degree of tuning can be made, the DTE of the antenna-bonded reflective delay line device can be suppressed.

A tunable PCB monopole antenna designed with a location for a tunable inductor has been shown previously by Abdulhadi [49]. The antenna used here evolves from the PCB folded dipole design. Different structures are incorporated in order to tailor the antenna impedance as appropriate for the device. The structure towards the center of the antenna in figure 6-4 looks like an interdigitated capacitor and the structures on the legs look like stubs, although these structures have not been separately studied. COMSOL was used to model the antenna and run optimizations where the length of the legs and width of lines, or some other geometry, is changed, in order to bring the impedance to or close to the target value. The tunability was tested in simulation by running an optimization where the shorting bars were moved in order to get to + and – some amount of real part impedance while still maintaining the imaginary part the same. The approach taken was to make an antenna with approximately real impedance and to primarily adjust the imaginary part by using the parallel-line tunable inductors used for phasing the group type unidirectionals (GUDTs are shown in Appendix A). The extra inductors near the feed point in Figure 6-5 were not simulated because it created more modeling complexity. Antennas designed for 35, 25 and 15ohm (top to bottom) are shown in figure 6-4. The tuning bars shown in red on bottom antenna are scratched out and replaced with shorting bars that can be moved with the soldering iron for tuning.

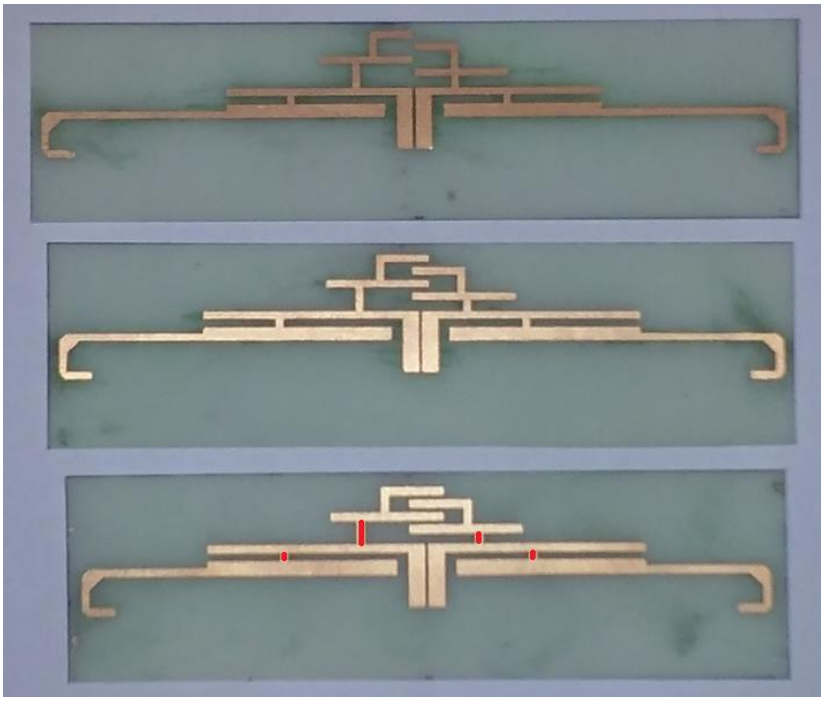

Figure 6-4. Preliminary antenna designs for 35, 25, and 15ohm impedance (top to bottom, respectively). The lengths are approximately 118mm, 115mm, and 108.5mm. The substrate is FR-4, .8mm thick, the legs are 1mm wide, and the port gap is .65mm wide. The red lines on the bottom antenna show the shorting bar locations, where the copper pattern is scratched out and replaced with a tunable wire stub that can be easily moved left and right with a soldering iron after the leg rails are wetted with solder.

A preliminary antenna design with the parallel inductors is shown in figure 6-5, and placed next to a diced 3in wafer full of devices with bond pads for antenna integration (middle of wafer).

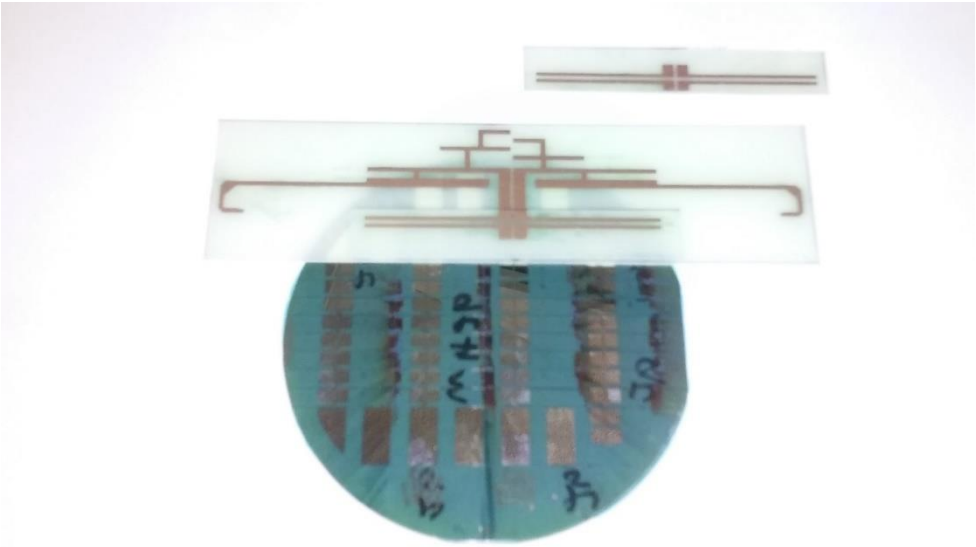

Figure 6-5. Preliminary antenna design for use with a separate PCB with inductors. The idea is to mount the device on the PCB with separate inductors to easily attach and detach the device to different antennas using solder on the other end of the inductor feed.

The device to be integrated with the antenna is a delay line device. A 10cell 3rd harmonic operating optimized2 SPUDT with a uniform reflector composed of 2nd harmonic operating shorted grating having 35 aluminum strips—this device is simulated in chapter 5. In order to find the antenna impedance value required to suppress the DTE, a wired PCB matching network is constructed using mostly tunable elements (shown Figure 6-6). The device is connected to this PCB matching network and the network is tuned for DTE suppression as well as low insertion loss. If the matching network loss is assumed negligible or constant, the mismatch insertion loss required to suppress the echo can be calculated by noting the insertion loss difference between a matched condition and the suppressed echo condition. In this case an insertion loss of 2.23dB is required to suppress the echo (figure 6-14). The matching network is shown first, then the wired measurement results.

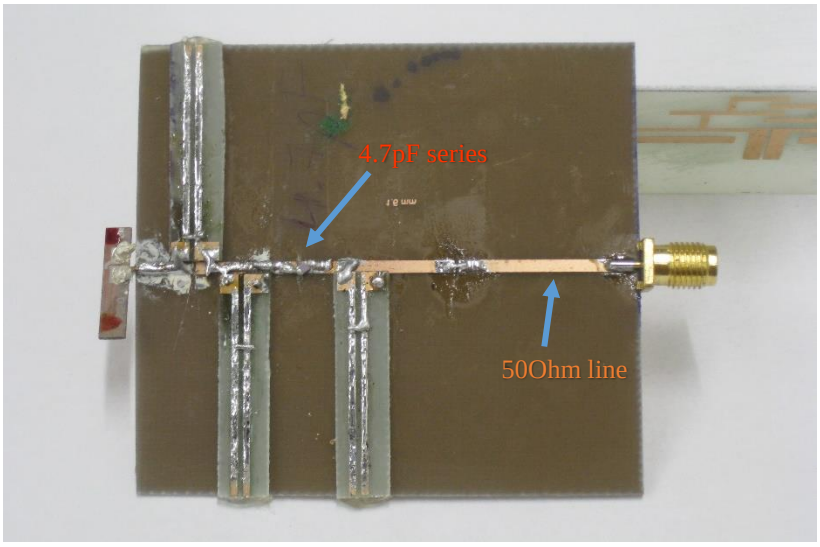

Figure 6-6. SPUDT device wired with tunable matching network. The last two tunable inductors (left to right), have their right contact shorted to the ground plane.

With the matching network set for best DTE suppression, the device is disconnected and the load impedance measured where the SPUDT was attached. The right port is terminated with a 50Ohm load to simulate the coaxial line termination used when measuring the device. The differential impedance measurement (Figure 6-7a) is compared to a single ended measurement (Figure 6-7b)—the agreement is good, 71+j18Ohm and 70+j19Ohm, respectively.

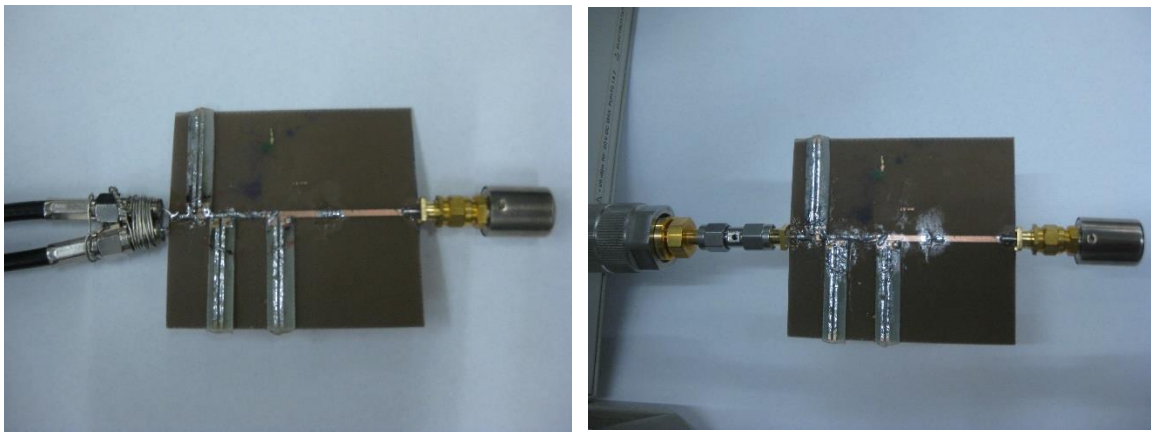

(a) (b)

Figure 6-7. Matching network impedance as seen by the SPUDT, measured with 2-port differential impedance approach (left) and with 1-port impedance analyzer (right). Left measures 71+j18Ohm and right measures 70+j19Ohm—measurements agree.

The impedance profile of the matching network is shown in figure 6-8.

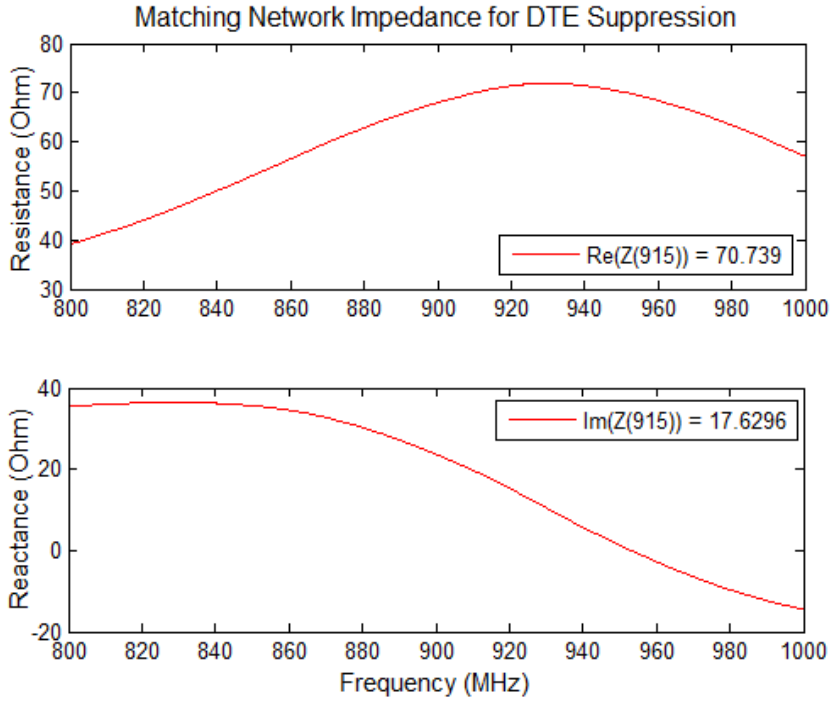

Figure 6-8. Impedance profile of the matching network as seen by the 3rd harmonic SPUDT, tuned for optimized DTE suppression—71+j18Ohm at 915MHz, Figure 6-7a.

The frequency and time domain results of the matched response and the optimized echo suppression response of the test device, are shown at the end of this chapter in figure 6-14.

Having measured the target impedance, the antenna design of Figure 6-4 needed modification because it was not reaching the required 70Ohm real without substantial modification, it was only reaching about 50Ohm real (0 Ohm imaginary). Figure 6-9a shows a slightly modified antenna configuration, the antenna feed is brought in further, making the legs look like a ladder where every step has tuning element. This design reaches about 60Ohm real (0 Ohm imaginary). The added inductors close to the antenna feed point (figure 6-9b) were not sufficient to bring down the DTE suppression by themselves. An external wire shown in figure 6-13 is attached to the point shown in orange (figure 6-9b top), while the shorting bars are in

locations marked red, with bottom right shorting bar replaced with a 4.7pF chip capacitor—this combination produced the wireless DTE suppression levels shown in figure 6-15.

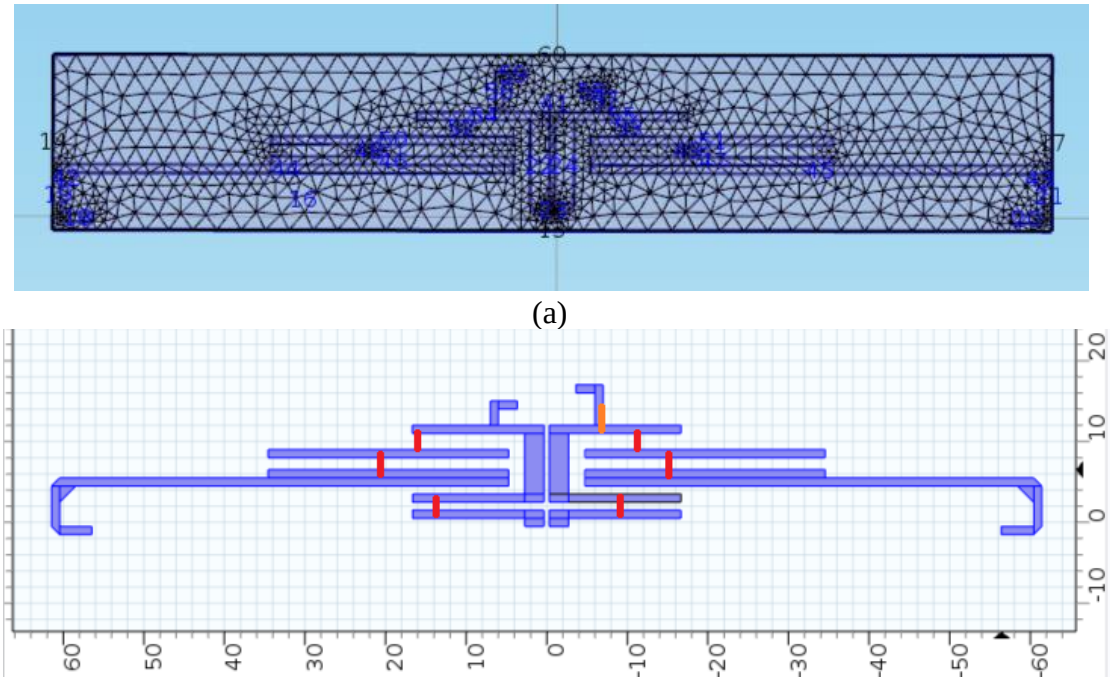

Figure 6-9. (a) Shows a slightly modified antenna configuration, the antenna feed is brought in further, making the legs look like a ladder where every step has tuning element. (b) An external wire shown in figure 6-13 is attached to the point shown in orange, while the approximate shorting bars are in locations marked red, this combination brought the antenna impedance close to the 71+j18ohm impedance required for DTE suppression levels shown at the end of this chapter—no external inductors used, but bottom right shorting bar was replaced with a small chip capacitor, 4.7pF. Design (b) was not simulated, but only experimentally tuned to show proof of concept of wireless echo suppression.

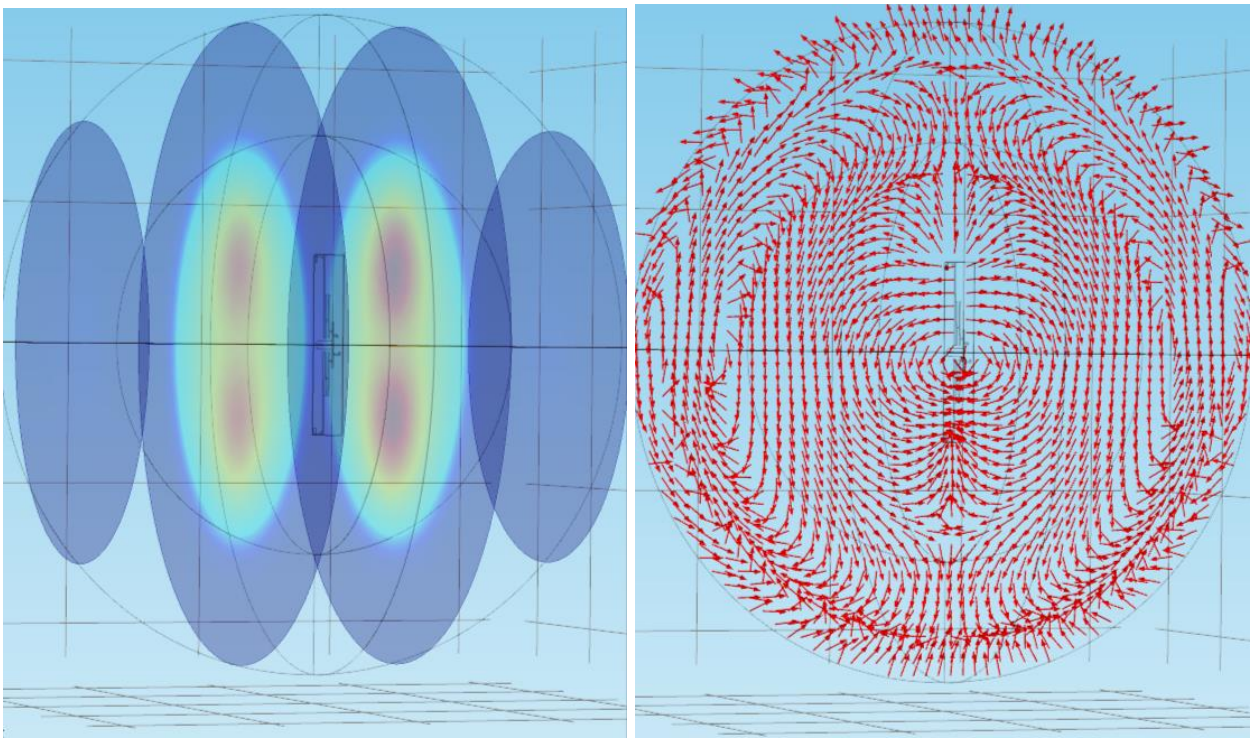

Figure 6-10. COMSOL simulation results of the nearfield (left) electric field magnitude and (right) displacement current direction (arrows normalized to equal length and don't show actual strength). Looking at the grid on the bottom, the plane of the antenna is on the plane that goes from the lower left corner to the upper right corner.

Figure 6-10 shows how the antenna simulation was set up. There is enough free space volume to see the field direction change direction. The inner sphere is the regular computational domain and the outer shell the complex perfectly matched layer (CPML). Since the CPML is a stretched coordinate system you can see the phase changing in a shorter distance. The directionality and other antenna parameters were not explored as part of this effort, only the impedance.

The design in figure 6-9b was never simulated and no attempt was made to further modify the antenna. The main goal of this dissertation, that is, of optimized echo suppression in a wireless configuration by using a 3rd harmonic unidirectional transducer, and demonstration of modeling and experimental techniques, is complete with the prototype setup shown in figure 6-13. The VNA is set up with a Tx and Rx antenna for a wireless S21 measurement. An amplifier is placed between

the Rx antenna and port 2 of the network analyzer in order to bring the echo out of the noise. The resulting frequency and time domain response showing wireless echo suppression of a passive wireless SAW 1-port delay line device is shown in figure 6-12b and figure 6-15.

The device was dismounted and some differential measurements of the antenna were made. These are shown in figure 6-11, it's a coarse measurement since the location was a bit different—perhaps the cables and my hand holding them could have affected the reading. The probe leads that were soldered to the antenna for measurement were slightly thin, the pressure applied was having an effect on the impedance reading. All this movement could have also slightly moved the external tuning wire. However, of the 5 impedance measurements taken, one of them (red trace) was very close to the expected value of 71+j18Ohm at center frequency, taken earlier from the wired matching network. This suggests that the differential measurement is valid for the modified differential dipole antenna used here. This chapter ends with plots of the antenna impedance measurement and various plots showing the wired and wireless optimized echo suppression results of the uniform reflector device.

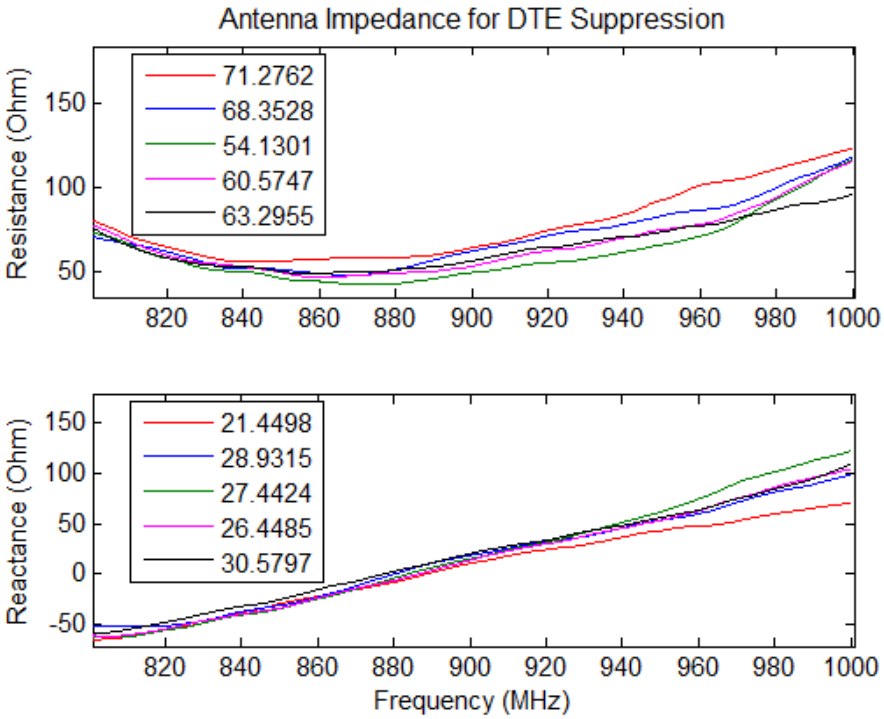

Figure 6-11. Differential measurements of antenna tuned for low DTE. The legend shows the corresponding real and imaginary part of the impedance measurement at 915MHz. The center frequency value of the 1st measurement (red trace) is very close to the wired matching network impedance value at the same frequency (figure 6-8).

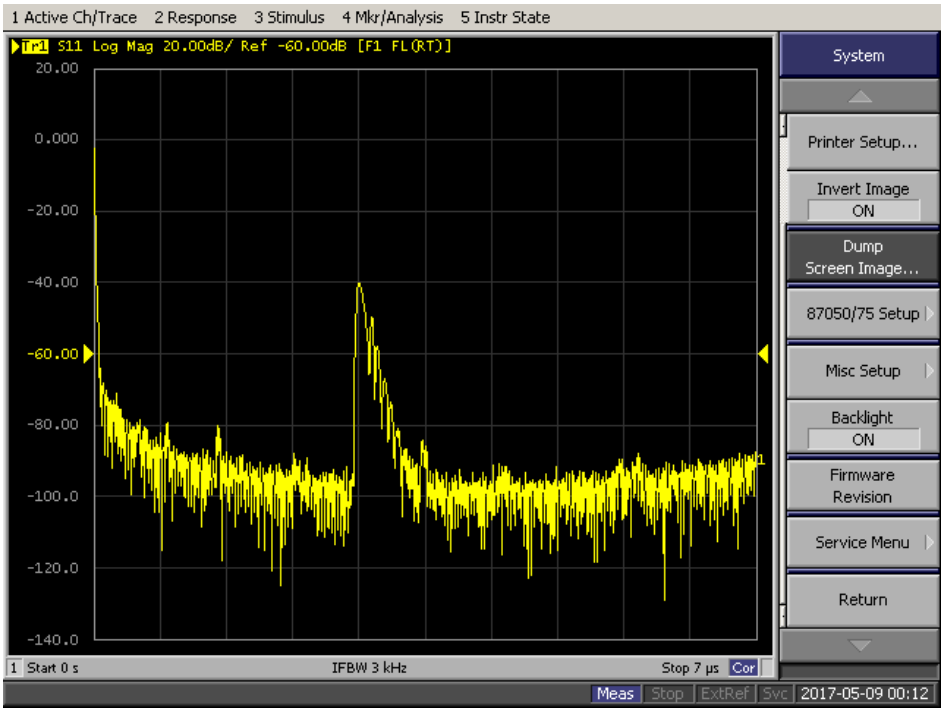

(a)

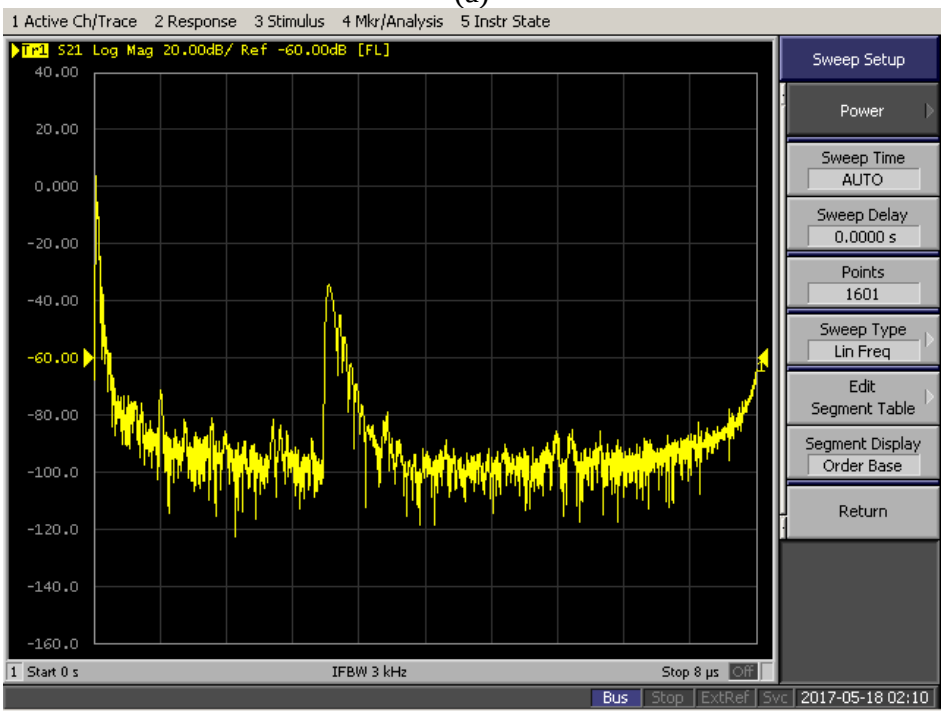

(b)

Figure 6-12. Screenshots of the VNA time response display showing proof of physical echo suppression. (a) Wired echo suppression using PCB matching network. (b) Wireless echo suppression using tunable antenna.

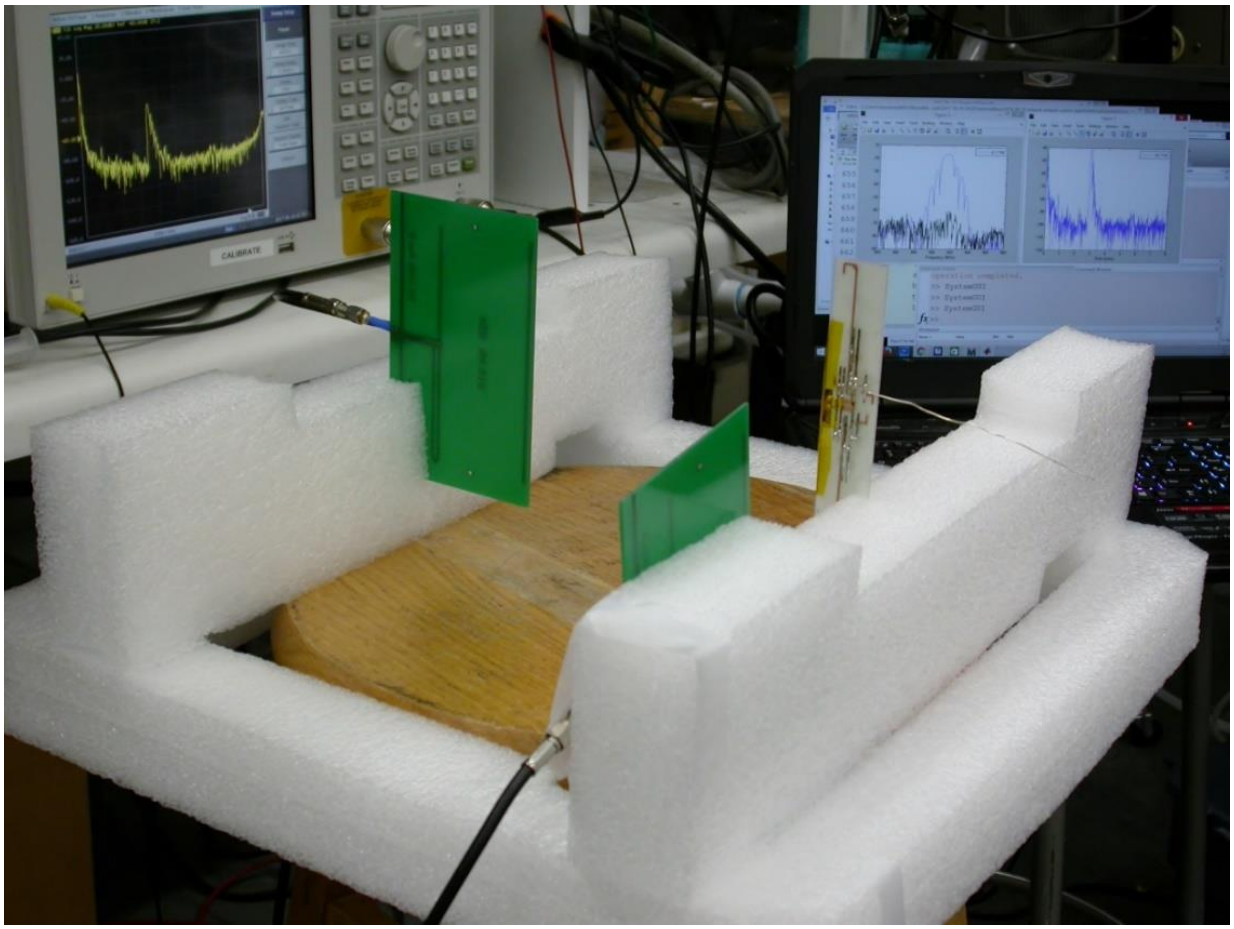

Figure 6-13. Experimental set up used to show wireless DTE suppression. A 2-port measurement is used, the Tx antenna is hooked up directly to the network analyzer, the Rx antenna is connected to an amplifier that is connected to port 2 of the VNA. The acquisition system on the back right shows the frequency domain echoes and time domain after some processing. Shown on the top left corner is the raw time domain response as measured by the VNA. As noted in figure 6-9b and shown in this Figure, an external wire is connected to suppress the DTE to the levels shown in the wireless results—objective completed.

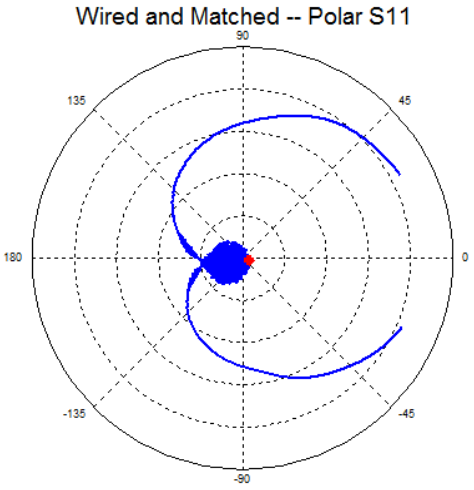
Wired and Matched -- Polar S11
90
135
45
180
0
-135
-45
-90

(a)

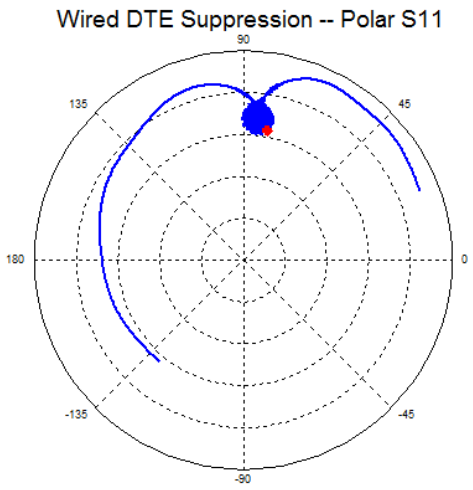
Wired DTE Suppression -- Polar S11
90
135
45
180
0
-135
-45
-90

(b)

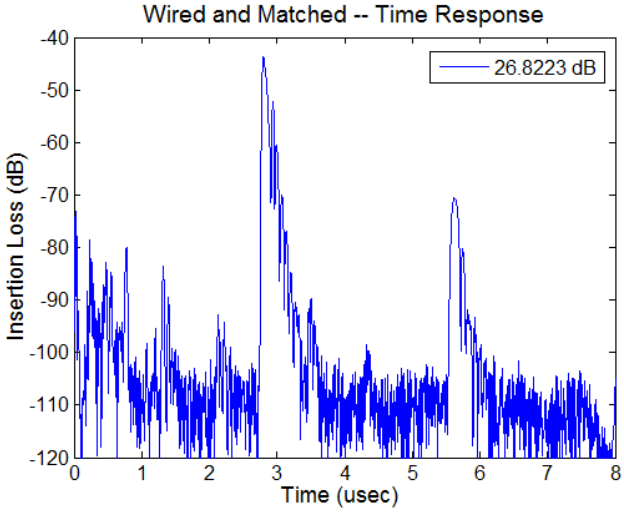
Wired and Matched -- Time Response
26.8223 dB
Insertion Loss (dB)
-40
-50
-60
-70
-80
-90
-100
-110
-120
0
1
2
3
4
5
6
7
8
Time (usec)

(c)

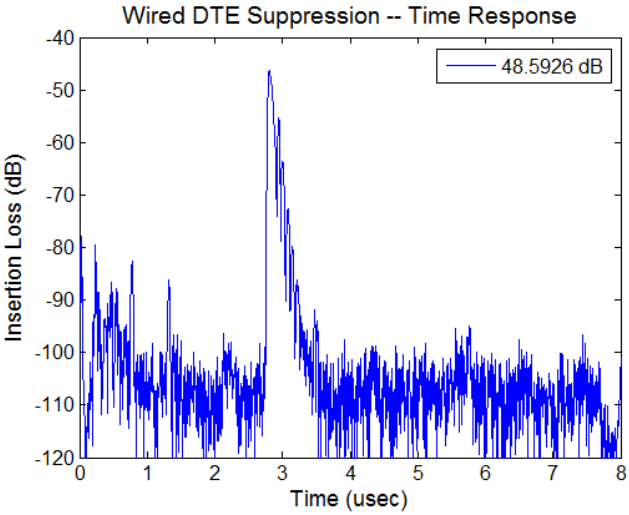
Wired DTE Suppression -- Time Response
48.5926 dB
Insertion Loss (dB)
-40
-50
-60
-70
-80
-90
-100
-110
-120
0
1
2
3
4
5
6
7
8
Time (usec)

(d)

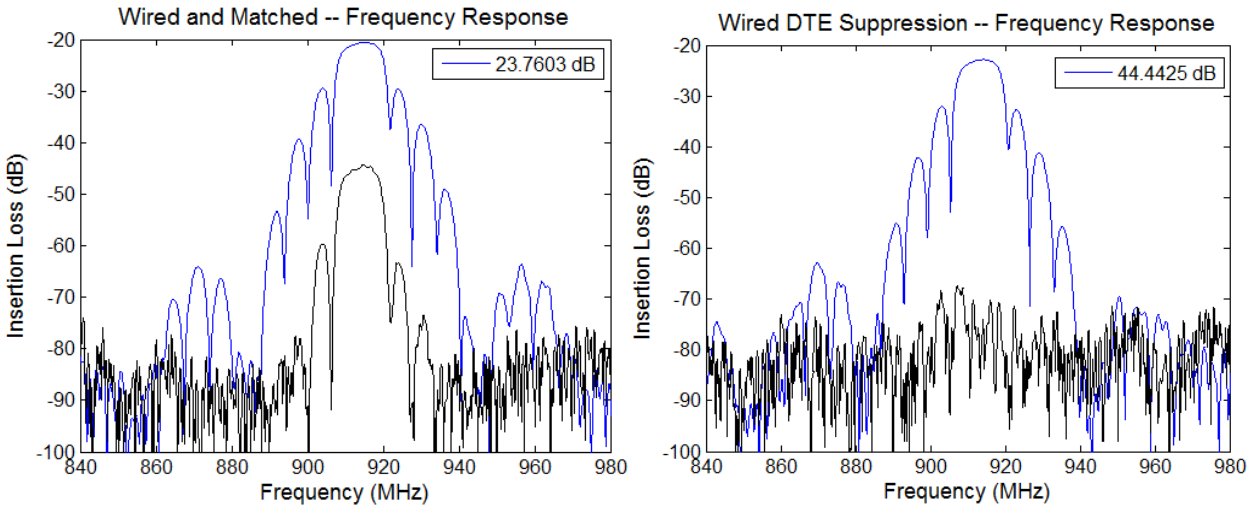

(e) (f)

Figure 6-14. Uniform reflector device response with wired tunable matching network set for low insertion loss (left column) and double transit echo suppression (right column). The maximum values and locations for the time and frequency 1st transit response are: frequency low IL (-20.59dB, 915.9MHz), freq. low DTE (-22.82dB, 914.3MHz), time low IL (-43.62dB, 2.8usec), time low DTE (-46.27dB, 2.8usec). That's ~2.23dB in extra insertion loss for the electrical and mechanical components of reflection to cancel each other to give ~44.4425dB DTE suppression. The time domain pulse shows a 2.65dB increase in IL from matched to low DTE.

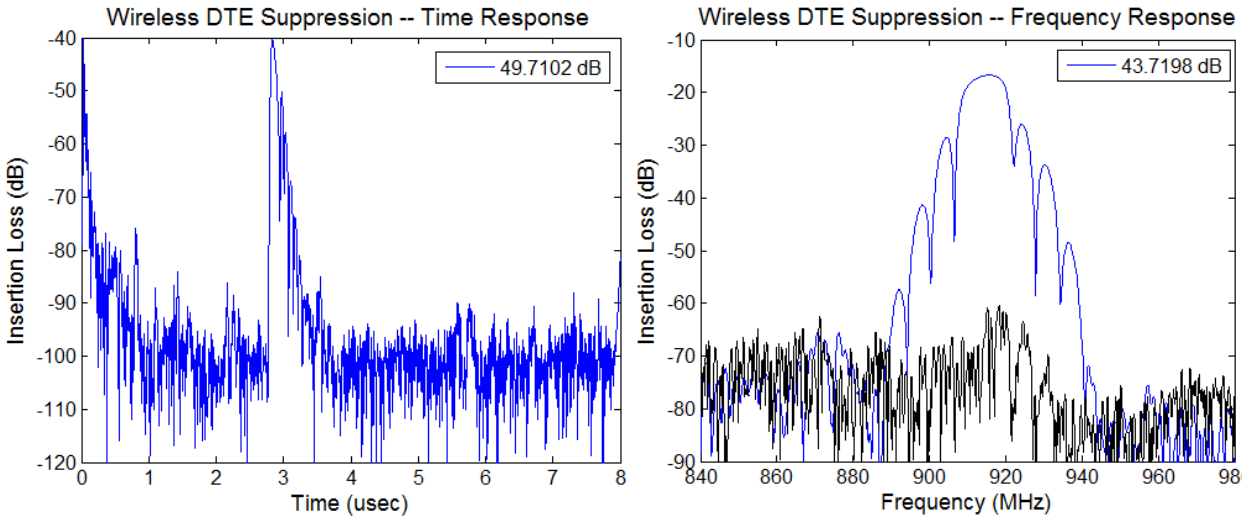

Figure 6-15. Wireless double transit echo suppression results. The time domain DTE pulse (left) is lowered to ~49.7dB below the main transit. The frequency domain DTE pulse (right) is lowered to ~44dB below the main transit

6.2 Chapter 6 Summary

This chapter demonstrated a passive wireless reflective delay line device with optimized echo suppression. The main contribution by the author is to show the physical echo suppression on an antenna mounted device. Another contribution by the author is the design of a tunable antenna, used here to fine tune the load impedance of the SAW device in order to suppress the echo. The echo suppression is bandwidth dependent. The demonstration with the uniform reflector device showed the double transit echo being suppressed 44dB in frequency over the whole band, and 50dB in the time domain. A differential measurement employing a special probe and a 2-port S-parameter measurement was successfully applied to measuring the differential antenna. This was essential in helping to make an antenna with the right impedance for echo suppression. The main goal of this dissertation effort, passive wireless echo suppression of a reflective delay line device has been successfully accomplished.

CHAPTER 7:
CONCLUSION

Chapter 2 gives a general introduction to passive wireless SAW sensor embodiments. It also shows a method of predicting the precision of a reflective delay-line SAW sensor as a function of SNR, and as a function of distance. Thus the precision performance of a wireless sensor in a practical environment can be estimated. It was introduced how the cavity that forms between the transducer and the reflectors gives rise to the interference of the double transit echo (DTE) in a multi-sensor system. In order to suppress the unwanted double transit echo, a single-phase unidirectional transducer (SPUDT) was used. It was decided to use a 3rd harmonic operating SPUDT. For this reason the standard electrode width controlled (EWC) SPUDT layout was modified and optimized for 3rd harmonic. Coupling-of-modes (COM) model simulations were used to match the measured devices in order to obtain the modeling parameters. With the modeling parameters in-hand, a 10cell optimized SPUDT was used in conjunction with special reflectors, and a wireless device was designed. New SAW reflector types were also designed, called Walsh-Hadamard-like reflectors. WHL1 have an AM-BPSK type chip configuration, and WHL2 have a PWM-BPSK type chip configuration. WHL2 devices were built and were compared to the COM model. After changing the characteristic impedance of the COM simulation and of the post-processed fabricated devices by using an optimization routine to suppress the DTE, the resulting echo suppression level was shown to be well predicted by the COM model simulation.

Finally, chapter 6 shows the physical echo suppression of a wireless operating reflective delay-line device. A tunable antenna was used to precisely tune the impedance of the SAW device in order to achieve an optimized echo suppression level. This concludes the dissertation, hopefully

it is another step on the journey to seeing passive wireless sensor systems introduced into the market—as a solution to current demands and future applications yet to be discovered. The author is thankful for the instruction and help received along the way, as well as for the opportunity. Thank you, “The End.”

APPENDIX A:
ANTENNA MOUNTED GROUP TYPE UNIDIRECTIONAL TRANSDUCER

Group type unidirectional transducers (GUDTs) were also explored here for the purpose of echo suppression in wireless devices prior to the SPUDTs. A synopsis of the GUDT operation principle and its extension to 3rd harmonic operation is presented in this appendix. The directionality of a narrowband and a wideband topology is compared. A phasing network that is appropriate for a differential antenna is presented. Operation of a GUDT interfaced with an antenna is presented. Finally, a wired matching network is used to match the phased GUDT device and then post-processed using an additional matching optimization.

Work on group type unidirectionals begins in the 70's with contributors that include Rosenfeld et al., Malocha et al., and Yamanouchi et al. [50-53]. One filter configuration given in [50] uses a hybrid GUDT with capacitive weighing, it shows a forward response max to reverse S21 max difference of 33dB—these transducers are highly directional. GUDTs consist of 2 groups of transducer sections having a spatial phase offset and also requiring voltage phase offset via some phase shifting network. Figure A-1 below shows the general layout of a standard GUDT, showing 3 electrical ports—the ground, the in-phase (I) and quadrature (Q) ports.

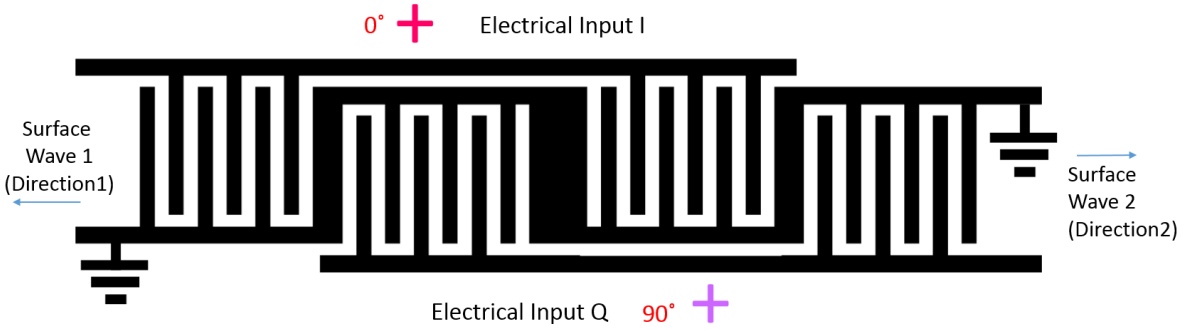

Figure A-1. Standard implementation of I and Q transducer groups using a meander ground. In-phase (I) and quadrature (Q) transducer groups are spatially out phase by λ0/4 (90^0) at f0, both 1st and 3rd harmonic.

The mechanism that causes unidirecionality can be explained by using a phasor representation of the spatial layout and the voltage phase across the I and Q transducer groups. From Figure A-1

the Q transducer is shifted 90^0 to the right at 1st harmonic—the surface wave phasor is advanced 90^0 for the right propagating wave (direction 2) and retarded 90^0 for the left propagating wave (direction 1). Without any electrical phasing, the SAW phasor in each direction is shown in Figure A-2a.

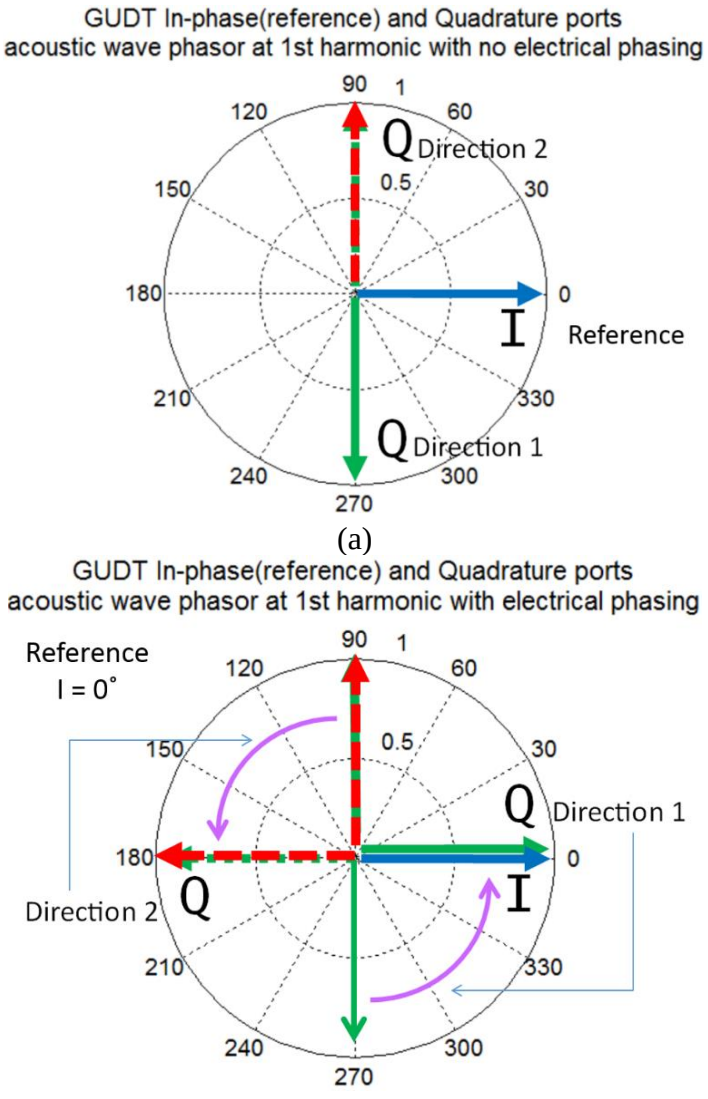

Figure A-2. Surface wave phasor in each direction, (a) before electrical phasing and (b) after electrical phasing.

After electrical phasing the Q phasor of both directions is advanced 90^0 as shown in Figure A-2b, making the waves generated by direction 1 I and Q groups in-phase, and the direction 2 I and

Q groups out of phase—left would be the propagation direction for the I and Q labeling in Figure A-1. Phasing accomplished with two inductors, placing the input impedance of one phase at -45^{0}and the other at 45^0. Hugli and Dill et al. show GUDT filters operating in the GHz using harmonic operation but the unidirectionality mechanism is not discussed. For 3rd harmonic operation the spatial offset gives a phase offset of 270^0, so the direction 1 and 2 Q phasors in Figure A-2. Surface wave phasor in each direction, (a) before electrical phasing and (b) after electrical phasing. change directions. Therefore the GUDT changes direction from 1st to 3rd harmonic given same I and Q electrical phasing angle.

Although many phasing approaches have been proposed [54-57], the work presented here uses Malocha's GUDT tuning approach [51], which consists of using 2 lumped elements—possibly just a single inductor under the right conditions. Usually 2 inductors are required, but it's possible to need a capacitor and inductor. For perfect directionality at center frequency, the GUDT I and Q groups require a voltage having equal magnitude with phase offset of 90^0. This places the phase of the input impedance of each GUDT leg ($j\omega L_{I/Q}$+Zidt) for network in Figure A-3) at +/-45^0, with equal magnitude, as given by equation 2 of [51]. Since Zidt is capacitive, according to equation A-3 below, L_I is the bigger inductor. Harmonic operation is also possible. The work here begins with the phasing scheme that uses two inductors, each in series with the respective I and Q electrical input port—the input voltage is applied to the I and Q groups in a parallel connection as shown in Figure A-3.

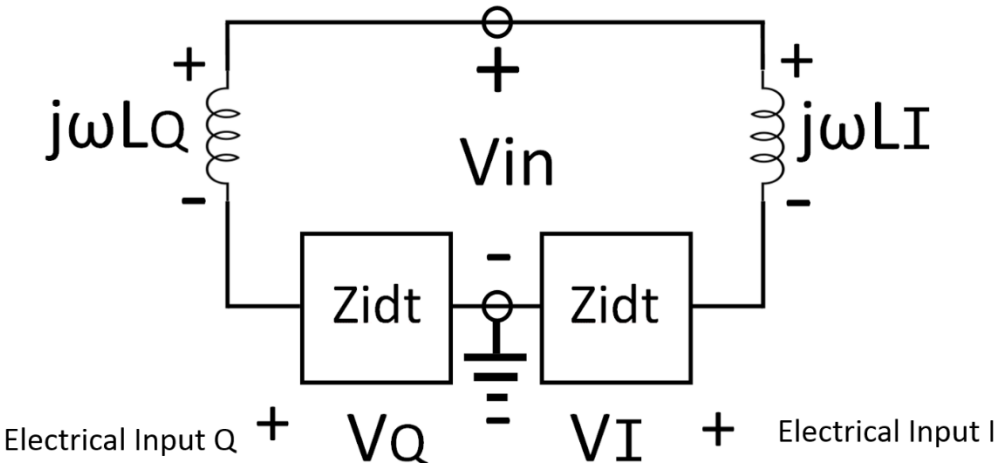

Figure A-3. Equivalent circuit for the GUDT phasing layout that places the voltage feed for the I and Q groups in parallel and inductors in series with the group. The meander ground is grounded.

The devices here use almost identical I and Q groups, so the impedance for each group is approximately the same, Zidt. Zidt can be approximated by disconnecting one of the phases and measuring the impedance across the other leg. Actually you should ground the other phase to get the correct impedance. For finding the inductor values 2 KVLs are solved:

$$Vin - i_Q \cdot j\omega L_Q - V_Q = 0 \; and \; Vin - i_I \cdot j\omega L_I - V_I = 0 \tag{A-1}$$

Then the constraint on the I and Q voltage relationship is given:

$$\frac{V_Q}{V_I} = j \tag{A-2}$$

The resulting equations from A-1 and A-2 are then solved for inductance values L_I and L_Q.

$$\omega L_I = ReZ_{idt} - ImZ_{idt} \text{ and } \omega L_Q = -ReZ_{idt} - ImZ_{idt} \tag{A-3}$$

Two GUDT topologies were laid out and fabricated which show the two extremes of the group layout options. Both use a total of 10 transduction periods. The layout with the more narrowband directionality uses 5 transduction periods per group with no interleaving of I and Q groups. It's based on 4f0 split finger electrodes to enable coupling at 3rd harmonic and has a

20 wavelength beamwidth at fundamental. The mask pattern used for these two GUDT layouts is shown in Figure A-4 below.

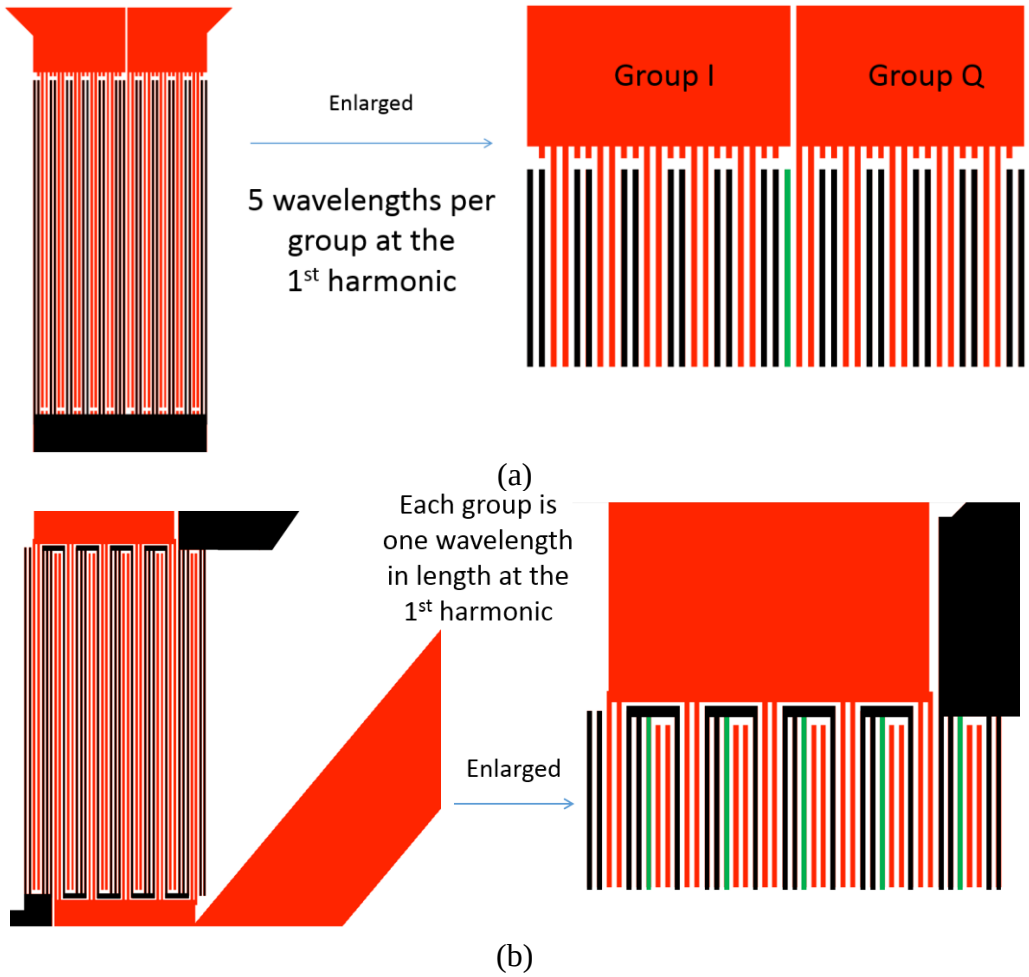

Figure A-4. Both GUDT layouts (a) and (b) have 10 transduction periods but the number of groups per phase is changed from (a) 1 to (b) 5.

The entire test device layout consists of the group type in the middle and two 5 pair 4f0 IDTs on either side, also big pads for using silver epoxy contacts—the two are shown in Figure A-5 below.

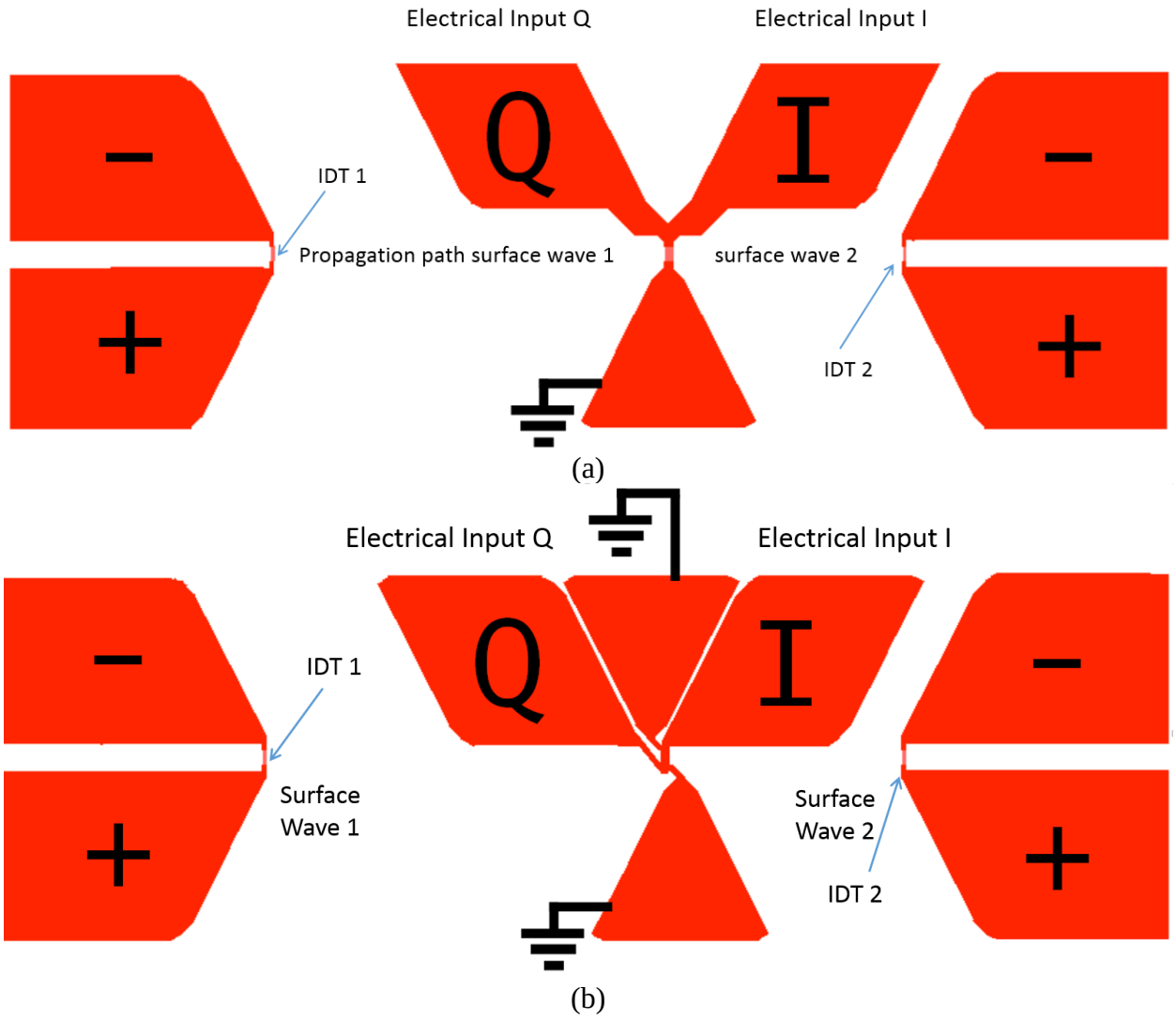

Figure A-5. Test device showing layout for bond pad connections for GUDT layouts in Figure A-4, and showing the 5pair bidirectionals used to show the forward and reverse characteristics.

Both configurations are fabricated and tested at 40MHz fundamental to verify the phasing element calculation with negligible bond pad and PCB trace parasitics. The inductors are hand wound and use ferrite cores for tuning. Inductors are tuned to the calculated inductance values by 1st mounting to an SMA, then soldering to the device PCB, only requiring fine tuning. The coils are held with superglue and isolated from the ferrite with plastic bag material. The plastic is then taken off after

glue dries. The PCB mounted device with phased inductors is shown in Figure A-6 below; the PCB has a backside ground plane.

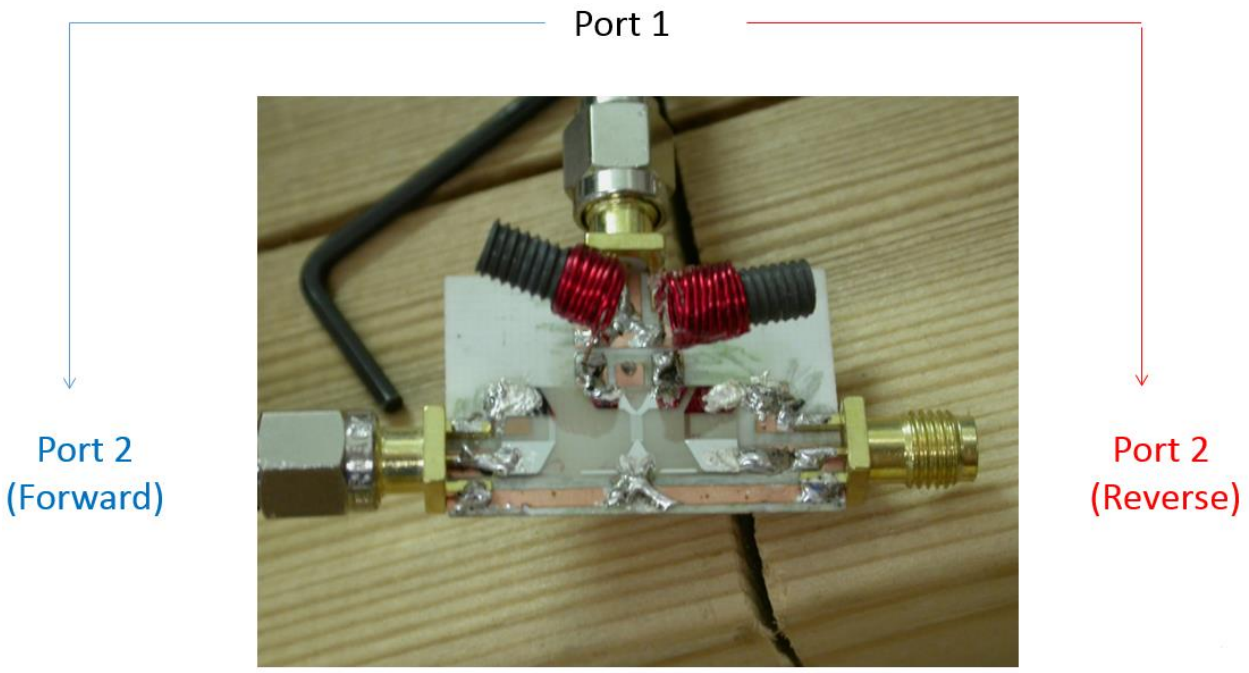

Figure A-6. A low frequency, 40MHz, test structure for verification of equation A-3, and proof of operation before continuing to work at higher frequency.

Port 1 measures the GUDT and port 2 measures one of the bidirectional IDTs. The forward and reverse response for both configurations is shown in Figure A-7 below.

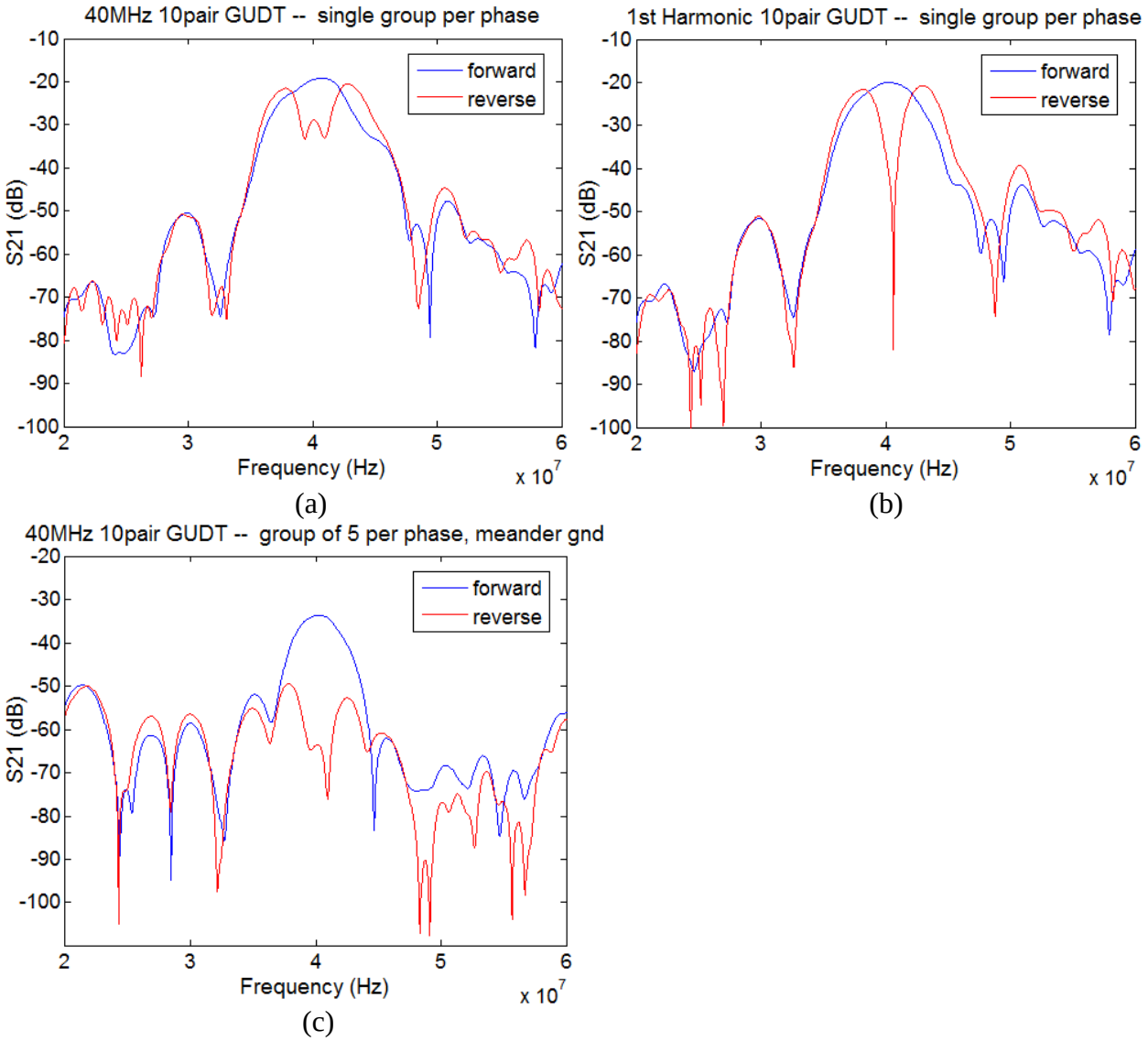

Figure A-7. Forward and reverse responses in (a) and (b) correspond to the single group per phase device shown in Figure A-6, with phasing inductors tuned slightly differently. Responses in (c) correspond to the meander ground device, also at 40MHz—showing a wider band directionality but narrower forward response than single-group-per-phase device of (a) and (b).

As can be seen from the GUDT responses above, the forward bandwidth narrows a bit for the wideband unidirectional device having the interlaced groups. A wider band device with wideband unidirectional response is the 3-phase group type unidirectional (TPUDT), similar to the GUDT but having 3 phases [58-60]. It shows the phasor representation similar to Figure A-2, but the

phasors of the 3 spatial phases and the required input voltage phases are 120^0 apart. The interesting thing is that the two voltage phases of 120^0 can be replaced by single 60^0 phase shift as shown in Figure A-8.

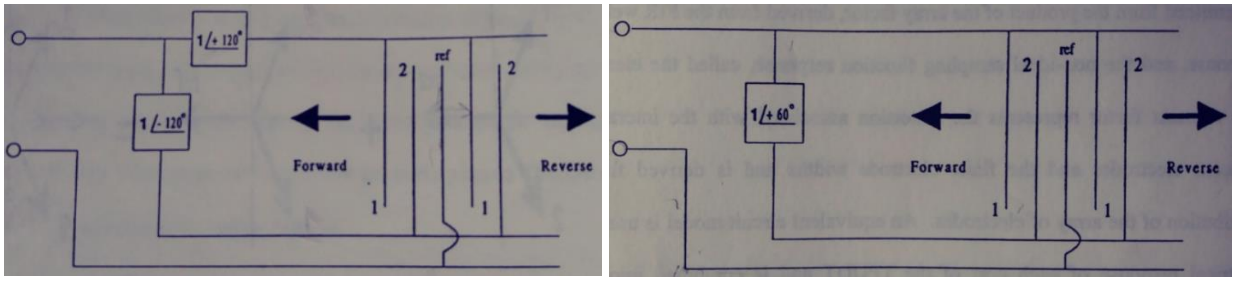

Figure A-8. Phasing of a 3-phase UDT (TPUDT), figure of S. Richie and D.C. Malocha in reference [58].

Continuing with the GUDT, from now on only the meander ground configuration is used. 300MHz fundamental devices are shown in Figure A-9 below.

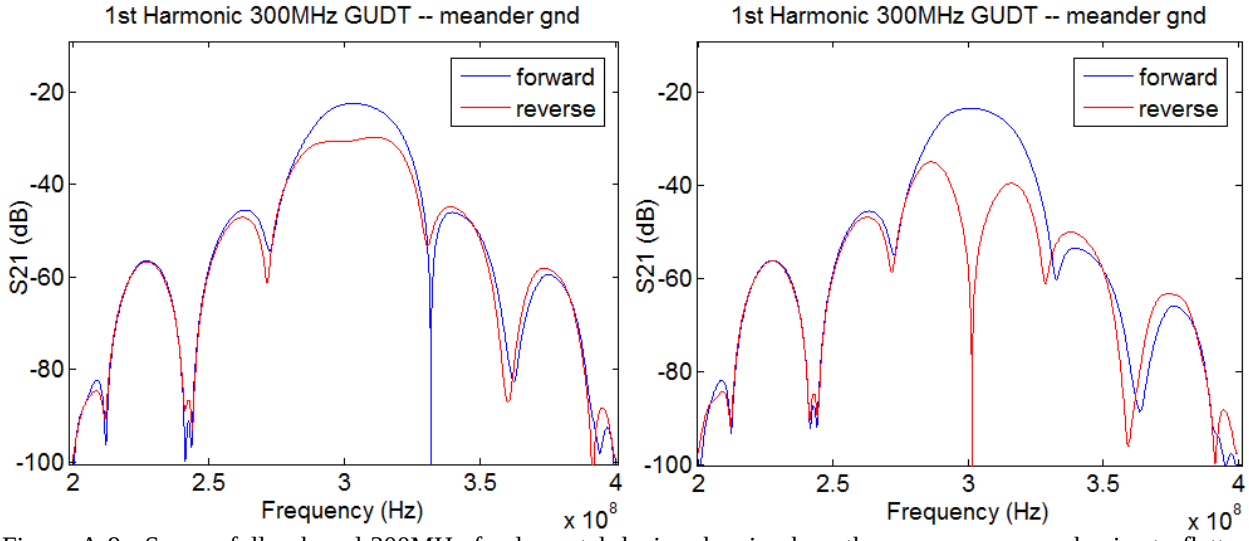

Figure A-9. Successfully phased 300MHz fundamental device showing how the reverse response begins to flatten before achieving an almost perfect null at center frequency.

Third harmonic operation of the 300MHz fundamental devices follow. First as proof of concept of 3rd harmonic operation, a 90^0coupler was used. Though probably not practical here since it may not allow for proper tuning, it demonstrates a possible phasing approach (Figure A-10).

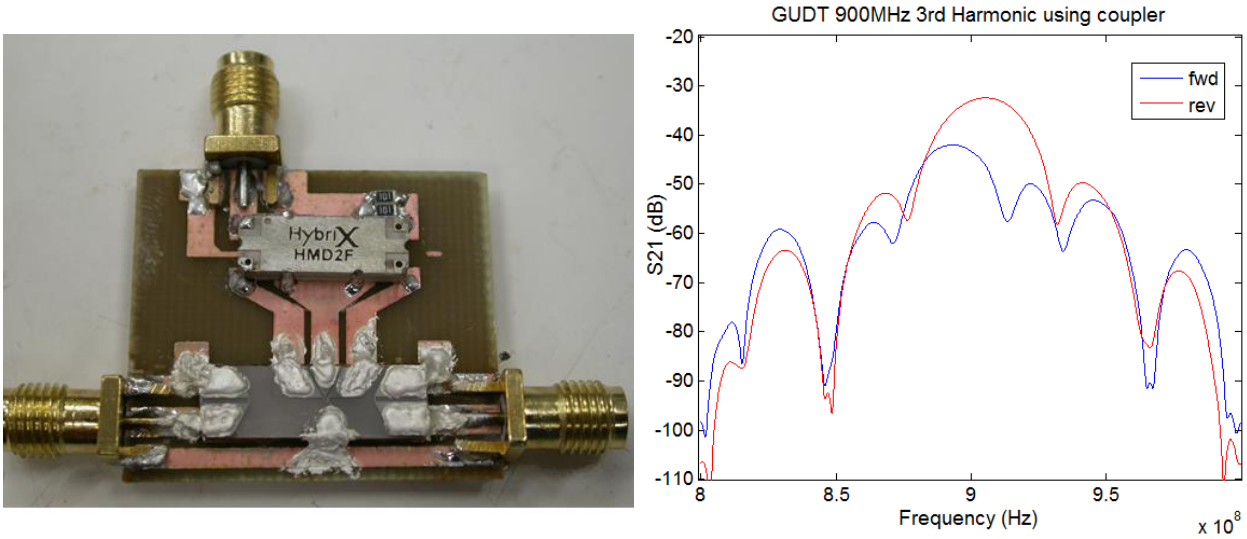

Figure A-10. Hybrid coupler used to provide the 90^0 phase shift with equal power split and demonstrate the operation of the 3rd harmonic device. Comparing the side lobe levels, it doesn't seem like an equal power split for forward and reverse direction was achieved, nor the 90^0 phase shift—an imbalance in the I and Q group impedance may contribute to the skewing of the reverse response.

Phasing inductors are very sensitive at 900MHz. The coil inductors become a single loop at this frequency (Figure A-11 below). The inductance values were in the order of 10nH, approximately.

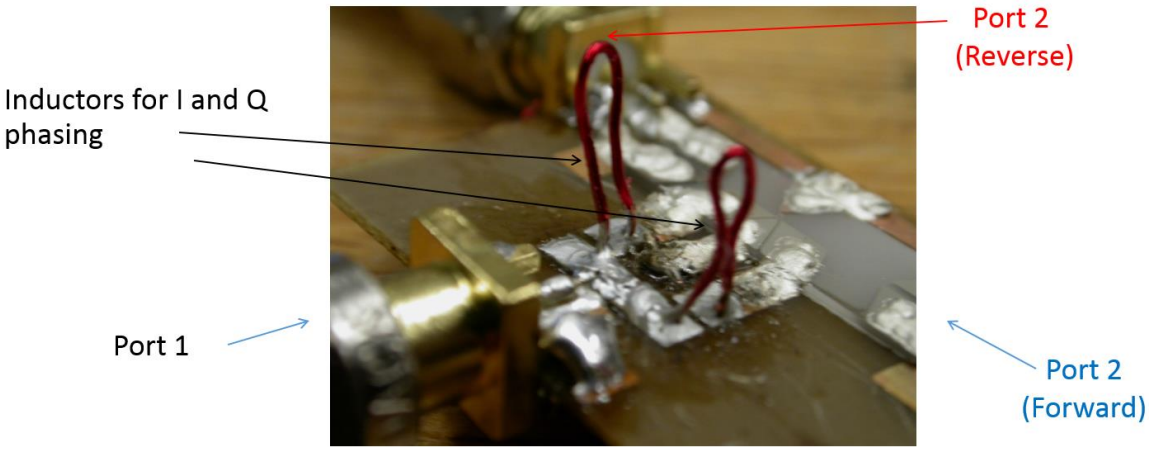

Figure A-11. Phasing inductors used at 900MHz 3rd harmonic operation. Only a slight difference in shape provides the required phasing.

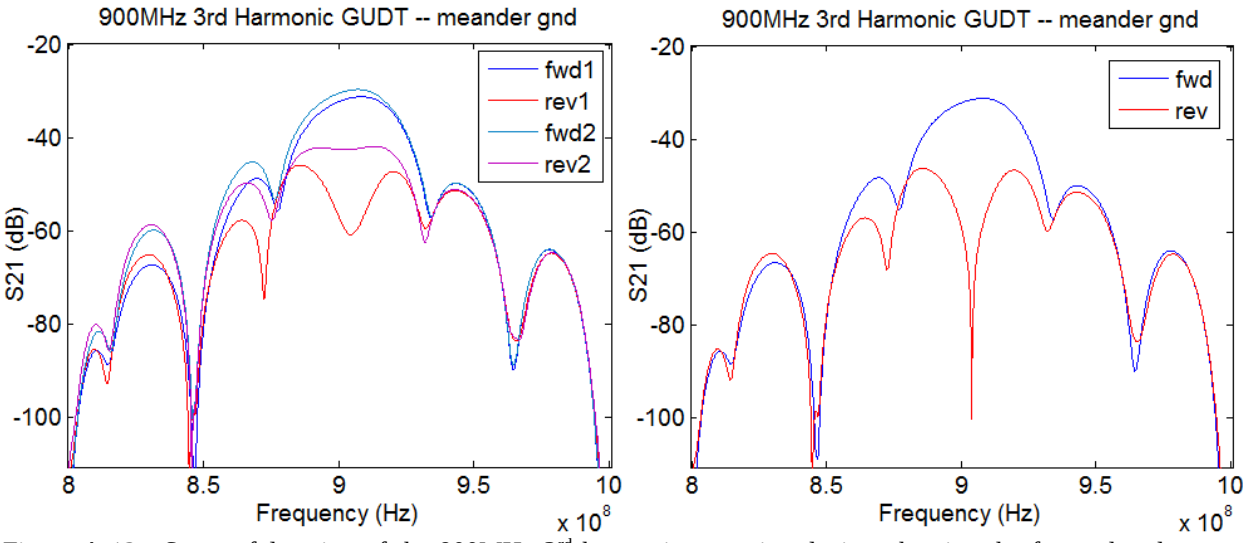

Figure A-12. Successful tuning of the 900MHz 3rd harmonic operating device, showing the forward and reverse response for various inductor values while tuning the device shown in Figure A-11.

The inductors were implemented as embedded parallel line PCB inductors with a tunable shorting bar (Figure A-13a). The forward and reverse response at 900MHz 3rd harmonic operation is shown in Figure A-13 below.

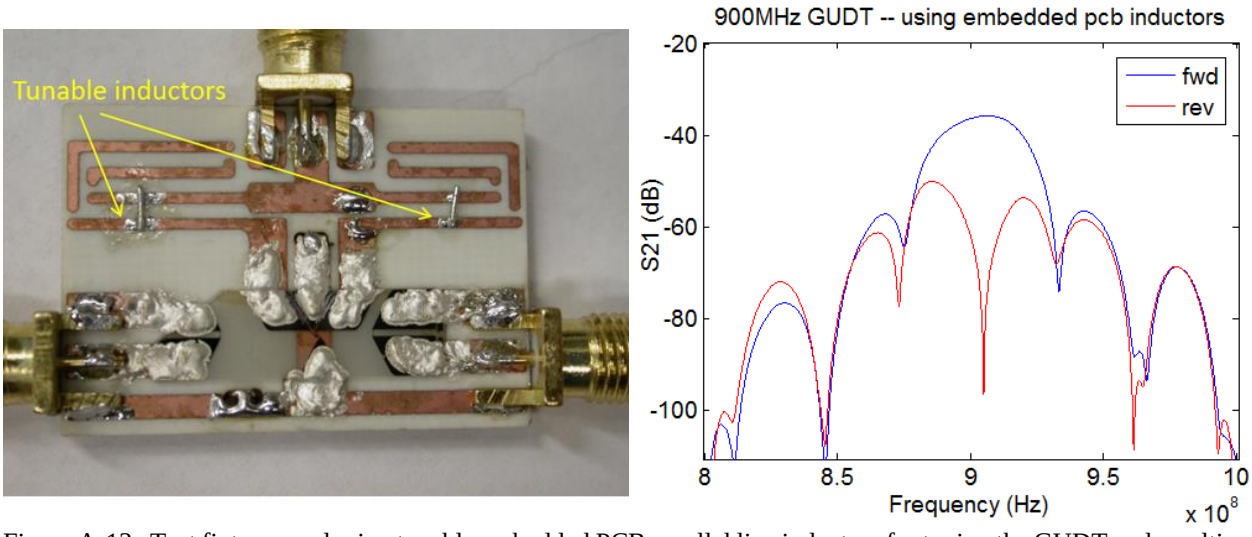

Figure A-13. Test fixture employing tunable embedded PCB parallel line inductors for tuning the GUDT and resulting forward and reverse response.

A differential antenna implementation could not make use of the ground plane used thus far. An attempt was made to mount the GUDT on the folded dipole antenna in Figure A-14.

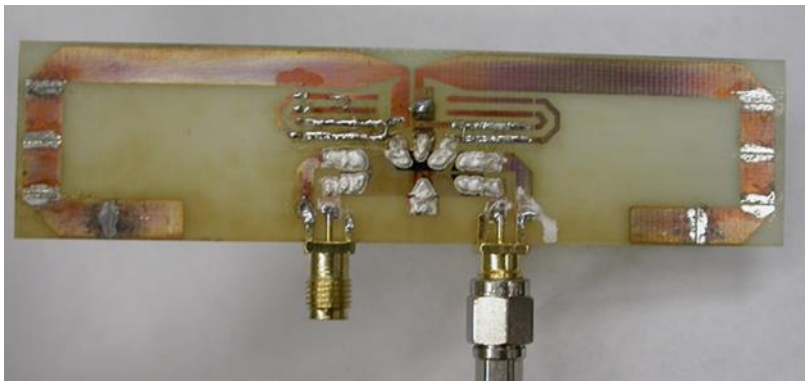

Figure A-14. 1st attempt at wireless operation using a folded dipole antenna and the phasing topology in Figure A-3. Proper phasing of the inductors was not successful and a new phasing topology was adopted (Figure A-15).

Tuning was more difficult to achieve with this antenna feed and it was abandoned. Other inductor phasing topologies were investigated for wireless implementation. The inductors were placed in parallel with the I and Q groups and fed using a series voltage source connection shown in Figure A-15 below.

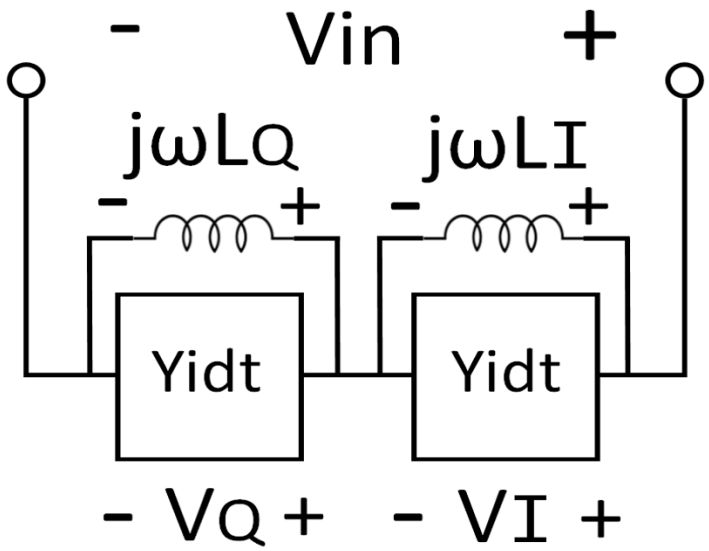

Figure A-15. Equivalent circuit for the GUDT phasing layout that places the voltage feed for the I and Q groups in series and inductors in parallel with the group. The meander ground is floating.

For finding the inductor values 1 KVL is solved:

$$Vin - V_I - V_Q = 0 \tag{A-4}$$

Then the constraint on the I and Q voltage relationship is given:

$$\frac{V_Q}{V_I} = j \tag{A-5}$$

The resulting equations from A-4 and A-5 are then solved for inductance values L_I and L_Q.

$$\omega L_Q = \frac{1}{ReY_{idt} + \frac{1}{ImY_{idt}}} \text{ and } \omega L_I = \frac{1}{\frac{1}{ImY_{idt}} - ReY_{idt}} \tag{A-6}$$

This configuration makes the meander ground a floating ground, and should give some improvement in resistive loss. This phasing topology is implemented in a wireless configuration by bringing the inductors to the backside of the antenna and having each antenna leg feed each group of the GUDT (Figure A-16).

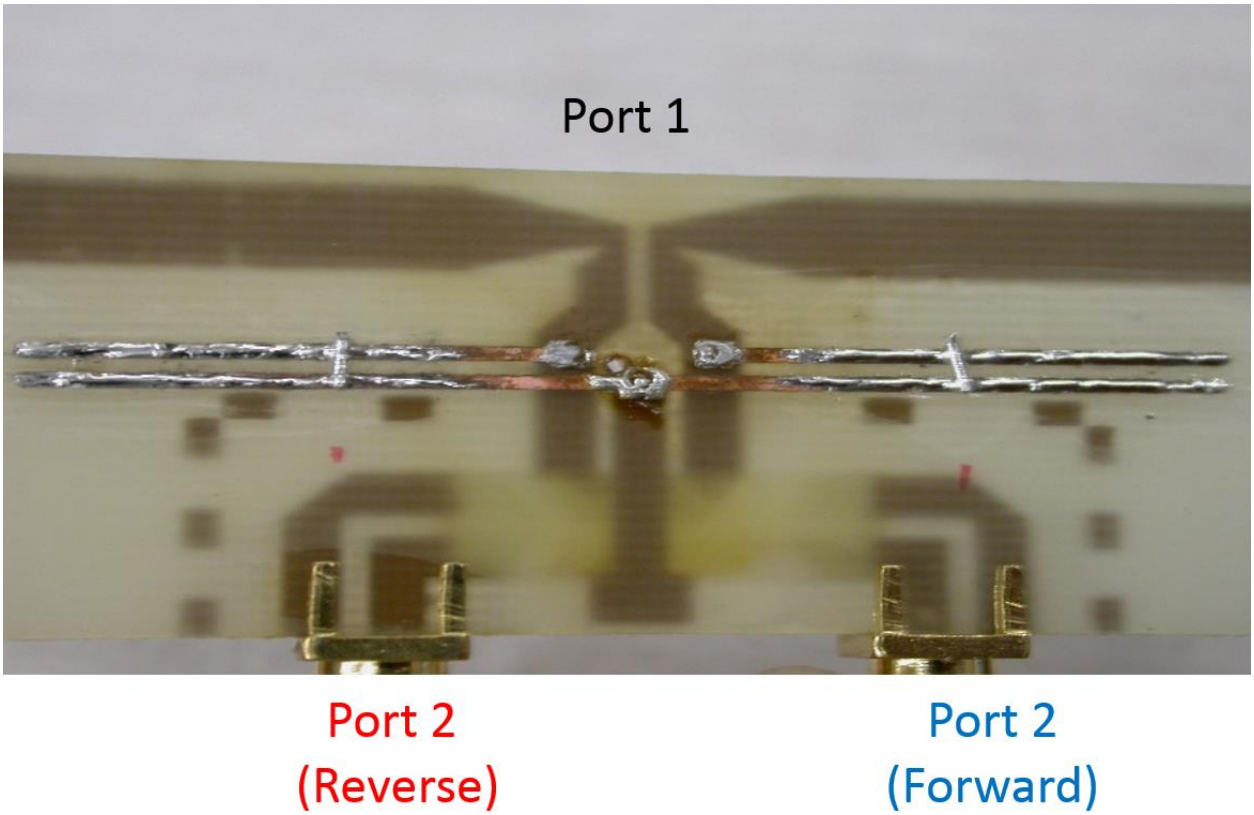

Figure A-16. Antenna implementation of phasing topology shown in fFigure A-15—inductors are placed on the reverse side.

The SMAs on the bidirectionals are left on the antenna for phasing purposes and to show the forward and reverse response characteristics of the GUDT. Figure A-17 below shows the response of the wireless operating GUDT. The 5pair wideband bidirectional only has a small effect on the shape of the group type response. The bidirectional is kept wired for phasing, but then would be disconnected and absorber placed on it, and SMA removed if desired.

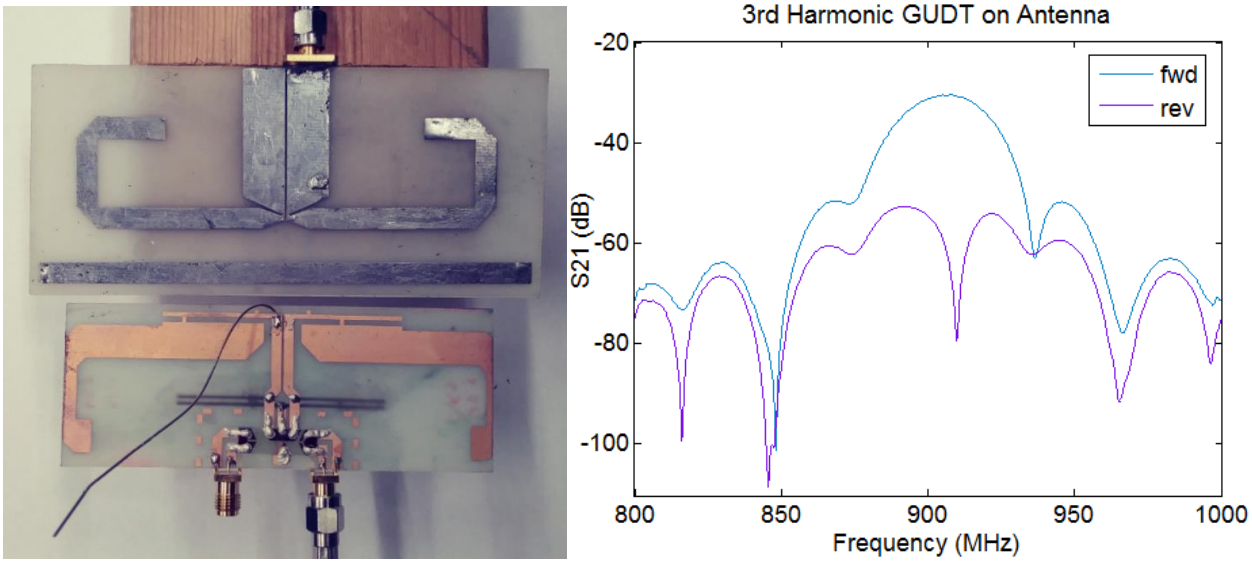

Figure A-17. Wireless GUDT operation showing the test setup (left) and the resulting forward and reverse response (right).

The direct response and triple transit echo levels, in frequency and time domain, for the device in Figure A-17 are shown in Figure A-18 below. The 50Ohm receive antenna in Figure A-17 was designed by Bianca Santos [61]. The arrows point to the direct and triple transit time domain echoes, other pulses are either bulk waves, edge reflections, or reflections from the second bidirectional.

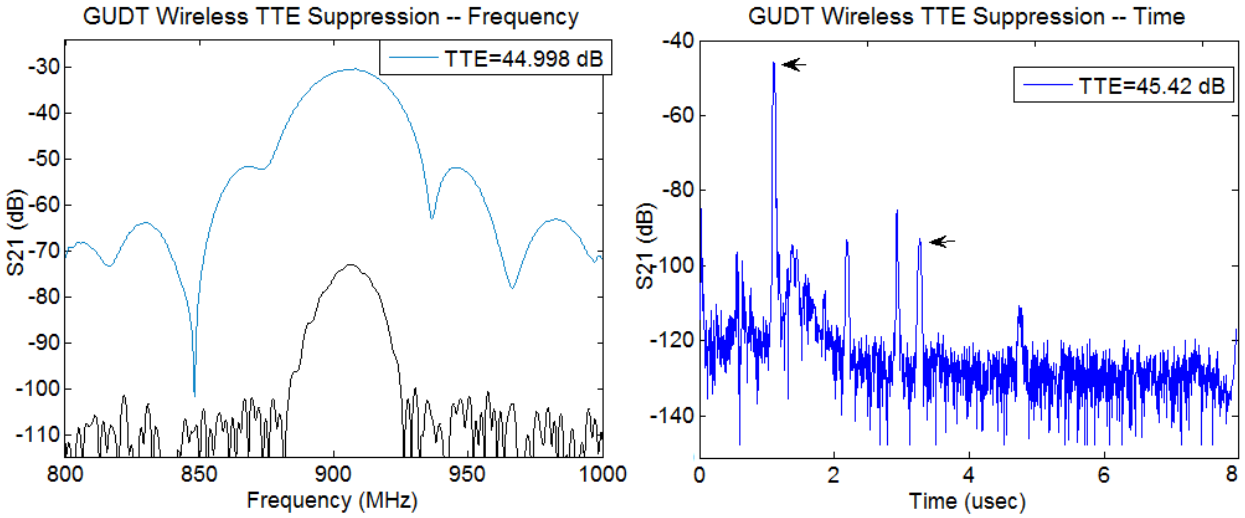

Figure A-18. Resulting frequency (left) and time domain (right) echo levels for the device in Figure A-17.

The echo suppression of this GUDT is not as good as that of the SPUDT. The level of TTE suppression is similar to that obtained by Malocha in [51] which showed a 44dB suppression. The TTE suppression of the device in Figure A-18 can be brought lower by increasing the mismatch, but this is not the idea behind echo suppression with the GUDT—the idea is to have a perfect match and perfect directionality in order to receive all of the energy from the direct response, at least at center frequency. For a better comparison to the SPUDT's echo suppression presented in chapters 6 and 7, a similar GUDT test device is fabricated, but one of the bidirectionals is replaced with a uniform reflector, the same design used for the uniform reflector in chapter 6 and 7.

The GUDT device with reflector has a bidirectional on one side in order to phase the GUDT. Then the GUDT is operated in S11 mode in order to see the double transit echo (DTE) suppression for better comparison with the SPUDT. The custom probe shown in Figure A-19 enables a preliminary test to see if the GUDT is working before bonding to test fixture, each leg is probed separately.

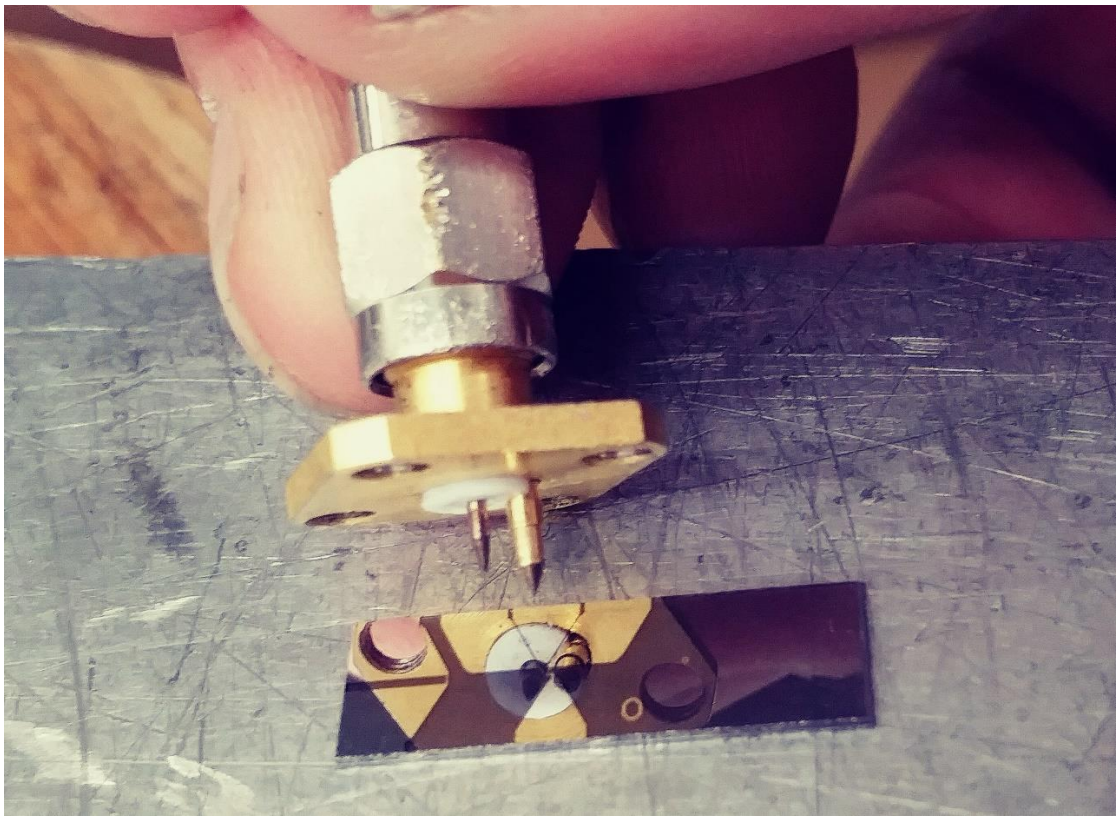

Figure A-19. Custom probe consisting of a pogo pin on the SMA ground, enables a preliminary test to see if the GUDT is working, each leg is probed separately.

There was only one fabrication run for this device, the reflectors were metalized at the same time as those of the WHL devices. The device has a bit of offset between the reflector and GUDT center frequency, skewing the reflector response. This may affect the best DTE suppression by a few dB, however, the GUDT was phased so that the reverse direction null does correspond to the peak of the reflector response. The device is phased by looking at the reverse S21 measurement as done before. The parallel PCB inductor on one side needed extra inductance so a wire inductor was added for phasing, shown in Figure A-20 below.

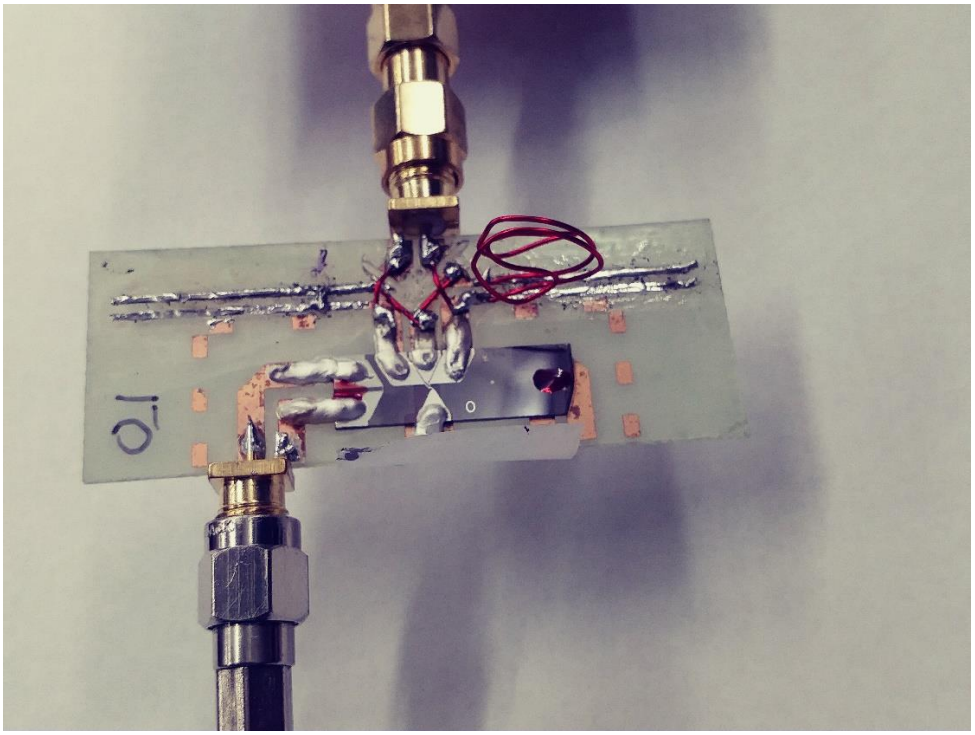

(a)

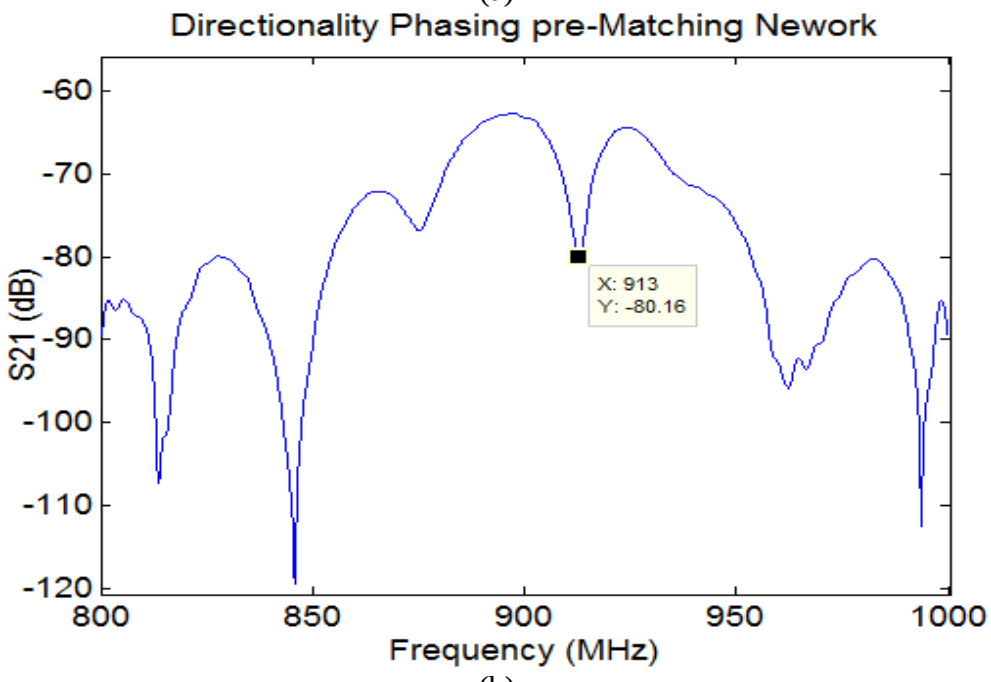

(b)

Figure A-20. (a) Test device having a wired bidirectional facing the reverse port of the GUDT and a uniform reflector on the right port. (b) Reverse response phased to place the null at the peak of the slightly skewed reflector response.

After phasing for center frequency directionality, a matching network was used to match the device for least insertion loss, which in theory would also correspond to best echo suppression in the ideal case of no bulk or other non-Rayleigh radiation and 100% conversion of electric to SAW energy at center frequency.

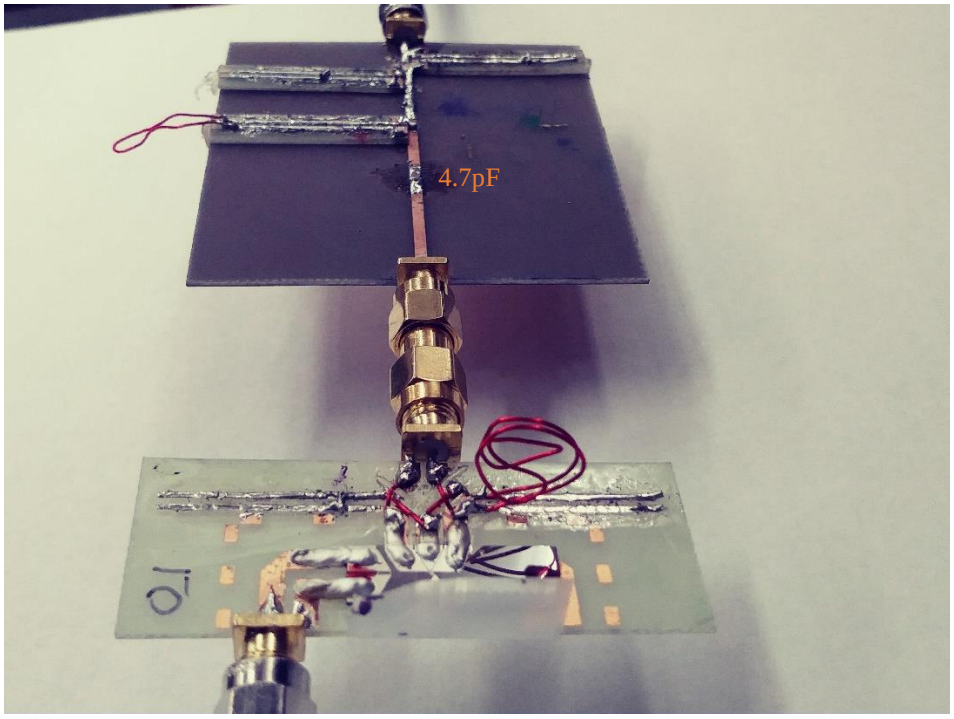

Figure A-21. GUDT connected to a tunable matching network and matched for least insertion loss by observing the polar S11 plot of Figure A-22

The resulting echo levels after matching are shown in Figure A-22.

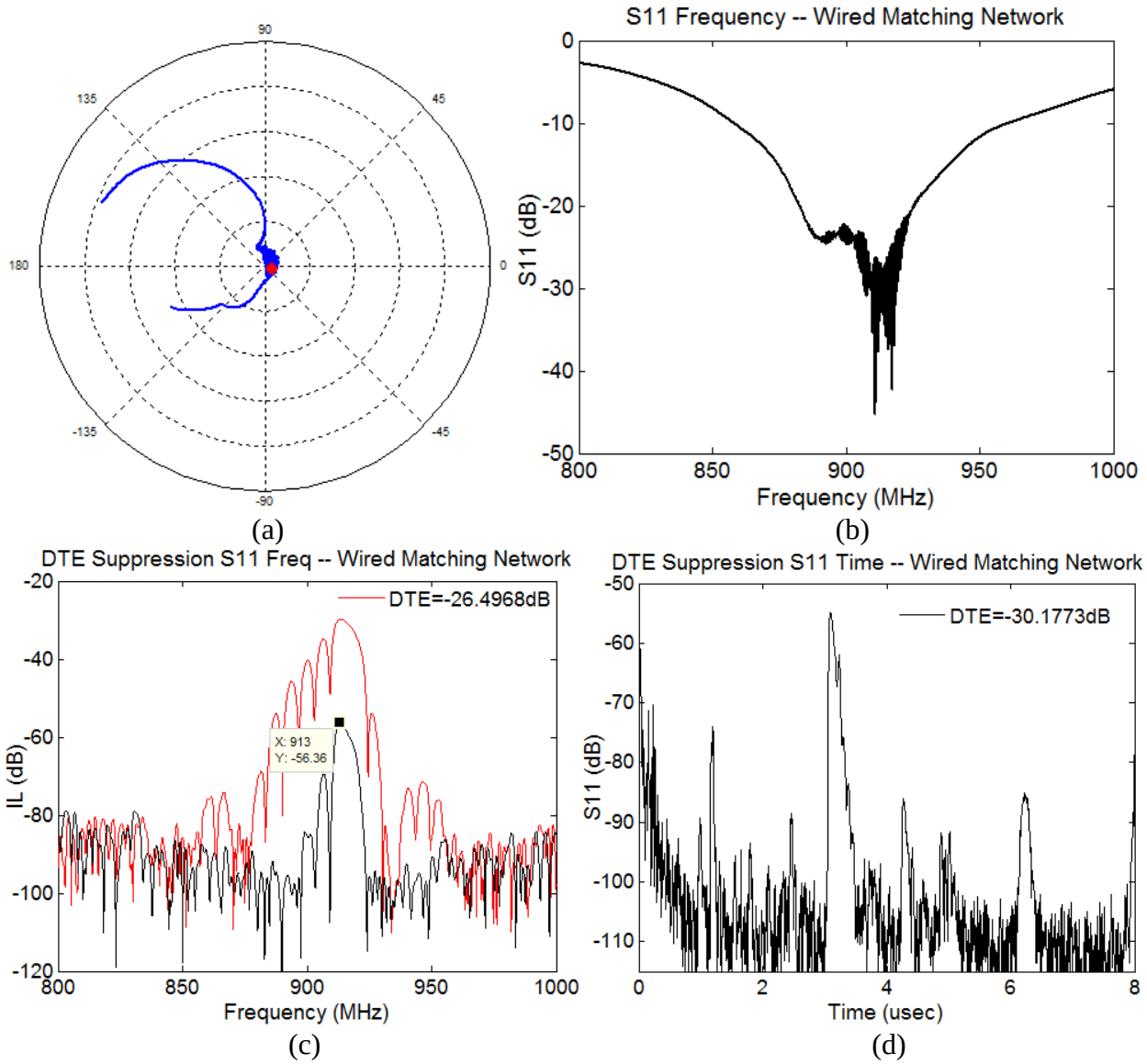

Figure A-22. Matched GUDT device, showing (a) polar and (b) magnitude of S11 in frequency. The (c) frequency and (d) time domain echo levels show that the echo suppression is not working that well.

The (c) frequency and (d) time domain echo levels show that the echo suppression is not working that well. It is highly suspected that the bulk radiation is affecting the acoustic port matching. With no bulk radiation, and a near perfect directionality at center frequency, there would be no energy left for the double transit echo at center frequency. The S11 response of Figure A-22 was then post-processed in order to optimize for echo suppression in the same way that was done for

the SPUDTs—by optimizing the characteristic impedance with a constant real and imaginary part and maximizing the ratio of the maximum of the direct response divided by the maximum of the DTE over the bandwidth. No constraints were placed on the real part of Z0.

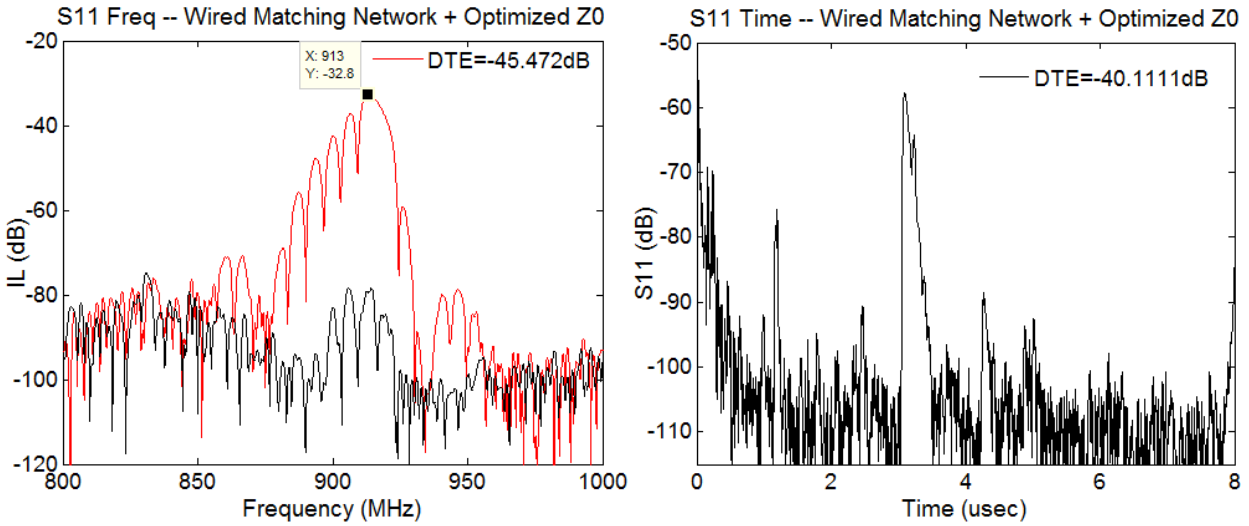

Figure A-23. (a) Frequency and (b) time domain echo levels after optimizing the real and imaginary part of Z0 for an optimized echo suppression level—Z0 = -11.2+j40.75.

The time domain echo suppression level is not measurable because it's below the noise floor. In order to achieve an optimized echo suppression, a characteristic impedance of Z0=-11.2+j40.75 Ohm is required. This is not realizable in a passive wireless sensor.

Based on these results the split-finger based GUDT is not good candidate for passive wireless echo suppression. A method for modeling the P-matrix of the phased GUDT with meander ground for COM model incorporation is given in Appendix F. Perhaps a hybrid SPUDT-GUDT would give better results.

APPENDIX B:
R-MATRIX FOR P-MATRIX CASCADE WITH ELECTRICAL SERIES CONNECTION

Consider the 3-port representation of a surface acoustic wave element in Figure B-1. This is the P-matrix, it's a mixed matrix with the acoustic ports in scattering form and the electrical port in admittance form.

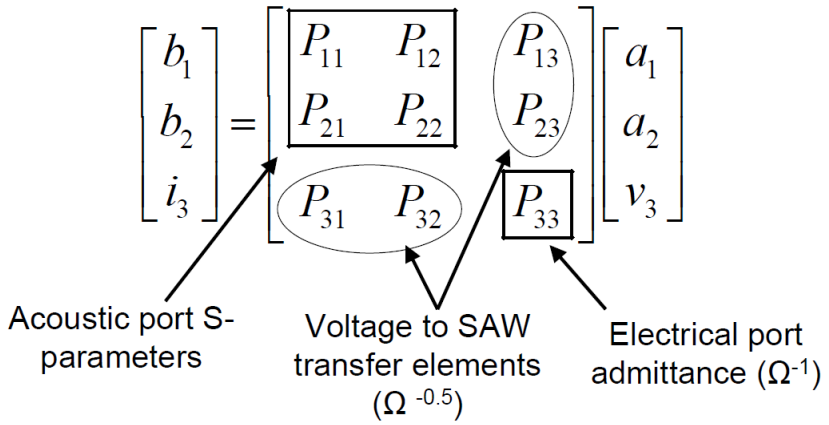

Figure B-1. The mixed P-Matrix description of 1 dimensional SAW structures with its entries grouped into like units. Image of D. Puccio, from Figure 4-4 of his dissertation [8].

The signal flow graph for obtaining the P-matrix elements in a parallel electrical connection (Figure B-2) is shown in Figure B-3.

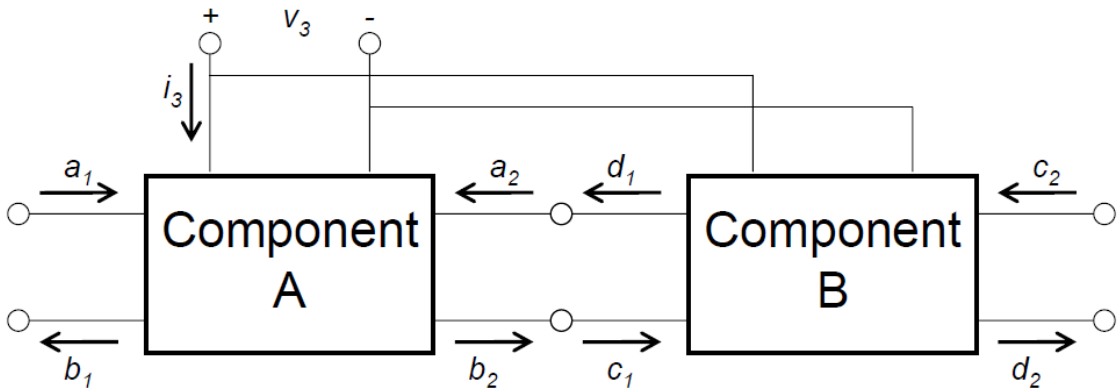

Figure B-2. P-Matrix cascade with parallel electrical connection. Image of D. Puccio, from Figure 4-5 of his dissertation [8].

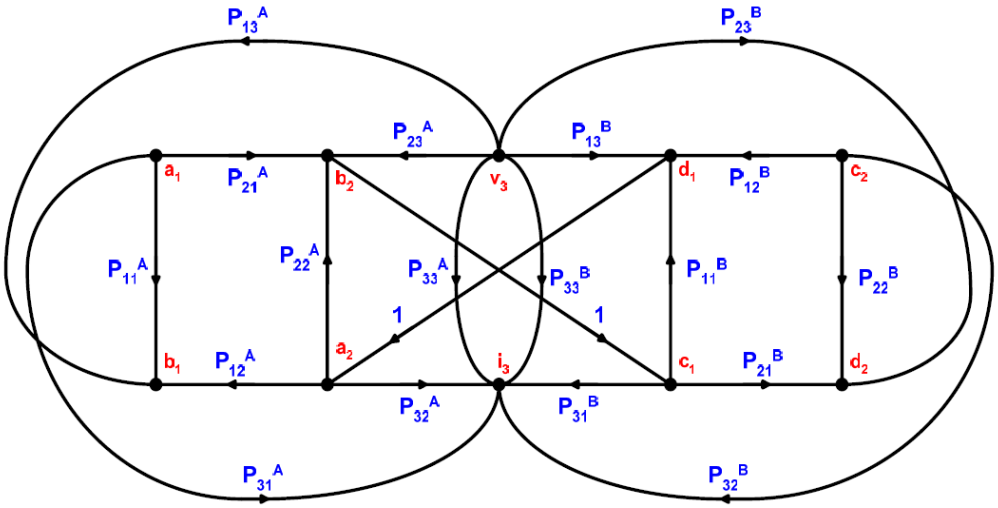

Figure B-3. Signal flow graph for P-Matrix cascade with parallel electrical connection. Image of D. Puccio, from Figure 4-6 of his dissertation [8]. Port 3 is the electrical port.

Using signal flow graph and Mason's Rule, the transformation equations can be obtained [8].

Now consider the series connection in Figure B-4.

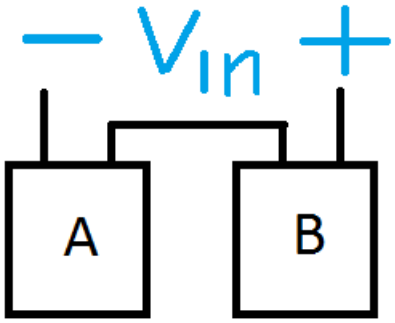

Figure B-4. Electrical series connection of 2 P-matrix elements in acoustic cascade.

Attempting to make a signal graph representation for this configuration will show that there are no signal paths joining V and I, so P33 can' be obtained. Inverting the P-matrix and interchanging the dependent and independent columns, [b1 b1 I] and [a1 a2 V], doesn't help either. Consider the signal flow graph of the inverse P-matrix representation in Figure B-5 (the notation shows $^{-}$I and $^{-}$Q labels instead of A and B.

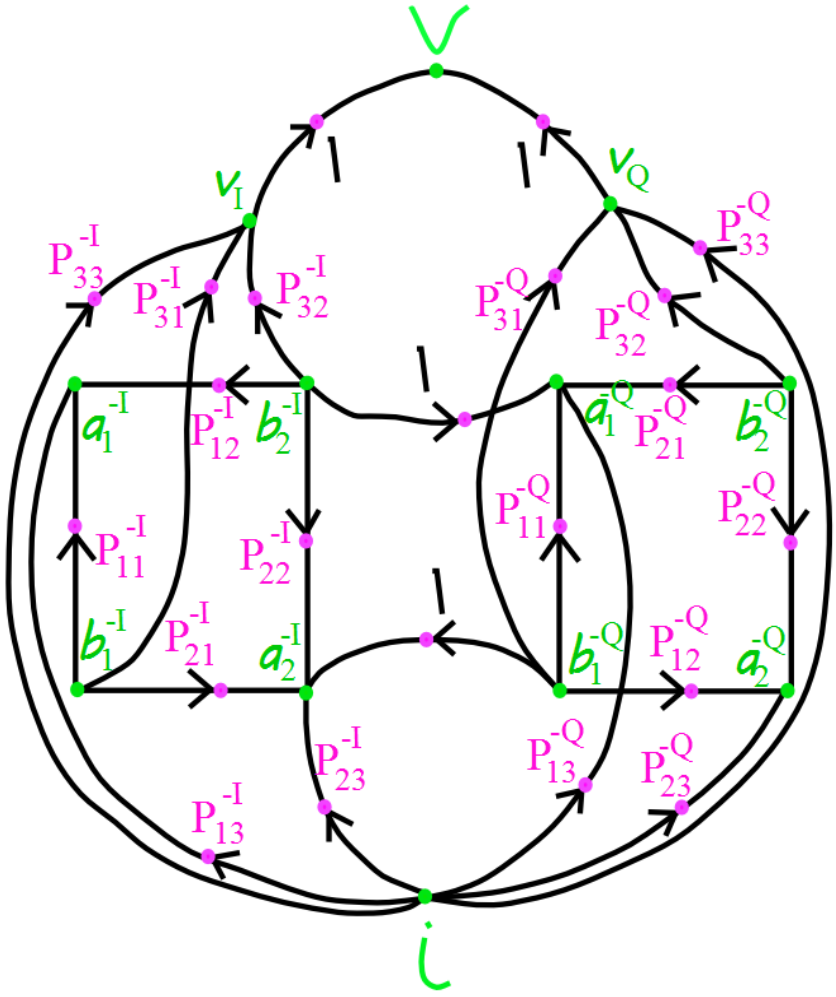

Figure B-5. Signal flow graph representation for an inverse P-matrix representation. Columns [b1 b1 I] and [a1 a2 V] are interchanged in the definition. It cannot be solved to get the transformation relationships since there is no path joining I and V.

There is no path joining I and V, so the transformation relationships can't be obtained directly by using Masons' Rule. However, if only V and I are interchanged, so that V becomes the depended variable and I the independent variable, the matrix obtained is shown in Figure B-6.

$$\begin{bmatrix} b_1 \\ b_2 \\ V \end{bmatrix} = \begin{bmatrix} R_{11} & R_{12} & R_{13} \\ R_{21} & R_{22} & R_{23} \\ R_{31} & R_{32} & R_{33} \end{bmatrix} \begin{bmatrix} a_1 \\ a_2 \\ I \end{bmatrix}$$

Figure B-6. R-matrix representation of SAW element. V and I are interchanged from the P-matrix definition.

The resulting R-matrix signal flow graph is give in Figure B-7.

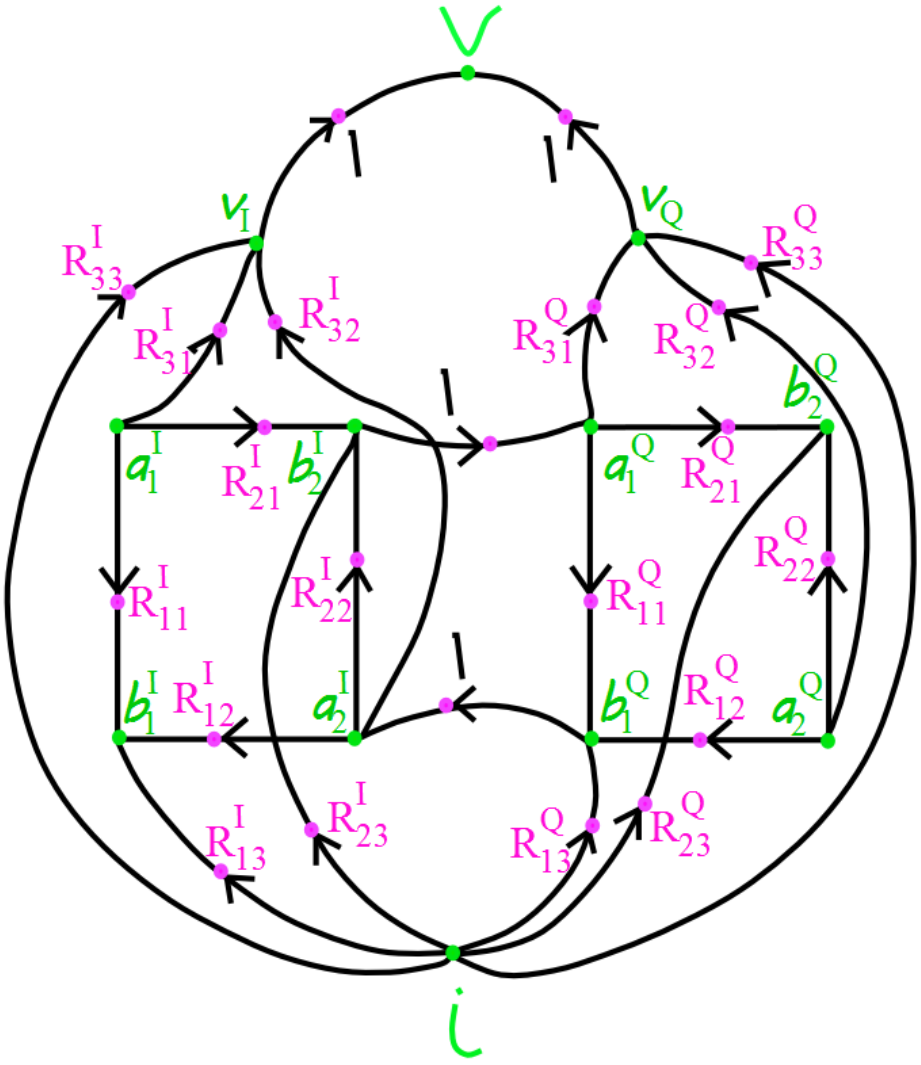

Figure B-7. Signal flow graph for R-matrix.

Solving the signal flow graph gives the R-matrix transformations in equations B-1 through B-11.

$$R11 = \frac{R21A * R11B * R12A + R11A * (1 - (R11B * R22A))}{-(R11B * R22A)} \quad \text{(B-1)}$$

$$R12 = \frac{R12B * R12A}{1 - (R11B * R22A)} \quad \text{(B-2)}$$

$$R13 = \frac{R13A * (1 - (1 * R11B * R22A)) + R13B * 1 * R12A + R23A * R11B * R12A}{1 - (1 * R11B * R22A)} \quad \text{(B-3)}$$

$$R21 = \frac{R21A * R21B}{1 - (1 * R11B * R22A)} \tag{B-4}$$

$$R22 = \frac{R12B * R22A * R21B + R22B * (1 - (R11B * R22A))}{1 - (R11B * R22A)} \tag{B-5}$$

$$R23 = \frac{R13B * R22A * R21B + R23A * R21B + R23B * (1 - (R11B * R22A))}{1 - (1 * R11B * R22A)} \tag{B-6}$$

$$R31 = \frac{R21A * R11B * R32A + R21A * R31B + R31A * (1 - (R11B * R22A))}{1 - (R11B * R22A)} \tag{B-7}$$

$$R32 = \frac{R12B * R22A * R31B + R12B * 1 * R32A + R32B * (1 - (R11B * R22A))}{1 - (R11B * R22A)} \tag{B-8}$$

$$Num1 = \mathrm{R13B} * \mathrm{R22A} * \mathrm{R31B} + \mathrm{R13B} * \mathrm{R32A} + \mathrm{R23A} * \mathrm{R11B} * \mathrm{R32A} \tag{B-9}$$

$$Num2 = \mathrm{R23A} * \mathrm{R31B} + \mathrm{R33A} * (1 - (\mathrm{R11B} * \mathrm{R22A})) + \mathrm{R33B} * (1 - (\mathrm{R11B} * \mathrm{R22A})) \tag{B-10}$$

$$R33 = \frac{Num1 + Num2}{1 - (R11B * R22A)} \tag{B-11}$$

Masons' rule is implemented using an open source program from Matlab file exchange to calculate the conversion parameters. The program is created by Rob Walton from TRLabs in the University of Calgary, Alberta, Canada.

The conversion parameters can then be performed with the transformations in Figure B-8.

$$\begin{bmatrix} b_1 \\ b_2 \\ V \end{bmatrix} = \begin{bmatrix} P_{11} - \frac{P_{13}P_{31}}{P_{33}} & P_{12} - \frac{P_{13}P_{32}}{P_{33}} & \frac{P_{13}}{P_{33}} \\ P_{21} - \frac{P_{23}P_{31}}{P_{33}} & P_{22} - \frac{P_{23}P_{32}}{P_{33}} & \frac{P_{23}}{P_{33}} \\ -\frac{P_{31}}{P_{33}} & -\frac{P_{32}}{P_{33}} & \frac{1}{P_{33}} \end{bmatrix} \begin{bmatrix} a_1 \\ a_2 \\ I \end{bmatrix}$$

Figure B-8. Transformation of P-matrix to R-matrix.

After performing the series connection R-matrix cascade, the R-matrix can be converted back to P-matrix parameters with the transformations in Figure B-9.

$$\begin{bmatrix} b_1 \\ b_2 \\ I \end{bmatrix} = \begin{bmatrix} R_{11} - \frac{R_{31}}{R_{33}} & R_{12} - \frac{R_{32}}{R_{33}} & \frac{R_{13}}{R_{33}} \\ R_{21} - \frac{R_{31}}{R_{33}} & R_{22} - \frac{R_{32}}{R_{33}} & \frac{R_{23}}{R_{33}} \\ -\frac{R_{31}}{R_{33}} & -\frac{R_{32}}{R_{33}} & \frac{1}{R_{33}} \end{bmatrix} \begin{bmatrix} a_1 \\ a_2 \\ V \end{bmatrix}$$

Figure B-9. Transformation of R-matrix to P-matrix

This may be applied to the meander-ground GUDT of Appendix A. Consider the schematic of the phased meander-ground GUDT in Figure B-10.

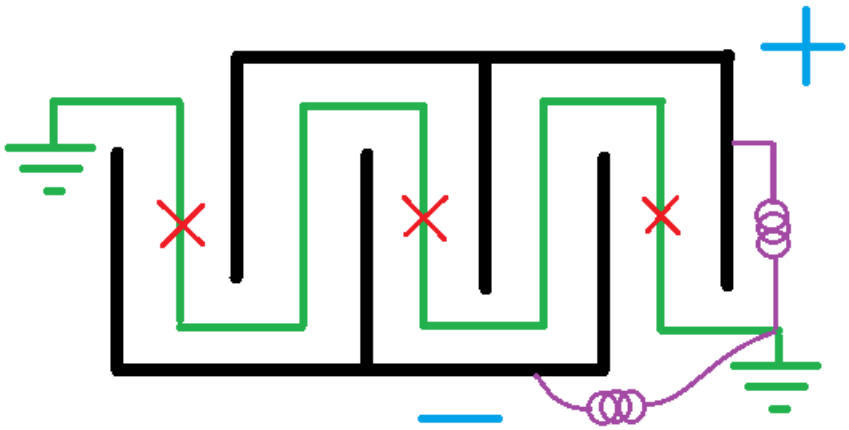

Figure B-10. Schematic of phased meander-ground GUDT. The x's correspond to the x's in Figure B-11.

If it is a reasonably good approximation to cut the floating meander ground in the location of the red x's, each inductor can be replaced with an individual inductor for each group with 1/3 the inductance. This is represented in Figure B-11; where the P-matrix blocks for each GUDT I and

Q groups are connected with separate inductors. The meander ground is cut at the locations with the red x's.

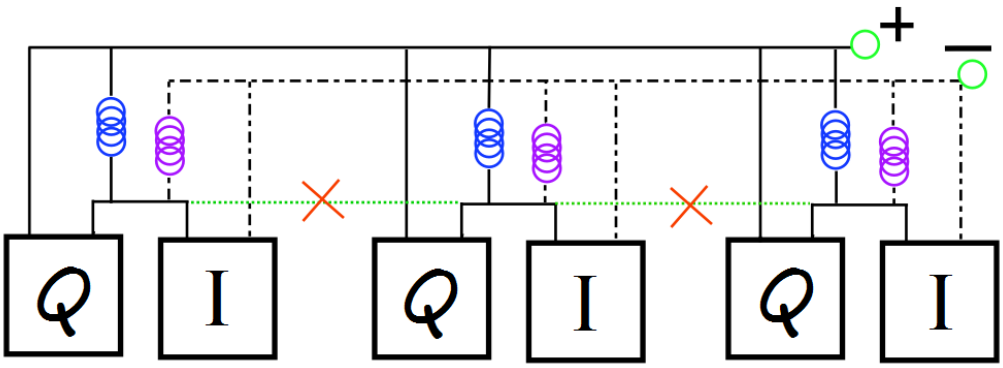

Figure B-11. P or R-matrix representation of a meander-ground GUDT. If the floating meander ground can be cut open at the red x's for modeling purposes, assuming that very little current passes through those points, the series cascade transformations presented in this appendix can be used to obtain the P-matrix of the device.

If this is a good approximation, the P-matrix of this device can be reduced to the series electrical connection of Figure B-4. Each inductor in Figure B-11 can be absorbed into P-matrix of the I or Q group it is attached to. Then the P-matrices are transformed to R-matrix, cascaded, and transformed back to P-matrix. The P-matrix of a meander-ground GUDT may be obtained in this fashion if opening the ground at the indicated locations is a valid approximation. This would be one possible way to model the meander-ground GUDT for anyone interested in doing so in the future.

APPENDIX C:
GREEN'S FUNCTION ANALYSIS OF PIEZOELECTRIC HALF SPACE USING QUASI-STATIC APPROXIMATION

This is a summary of Morgan's derivation of the SAW potential in the free-surface region, just beyond the IDT [62]. It is important to know the phase of this wave as a function of frequency. The result of this analysis provides this information, under certain approximations that are used by the derivation. The phase is of interest because if it's accurate enough, it can be used to help model the directionality of SPUDT transducers.

The potential and charge density at the surface of a piezoelectric half space is related by an effective permittivity, first by Ingebrigtsen, then Greebe et al. and Milsom et al. In the second edition of *Surface Acoustic Wave Filters* Morgan spends chapters 2, 3 and 5 delving in the subject of surface acoustic wave excitation described by the effective permittivity concept. It provides information about electrical parameters on the surface like charge density, electric potential and current as a result of IDT electrodes and their interaction with the acoustic wave being launched, even including bulk waves. It assumes infinitely thin electrodes with no resistivity and the effects of reflectivity ignored (although possible to introduce as shown in section 8.1.4 of Morgan's book). Morgan begins the development with the electric displacement field equations in the dielectric region and the free space region. With mechanical displacements and electric potential of the form $\exp(j\gamma z) \cdot \exp[j(wt + \beta x)$ and appropriate boundary conditions, the charge density in the electrode region can be found. A resulting effective permittivity is defined as

$$\varepsilon_S(\beta) = \frac{\bar{\sigma}}{|\beta|\bar{\Phi}(\beta)} \tag{C-1}$$

where ω is held constant, σ and Φ are the charge density and potential, respectively, and the line on top stands for Fourier transform in β domain. Since boundary conditions are usually expressed in the x domain, the relationship in equation D-1 is transformed into a Green's function

$$\bar{G}(\beta,\omega) = \frac{1}{|\beta|\varepsilon_S(\beta)} \tag{C-2}$$

$$G(x,\omega) = \frac{1}{2\pi}\int_{-\infty}^{\infty} \frac{\exp(j\beta x)}{|\beta|\varepsilon_S(\beta)}\, d\beta \tag{C-3}$$

The total Green's function, $G(x,w)$, includes an electrostatic term, a surface wave term and a bulk wave term.

$$\bar{G}(\beta,\omega) = \frac{1}{|\beta|\varepsilon_S(\beta)} \tag{C-4}$$

$$G(x,\omega) = G_e(x) + G_s(x) + G_b(x) \tag{C-5}$$

No bulk waves (or other non-Rayleigh waves) are assumed and the term drops out, so the surface potential is given in terms of the charge density as

$$\Phi(x,\omega) = [G_e(x) + G_s(x)] * \sigma(x,\omega) \tag{C-6}$$

with

$$G_e(x) = -\frac{\ln|x|}{\pi\varepsilon_\infty} \tag{C-7}$$

and

$$G_s(x) = j\Gamma_s \exp\left(-jk_f|x|\right) \tag{C-8}$$

Γ_s is an important constant related to the piezoelectric coupling. The development introduces Ingebrigtsen's approximation for $\varepsilon_S(\beta)$, which is appropriate when only a Rayleigh wave is

present. It is composed of $\varepsilon_\infty \equiv \varepsilon_S(\infty)$, and $k_f \; and \; k_m$, the free space and metalized surface wave numbers, respectively, giving the approximation

$$\varepsilon_S(\beta) \approx \varepsilon_\infty \frac{\beta^2 - {k_f}^2}{\beta^2 - {k_m}^2} \tag{C-9}$$

Based on differentiating equation C-9, Γ_s is simplified from

$$\frac{1}{\Gamma_s} = -k_f \left[\frac{\partial \varepsilon_S(\beta)}{\partial \beta}\right]_{k_f} \tag{C-10}$$

to

$$\Gamma_s \approx \frac{1}{\varepsilon_\infty} \frac{v_f - v_m}{v_f} \tag{C-11}$$

where the coupling coefficient K^2 used in the impulse response model [63, 64] is related to Γ_s as

$$K^2 = 2\varepsilon_\infty \Gamma_s \tag{C-12}$$

The quasi-static approximation is then introduced, which assumes the charge density $\sigma(x, \omega)$ is dominated by an electrostatic term $\sigma_e(x, \omega)$ when acoustic wave excitation is ignored (equation C-13).

$$\Phi_e(x, \omega) = G_e(x) * \sigma_e(x, \omega) \tag{C-13}$$

where $\Phi_e(x, \omega)$ is equal to the voltage on the electrode when x is on an electrode, and equal to 0 on free space regions—if the voltages are independent of ω, then $\sigma_e(x, \omega)$ is independent of ω. The quasi-static approximation gives

$$\Phi(x, \omega) = [G_e(x) + G_s(x, \omega)] * \sigma_e(x, \omega) + G_e(x) * \sigma_a(x, \omega) \tag{C-14}$$

where $\sigma_a(x, \omega)$ is a piezoelectric contribution because of acoustic waves—the $G_s(x, \omega) * \sigma_a(x, \omega)$ has term has been removed. Away from the electrodes the potential is due primarily to the surface

wave because electrostatic potentials are assumed to have died out, and therefore the surface wave potential is given by

$$\Phi_s(x,\omega) = j\Gamma_s\,\overline{\sigma_e}\left(k_f,\omega\right)\exp\left(jk_f\mathrm{x}\right) \tag{C-15}$$

for a left propagating wave. When the applied electrode potentials are known and assumed independent of ω (and therefore close to center frequency so the electrical network applies the same voltage), then equation C-15 can be solved for charge density $\sigma_e(x,0)$. Then taking the transform $\sigma_e(x,\omega)$ at $\omega = 0$ and using equation C-16, the potential of the traveling surface wave can be obtained for all ω.

This result leads to the point that needed to be emphasized; by knowing the electrostatic charge distribution, frequency response characteristics of the surface wave can be known. According to equation C-15, the Fourier transform of the charge distribution needs to be taken. The frequency component corresponding to the frequency of interest ($f = v\,k/(2\pi)$) determines the amplitude and phase of the wave's electric potential. The other factors in the equation are only constants. Thus given time reference and position reference, the charge distribution frequency component of interest gives the relative phase of the wave. For the purpose of applying this result to the TC-RC calculation, it is assumed that the phase of the SAW electric potential is in phase with the mechanical displacement of the SAW, either + or -. Otherwise some phase offset would be needed.

Appendix D attempts to use this result to give the phase of the transduction center for the TC-RC angular distance calculation.

An intuitive help for accepting the general idea of the term "quasi-static approximation" is that acoustic waves travel on the order of 4 orders of magnitude slower than the EM waves, so as

the acoustic wave travels, charge affected by the associated traveling E-field has time equilibrate. As a student it would be nice to have a visual aid accompany the equations and approximations that appear in Morgan's development of the quasi-static approximation for the Green's function of piezoelectric Rayleigh waves, and thus see (in time and frequency) what are the pieces of the puzzle as well as gauge what kind of errors are involved.

The fact that a zero frequency, electrostatic charge density determines the high frequency surface wave potential seems like a strange result. It may help to remember how electrostatic charge is related to capacitance, and capacitance is related to high frequency current as $I = j\omega CV$.

APPENDIX D:
DESIGN METHOD FOR SPUDT CELL DIRECTIONALITY AND COUPLING

The analysis presented in this appendix is an unfinished work. The aim is mainly to present the problem for anyone interested in predicting the directionality of a cell design by using the concept of a cell reflection center (RC) and a point source transduction center (TC). These are the two coupling-of-modes (COM) parameters that determine the directivity of a transducer. A coarse method of predicting these is shown in section D.1 and D.2, respectively. The RC and TC calculations need further work; both can be worked on separately and joined once sufficient accuracy is obtained.

Another aspect of transducer design is the electro-acoustic coupling. The coupling is approximated from the electrical Q of the transducer, which can be obtained from Fourier transform magnitude of the static the charge distribution. The theory for obtaining the coupling from the charge distribution is taken from Morgan's book [62]. The method for obtaining the charge distribution uses Lentine's matrix method. Matlab scripts used are attached as part of this electronic dissertation submission. Section D.3 shows how to approximate the relative coupling strength by use of the static charge distribution.

Section D.4 discusses an optimization that uses a dual objective in order to find an enhanced SPUDT cell layout. The idea is to estimate the RC-TC angular distance and reflectivity magnitude using the small reflections analysis and TC estimate discussed in sections D.1 and D.2, respectively. A directionality measure is defined and used as one of the objectives of the optimization. A second objective is introduced that simultaneously tries to optimize for a high effective coupling of the electrode layout.

The coupling part of the calculation works well, the TC-RC angle calculation does not. Based on an optimized coupling layout, a matrix of smaller shifts in electrode positions can be

carried out experimentally to possibly find a good TC-RC angle near the desired coupling characteristics. This part-experimental approach is successfully used to find an enhanced SPUDT layout for both 1st and 3rd harmonic operation (shown in Appendix E and chapter 4). It has improved coupling and directionality at 3rd harmonic, and improved directionality with slightly less coupling at 1st harmonic. The reader is also directed to an enhanced SPUDT design by J. Galipeau. He uses a FEM/BEM based optimization scheme for enhancing a 1st harmonic SPUDT [65] that is quite accurate. His design moves the thick ground electrode left, the optimized design presented in chapter 5 moves it right.

D.1 Reflection Center from Small Reflections Theory

In seeing how the unidirectional behavior is essential to efficient suppression of multiple transits, whether this is for use in a 2 port SAW filter or a 1 port IDT-reflector device, it is important to understand the basic building block of the SPUDT and how the unidirectionality comes about. A straightforward and simple way to describe this is through the theory of small reflections in order to model the electrode reflections. Consider a wave on a transmission line encountering a finite section with different velocity. Multiple reflections will take place within the center region as depicted in Figure D-1.

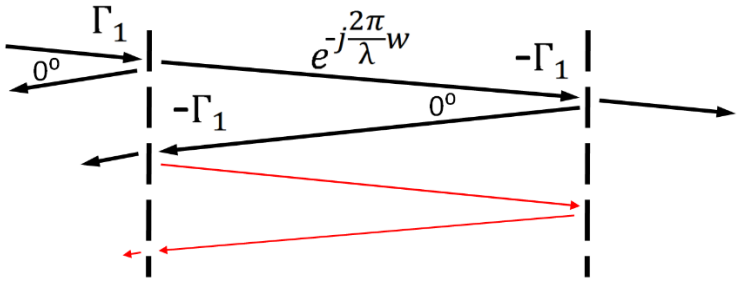

Figure D-1. Multiple reflections as a wave enters a different velocity medium, the time axis is downward. The red transits and reflections are ignored in the theory of small reflections approximation.

The theory of small reflections basically assumes a couple of things about transmission and reflection when the wave velocity discontinuity is small. One being that since the reflected wave is small compared to the transmitted wave, then lossless transmission can be assumed. In the analysis to come, regarding transducer electrodes, not even the loss due to the 1st two edge reflections will be subtracted from the transmitted wave amplitude. The second assumption is regarding the reflected wave. The multiple transits in the finite region after the 2nd are ignored, illustrated in Figure D-1 as the red arrows. The reflected wave is assumed to be composed of the sum of the 1st reflection Γ_1, and the transmission resulting from the back edge reflection, $-\Gamma_1 e^{-j\frac{2\pi}{\lambda}2w}$, where w is the width or length of the finite region. Using this model the net reflection encountered by the generated wave inside the SPUDT cell can be approximated to 1st order. An advantage of the simplification is that individual electrode contributions can be treated independently of the rest, making it easier to represent visually. Consider the reflection off a single reflector as shown in Figure D-2.

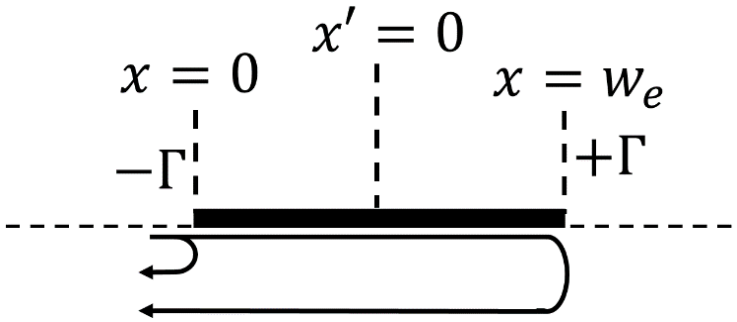

Figure D-2. Single electrode effective reflection coefficient referenced to center of electrode. Modeled by adhering to the theory of small reflections and using only real reflections at the edges without taking into account stored energy effects.

The single edge reflection coefficient is negative when going from free surface to electrode when the velocity under the electrode is slower than the free surface. After factoring out an exponential, the equation describing the two-edge reflection is given by

$$-\Gamma + \Gamma e^{-jk_x 2w_e} = \frac{-\Gamma e^{-jk_x w_e} 2j(e^{jk_x w_e} - e^{-jk_x w_e})}{2j} \tag{D-1}$$

where Γ is assumed positive and the sign assumes a slower velocity electrode region. Recognizing the sine term and shifting reference to x'=0, the single reflector reflection coefficient is written as

$$-2\Gamma j sin(k_x w_e) \tag{D-2}$$

This equation shows that the reflection coefficient can be referenced to the center of the electrode, with the phase of -90^0. The maximum amplitude of 2Γ occurs when the width of the electrode is $\frac{\lambda}{4}$.

The concept of the SPUDT operation is based on an electrode layout that will couple wave energy from one direction to the other, with preference to one direction—the forward direction. Two basic mechanisms are taking place within the transducer—transduction and reflection. Transduction, or wave generation, is assumed to occur somewhere within the transducer cell as if it was a point source. At center frequency these point sources are synchronous—the wavelength

is equal to the transduction period, or cell length. The transducer is assumed to be infinite so that end effects don't affect the assumption of periodicity. A single cell can be directly analyzed to observe how the wave is coupled from one direction to another, and in what proportion. The point source, or transduction center, will be sending waves out in both directions. A cell is analyzed by 1st launching the wave in one direction. The effective reflection coefficient of the cell is calculated at the transduction center for that particular direction—then the other. For illustration it helps to start with a bidirectional IDT that is symmetric. The center of the hot electrode is a convenient location for the transduction center, the other choice would be the center of the gap—it has to be at a point of symmetry since the bidirectional IDT is symmetric. A reference of 0^0 is placed at the point source on the center of the hot electrode—for each direction. It is convenient to define the IDT cell from center to center of hot electrode for later comparisons with the asymmetric electrode layouts of the SPUDT. At center frequency it's equivalent to split the hot electrode and place one of its edges 1 transduction period away so it falls within the cell. This is illustrated in Figure D-3

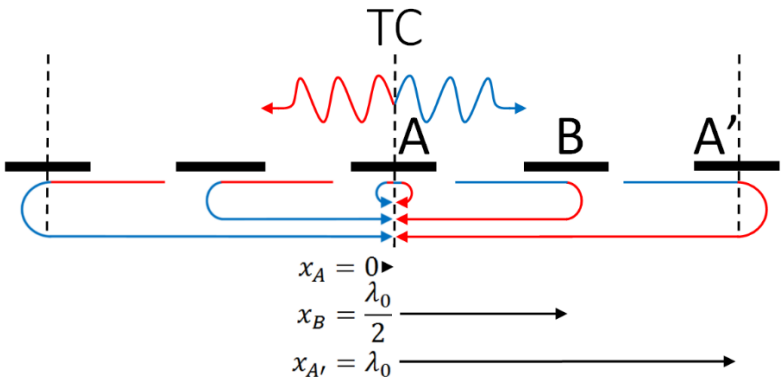

Figure D-3. Illustration of modeling the effective cell reflection coefficient of a 2f0 bidirectional. A wave is launched in both directions over a transduction period and the reflection coefficient phasor is calculated at the transduction center.

Waves are launched in both directions, blue right and red left. The electrode edge reflections are combined into 1 effective reflection at the electrode center. Electrode reflections are handled one at a time and then superimposed—no multiple reflections between electrodes are assumed. The resulting effective cell reflection coefficient in both the right and left direction is

$$\Gamma_{R2L} = -\frac{1}{2}2\Gamma j \sin(k_x w_A)\, e^{-jk_x 2x_A} - 2\Gamma j \sin(k_x w_B)\, e^{-jk_x 2x_B} - \frac{1}{2}2\Gamma j \sin(k_x w_{A'})\, e^{-jk_x 2x_{A'}}$$
$$= \Gamma_{L2R} = -4\Gamma \mathrm{j} \qquad \text{(D-3)}$$

The subscript "R2L" is used because Γ_{R2L} couples right propagating waves to the left direction. To maintain the systematic approach of combining the 2 edge reflections into a single effective reflection at the center, the contribution from the hot electrodes is multiplied by $\frac{1}{2}$. The resulting effective cell reflection coefficient of -4Γj shows that the reflected wave adds in quadrature, -90^0 $\left(-\frac{\lambda_0}{4}\right)$, with respect to the wave being generated in the left direction by the transduction center. The same is true for the other direction, Γ_{L2R}, since the cell is symmetric—therefore no net amplitude gain in either direction. A term very often found in literature regarding SPUDTs is the term "Reflection Center (RC)." One would think this is the location where the effective cell reflection coefficient has an angle of 0^0 with respect to the TC, but this is not the case. The reflection center is the location where effective cell reflection coefficient has an angle equal to that of the single electrode, an angle of -90^0. This definition of reflection center is inferred from the statements in literature that for proper SPUDT operation, the 1-way distance between TC and RC is $\frac{\lambda_0}{8}$ [66-68]. The reflection

center for bidirectional IDTs thus coincides with the transduction cernter. The -90^0 RC condition is actually found in two locations within the cell—because of the round trip the RC is technically also found half a wavelength away, whichever direction falls inside the cell.

Under the simplification of small reflections, the RC for ideal SPUDT operation is $\frac{\lambda_0}{8}$, which is the value normally quoted in literature and to be calculated shortly. Next consider the asymmetric cell structure of a type of SPUDT cell—the electrode width controlled (EWC). Figure D-4 shows two EWC SPUDT cells with the hot electrode in the middle. The width of the thick ground is $\frac{\lambda_0}{4}$ and the rest of the electrodes are $\frac{\lambda_0}{8}$. For now it is assumed that the transduction center coincides with the middle of the hot electrode, and it's not a bad approximation according to experimental results to be shown later. A method to approximate the transduction center is given in the next section. The calculations for RC can be set up and performed with the current TC assumption and then simply shifted to the correct TC location.

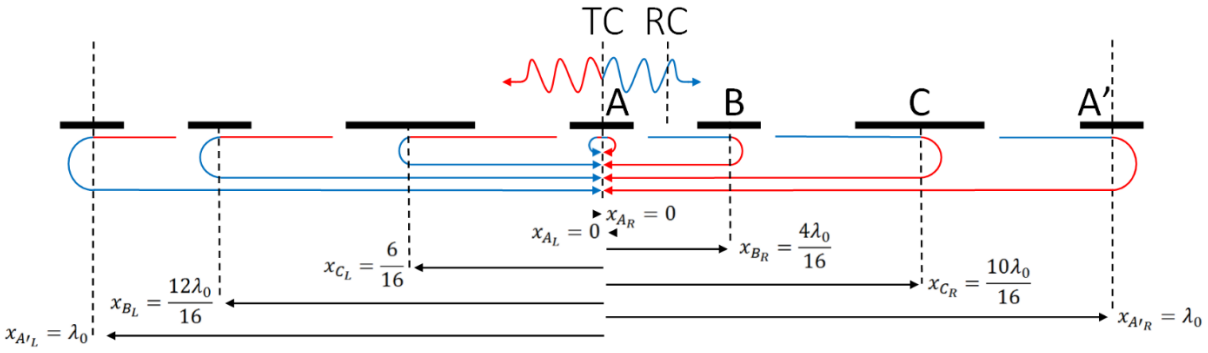

Figure D-4. Illustration of modeling the effective cell reflection coefficient of an EWC SPUDT cell. A wave is launched in both directions over a transduction period and the reflection coefficient phasor is calculated at the transduction center.

The two EWC SPUDT cells in Figure D-4 show the reflected wave contribution to the generated wave in each direction. The effective cell reflection coefficient at the transduction center for each direction is calculated as

$$\Gamma_{\mathrm{R2}L} = -\frac{1}{2}2\Gamma j\sin(k_x w_A)\,e^{-jk_x 2x_{A_R}} - 2\Gamma j\sin(k_x w_B)\,e^{-jk_x 2x_{B_R}} - 2\Gamma j\sin(k_x w_C)\,e^{-jk_x 2x_{C_R}} - \frac{1}{2}2\Gamma j\sin(k_x w_A)\,e^{-jk_x 2x_{A'_R}} = -2\Gamma \quad \text{(D-4)}$$

$$\Gamma_{\mathrm{L2}R} = -\frac{1}{2}2\Gamma j\sin(k_x w_A)\,e^{-jk_x 2x_{A_L}} - 2\Gamma j\sin(k_x w_B)\,e^{-jk_x 2x_{B_L}} - 2\Gamma j\sin(k_x w_C)\,e^{-jk_x 2x_{C_L}} - \frac{1}{2}2\Gamma j\sin(k_x w_A)\,e^{-jk_x 2x_{A'_L}} = 2\Gamma \quad \text{(D-5)}$$

The negative sign on $\Gamma_{\mathrm{R2}L}$ indicates that the reflected wave adds out of phase with the left propagating wave. The positive sign on $\Gamma_{\mathrm{L2}R}$ indicates that the reflected wave adds in phase with the right propagating wave. Right is the forward direction.

By moving the reference plane of the TC from the center of the hot electrode to the location where angle of $\Gamma_{\mathrm{R2}L}$ or $\Gamma_{\mathrm{L2}R}$ equal -90^0, the RC is found. Equation D-6 shows $\Gamma_{R2L(L2R)}$ being shifted from the center of hot electrode by the unknown 1-way angular distance $\Delta\theta_{TC2RC}$. Solving equation D-6 for $\Delta\theta_{TC2RC}$ gives the distance from TC to RC—for $\Gamma_{\mathrm{R2}L}$ it is to the right and for $\Gamma_{\mathrm{L2}R}$ it is to the left

$$\Gamma_{R2L(L2R)}e^{+j2\Delta\theta_{TC2RC}} = \left|\Gamma_{R2L(L2R)}\right|e^{-j\frac{\pi}{2}} \quad \text{(D-6)}$$

Solving for $\Delta\theta_{TC2RC}$ gives the distance from TC to RC—for $\Gamma_{\mathrm{R2}L}$ it is to the right and for $\Gamma_{\mathrm{L2}R}$ it is to the left. Locations $\frac{\lambda_0}{2}$ apart within the cell are equivalent because of the round trip and thus it turns out to be the same location for both directions. Calculating the RC is important because the coupling of modes (COM) model uses the RC angle as the reflection coefficient angle.

This analysis is extended to 3rd harmonic by multiplying the propagation constant by 3—replacing k_x by $3k_x$ in equations D-4 and D-5 above. Performing this analysis at the 3rd harmonic shows that the effective cell reflection coefficient is the same in both magnitude and direction—and thus the EWC SPUDT electrode layout can be operated at 3rd harmonic. The same analysis for the DART SPUDT which has a $\frac{3\lambda_0}{8}$ wide thick ground electrode shows that the direction changes from 1st to 3rd harmonic, but the effective reflection magnitude is $\sqrt{2}\Gamma$ instead of 2Γ. Besides the better directionality of the EWC over the DART according to this analysis, the thinner electrode gives more room to optimize the electrode. Also to mention is that the electrode reflectivity model is simplified, I have not properly experimentally compared the EWC versus DART effective electrode reflection coefficient. The phasor representation of the individual electrode contributions of the EWC SPUDT cell is shown in Figure D-5.

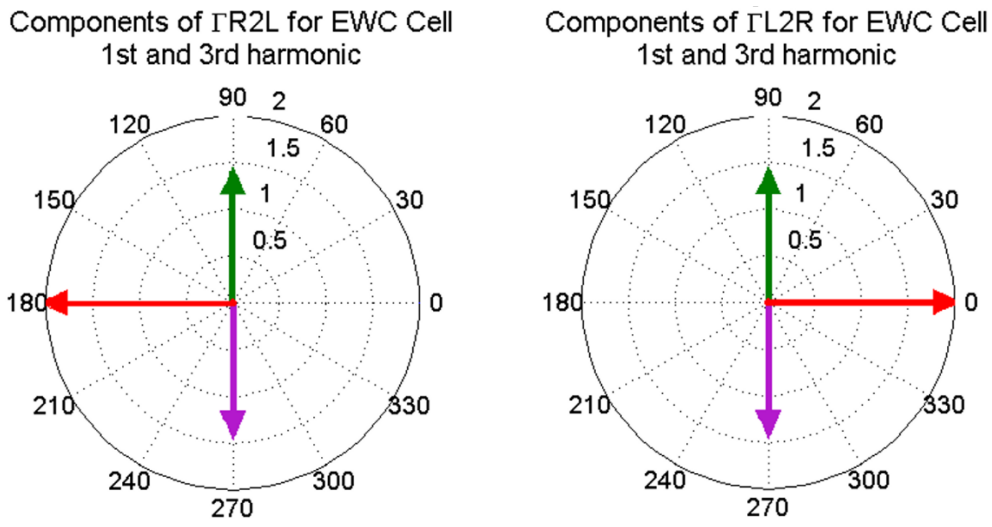

Figure D-5. Individual phasor components of the effective cell reflection coefficient, ΓR2L and ΓL2R. Each arrow corresponds to the reflectivity phasor of each electrode in a cell or transduction period. The thin electrodes cancel, leaving the resultant as the contribution of the thick ground electrode. The contribution of ΓL2R adds in-phase and ΓR2L adds out of phase.

The phasors of the individual electrode reflections show that the two thin electrodes cancel each other, leaving the resultant as only the contribution of the thick ground electrode.

Besides the small reflections assumption, the single electrode reflectivity model is simplified because a stored energy effect at the edges of the electrodes was not taken into account. This stored energy effect was modeled as a reactive impedance term by Li and Melngailis, Wright, and Saldanha et al. 3 [38, 69-71]. Starting with a lower frequency characterization having more accurate geometries, and also varying electrode thickness from low reflectivity to high reflectivity might be a place to start for someone wanting to better characterize and improve the model presented here.

The next section presents a SPUDT modeling method to approximate the true transduction center.

D.2 Transduction Center from Electrode Charge Distribution

Knowledge of the transduction center is required to give a reference to the effective reflection coefficient calculation. The TC-RC angular distance is the COM parameter that determines directionality. For modeling transducers with uniform SPUDT sections, the TC-RC angular distance can be substituted into the reflectivity phase, with the transduction coefficient left at zero phase. If the IDT is formed from sections containing different types of cells, then the TC-RC distance cannot be lumped into reflectivity phase; the TC and RC angles would have to be kept separate to give the appropriate transduction phase offsets between groups of cells.

A method to estimate the TC of an arbitrary SPUDT cell is presented in this section. It is divided into 2 parts:

(1) A theoretical approximation based on a Green's function analysis that implies the following: the phase of the wave generated by and IDT is proportional to the phase of the static charge distribution Fourier Transform, at the frequency of interest.

$$\Phi_s(x,\omega) = j\Gamma_s\,\overline{\sigma_e}\left(k_f,\omega\right)\exp\left(jk_f\mathrm{x}\right) \tag{D-7}$$

$\Phi_s(x,\omega)$ is the electric potential of the SAW, Γ_s is proportional to the coupling coefficient, k_f is the free-surface wave number, and $\overline{\sigma_e}\left(k_f,\omega\right)$ is the Fourier Transform of the electrostatic charge distribution. Therefore, the TC (the unperturbed/free-surface SAW 0^0-phase reference) in the RC-TC calculation is equated to the phase of the static charge distribution's Fourier Transform—after shifting to a reference position, obtained from a reference bidirectional transducer calculation. A summary of equations and arguments used by D. Morgan in the approximation of D-21 is given in appendix C, as a summary of the explanation presented in the book *Surface Acoustic Wave Filters* by David Morgan [62].

(2) A way of generating the static charge distribution of an arbitrary IDT cell in order to obtain the phase of a SPUDT cell at center frequency; at center frequency the TC of all cells are synchronized. The TC-RC angular distance is approximated as constant over frequency, in this analysis, and in chapter 5 when using this parameter in COM simulations. Some comments on extending as a function of frequency are given at the end of this appendix.

Based on Greens' function analysis of a piezoelectric half-space and the quasi-static approximation [62], the center frequency component of the Fourier transform of the charge distribution for the SPUDT cell is used to give the phase of the transduction center. Absolute

quantities are not necessary. The reference phase of 0^0 is obtained from the cell of a bidirectional IDT that is known to be 0^0. First the charge distribution of a single cell of a bidirectional IDT is Fourier transformed. The spatial offset of the distribution is then adjusted so that the FFT gives a 0^0 phase for the center frequency component—the starting point of the cell turns out to be the center of the hot electrode. In order to obtain the correct TC phase for the SPUDT cell, it will also start from center of hot electrode and end at the center of the next hot electrode. The phase of the center frequency component will be regarded as the TC phase for the SPUDT cell.

In obtaining the SAW potential from equation C-15 there are many assumptions, starting with no reflectivity (which the design is actually trying to increase). Also, no bulk or other wave modes besides the Rayleigh wave are assumed. No mechanical loading of the finite-thickness electrodes is assumed.

The method used for obtaining the charge distribution was developed by A. Lentine. It is also referred to here as Lentine's matrix method, for calculation of the charge distribution and voltage potential distribution on arbitrarily spaced electrodes. It is a 1-dimentional model that assumes infinitely thin electrodes with perfect conductivity. The model works by sampling both the electrode and gap region with tiny electrodes. In the electrode region the tiny sampling electrodes are connected with perfect wires. In the gap region the sampling electrodes are connected with perfect capacitors. The capacitance relationship for electrodes having a 50/50 width to gap ratio is known. From this relationship, and a known voltage applied to the sampling electrodes in the actual electrode region, the equation Q=CV can be solved. A matrix equation is written which includes the Q=CV relationship of N nearest neighbors, thus a sampled charge distribution is obtained. A simplified explanation that uses a graphical aid and visually shows the

matrix equation setup is shown in Appendix G. The resulting calculation of the charge distribution is shown for the 4f0 bidirectional and the EWC SPUDT cell in Figure D-6 and Figure D-7, respectively. The phase of the center frequency component of the EWC SPUDT cell charge distribution shows that the starting assumption of keeping the TC at the center of the hot electrode was not too bad of an assumption. Since the hot electrode is split, the cell will begin in the middle of the two hots. The graph of the charge distribution plots the total charge in each of the equally spaced sampling locations. Therefore in order to find the total charge on an electrode, the individual charges need to be added in that region. For this reason the Figure legend says the number of points used for the given cell. By knowing the width of an electrode and the number of points in the cell, the total charge on an electrode, per unit beamwidth, can be calculated. To save some time to anyone interested in obtaining these values, the Matlab script used to is attached as part of this electronically submitted dissertation.

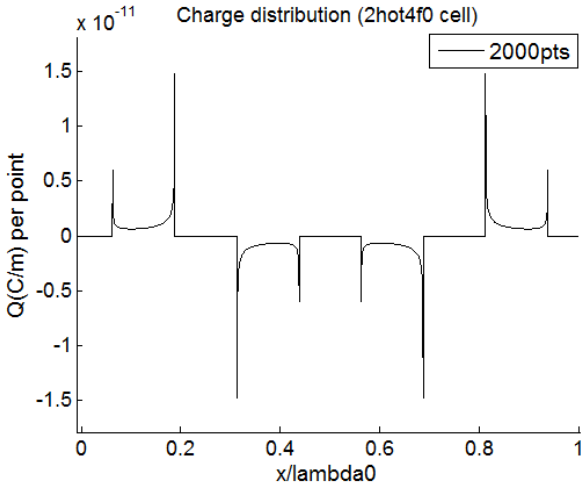

(a)

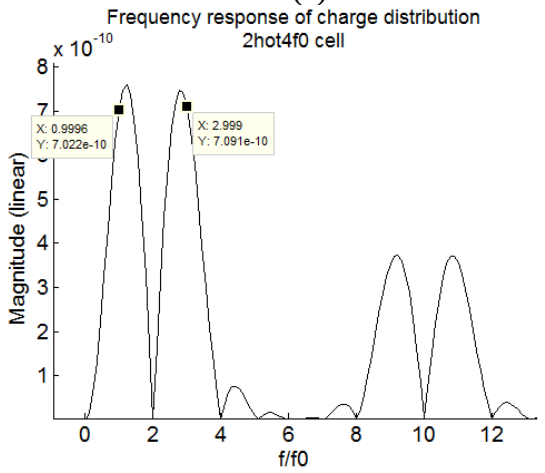

(b)

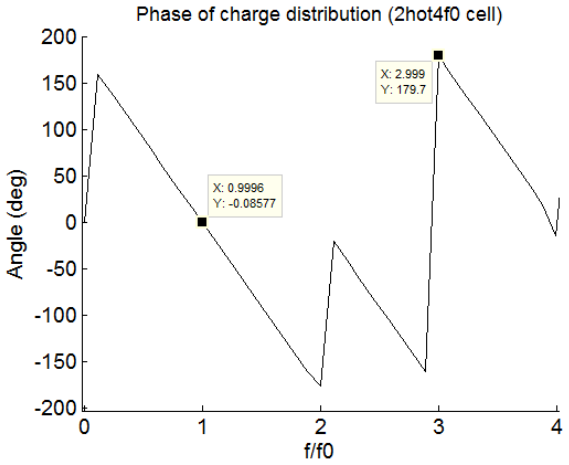

(c)

Figure D-6. (a) Charge distribution of a 2hot4f0 bidirectional IDT cell. (b) Fourier Transform (FT) of 2hot4f0 cell charge distribution—magnitude. (c) Phase of 2hot4f0 cell charge distribution FT. A voltage of +/- 1/2V is placed on the electrodes in order to generate these values—the total (+) charge of (a) 5.6504e-10C/m

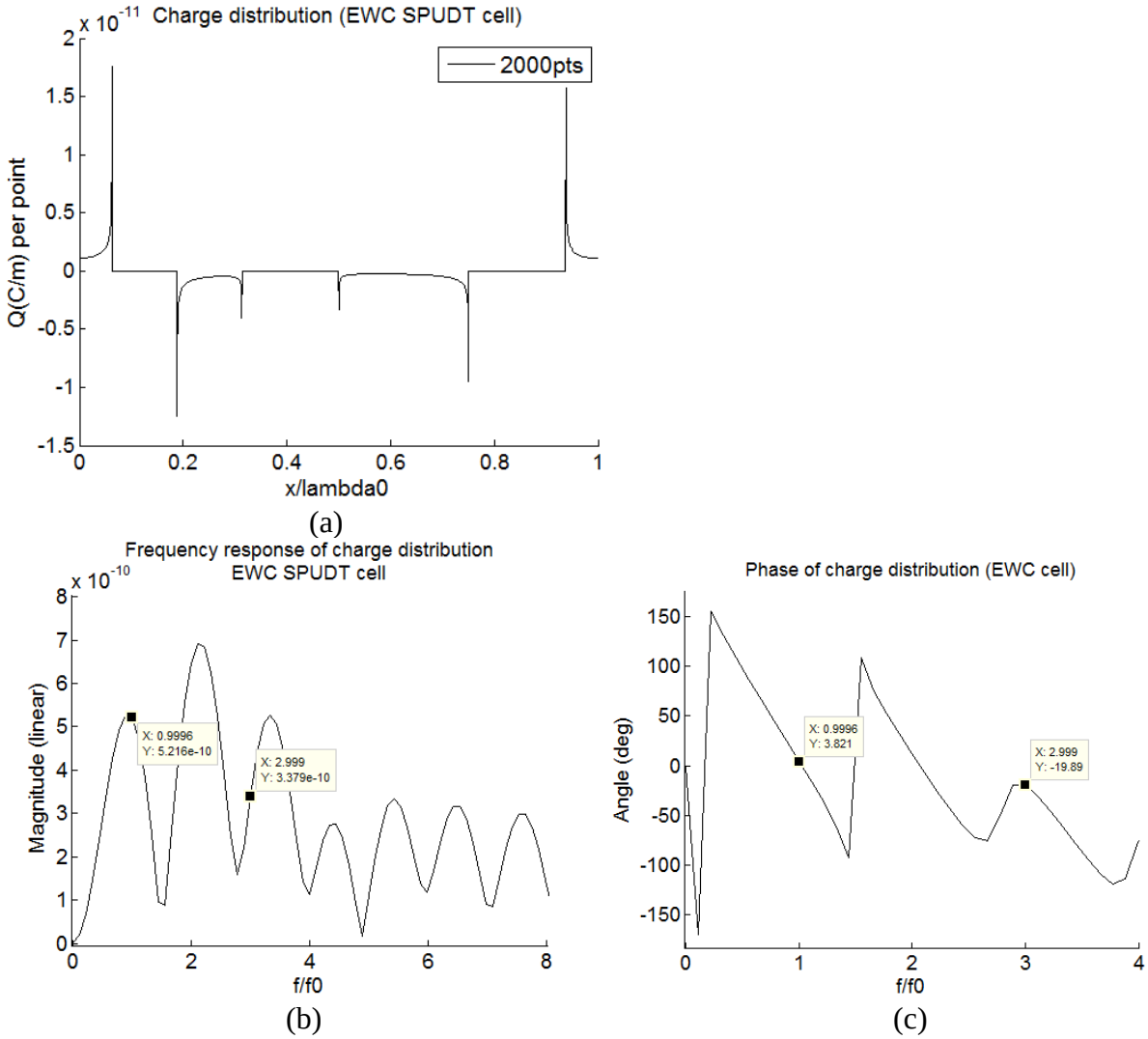

Figure D-7. (a) Charge distribution of an EWC SPUDT cell. (b) Fourier Transform (FT) of EWC cell charge distribution—magnitude. (c) Phase of EWC cell charge distribution FT. A voltage of +/- 1/2V is placed on the electrodes in order to generate these values—the total (+) charge of (a) is 4.5041e-10C/m.

As can be seen from the simulated charge distributions above, by setting up the cell from middle to middle of hot electrode(s) on the split finger (2hot, 4f0 sampled) bidirectional IDT cell, the frequency component at f0 has phase of 0^0. The same center-to-center cell layout for the EWC SPUDT gives a phase of 3.8^0 at center frequency. This corresponds to a TC shift of 3.8/360*lambda0 to the left of the hot electrode center—not a significant distance from the

center of the hot electrode. However, 3rd harmonic is a different story, the phase is now approximated as -20^0 according to the analysis.

D.3 Effective Coupling and Electrical Q Calculation of Non-Periodic SAW Transducers Using Lentine's Matrix Method

This section shows how to calculate the conductance and the capacitance of a nonperiodic IDT. This is important to transducer design because from these two parameters both the coupling and the electrical Q of the transducer can be obtained. From the electrical Q the effective coupling can be obtained.

In chapter 5 of his book, Morgan's analysis uses charge superposition to describe the charge distribution on multiple electrodes combined to form an IDT. He also finds the current flowing into an electrode and then the IDT. After defining the electrostatic charge density on the electrodes for a unit applied voltage as $\rho_e = \sigma_e(x,\omega)/V_t$, the conductance is found to be

$$G_a(\omega) = \omega W \Gamma_s |\overline{\rho_e}(k)|^2 \tag{D-8}$$

where $\overline{\rho_e}(k)$ is the Fourier transform of ρ_e, W is the beamwidth, and $k = \omega/v$.

The conductance is proportional to the square of the frequency component of the charge distribution at the frequency of interest.

After application of Lentine's matrix method simulation, both the voltage and the resulting charge distribution on the IDT electrodes are known, therefore the transducer capacitance is found. Since capacitance adds in parallel, only needed to know is the capacitance per electrode pair, or more appropriate for irregular electrodes—per cell.

The center frequency electrical Q, Q_t, of the transducer is a parameter of interest because it is a measure of how well the device can be matched over a bandwidth. It is given by the equation

$$Q_t = \frac{M\omega_0 C_t}{G_a(M\omega_0)} \tag{D-9}$$

where ω_0 is the angular center frequency at fundamental operation, M is the harmonic, and C_t is the transducer capacitance. The quantity $1/Q_t$ is also approximately proportional to the effective coupling, which takes into account the piezoelectric coupling factor of the crystal cut, k^2, and the coupling due to the effectiveness of the electrode layout—this information can be found in equation 2-16 of B. Fisher's dissertation [12] and initial work during early SAW device work (in the paragraph under equation 13 of reference [72]) [63, 64, 73] as well as in attached personal notes of D. Malocha on the impulse response model derivation. Morgan goes on to define a normalized capacitance, $\widetilde{C_t}$, a normalized conductance, $\widetilde{G_{aM}}$, and Q-factor, $\widetilde{Q_t}$.

$$C_t = WN_p\varepsilon_\infty\widetilde{C_t} \tag{D-10}$$

$$G_a(M\omega_0) = M\omega_0{\varepsilon_\infty}^2 N_p^2 W\Gamma_s\widetilde{G_{aM}} \tag{D-11}$$

$$Q_t = \frac{\widetilde{Q_t}}{N_p\varepsilon_\infty\Gamma_s} \tag{D-12}$$

where N_p is the number of transduction periods in the transducer.

Morgan prepares a table comparing the normalized values between different types of transducer cells having regularly spaced electrodes—the 2f0 sampled, 3f0 sampled, the split finger or 2hot4f0, and the 1hot4f0. The "f0" in the names of these IDT's corresponds to the number of electrodes, or samples, per period—not to be confused with the fundamental center frequency. The latter two have 1/8 wavelength electrodes, and the 1hot4f0, having only 1 hot, closely resembles the electrical characteristics of the EWC SPUDT.

Table 5.1 in Morgan's book is constructed by modeling the IDTs based on the notion of an element factor and an array factor [74], which requires equal width and equally spaced electrodes. The charge distribution for a single hot with all the other electrodes in an infinite array being grounded is called the element factor. The charge distribution of the element factor is described using a Legendre function and a Legendre polynomial. The electrode positions and polarities are given by an array factor. By using charge superposition, the element factor is convolved with the array factor in the spatial domain and multiplied in the frequency domain. Using these functions Morgan defines the transducer capacitance for these 4 regular IDT cells analytically. Although described analytically, the functions are transcendental and require numerical approximations. A Matlab script for calculating the charge distribution of the element factor and also using the array factor method to build up the charge distribution of a regular IDT cell is attached as part of this electronically submitted dissertation. The analytic solution to the charge distribution of the cell can also be found directly as done by B. P. Abbott and C. S. Hartmann [75], S. Biryukov and V. Polevoi [76, 77], and S. Malocha and B. Abbott [78].

Except for the 3f0 sampled IDT cell, table 5.1 of Morgan's book is replicated in a slightly modified manner. The normalized capacitance, conductance and coupling as defined in the above equations, are normalized to the 2f0 IDT cell.

The same table is then reconstructed based on Lentine's method for obtaining the charge distribution. It was noticed that it takes about 4 adjacent cells of nearest neighbors to converge, so that is what it's used, using 2000 points per cell—results may vary slightly based on the set up of the script (attached as part of this electronically submitted dissertation). Also to remember is that this analysis assumes an infinite number of cells, which the script approximates by using 11.

Table D-1. Comparison of electrical parameters by using results from Morgan vs. Lentine for different IDTs having regularly spaced electrodes.

Morgan Cell Type	$\widetilde{C_t}$	$\widetilde{G_{aM}}$	$1/\widetilde{Q_t}$	Lentine Cell Type	$\widetilde{C_t}$	$\widetilde{G_{aM}}$	$1/\widetilde{Q_t}$
2f0(f0)	1	1	1	2f0(f0)	1	1	1
2hot4f0(f0)	1.414	1.0836	.7663	2f0(f0)	1.4181	1.0864	.7661
2hot4f0(3f0)	1.414	1.0836	.7663	2hot4f0(3f0)	1.4181	1.1066	.7803
1hot4f0(f0)	1.207	.542	.4486	1hot4f0(f0)	1.2177	.5466	.4489

The results of Table D-1 above show that Lentine's matrix method of calculating the charge distribution is consistent with the results given by Morgan for transducers with regularly spaced electrodes. Electrical parameters obtained from the charge distribution can be used to help improve, and therefore decrease, the electrical Q-factor of the optimized SPUDT cell.

D.4 Directivity and Electrical Q Optimization Using Nelder-Mead Algorithm

In a previous section a phasor representation of the reflectivity contribution of each electrode in a transduction period showed that the thick ground electrode in an EWC cell was the only electrode contributing to the effective cell reflection coefficient. The $1/8^{th}$ wavelength electrodes were out of phase with each other. As done by many others, it was decided to modify the electrode positions in order to increase directionality. At 1^{st} harmonic there would be less room for the thin electrodes to move their reflection by 90^0, or a $1/8^{th}$ wavelength spatial shift, since some electrodes would touch. An electrode position movement at 3^{rd} harmonic operation would

give 3 times more sensitivity to reflectivity phasors. Taking advantage of this, the electrodes of the EWC are moved with a Nelder-Mead optimization algorithm that optimized for both, high directionality and high coupling. The directionality measure used is

$$UDTmeasure = |real(\Gamma_{R2L}) - real(\Gamma_{L2R})|/2 \quad \text{(D-13)}$$

Since it is possible to have very high directivity but very little coupling, a second objective is used in the optimization which seeks to increase the coupling.

As mentioned in section D.3, the effective coupling of the cell is obtained from the inverse of the electrical Q-factor. Therefore a second objective is introduced—maximize the coupling by minimizing the electrical Q-factor. The Matlab program is attached as part of this electronic dissertation submission, the algorithm follows the steps described in Wikipedia under the subject "Nelder-Mead method". Weights to the two values are given such that the objective values to be minimized are of the same order of magnitude. The simulation gives at least two good results—one in which both ground electrodes move to the left and the other moves the thin ground left and thick ground right.

The optimization result with the grounds moved apart is shown in Figure D-8. The thin ground of the EWC SPUDT cell is moved left by .0417*λ0 and the thick ground is moved right by .0995*λ0; λ0 being the fundamental wavelength, transduction period or cell length. The starting center point for the thin ground is 4λ0/16, for the thick ground is 10λ0/16. The calculated phase of the individual electrode reflection coefficient with respect to the calculated TC reference is shown in Figure D-8. Notice how the reflectivity phasor of the individual electrodes attempts to align to the real axis.

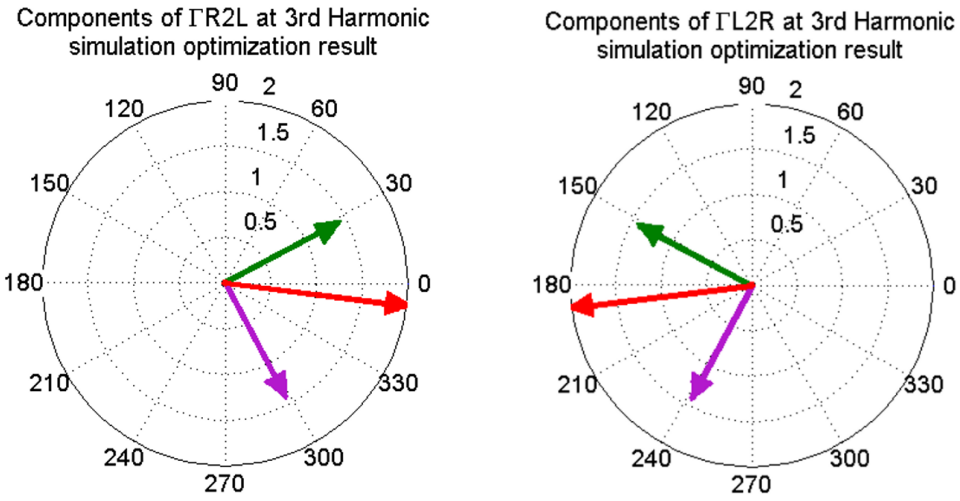

Figure D-8. Small reflections based 3rd harmonic reflection coefficient phasor of individual electrode contributions for the simulated optimized SPUDT. The summation of the real parts either contribute in phase or out of phase with the TC, depending on their direction, (a) ΓR2L or (b) ΓL2R.

Unfortunately, after much verification, the simulation is highly inaccurate for the 3rd harmonic optimized SPUDT case. The calculated direction is reversed in comparison to the standard EWC but fabricated devices showed the same direction. Figure D-8 does serve as an example of what the directionality objective of the optimization concept is attempting to accomplish—the reflectivity phasors of the individual electrodes need to align as much as possible to the real axis. This simulation calculated a UDT-measure of 3.9, compared to 2 in the ideal EWC case shown in Figure D-5. Fortunately, an experimental tuning of the electrode positions did result in a similar directionality improvement. Filter 5 in chapter 4 Figure 4-5 shows a reflectivity magnitude that is approximately 1.68 times that of the EWC at 3rd harmonic.

Possible reasons why the cell reflection coefficient calculation failed to work at 915MHz are now given. The small reflections based optimization has two components; the reflection center and the transduction center calculation. The RC calculation used a simplistic model for the electrode reflection. The electrode reflections also have stored energy component, besides the real

valued single edge reflection Γ. The electrode metal thickness used here is quite high at 2-2.2kAng, possibly making a significant contribution to the stored energy component.

The Green's function TC calculation had two assumptions that were violated; non-reflecting electrodes and no bulk mode generation. Coupling of modes simulations of measured data in chapter 4 show that there is significant non-Rayleigh radiation at the 3rd harmonic. The closely spaced electrodes might also be adding to the non-ideal conditions. These factors are probably throwing off the phase calculations at 3rd harmonic since every aspect becomes more sensitive. For practical implementation of this model at 915MHz or higher, more characterization at lower frequency would be necessary. The Matlab script will be included as an attachment for anyone wishing to explore this further. What is important to understand is the concept that Figure D-8 is illustrating, that the different electrode contributions to the reflectivity phasor can be enhanced by trying to align the phasors in the same direction while increasing the real part of the resultant reflectivity phasor.

Although the TC-RC calculation did not work for the 915 MHz operating device, it was close for the 1st harmonic (305 MHz) EWC, but less close for the 1st harmonic optimized SPUDT. This was tested by building three sets of forward and reverse filters for both the EWC and optimized SPUDT—similar to filter 3 and 4 in Figure 4-5. On two of the 3 sets, the thick ground electrode was shifted a few degrees, left for 1 set and right for the other. The corresponding TC-RC angles of the calculation and the measured devices are given in Figure D-10 and Figure D-11.

Table D-2. Calculated vs. extracted TC-RC angles by shifting the thick ground on the EWC SPUDT to the left and to the right.

	Thick Ground Electrode Shift (fraction of λ0)	1way Spatial Shift (deg)	Calculated TCRC, 2way Angular Distance (deg)	COM Extracted TCRC, 2way Angular Distance (deg)
EWC SPUDT 1 (In filter)	-7.4074x10^-3	-2.67	92.9	97.5
EWC SPUDT 1 (Out filter)	-7.4074x10^-3	-2.67	92.9	98
EWC SPUDT 2 (In filter)	0	0	97	101
EWC SPUDT 2 (Out filter)	0	0	97	102
EWC SPUDT 3 (In filter)	+7.4074x10^-3	+2.67	100.7	106
EWC SPUDT 3 (Out filter)	+7.4074x10^-3	+2.67	100.7	107

Table D-3. Calculated vs. extracted TC-RC angles by shifting the thick ground on the optimized SPUDT to the left and to the right.

	Thick Ground Electrode Shift (fraction of λ0)	1way Spatial Shift (deg)	Calculated TCRC, 2way Angular Distance (deg)	COM Extracted TCRC, 2way Angular Distance (deg)
Opt SPUDT 1 (In filter)	-0.0185	-6.67	117	108
Opt SPUDT 1 (Out filter)	-0.0185	-6.67	117	109
Opt SPUDT 2 (In filter)	0	0	134	114
Opt SPUDT 2 (Out filter)	0	0	134	114
Opt SPUDT 3 (In filter)	+0.0185	+6.67	149	120
Opt SPUDT 3 (Out filter)	+0.0185	+6.67	149	120

The calculation is closer for the EWC. The calculated angles do move in the correct direction of the electrode shift.

Perhaps a more sophisticated modeling approach is needed. For another SPUDT cell modeling method the interested reader is referred to the paper by S. Malocha and B. Abbott, "Calculation of COM Parameters for an Arbitrary IDT Cell" [78]. The goal of the analysis presented in this paper is also to find SPUDT modeling parameters—reflectivity magnitude, TC-RC phase, and coupling. Based on that analysis technique, J. Galipeau also develops an optimization scheme for enhancing a SPUDT [65]. He uses the FEM/BEM analysis and the

electrostatic approximation to find the same parameters for inclusion in the coupling of modes model. He comes up with an enhanced SPUDT at 1st harmonic that shifts the thick ground electrode towards the thin ground, instead of away as was done here.

If the interested reader wishes to attempt to work on the TC and RC calculations, the method used by Abbott and Hartmann may be used to experimentally determine the magnitude and phase of these [79]. It uses a 5-transducer test device and the parameter fit of ratios of certain P-matrix equations. It's unclear if bulk mode radiation will affect the accuracy of the calculation for 3rd harmonic devices. An optimization is used to fit the curves of the ratios involved. If needed, the Nelder-Mead optimization routine mentioned here could also be used.

The TC-RC calculation method presented in this appendix may be extended to also work as a function of frequency. Assuming this calculation can be performed accurately, some work would have to be done to make sure this is properly incorporated into the COM model. One of the things to sort out is that a frequency dependent calculation for the TC-RC angle and the reflectivity magnitude will give a different profile if the cell is simulated by starting at the gap between electrodes.

This concludes the presentation of a possible approach to design a SPUDT cell will the necessary directionality and coupling. The TC-RC angle calculation is not usable in its current form, but is open for further development by anyone who may find it useful to do so. However, the effective coupling calculation does work sufficiently well. Fortunately based on the coupling calculation, an optimized SPUDT layout was found by experimentally tuning the electrode positions (please see Appendix E).

APPENDIX E:
EXPERIMENTALLY OPTIMIZED 3rd HARMONIC SPUDT CELL

This appendix presents an experimentally optimized 3rd harmonic SPUDT cell based on EWC SPUDT electrode widths. SPUDTs using this design are modeled in chapter 4 and used for the reflective delay line devices in chapter 5. The first step is to identify an electrode layout with good effective cell reflectivity magnitude and good effective coupling.

The effective cell reflectivity magnitude is estimated using a small-reflections analysis of the electrode layout. This is discussed in appendix D-1. Appendix D-3 discusses how the coupling is approximated from the charge distribution of the transducer. The coupling is proportional to the inverse of the electrical Q. The conductance is proportional to the square of the magnitude of the charge distribution's Fourier transform at the frequency of interest. The capacitance is proportional to the charge on the positive electrodes for a given applied voltage. Therefore the electrical Q can be approximated by knowing the charge distribution. The method used to calculate the charge distribution is Lentine's matrix method, discussed in appendix G. It is used in conjunction with a Nelder-Mead optimization routine for automatic varying of the electrode positions. The Matlab program script to do this is attached as part of this electronic dissertation submission.

The second step is to experimentally tune the identified electrode positions to see if small shifts in electrode positions can result in a 2-way transduction center to reflection center (TC-RC) angular distance near 90^0 for good unidirectional behavior. The principle behind the unidirectional behavior is discussed in appendix D. The physical electrode layout, in general, will not obtain the highest cell reflectivity magnitude at the optimum TC-RC angle of 90^0. A unidirectionality measure is given in equation D-13 which uses the projection of the effective cell reflection coefficient phasor on the real axis—the real axis being the TC 0^0 reference.

After a good electrode layout starting point is identified, a 2-dimentional matrix of electrode shifts needs to be built. Sets of 40-cell forward and reverse SPUDT filter sets are built for each combination. The large number of cells makes the unidirectional characteristics more pronounced and makes for easier parameter extraction. The fundamental center frequency is 305MHz and the beamwidth is 20 wavelengths at fundamental. The film thickness was chosen as 2100 angstroms after some preliminary tests that looked at insertion loss and directivity as a function of film thickness. Changing this film thickness value will affect the optimized layout, and would add a 3rd degree of freedom to the experimental optimization, so a constant thickness of 2100 angstroms +/-150 angstroms, is used here. The initial mask layout for each SPUDT filter set is shown in Figure E-1.

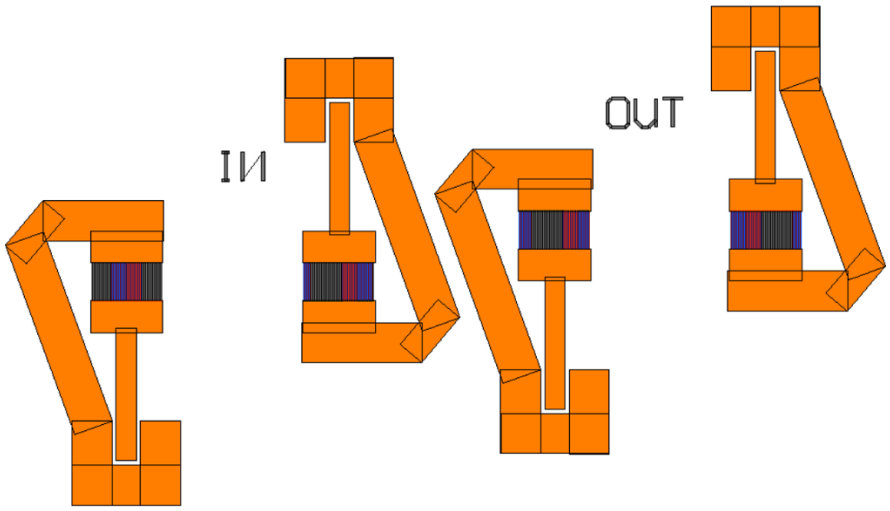

Figure E-1. Initial mask layout of 40cell forward and reverse SPUDT filter sets.

Problems were encountered with being able to reproduce similar transducers on each of the 2-ports of a filter. Each of the 4 transducers in a forward and reverse SPUDT filter

set seemed to have different, but consistent characteristics. It is very likely that part of the problem is attributed to the mask pattern generator not producing rectangular electrodes, as shown in Figure E-2.

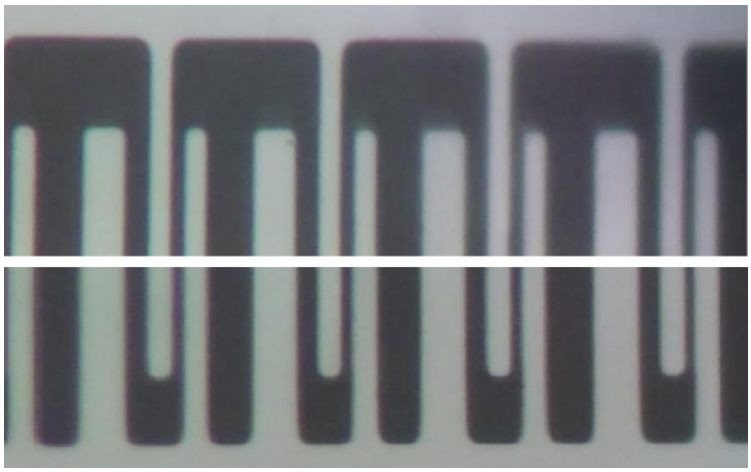

Figure E-2. Optical microscope picture of an optimized SPUDT section. The top and bottom of the electrodes show a varying electrode width. The beam width is 20 wavelengths at fundamental. The blades of the pattern generator may not be parallel. This adds some error to the 1D model being used and may contribute to the different S11 (S22) responses of Figure 4-8(b).

To circumvent this problem, 1 of the 4 possible probe pad and forward-reverse layout directions is chosen. Thus the SPUDT layout, including probe pad polarity orientation, is kept the same. The forward and reverse characteristics are then obtained by placing an 8-pair split-finger bidirectional transducer on either side of the SPUDT. The mask layout for the forward/reverse test set is shown in Figure E-3.

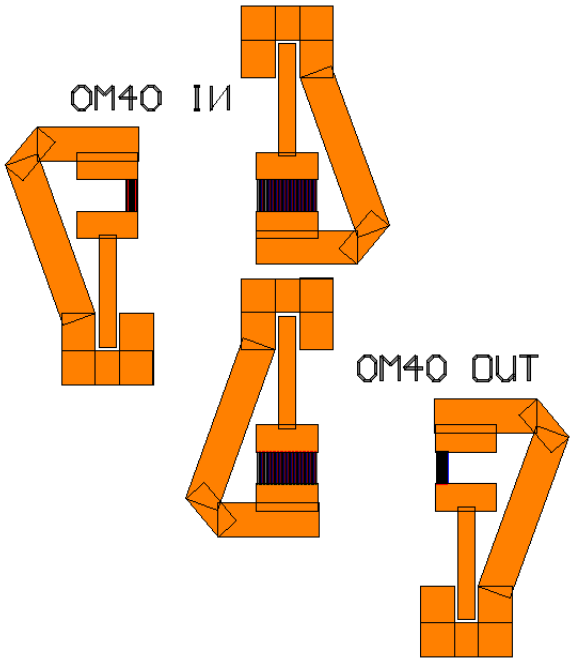

Figure E-3. Test structure for SPUDT characteristics using wideband bidirectional IDTs on either side of a two filter set. This help minimize fabrication variations between the SPUDTs and also makes the second transducer of the filter have more consistent characteristics; this gives a more reliable S21 from which to better appreciate unidirectional characteristics as well as insertion loss values.

The wideband bidirectionals are very consistent in their characteristics (this can be verified from devices shown in chapter 4). Devices using this layout are used for demonstrating the coupling of modes (COM) matching simulations in chapter 4.

An optimized SPUDT cell layout was found and it's shown as a microscope picture in Figure E-2. The ground electrodes are both shifted apart towards the hot electrode. A charge distribution analysis of this cell layout using Lentine's matrix method is show in Figure E-4c. The ground electrode edge locations are marked with values shown in Figure E-4c.

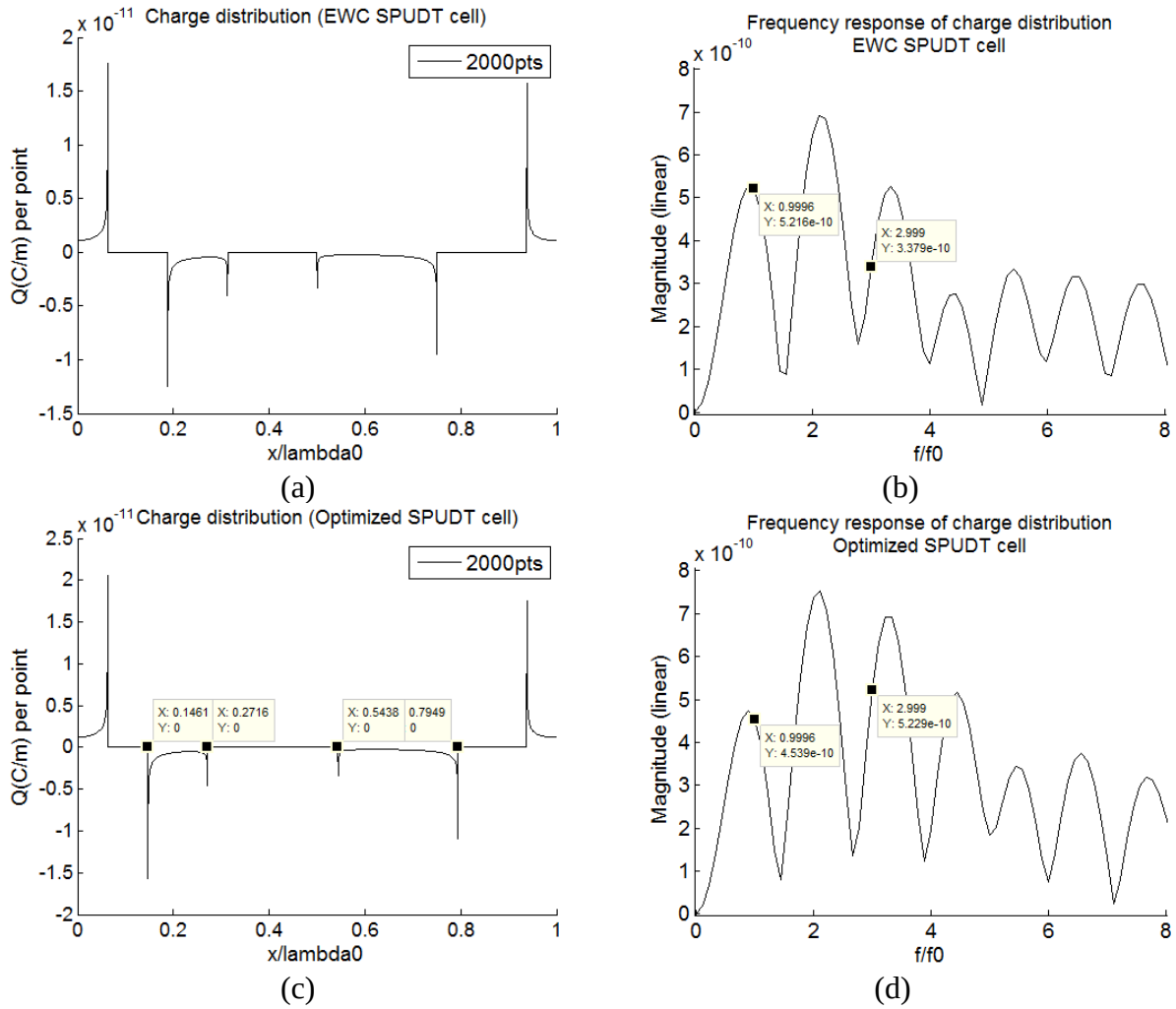

Figure E-4. The charge distribution (a) (c) and frequency domain representation of charge distribution (b) (d) for both the EWC and enhanced 3rd harmonic SPUDT, respectively. A voltage of +/- 1/2V is placed on the electrodes in order to generate these values. —the total (+) charge of (c) is 5.06e-10C/m.

The EWC layout is shown in Figure E-4a to compare with the optimized layout in Figure E-4c. The magnitude of the charge distribution Fourier transform is also shown and marked at the point corresponding to 1st and 3rd harmonic.

The S21 response and corresponding admittance of the 4 transducers in an optimized forward and reverse SPUDT filter set is shown in Figure E-5. It shows the best directionality found in a 40cell forward/reverse filter set, an average of 10.7 dB per SPUDT in the 2-SPUDT

filter. The best insertion loss is found on the adjacent 30cell filter set, an average of 3.65 dB per transducer.

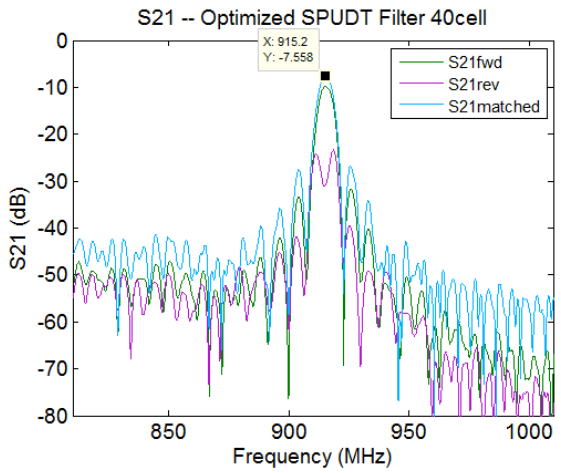

(a)

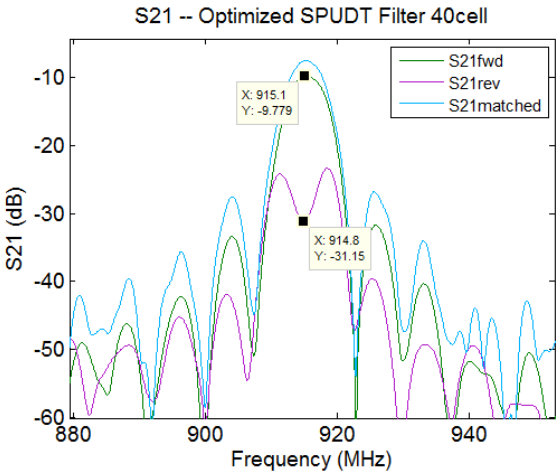

(b)

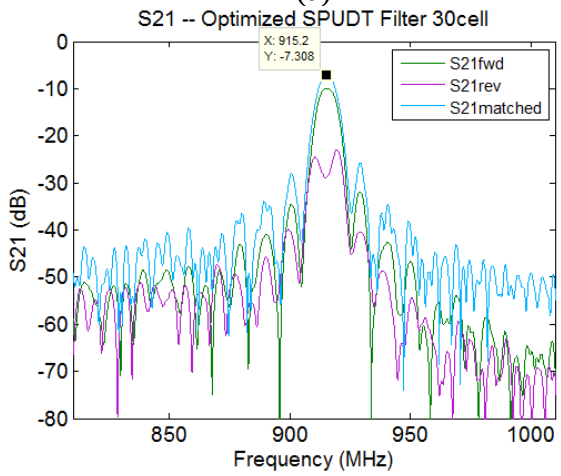

(c)

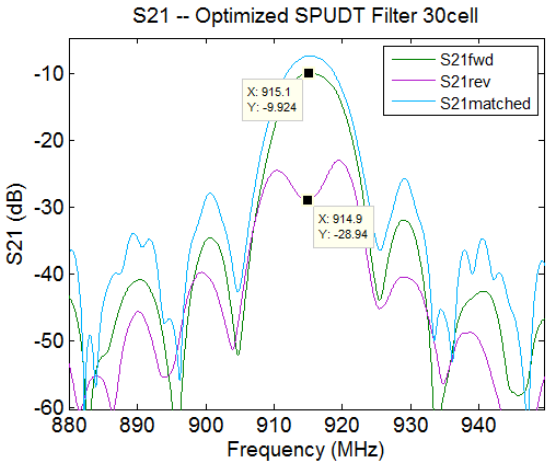

(d)

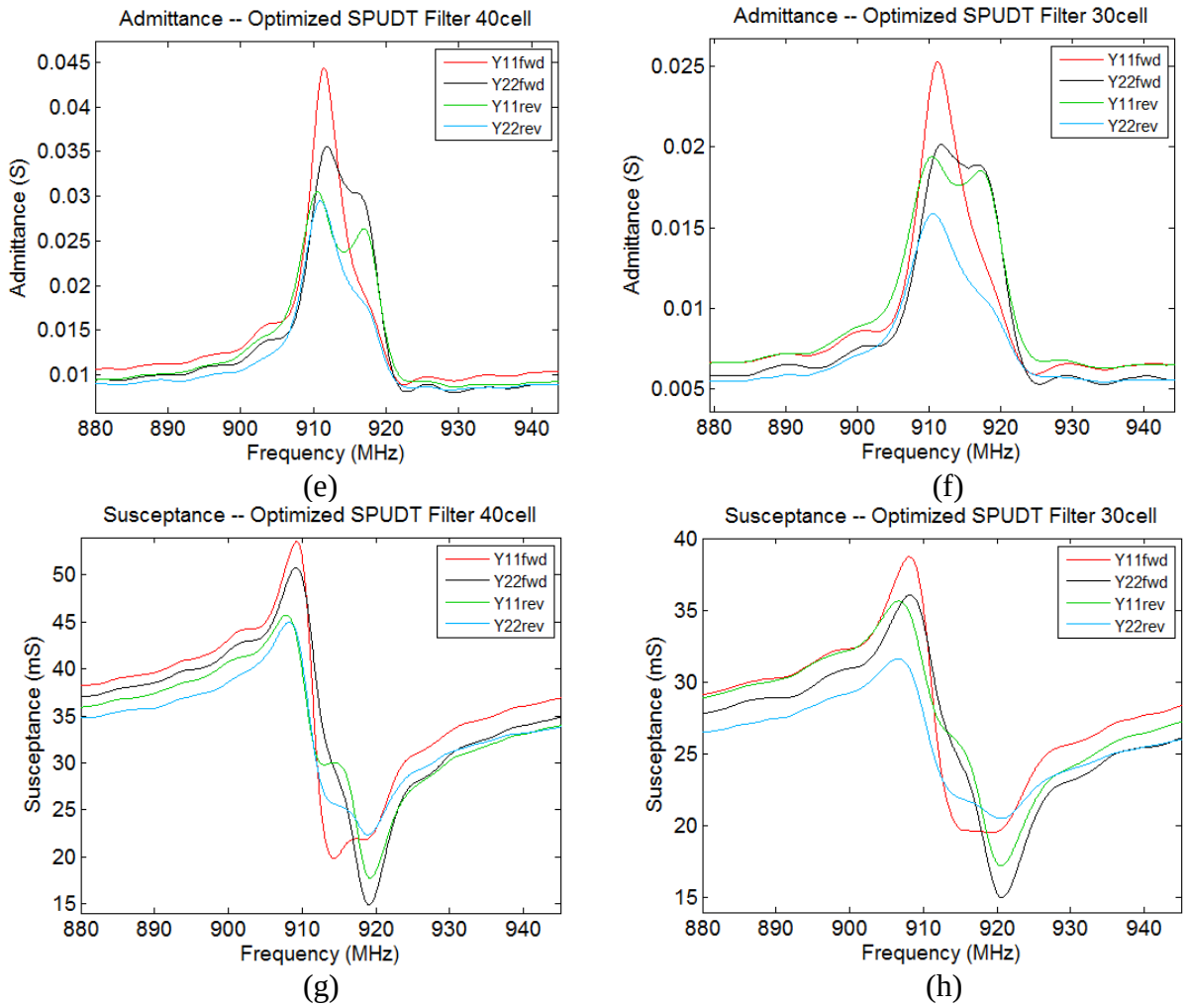

Figure E-5. S21 (a,b,c,d) and admittance (f,g,h,i) characteristics for forward and reverse filter sets of optimized SPUDTs. The 40cell and 30 cell sets are adjacent on the photolithographic mask. The wide sweep S21 plots for both (a) 40cell and (c) 30cell devices show similar out of band levels at 810MHz for both the forward and reverse filters—that is, comparing 40cell fwd with 40cell rev, and separately comparing 30cell fwd with 30cell rev. This suggests that there is no excess loss in the propagation path and directionality values are reasonably trustworthy.

The responses of similar devices are shown and COM modeled in chapter 4. Modeling parameters are given for comparison between the EWC, the optimized SPUDT, and the split-finger bidirectional in Figure 4-5. The filter pairs modeled in chapter 4 follow the layout of Figure E-3.

APPENDIX F:
COUPLING OF MODES PARAMETERS, AND SIMULATION SETUP

This appendix is provided so that the device simulations in chapter 4 can be replicated. First a background of the coupling of modes (COM) model is given. Then a discussion of the COM parameters is given. A special emphasis is given to being able to replicate the model used in chapter 4; by giving the exact equations used and giving instructions on how to input the design parameters in order to model both 1st and 3rd harmonic devices.

F.1 Coupling of Modes Background

The coupling of modes model was introduced to SAW device modeling by Suzuki and Haus in the 70s as mentioned in a very comprehensive paper on the COM model by Plessky in 2000 [80]. In the early 80s Hartmann included the effects of internal reflections in order to model SPUDTS. In the late 80s Abbott included the exact solution for the transducer's acoustic admittance [81] by working with a more explicit form of the equations and arrived at a set of COM model equations using a very clear mathematical derivation, ending up with a set of analytical solutions for a uniform transducer P-matrix description [32, 82]. This COM model version makes some assumptions in its derivation in order to achieve the analytical forms of its equations. For example, the reflectivity derivation uses only the constant term and the 1st harmonic term of spatial harmonics used to describe periodic stepped impedance discontinuities—this is called the Bragg harmonic, or synchronous harmonic. A detuning factor is used to take into account the effects that ignoring the other non-synchronous components have on the velocity—it would be interesting to compare results between the synchronous harmonic approaches to a rigorous approach on the impedance description, especially to see what happens to this detuning factor. A more detailed explanation of certain assumptions, as for example in the paragraph following equation 2.3.19,

would be of benefit to many readers. The assumptions, approximations, and derivations, although quite resourceful, can be difficult to follow especially when introducing transduction coupling and reception by the contribution to the bus bar current. Finally those differential equations describing the coupling of forward and reverse propagating waves take on a very elegant closed form solution. It would be great if the parts of the derivation where the assumptions are made would be described in greater detail, as would be found in a text book, and at some point be provided by Abbott for the benefit of future students. The transaction paper "Transduction Magnitude and Phase for COM Modeling of SAW Devices" [83] gives a summary of the results, including an approximation of the transduction coefficient COM parameter based on the Green's function analysis and array factor analysis as mentioned in chapter 2 of this dissertation and detailed by Morgan in chapter 5 of his book "Surface Acoustic Wave Filters" [62].

F.2 Concise Derivation of Original COM Equations

The equation development in this section is duplicated from a set of notes by D. Malocha on the coupling of modes analysis, based on the original analysis of Chen and Haus [84] and Abbott's dissertation [32]—the reader is also referred to these for a concise and clear presentation of the COM equations and parameters.

The COM model analysis starts with the first order wave equations of two counter propagating waves as shown in Figure F-1:

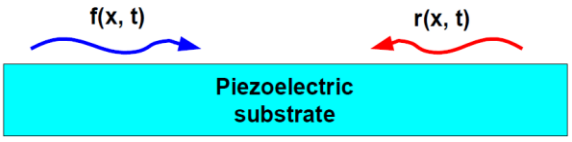

Figure F-1. One dimensional counter propagating surface acoustic waves on a free surface.

$$\frac{df'(x,t,\omega)}{dx} = -\frac{1}{v_R(x,\omega)}\frac{df'(x,t,\omega)}{dt} \tag{F-1}$$

$$\frac{dr'(x,t,\omega)}{dx} = +\frac{1}{v_R(x,\omega)}\frac{dr'(x,t,\omega)}{dt} \tag{F-2}$$

The prime in the amplitude variables (i.e. f' and F') does not denote a derivative, but an initial notation for a later change of variables. Taking the Fourier Transform of F-1 and F-2 with respect to the spatial variable gives:

$$\frac{dF'(x,t,\omega)}{dx} = -jk_R F'(x,t,\omega) \tag{F-3}$$

$$\frac{dR'(x,t,\omega)}{dx} = +jk_R R'(x,t,\omega) \tag{F-4}$$

$$k_R(x,t,\omega) = \frac{\omega}{v_R(x,t,\omega)} \tag{F-5}$$

where v_R is the free-surface Raleigh surface wave velocity and k_R its wave number. The ω in the arguments (inside parenthesis) just indicates that temporal frequency dependent parameters are expected, and these equations have to be solved for every frequency of interest—the ω dependence is dropped form the notation from now on, only appearing as a factor in the equations because of differentiation with respect to time or the relationship of equation F-5. The time variable is dropped as well because of the periodic $e^{j\omega t}$ time dependence. The presence of a reflective grating couples the forward and reverse waves as depicted in Figure F-2:

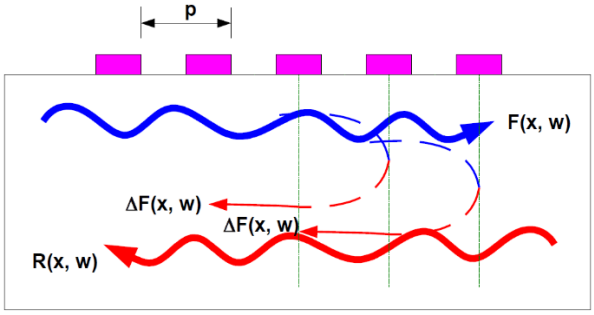

Figure F-2. Forward to reverse mode coupling in the presence of a periodic grating.

Since the average wave velocity typically slows down in the grating, the wave number is increased from the free-surface value, k_R, by Δk. Then a reflection coupling coefficient term is added k_{21} and k_{12}—assuming a small change in amplitude and no loss, these are related as $k_{21} = -k_{12}^*$. These coefficients describe the coupling of the waves from 1 direction to the other as given in equations F-6 and f-7.

$$\frac{dF'(x)}{dx} = -j(k_R + \Delta k)F'(x) + jk_{21}R'(x) \tag{F-6}$$

$$\frac{dR'(x)}{dx} = -j(k_R + \Delta k)R'(x) + jk_{12}F'(x) \tag{F-7}$$

Where Δk is usually determined empirically. The reflection coupling coefficient for a periodic grating can be expressed as a Fourier series of spatial harmonics as follows:

$$k_{12} = \sum_{n=-\infty}^{\infty} K(n)e^{jn\frac{k_g}{2}x} \tag{F-8}$$

where $k_g = 2\pi/p = 2\pi/\lambda_g$, p being the period of the grating (an infinite grating has been assumed). Introduction of a substitution of variables as follows:

$$F(x) = F'(x)e^{-j\frac{k_g}{2}x} \tag{F-9}$$

$$R(x) = R'(x)e^{+j\frac{k_g}{2}x} \tag{F-10}$$

Unfortunately the reason for this change of variables is not explicitly stated in [84], it may have something to do with standing waves. Abbott does not seem to include it in his derivation when inspecting equation 2.5.11 in [32], neither does Saldanha in equation 3.7 in [11]. The resulting new set of coupled differential equations is as follows:

$$\frac{dF(x)}{dx} = -j(k_R - \frac{k_g}{2} + \Delta k)F(x) + j\sum_{n=-\infty}^{\infty} K(n)F(x)e^{j(n+1)\frac{k_g}{2}x} \tag{F-11}$$

$$\frac{dR(x)}{dx} = +j(k_R - \frac{k_g}{2} + \Delta k)R(x) - j\sum_{n=-\infty}^{\infty} K^*(n)F(x)e^{-j(n+1)\frac{k_g}{2}x} \tag{F-12}$$

Only the spatial harmonic corresponding to $n = -1$ is kept, this keeps the mode coupling spatially independent of x. Also, only $n = -1$ couples wave mode energy. A loss term within the grating, $j\alpha$, is introduced, and the propagation term becomes complex:

$$\delta = k_R - \frac{k_g}{2} + \Delta k - j\alpha \tag{F-13}$$

The equations now become:

$$\frac{dF(x)}{dx} = -j\delta F(x) + jKR(x) \tag{F-14}$$

$$\frac{dR(x)}{dx} = +j\delta R(x) - jK^*F(x) \tag{F-15}$$

The linear operator $< X = d/dx$ is introduced in order to find the wave propagation constant. Applied to equations F-14 and F-15, it gives:

$$(< X + j\delta)F(x) = +jKR(x) \tag{F-16}$$

$$(< X - j\delta)R(x) = -jK^*F(x) \tag{F-17}$$

$$R(x) = -jK^*F(x)/(< X - j\delta) \tag{F-18}$$

Equation F-18 is F-17 solved for $R(x)$. Then substituting for $R(x)$ in F-16 by using F-18 gives:

$$(< X^2 + \delta^2)F(x) = |K|^2 F(x) \tag{F-19}$$

$$\frac{d^2F(x)}{dx^2} = (|K|^2 - \delta^2)F(x) \tag{F-20}$$

It is know that a 2nd derivative with respect to time gives the following relationship:

$$\frac{d^2F(x)}{dt^2} = -\omega^2 F(x) \tag{F-21}$$

Solving F-21 for $F(x)$ and substituting into F-20 gives:

$$\frac{d^2F(x)}{dx^2} = \frac{(|K|^2 - \delta^2)}{\omega^2}\frac{d^2F(x)}{dt^2} = \frac{1}{v^2}\frac{d^2F(x)}{dt^2} \tag{F-22}$$

Remembering that $v = \omega/k = \omega/\gamma$, the variable γ is the new wave propagation constant:

$$\gamma = \sqrt{\delta^2 - |K|^2} \tag{F-23}$$

After applying the boundary conditions $F(0) = 1\ and\ R(L) = 0$ to the beginning and end of the grating, respectively, where $L = np$ is the length of the grating, with n being the number of electrodes in the reflector and p the period as shown in Figure F-2 (half a wavelength for fundamental reflectors), the solutions to $F(x)$ and $R(x)$ become:

$$F(x) = \frac{\gamma cos[\gamma(L-x)] + j\Delta sin[\gamma(L-x)]}{\gamma cos(\gamma L) + j\Delta sin(\gamma L)} \tag{F-24}$$

$$R(x) = \frac{jK^* sin[\gamma(L-x)]}{\gamma cos(\gamma L) + j\Delta sin(\gamma L)} \tag{F-25}$$

As mentioned in the paragraph before equation 2.6.15 in [32], a detuning factor arises in the solution of the coupling of modes equations—unfortunately I don't have this derivation. The detuning factor Δ(ω) is basically the difference in the average propagation constant of the wave

traveling through the grating as compared to the center frequency (or synchronous frequency) value (it's zero at center frequency). For the grating it can be written as:

$$\Delta(f) = \frac{2\pi f}{v_{grat}} - \frac{\pi}{p} \tag{F-26}$$

From these solutions, the acoustic S-parameters for the grating can be obtained as:

$$S = \begin{bmatrix} R(0) & F(np) \\ F(np) & R(0) \end{bmatrix} = \begin{bmatrix} S_{11} & S_{12} \\ S_{21} & S_{22} \end{bmatrix} \tag{F-27}$$

$$S_{11} = S_{22} = \frac{jK^* sin[\gamma(L)]}{\gamma cos(\gamma L) + j\Delta sin(\gamma L)} \tag{F-28}$$

$$S_{12} = S_{21} = \frac{j(-1)^n \gamma}{\gamma cos(\gamma L) + j\Delta sin(\gamma L)} \tag{F-29}$$

These acoustic S-parameters can be converted to P-matrix parameters with the transformation formulas given in appendix B of [32]—first expanding a 2x2 purely acoustic P-matrix to a 3x3 by inserting a bottom row and right column full of zeros. Going back to the COM equation development of the initial paper by Chen and Haus, a coupling term, ξ, is added to equations F-14 and F-15, to describe the presence of a voltage on the bus bar. Another equation is added to describe the bus bar current relationship with the forward and reverse waves, and also the voltage on the bus bar. The equations now become:

$$\frac{dF(x)}{dx} = -j\delta F(x) + jKR(x) + j\xi V \tag{F-30}$$

$$\frac{dR(x)}{dx} = +j\delta R(x) - jK^* F(x) + j\xi^* V \tag{F-31}$$

$$\frac{dI(x)}{dx} = +2j\xi R(x) - j2\xi^* F(x) - j\omega C_f V \tag{F-32}$$

A derivation of the transduction term as well as the inclusion of parasitic resistance are given by Abbott and shown in equation 2.6.26-2.6.28 of [32]. These COM equations for the transducer can then be solved and placed in P-matrix form in a similar way as the simpler equations for the grating. The list of P-matrix entries for a uniform transducer can be found in appendix A of [32] and chapter 3 of [11] (also giving some P-matrix properties for reciprocal devices). The COM model is also discussed in section 8.2 of Morgan [62].

From the general coupling-of-modes equations above, F-30 through F-32, the 4 COM parameters can be seen explicitly—the reflection coefficient, K, the transduction coefficient, ξ, the finger capacitance or capacitance per cell, C_f, and the detuning parameter, δ. The parameters calculated in Appendix D pertain to 3 of these 4 COM parameters, with the detuning being excluded. All of the parameters needed to model the SPUDT are now discussed; referring here to the 4 classic COM parameters and values related to geometry and physical constants needed in this implementation of the COM model. The full set of COM-based P-matrix equations will be given at the end. The equations can be populated with the information given here and/or parameter values given in chapter 4 Figure 4-5.

F.3 Parameters of COM Equations

F.3.1 Transducer Geometry Parameters of COM Equations

The transducer geometry parameters needed in this version of the COM model are now given.

Length in Number of wavelengths: Number of cells multiplied by harmonic.

Wavelength, λ, (meter): Transduction period, λ_T, divided by harmonic, M.

Beam width (meter): Overlapping length of (+) and (-) electrodes.

Electrode widths: Not used. Its effects on transduction and capacitance seem well estimated based on results in Appendix D.3 Figure D-8, but further work would be needed to validate the model—including a highly accurate fabrication. Reflectivity calculations using the small reflections reflectivity model and TC-RC distance calculations presented in Appendix D.1 can be improved as well.

Metal thickness: Not used. Similarly to electrode widths, it is left to the interested reader to further improve the modeling of variable metal thickness.

F.3.2 Coupling-of-Modes Parameters – Capacitance

Capacitance, in units of (per cell per meter): Since electrodes are connected to the bus bar in parallel, increasing the number of cells adds capacitance in parallel. Also, since capacitance is proportional to the area of the plates in a parallel plate capacitor, it follows that increasing the length of the electrodes increases the capacitance proportionally. The COM model input for capacitance is often termed finger pair capacitance (in this case the term "cell" instead of "finger pair" may be more descriptive), simply given as

$$C_f = \frac{C_t}{W N_p} \tag{5-33}$$

with W being the beamwidth and N_p the number of cells (or transduction periods). The examples of SPUDT modeling in this chapter will basically be COM model fits of the experimental data. It is not practical to use the modeled capacitance (appendix D.3) to strictly compare or predict the measured results since the fabrication process used throughout is not very accurate or precise—for example, from two 4f0 bidirectional devices of 2 different wafers, a capacitance variation of 15% has been seen. However, assuming accurate fabrication and accurate modeling of capacitance

based on the charge distribution, there are two similar approaches that can be taken, which both require a baseline. One is to extract the capacitance of a fabricated device (either from an equivalent circuit that is shown in section 4.1 or by fitting the COM model), and based on this baseline value, then scale it based on results of the charge distribution, for which Lentine's matrix method has been used. Assuming no baseline device is available, the capacitance can be estimated from the semi-analytical solutions given by Morgan in chapter 5 of [62] for a transducer with regular electrodes. Using a known baseline capacitance that is tested with the model is more of safeguard for any scaling factor errors since Lentine's matrix method should in theory give a correct absolute value of charge; since the applied voltage is specified, the capacitance follows. Based on the charge calculated by Lentine's method the capacitance of the presented optimized SPUDT is 1.12 times greater than the EWC, and the 2hot4f0 is 1.25 times greater than the EWC. For the sake of validation of the capacitance as given by Morgan, the following series of equations give a step by step example so that Morgan's capacitance values can be reproduced:

$$C_t = \gamma W N_p \varepsilon_\infty \frac{sin(\pi/S_e) P_v(\mathrm{x})}{P_v(-\mathrm{x})} \tag{F-34}$$

where $\gamma = 2$ and $S_e = 4$ for the 2hot4f0 transducer, $\gamma = 1$ and $S_e = 2$ for the 2f0 transducer, and for the 1hot4f0 transducer $S_e = 4$ and γ, although not specified by Morgan, seems to be equal to $\gamma = (1 + \sqrt{2})/\sqrt{2}$ which gives the value of 1.207 found in table 4.1 of his book for the 1hot4f0—meaning that the capacitance is 1.207 times greater than the 2f0 transducer. This value of γ was found by trial and error, but based on Morgan, this is a value that is supposed to be found analytically but it is not given following his equation 5.79 as it's done for the other transducer configurations, so it is left as a challenge to the interested reader to verify the analytical form of

the γ value. W is the aperture, or beamwidth. N_p is the number of cells (or transduction periods). The effective permittivity is given as

$$\varepsilon_\infty = \varepsilon_0 + \sqrt{\varepsilon_{11}^T \varepsilon_{33}^T - (\varepsilon_{13}^T)^2} \tag{F-35}$$

where ε_0 is the permittivity of free space, and the other values in equation F-35 are the permittivity tensors of Y-Z lithium niobate under constant stress ($\varepsilon_{11}^T = 28.85$, $\varepsilon_{33}^T = 84.45$, and $\varepsilon_{13}^T = 28.85\ (F/m)^{.5}$) which is part of Ingebrigtsen's approximation and Blotekjaer et al. [85, 86], as mentioned in section 3.3 of [62]. $P_v(\mathrm{x})$ and $P_v(-\mathrm{x})$ are Legendre polynomials, with $\mathrm{x} = \cos(\pi \mathrm{a}/\mathrm{p})$ (a being width of the electrode and p the width plus gap), and the calculation of the Legendre polynomial given by the script:

```
aprev=1;
le=1;
for m=1:50
    am=aprev.*(m-1-v).*(m+v).*(1-x)./(2*m.^2);
    aprev=am;
    le=le+am;
end
```
(F-36)

where $v = -1/S_e$. This formula is found in appendix C of [62] and taken from volume II of [87] which is a great reference for special functions and can be found as a pdf document from multiple internet sites. The resulting calculation for a 2hot4f0 transducer with 40cells and a 20 wavelength aperture at fundamental (fundamental $\lambda 0 = 11.213\mathrm{x}10^{-6}\mathrm{m}$) gives a transducer capacitance of 4.8281pF when using Morgan's calculation. In comparison, the coupling-of-modes 3rd harmonic extracted values of capacitance of two 2hot4f0 fabricated transducers are 4.6 and 5.4pF (only one is shown in Figure 4-5). This concludes that the analytical prediction of capacitance presented by Morgan is very much within the ballpark.

F.3.3 Coupling-of-Modes Parameters – Transduction Coefficient

Transduction coefficient, in units of $(\sqrt{(S)}/m)$: At least three definitions can be found in the literature [78, 83, 88]. The definition found in the RSPUDT paper has apparently different units but enough time has not been spent trying to decipher the root cause.

Optional paragraph, please skip if not interested. The problem with units really comes down to not having a full and detailed analysis of the derivation for the particular version of the coupling-of-modes equations used, or whatever the subject might be. Some of this work is done while working for a company, so mainly the results and approach used are reported—and there is very little incentive by another researcher to replicate this since he will not be getting any credit for it as research merit is usually given in an academic setting. Perhaps someone might write a book on the subject, but it is rarely detailed enough for quick and easy replication of the results—especially by a student. For example, consider James C. Maxwell's book, *A Treatise on Electricity and Electromagnetism* which was published in 1881 [89], for an example of how much detail was given in the derivations in times past (the book is readily available online as a pdf). Of course, the demands of the modern era make it so that it isn't always practical for one person to expound on all their work with the detail that students of the subject would like to see. Biryukov's and Polevoi's derivations [77], Auld's book *Acoustic Fields and Waves in Solids* [1, 90], and Abbott's COM equation derivations [32], are among great examples of works in the field of acoustics that are attainable to the student by virtue of the rich step-by-step analysis. This is mentioned since I have a certain concern that 50 or 100 years from now it might prove very difficult or cumbersome to replicate much of the body of knowledge in this field, and this might be the case for many other fields. It is my opinion that whenever similar words to "it can be shown" appear, it would be very

useful if someone that needs to show or prove such property for his confidence in the matter, that there would be a way for this person to attach such derivation or proof as a link to the words "it can be shown" in the original document. This would be less official and in addition to the current referencing system used. Even in the current referencing system, one could specify specific locations in the document. I suggest that a Wikipedia-like approach be provided by the electronic repositories of dissertations and other research papers. In this way, people other than the authors can make clarifications and corrections, add derivations and even example code—thus lowering the learning curve and making the information more accessible, specially for students, specially as fields advance and the body of knowledge grows in volume and complexity. It's ok to have a systems or black box approach, but what is inside should be easily verifiable. Having a distributed effort on such contributions and fillings makes for light work so that unnecessary demands are not placed on a single person. Back to the discussion of the transduction coefficient.

For the transduction coefficient used in the UCF CAAT research group version of the COM model, a modified version of the original version presented in [83] is used. The semi-analytic approximation for the transduction coefficient takes the following form:

$$\alpha(\omega) = \alpha_{SF}\sqrt{\frac{\omega W \Gamma_s}{2}}\frac{\left|Q_f(\omega)\right|}{\lambda_T}e^{j\Phi_T} \tag{F-37}$$

where W is the beamwidth, Γ_s is defined in equation C-11, λ_T is the transduction period (or cell length), Q_f Fourier Transform of the elemental charge distribution in the frequency band of interest, and Φ_T is the phase of the transduction center at the harmonic of interest. α_{SF} is a scaling factor that is added here, to be defined in F-41. It should be noted that for $\alpha(\omega)$ to have the correct units that will give P33 the units of Siemens, Q_f actually needs to have the units of capacitance

per meter (F/m), not charge per meter (Coulomb/m=V·F/m)—per meter because it scales per beam width. It also makes sense that the transduction coefficient is independent of voltage. Also, in [83] the transduction coefficient is split into three factors; a substrate denormalization factor based only substrate parameters, a beam width denormalization factor, and a normalized transduction magnitude. It just needs to be stated that in equation 49, the normalized transduction magnitude, should have $\sqrt{\lambda_T}$ in the denominator. This makes it have units of (per meter), or per wavelength. Γ_s has a coupling coefficient (k^2) factor, so the transduction coefficient is proportional to the square root of the coupling (see Dr. Malocha's attached Impulse Response notes for simple derivations of how coupling, Q-factor, capacitance, conductance, are related or have proportional relationships).

From section 5.5.1 in [62], the elemental charge distribution (single hot with all other electrodes at ground) can be convolved with an array factor corresponding to the center of the electrode positions with appropriate polarity to give the charge distribution of the entire transducer. In the frequency domain the transducer charge distribution becomes

$$Q_e(k) = A_f(k)Q_f(k) \tag{F-38}$$

$$A_f(k) = \frac{sin\left(kN_p\lambda_T/2\right)}{sin(k\lambda_T/2)}e^{j\Phi_{off}} \tag{F-39}$$

with the associated phase, $\Phi\_off = -k(N\lambda\_T/2)$, shifting the reference by half a transducer length, but not of importance in this discussion. In [83] a simplified version of the transducer's P-matrix solutions are given without attenuation or reflectivity—these are based on Morgan's quasi-static modeling of the transducer based on the Green's function analysis. This array factor can be absorbed into these sets of equations since a factor $Q_e(k)$ was present. Another simplified

version of the P-matrix solutions are given in [83] which are based on Abbott's coupling-of-modes solutions. After an equivalence is made, the transduction coefficient is deduced and given as that of equation F-37, except that Q_f has no absolute value. The coupling-of-modes based P-matrix equations, either the simplified version given in [83] or the complete version found in [32, 91] have a term that resembles the array factor of equation F-39 (though other effects like propagation loss, reflectivity, and detuning are included). The array factor of F-39, which has a sine on both the numerator and denominator, is approximated by a sin(x)/x form, which the coupling-of-modes based equations have (approximation found in [83] as well as in section 5.5.1 of [62]). Even though there is a frequency dependence in Q_f and the $\sqrt{\omega}$ factor in equation F-37, the array factor dominates the off-center frequency transduction.

In section 5.5.1 of [62] Morgan breaks down the array factor into a portion corresponding to the electrode layout within the cell (composed of sampling functions, one for each electrode hot electrode) and another portion corresponding to the number of cells or length (composed of sampling functions, one for each cell). The frequency response of the later is basically the same for all uniform transducers. The frequency response of the intra-cell part is basically given a factor of 1 for a 2f0 IDT and $\sqrt{2}$ for a 2hot4f0 IDT (equation 5.70 in [62])—this factor is basically the array factor for 1 period. The complete array factor is multiplied in frequency by the elemental charge distribution to obtain the charge distribution of the entire transducer. According to equation 5.72 in [62], the conductance is proportional to the charge distribution Fourier Transform magnitude squared.-- After defining the electrostatic charge density on the electrodes for a unit applied voltage as $\rho_e = \sigma_e(x,\omega)/\mathrm{V}_t$, Morgan finds the conductance is found to be

$$\mathrm{G}_a(\omega) = \omega W \Gamma_s |\overline{\rho_e}(k)|^2 \qquad \text{(F-40)}$$

where $\rho_e = \sigma_e(x,\omega)/V_t$ is the electrostatic charge density on the electrodes for a unit applied voltage, $\overline{\rho_e}(k)$ is the Fourier transform of ρ_e, W is the beamwidth, and $k = \omega/v$.

Since the conductance is proportional to the coupling coefficient (k^2) (see Prof. Malocha's impulse response notes attached) and the transduction coefficient ($\alpha(\omega)$) is proportional to the square root of the coupling coefficient, then the transduction coefficient is proportional to the array factor. Thus the transduction coefficient of either the 2f0 or the 2hot4f0 can be calculated by multiplying equation F-37 (but with no α_{SF}) by 1 for the 2f0 or by $\sqrt{2}$ for the 2hot4f0. The elemental charge distribution frequency response is given in [62, 83] as

$$Q_f(k) = \varepsilon_\infty \frac{2sin(\pi s)P_m(\mathrm{x})}{P_{-s}(-\mathrm{x})} \tag{F-41}$$

where m= (M-1)/2, M being the harmonic of operation, and s=f/v*p – m, v=velocity and p the electrode width plus gap, and the units being charge per unit voltage per unit beam width. Just as with the capacitance, if the 2f0 or 2hot4f0 is used as the transduction coefficient baseline, then using the numerical calculation for the SPUDT cell charge distribution, the SPUDT coupling coefficient can be obtained by scaling the baseline (or reference). Scaling the transduction coefficient is done by obtaining the relative coupling from the capacitance and conductance as performed to populate Figure D-8. Even though Q_f isn't constant over frequency, assume that Q_f reference can be scaled (that of a regular electrodes from equation 5-40) uniformly over frequency by same factor used at center frequency. The following formula can be used for the scaling factor (α_{SF}) when the reference is the 2hot4f0 transducer configuration:

$$\alpha_{\mathrm{SF}} = \frac{\alpha_{SPUDT}}{\alpha_{4f0Reference}}\alpha_{\mathrm{SF2hot4f0}} = \alpha_{Ratio}\alpha_{\mathrm{SF2hot4f0}} = \cdots$$

$$\alpha_{\mathrm{SF}} = \sqrt{\frac{|\mathrm{Qe}_{SPUDT}(Mf_0)|^2}{\left|\mathrm{Qe}_{4f0Reference}(Mf_0)\right|^2} \cdot \frac{\mathrm{Ct}_{4f0Reference}}{\mathrm{Ct}_{SPUDT}}} \cdot \alpha_{\mathrm{SF2hot4f0}} \qquad \text{(F-42)}$$

where $\mathrm{Qe}_{SPUDT}(Mf_0)$ and $\mathrm{Qe}_{4f0Reference}(Mf_0)$ are the Fourier transforms of the static charge distributions for the SPUDT (or any other transducer) and the 2hot4f0 transducers, respectively—using the charge distribution of a single cell or the entire transducer, but obviously have to be consistent. M is the harmonic of operation, but for the 2hot4f0 the values are the same at the 1st and 3rd harmonic (Figure D-8). $\mathrm{Ct}_{4f0Reference}$ and Ct_{SPUDT} are the transducer capacitance for the 2hot4f0 and SPUDT (or any other transducer)—probably safer to use Lentine's model (or an equivalent method) for both by using the total charge of a single cell which is proportional to capacitance, this would avoid scaling errors (same advice for $\mathrm{Qe}_{SPUDT}(Mf_0)$ and $\mathrm{Qe}_{4f0Reference}(Mf_0)$). $\alpha_{\mathrm{SF2hot4f0}}$ is equal to $\sqrt{2}$ as discussed above. Even though $\alpha_{\mathrm{SF2hot4f0}}$ and $\alpha_{4f0Reference}$ are technically the same thing, $\alpha_{4f0Reference}$ can be a scaled (by the same factor as α_{SPUDT}). The coupling coefficient approximation (F-37) for the 2hot4f0, which uses the semi-analytical calculation of Q_f (F-41) times the $\sqrt{2}$ factor, has been verified to be another very good ballpark estimate at 1st harmonic. In fact, on two sets of split finger devices, a total of 4 IDTs, the COM model fit uses almost the exact theoretical scaling factor of $\sqrt{2}$ at 1st harmonic, with $\alpha_{Ratio} = .99$. The results of the simulation for this device, both 1st and 3rd harmonic, are given in sections 4.2 and 4.3, respectively.

The transduction phase Φ_T of F-37 is left at zero, and for our purposes there's no interest in any relative phase shifts for exact time delays. Modulating Φ_T over frequency is not looked

into—the SPUDT would have different characteristics over frequency than 2f0 or 2hot4f0, which is what frequency dependent coupling coefficient is more accurately modeling. Leaving it a constant 0° seems sufficiently accurate for the SPUDT devices being modeled. What needs to be noted is that non-uniform IDTs, where each section is composed of a different cell layout such as an OFC SPUDT, would need to include the appropriate relative transduction phase between them. When cascading transducers in a single port as shown in figure 3-5, one would need to make sure that each section has a length equal to an integer number of wavelengths at the respective wavelength of each section. If this is done, then the next section would have the appropriate transduction phase; only the last section can have non-integer length of wavelengths without having to somehow compensate by changing Φ_T for that section. SPUDTs have transduction centers that are shifted from the reflection center. Even under a constant cell periodicity (transduction period length), Φ_T changes for each section if the SPUDT layout is varied. Different SPUDT sections, for example, would need to include the appropriate relative transduction phase between them—speaking of a constant Φ_T for each section as is currently implemented in the model. Similar to the capacitance parameter discussion, the baseline transduction coefficient magnitude can just be obtained experimentally by fitting the COM model to a baseline device and adjusting the model based on coupling factor calculations using Lentine's numerical analysis and scaling using equation F-42.

F.3.4 Coupling-of-Modes Parameters – Reflection Coefficient, Detuning and Others

Reflectivity, K, in units of (per meter) or (per wavelength). The effective cell reflection coefficient has been discussed in Appendix D. It started by assigning an effective reflection coefficient to the electrode and then using that to come up with an effective reflection coefficient

for the entire cell using small reflections theory. N. Saldanha et al. has characterized the reflection coefficient, or reflectivity, on a per strip basis for aluminum Bragg gratings in Y-Z LiNb03 at different harmonics [11, 38, 71] for different metallization ratios and thicknesses. She adds an energy storage element to the model, which has not been addressed here. Therefore the reader is advised to start there, in conjunction to the theory presented in this dissertation, for predicting reflectivity. The COM model presented here starts with a reflectivity profile as that of a 2f0 transducer, which basically has 2 strips per transduction period. The coupling-of-modes derivation then uses a Bragg harmonic component of reflectivity instead of an abrupt discontinuity [32]. The coupling of modes parameter for reflectivity, K, is given as

$$K(f) = \frac{2R}{v/f} \tag{F-43}$$

where v is the velocity of the transducer (or reflective grating), f is the frequency, and R is the reflectivity per strip (having both magnitude and phase). Therefor $K(f)$ is basically the reflectivity per wavelength. For 3rd harmonic modeling, $|R|$ is approximately divided by 3 from the value used at 1st harmonic because there are 3 more wavelengths; generally the true $|R|$ will probably change from 1st to 3rd, the approximate decrease by factor of 3 is because of model setup ($|R|$ entered per wavelength instead of per transduction period). For a shorted grating $|R|$ is approximately .015 [38, 71], which is also a good value for a 2f0 transducer—keeping in mind that electrical loading affects reflectivity as well (some sensors are based on this concept [61]). The form of R used in the model is as follows:

$$R = |R|e^{-j\pi/180 \cdot \Phi_{TCRC} \cdot polarity} \tag{F-43}$$

where $polarity$ is either 1 or -1, used to change the direction of the forward and reverse ports. Φ_{TCRC} is the TC-RC 2 way distance, in degrees, that has been discussed in previous chapters.

Since the transducers dealt with here are uniform SPUDTs, the transduction phase can be lumped with the reflection center phase. As mentioned in the transduction coefficient section, SPUDTs consisting of non-uniform sections would need to address the transduction and reflection phase separately.

The detuning factor, Δ, has units of (per meter): As mentioned in the early part of this chapter, the detuning factor is used is said to compensate for some simplifications used in the COM derivations. It compensates for non-synchronous wavenumber between transducer or grating structure and the current frequency of operation. For the transducer it's given as

$$\Delta(f) = k_R - M\frac{2\pi}{\lambda_T} + dk \tag{F-44}$$

$$k_R = \frac{2\pi f}{v_f} \tag{F-45}$$

$$dk = \frac{2\pi f}{v_{idt}} - \frac{2\pi f}{vf} \tag{F-46}$$

where M is the harmonic, vf is the free surface velocity, and v_{idt} is the average wave velocity in the IDT region. For a reflector, the detuning factor becomes

$$\Delta(f) = \frac{2\pi f}{v_{grat}} - Mg\frac{\pi}{p} \tag{F-47}$$

where v_{grat} is the average velocity in the grating and Mg is the harmonic of operation for the grating, and p is the period of the grating.

Some other parameters necessary to populate the coupling-of-modes equations are the propagation loss, γ_{loss}, in units of (per meter)—about 70 for a grating at 915MHz (but highly dependent on thickness), about 100 for an IDT at 305MHz, and unfortunately anywhere from 1000 to 2500 at 915MHz for the 3rd harmonic operating devices that are modeled in chapter 4. This loss

mainly models viscous losses and diffraction loss. It will also be used to roughly incorporate what are probably bulk-mode losses at the 3rd harmonic.

Another loss mechanism within the transducer is the electrical resistive loss of the electrodes. It is modeled by the parameter Rf, the electrode or finger resistance in one transduction period, and it's incorporated in the derivation of the coupling-of-modes equations in sections 2.5 and 5.2 of [32]. Some other information on this can be found in [92]. Rf is obtained from the sheet resistance of the film, Rs (units of ohm/square), and approximated from the beam width, electrode width, and IDT configuration as:

$$R_n = R_s \frac{W}{a} \tag{F-48}$$

$$R_f = R_n(3 - S_e/2) \tag{F-49}$$

where a is the electrode width, W is the beamwidth, R_n is the end-to-end electrode resistance approximation, and equation F-49 accounts for the type of cell configuration, with S_e equal to 2 for the 2f0 and 4 for the 2hot4f0 transducer. The modeling here will assume that the SPUDT is similar to the 2hot4f0 in Rf. These modeling approximations are given in Figure 2.5.3 of [32]. However, the current in the electrode is not exactly equal across the beam width. It would be interesting to see if an FEM simulation can accurately capture the current profile along the electrode, and if so, can the current distribution along the electrodes be modeled by a circuit of the form shown in Figure F-3.

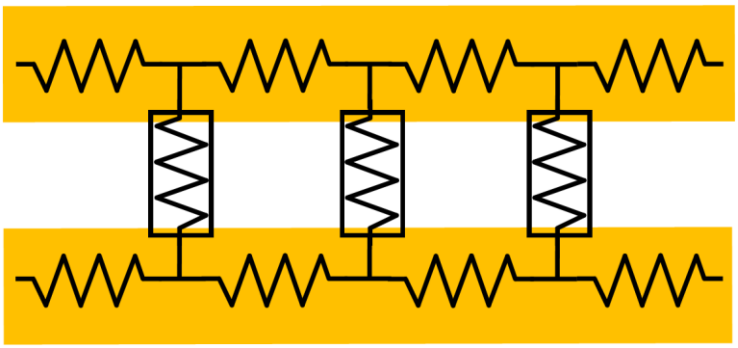

Figure F-3. Circuit model for current along the electrodes (in gold). The horizontal impedances would model the sheet resistance and the vertical elements would model the radiation admittance—both complex impedances, but more so the radiation. This circuit has not been modeled by Lakin using differential equations.

The many horizontal resistors along the length of the electrodes (gold lines) would model the sheet resistance and the vertical resistors represent the radiation admittance—both complex impedances, but more so the radiation. In fact, this circuit model has been proposed and solved by Lakin in the 70s using differential equations, in a similar fashion as RF transmission lines. Perhaps if more electrodes were included, a circuit analysis program would be needed or just easier to solve than trying to find the differential equations. Since the actual device has many electrodes, it's probably not a bad idea to verify that the single pair solution is consistent with a multi-pair solution—obviously things were much different in the 70s in regards to computational capabilities. Also, if irregular electrodes are used, then different impedance values would be required for each electrode width and gap, and possibly difficult to find the appropriate radiation impedances. Of course, back-solving from an FEM program solution would help, especially if applying an optimization routine to the problem. In any case, for the modeling purposes here, equations F-48 and F-49 work pretty well.

The last parameter needed is the propagation constant:

$$D = \sqrt{-|K|^2 + (\Delta - j\gamma_{loss})^2} \tag{F-50}$$

The P-matrix representation of the IDT, based on the COM model is given in equations F-51 through F-65. Based on the parameters given up to now in this chapter, the equations can be populated and solved in a script by sweeping over the frequency of interest.

$$AF = \sin\left(\frac{DL}{2}\right)\Big/\left(\frac{DL}{2}\right) \tag{F-51}$$

$$den = D\cos(DL) + i\cdot\Delta\sin(DL) \tag{F-52}$$

$$P_{11} = i\cdot K^{*}\sin(DL)/\text{den} \tag{F-53}$$

$$P_{12} = D\cdot \mathrm{e}^{-i\cdot k0\cdot Lt}/\text{den} \tag{F-54}$$

$$P_{13} = \left(i\cdot Lt\cdot AF\cdot\alpha^{*}D\cos\left(\frac{DL}{2}\right) + i\cdot K^{*}\alpha + \Delta\alpha^{*}\sin\left(\frac{DL}{2}\right)\right)/den \tag{F-55}$$

$$P_{21} = P_{12} \tag{F-56}$$

$$P_{22} = i\cdot K\cdot\sin(DL)\cdot \mathrm{e}^{-i\cdot 2k0\cdot Lt}/\text{den} \tag{F-57}$$

$$P_{23} = i\cdot Lt\cdot AF\cdot\left(\alpha\cdot D\cos\left(\frac{DL}{2}\right) + i\cdot(K\cdot\alpha^{*}+D)\cdot\sin\left(\frac{DL}{2}\right)\right)\cdot \mathrm{e}^{-i\cdot k0\cdot Lt}/\text{den} \tag{F-58}$$

$$P_{31} = -2P_{13} \tag{F-59}$$

$$P_{32} = -2P_{23} \tag{F-60}$$

$$Group1 = -i\cdot 2\cdot\left[\left(K^{*}\alpha^{2} + K\cdot\alpha^{*2} + 2\Delta|\alpha|^{2}\right)/D^{3}\right] \tag{F-61}$$

$$Group2 = [DL - (D\cdot\sin(DL) + i\cdot\Delta(1-\cos(DL)))/den] \tag{F-62}$$

$$Group3 = -2\cdot\left[\left(\Delta\cdot\left(K\cdot\alpha^{*2} + K^{*}\alpha^{2}\right) + 2|K|^{2}|\alpha|^{2}\right)/D^{3}\right]\cdot(1-\cos(DL))/den \tag{F-63}$$

$$Group4 = i \cdot 3 \cdot 2\pi \cdot Cf \cdot L \cdot f / \left(\lambda 0 \cdot (3 + i \cdot 2\pi \cdot Cf \cdot Rf \cdot f)\right) \quad \text{(F-64)}$$

$$P_{33} = Group1 \cdot \ Group2 + Group3 + Group4 \quad \text{(F-65)}$$

APPENDIX G:
LENTINE'S MATRIX METHOD APPROACH TO CALCULATING THE STATIC CHARGE DISTRIBUTION OF A SAW TRANSDUCER CELL

This appendix gives a simplified visual description of Lentine's matrix method [93] for approximating the static charge distribution of a transducer cell with arbitrary electrode widths. It calculates the profile of the electric potential profile as well. This appendix is given in the style of a proof, since every line follows a sequential logical order, figure numbers may not be given.

Consider the charge density distribution on the periodic IDT electrodes with a/p ratio = .5. All of the electrodes except the center electrode are shorted. A voltage is applied across the center and shorted electrodes as shown in Figure G-1.

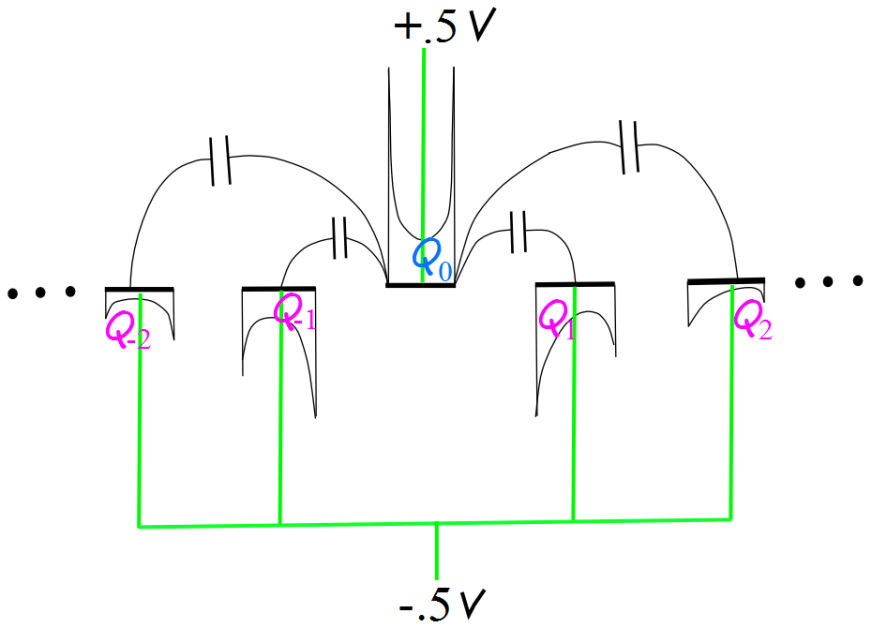

Figure G-1. Regularly spaced electrodes with voltage applied to center electrode and the rest grounded.

Because of symmetry, $Q_{-1} = Q_1$, $Q_{-2} = Q_2$, and so on. The individual electrode charge gets smaller for electrodes further away, with the sum of the negative charges equaling the positive charge on Q_0 since the system is in equilibrium. Now consider how the structure looks like capacitors in parallel. This is illustrated with the analogous structure in Figure G-2.

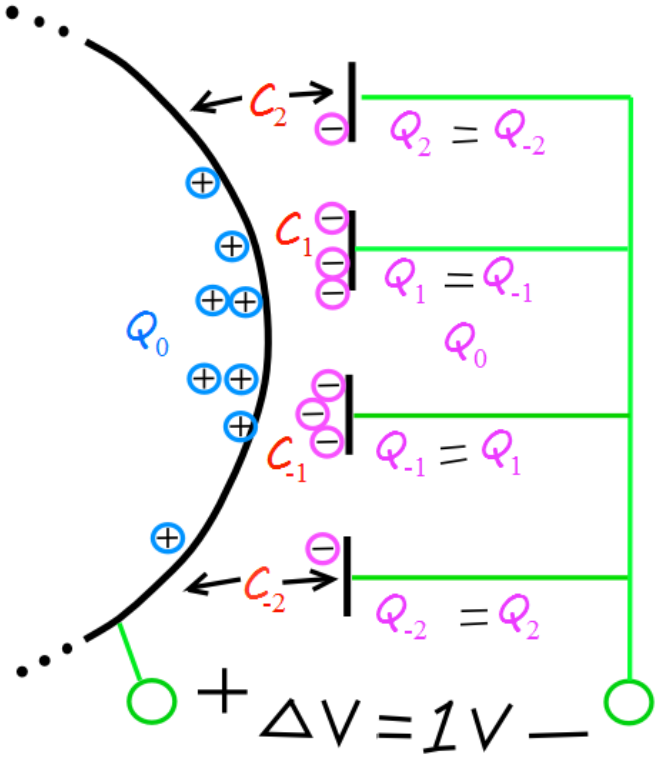

Figure G-2. Analogous structure to Figure G-1. The hot electrode is shaped in a way that produces a smaller electrode capacitance as the electrodes move away from the center, similar to Figure G-1.

The equation for charge on either side of the capacitor is:

$$Q = C\Delta V \tag{G-1}$$

$$C_0 = C_{Total} \cdot \Delta V \tag{G-2}$$

Capacitance adds in parallel:

$$C_{Total} = 2C_1 + 2C_2 + \cdots \tag{G-3}$$

Therefore:

$$Q_0 = (2C_1 + 2C_2 + \cdots) \cdot \Delta V \tag{G-4}$$

$\Delta V = 1V$, therefore:

$$Q_0 = (2C_1 + 2C_2 + \cdots) \cdot 1V \tag{G-5}$$

Therefore:

$$Q_1 =\cdot 1V, Q_2 = C_2 \cdot 1V \text{ , ...} \tag{G-6}$$

Because the total (+) and (-) charge must be equal in equilibrium, or static charge conditions, the summation of the individual charges $|Q_1|$, $|Q_2|$, … , add up:

$$|C_{Total}| = 2|C_1| + 2|C_2| + \cdots \tag{G-7}$$

And $Q_1 =\cdot 1V, Q_2 = C_2 \cdot 1V$, ... , so the capacitance from center electrode to each neighbor electrode is proportional to the charges on the neighbor electrodes, and found by placing $1V$ across the electrode structure.

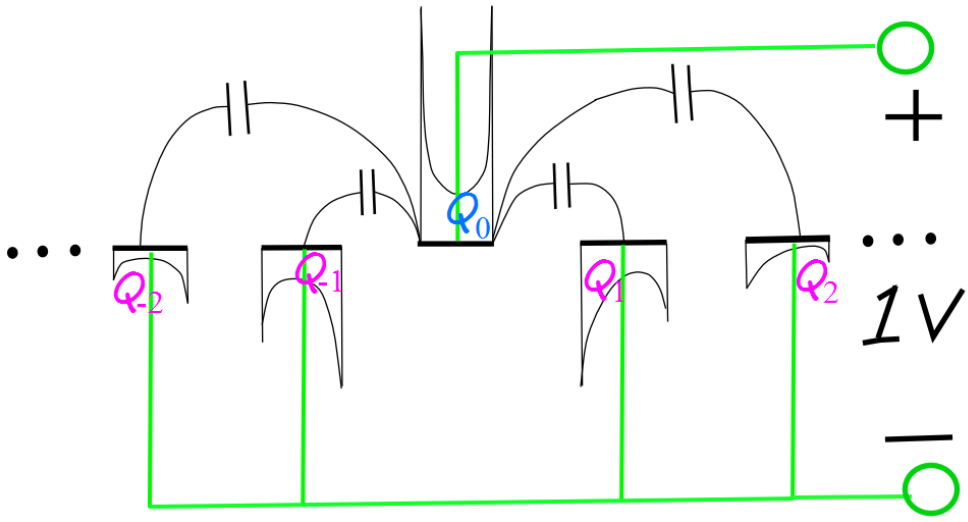

Figure G-3. Showing individual electrode capacitance and charge relationship.

The charge goes as:

$$Q_m = \frac{4\varepsilon_\infty}{\pi(1 - 4m^2)} \tag{G-8}$$

for m=1, 2, …, for a/p = .5. Therefore:

$$C_m = \frac{4\varepsilon_\infty}{\pi(1-4m^2)} \tag{G-9}$$

since $Q_m = C_m$ when $\Delta V = 1V$.

Now the capacitance is known. To find the charge distribution (meaning not the distribution within the electrode but the total charge on each electrode) for arbitrary voltages on the different electrodes—for example, for (+) voltages on more than 1 electrode—charge superposition can be used. That is, add charges with 1 voltage source at a time with the rest shorted. Or, one can solve equation $Q = C\Delta V$, taking into account all of the neighboring electrodes. This equation takes the form:

$$Q_i = \sum_{-nn}^{nn} C_k(v_i - v_{i-k}) = \sum_{-nn}^{nn} C_k \Delta v_{i-k} = \sum_{-nn}^{nn} C_k \Delta v_{i+k} \tag{G-10}$$

Where *nn* is the number of nearest neighbors included—*nn* electrodes to the left and *nn* electrodes to the right.

Consider the following structure with perfect conductor electrodes of equal electrode widths (f stands for floating electrode):

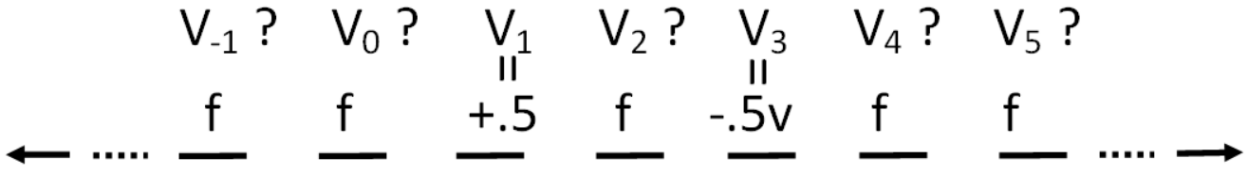

Figure G-4. Example structure for solving the equation Q=CV. Perfect conductor electrodes of equal electrode widths. Two electrodes have an applied static voltage, electrodes with an "f" are floating.

Voltages have been applied on electrodes 1 and 3. To find the charge on the non-floating electrodes, write equation G-10 for each electrode. Consider the approximation of only 2 nearest neighbors:

$$
\begin{aligned}
Q_1 &= C_{-2}(V_1 - V_{-1}) + C_{-1}(V_1 - V_0) + C_1(V_1 - V_2) + C_2(V_1 - V_3) \\
&= \underbrace{(C_{-2} + C_{-1} + C_1 + C_2)}_{C_0} V_1 - C_{-2}V_{-1} - C_{-1}V_0 - C_1V_2 - C_2V_3 \\
Q_1 &= -C_{-2}V_{-1} - C_{-1}V_0 + C_0V_1 - C_1V_2 - C_2V_3 \\
Q_2 &= -C_{-2}V_0 - C_{-1}V_1 + C_0V_2 - C_1V_3 - C_2V_4 \\
Q_3 &= -C_{-2}V_1 - C_{-1}V_2 + C_0V_3 - C_1V_4 - C_2V_5
\end{aligned}
\tag{G-11}
$$

The C_ks are given by equation G-9 for 50% a/p ratio, with k=m. The subscripts on C_m are relative to the current electrode being considered (-1 for 1st on the left, +1 for 1st on right and so on). The subscripts on v_i are fixed to the identity or global location of each electrode.

In matrix form:

$$
\begin{bmatrix} Q_1 \\ Q_2 \\ Q_3 \end{bmatrix} = \begin{bmatrix} -C_{-2} & -C_{-1} & C_0 & -C_1 & -C_2 & \\ & -C_{-2} & -C_{-1} & C_0 & -C_1 & -C_2 \\ & & -C_{-2} & -C_{-1} & C_0 & -C_1 & -C_2 \end{bmatrix} \begin{bmatrix} V_{-1} \\ V_0 \\ V_1 \\ V_2 \\ V_3 \\ V_4 \\ V_5 \end{bmatrix} \tag{G-12}
$$

All C_m's are known in the matrix. In the vectors, the unknowns are in red, the knowns are in blue. The charges on the floating electrodes are zero because there is no source to inject charges. There is a polarization of the charges on the floating metal electrode, but just as bound charges in the atoms in the dielectric between a capacitor are polarized and separated locally—charges may separate within the floating electrode—but the total charge within the floating electrode will be zero.

Back to the system of equations. There are more unknowns than the number of equations:

$$\begin{bmatrix} Q_1 \\ Q_2 \\ Q_3 \end{bmatrix} = \underbrace{\left[\begin{array}{cc:ccc:cc} -C_{-2} & -C_{-1} & C_0 & -C_1 & -C_2 & \square & \square \\ \square & -C_{-2} & -C_{-1} & C_0 & -C_1 & -C_2 & \square \\ \square & \square & -C_{-2} & -C_{-1} & C_0 & -C_1 & -C_2 \end{array}\right]}_{\text{discarded}\qquad\text{keep}\qquad\text{discarded}} \begin{bmatrix} V_1 \\ V_2 \\ V_3 \end{bmatrix} \quad \text{(G-13)}$$

After keeping the C-matrix within the dashed lines, 3 equations and 3 unknowns are left. The truncation will introduce end effect errors, but if it is desired to obtain the charge distribution of a cell that repeats, the error due to the end effects is quickly negligible after 1 or 2 cells into the structure. In general the matrix will have many more equations than nearest neighbors, so the lower left and top right areas will have zero entries, leaving most of the entries near the diagonal. Solving for unknowns in a linear system of equations is done in the form $b = Ax$, where b is a vector of knowns, and x is a vector of unkowns to be solved for. Writing the truncated system of equations gives:

$$\begin{array}{lll} & & \overbrace{\qquad}^{\text{knowns}} \quad \overbrace{\qquad}^{\text{unknowns}} \\ Q_1 = C_0V_1 - C_1V_2 - C_2V_3 & \Rightarrow & \overbrace{-C_0V_1 + C_2V_3}^{} = \overbrace{-Q_1 - C_1V_2}^{} \\ Q_2 = -C_{-1}V_1 + C_0V_2 - C_1V_3 & & Q_2 + C_{-1}V_1 + C_1V_3 = C_0V_2 \\ Q_3 = -C_{-2}V_1 - C_{-1}V_2 + C_0V_3 & & C_{-2}V_1 - C_0V_3 = -Q_3 - C_{-1}V_2 \end{array} \quad \text{(G-14)}$$

Currently there are unknowns in both the b and x vector. The charge $Q_2 = 0$ because it is a floating electrode. Grouping the knowns and the unknowns and setting up the equations in the solvable form of $b = Ax$ gives:

$$\underbrace{\begin{bmatrix} -C_0V_1 + C_2V_3 \\ C_{-1}V_1 + C_1V_3 \\ C_{-2}V_1 - C_0V_3 \end{bmatrix}}_{\text{b'}} = \underbrace{\begin{bmatrix} -1 & -C_1 & 0 \\ 0 & C_0 & 0 \\ 0 & -C_{-1} & -1 \end{bmatrix}}_{\text{A'}} \underbrace{\begin{bmatrix} Q_1 \\ V_2 \\ Q_3 \end{bmatrix}}_{\text{x'}} \quad \text{(G-15)}$$

The procedure for re-writing the matrix in the solvable form is as follows: (1) The column (j) of the original A matrix that contains a known voltage is multiplied by that known voltage and added to the b vector and removed from the A matrix. (2) A matrix column (j) that is removed is replaced by zeros and a (-1) on the A(j,j) entry. (3) The unknown Q is the new x vector multiplier on the column with zeros and a -1.

The new b'=A'x' system can be solved. Up to now the charges on the IDT electrodes were considered as total charge on the electrode, without regard for the distribution within the electrode. To obtain the shape of the charge distribution within the electrode and to be able to handle any electrode width and center location, the electrodes and free surface between electrodes is constructed by much smaller electrodes with a/p ratio = .5—the IDT structure is basically sampled. The IDT electrodes are sampled with small electrodes of a known voltage. The free surface is sampled by small floating electrodes where no external charge can be injected—so the charge on those electrodes is zero. The nearest neighbor electrode Q=CV analysis presented above is carried out with a large number of small electrodes to give the charge and voltage distribution in an arbitrary electrode configuration like that of the SPUDT.

The charge distribution for the EWC SPUDT has been calculated and is shown in Figure G-5. The end effects fade away within a couple of cells.

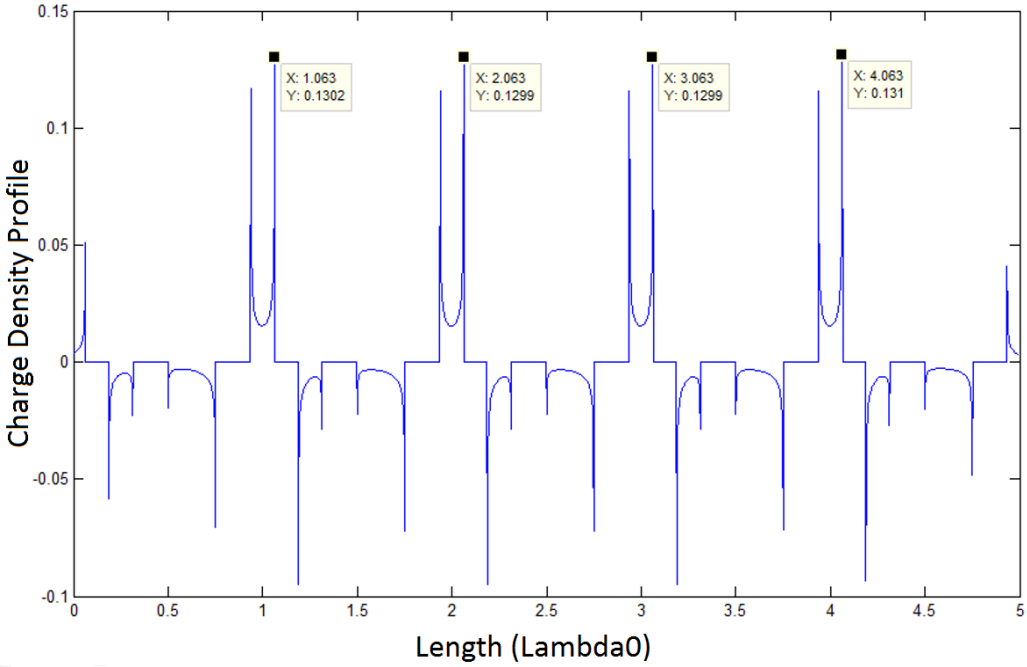

Figure G-5. Charge distribution calculation of EWC cells using Lentine's matrix method.

APPENDIX H:
DOUBLE TRANSIT ECHO CHARACTERISTICS OF 3rd HARMONIC SPUDT CELL

The purpose of this appendix is to show that for the same uniform SPUDT parameters, the echo suppression ability over the whole bandwidth diminishes with increasing transducer length. A DTE optimization has been run by modeling a uniform SPUDT of varying length and optimizing the load impedance to lower the DTE as much as possible over the entire bandwidth. The simulation uses the SPUDT COM model parameters in the first line of Figure 5-14 in chapter 5. The insertion loss of the main transit and the optimized DTE response is shown in Figure H-1.

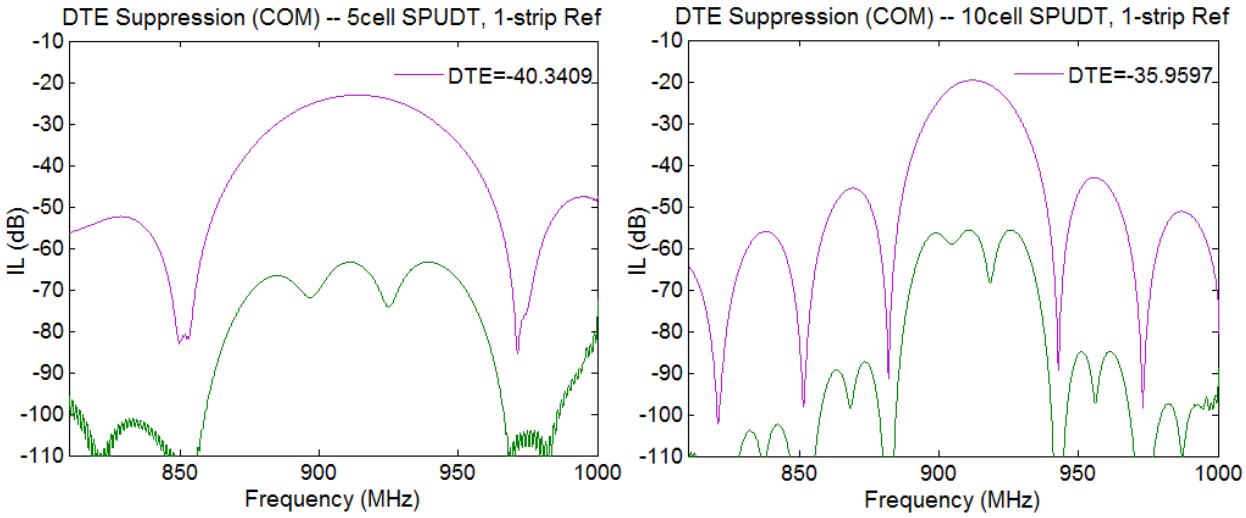

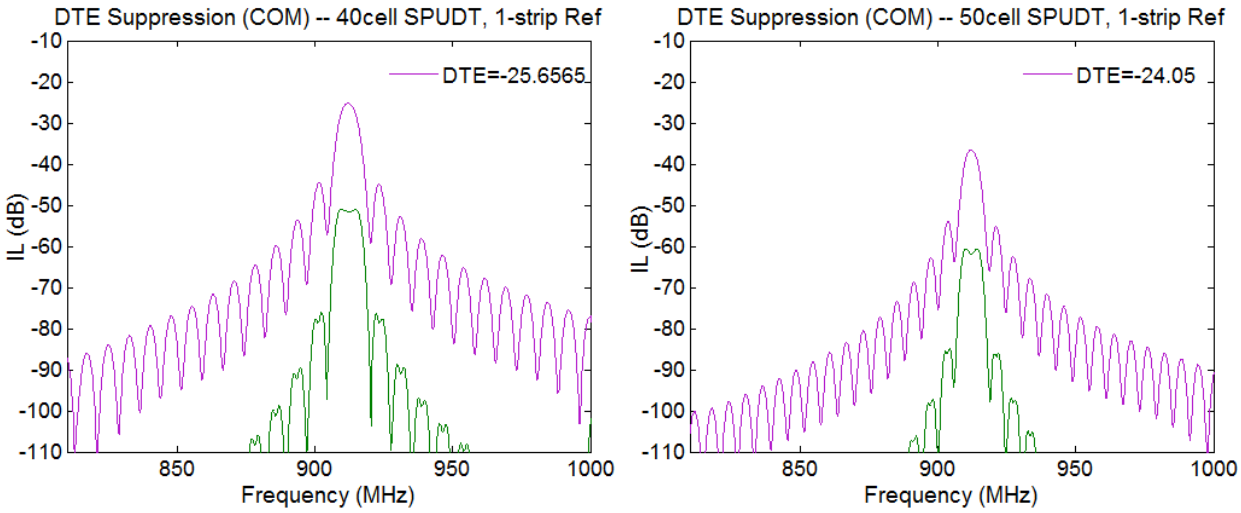

(e) (f)

Figure H-1. Optimized DTE suppression level as a function of transducer bandwidth. The reflector is a single strip with reflectivity of 1 in order to have a flat reflection coefficient over bandwidth. The echo suppression is optimized by forcing the maximum DTE echo level to be a slow as possible over the whole bandwidth. The ability to suppress the echo decreases with increasing number of cells. (a) 5 cells, (b) 10cells, (c) 20cells, (d) 30cells, (e) 40cells, (f) 50cells.

The simulation shows the reduced echo suppresison ability over the whole bandwidth as the number of cells in a uniform SPUDT are increased. Figure H-2 shows the S21 response of a fabricated SPUDT filter with 10cell transducers.

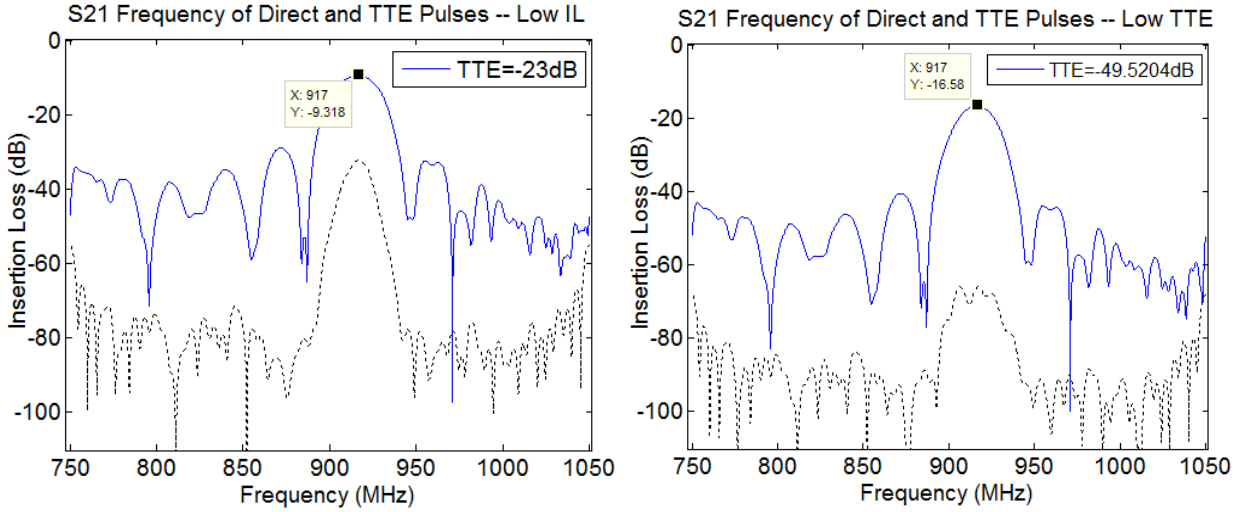

Figure H-2. S21 response of a fabricated optimized SPUDT device. This is a 10cell forward facing SPUDT filter of the same type and same wafer as the experimentally optimized device shown at the end of Appendix E. The post-processed matching is optimized for low insertion loss (left) and low DTE (right). The optimization is discussed in chapter 5.

APPENDIX I:
WIDEBAND UNIFORM SPUDT USING AN ALUMINUM NITRIDE GRATING FOR SUPER HIGH REFLECTIVITY

This appendix shows a type of SPUDT that uses a dielectric grating on top of the electrodes in order to shift the reflection center (RC) from the transduction center (RC). The work here was done in collaboration with Yuske Satoh and K. Yamanouchi. Satoh and Yamanouchi primarily used 128^0 YX lithium niobate substrate to make these type of devices. Normally the dielectric grating is made of SiO2 for devices working on 128^0 YX LN [94-96]. When attempting to use SiO2 grating material on the YZ LN substrate, the directionality was noticeably less. Yuske Satoh suggested using another grating material. Both tellurium oxide and aluminum nitride were considered. Tellurium oxide having a lower velocity than YZ LN, and aluminum nitride having a higher velocity than YZ LN. Because sputtering tellurium oxide can be problematic because of residue and dangers of injecting oxygen into a cryogenic pump, aluminum nitride was used. Both argon and nitrogen were injected in the sputtering chamber and an aluminum target was used. A sample grating is shown in Figure I-1.

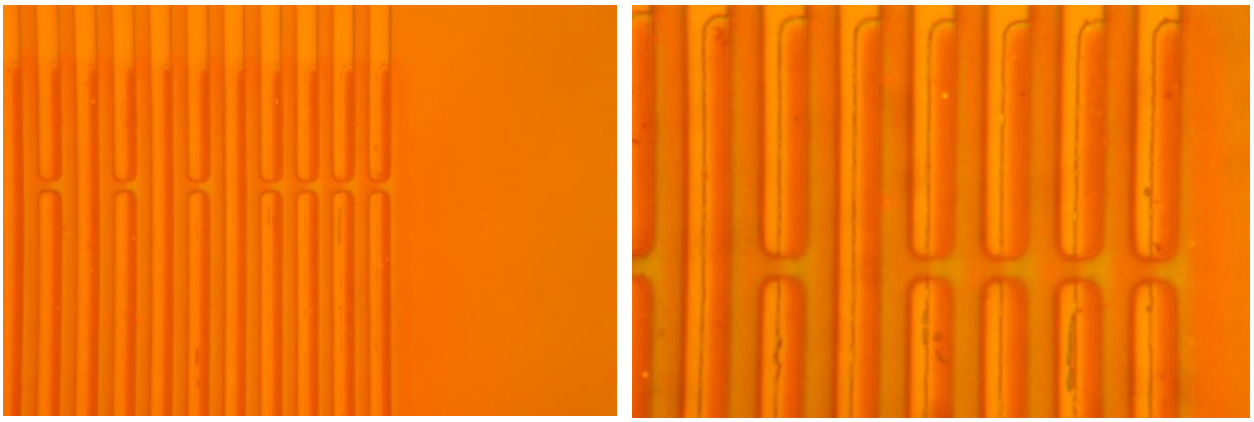

Figure I-1. Microscope picture of dielectric grating on top of transducer electrodes.

The dielectric was sputtered on top of the aluminum electrodes. The devices shown here will use a structure composed of a SPUDT in the middle of two wideband bidirectional IDTs (Figure I-2a). The SPUDT devices presented here have 5 pairs and are of the 2f0 type, using ¼ wavelength

electrodes (Figure I-2b). The bidirectional IDT's have 3 pairs of electrodes and are also of the 2f0 type, with no 2nd or 3rd harmonic operation. These devices are operating at 1st harmonic. The aperture has 50 wavelengths and the wavelength is 13.6144um. A picture of a test device mask layout is shown in Figure I-2.

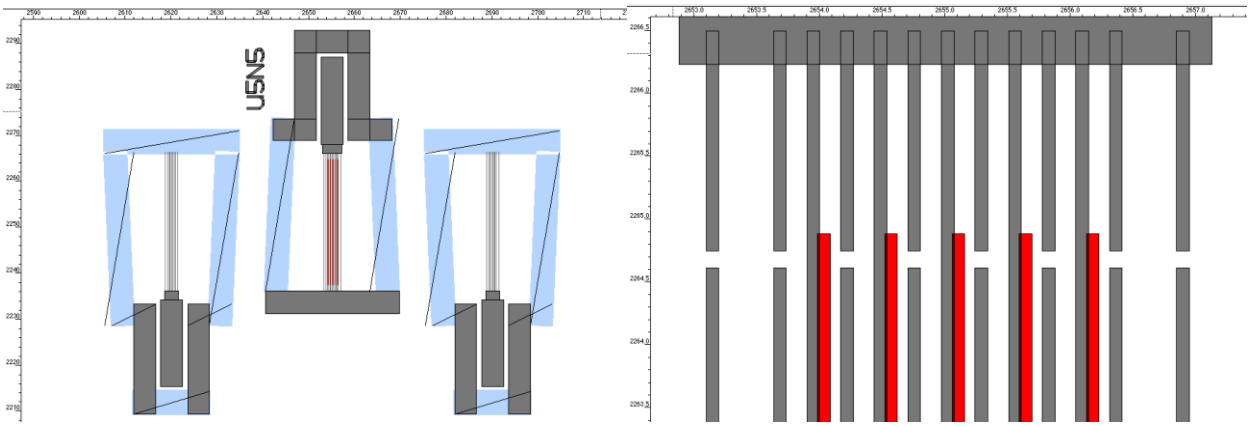

(a) (b)

Figure I-2. (a) Mask layout of test device with 3-pair 2f0 bidirectionals on both sides. (b) Mask layout of 5 pair SPUDT device showing the 2nd mask layer for the dielectric grating.

The devices require an alignment, which is quite difficult to obtain accurately. Because of this, 8 sets of these devices are made, all with different shifts of the grating. Grating location number 0, N0, corresponds to the grating being directly on top of the electrodes. Grating location number 7, N7, corresponds to the location where the grating is in the middle of the gap. The device shown in the mask layout has the grating at location N5. The name U5N5 in Figure I-2a means, unidirectional of 5 pairs, with grating shift of 5.

These are very small number of pairs, so a large reflectivity is necessary to obtain a substantial SPUDT effect. Fabricated device measurements shown here will use an aluminum nitride grating thickness of 11k angstroms and 15k angstroms. The 11kAng devices have a reflectivity of about 14 to 18%, as per the COM matching parameters. The devices with 15kAng have even stronger reflectivity. An 11kAng forward and reverse device set is shown first, with

COM simulation matching, in Figure I-3. The forward and reverse responses are from 2 distinct SPUDT devices.

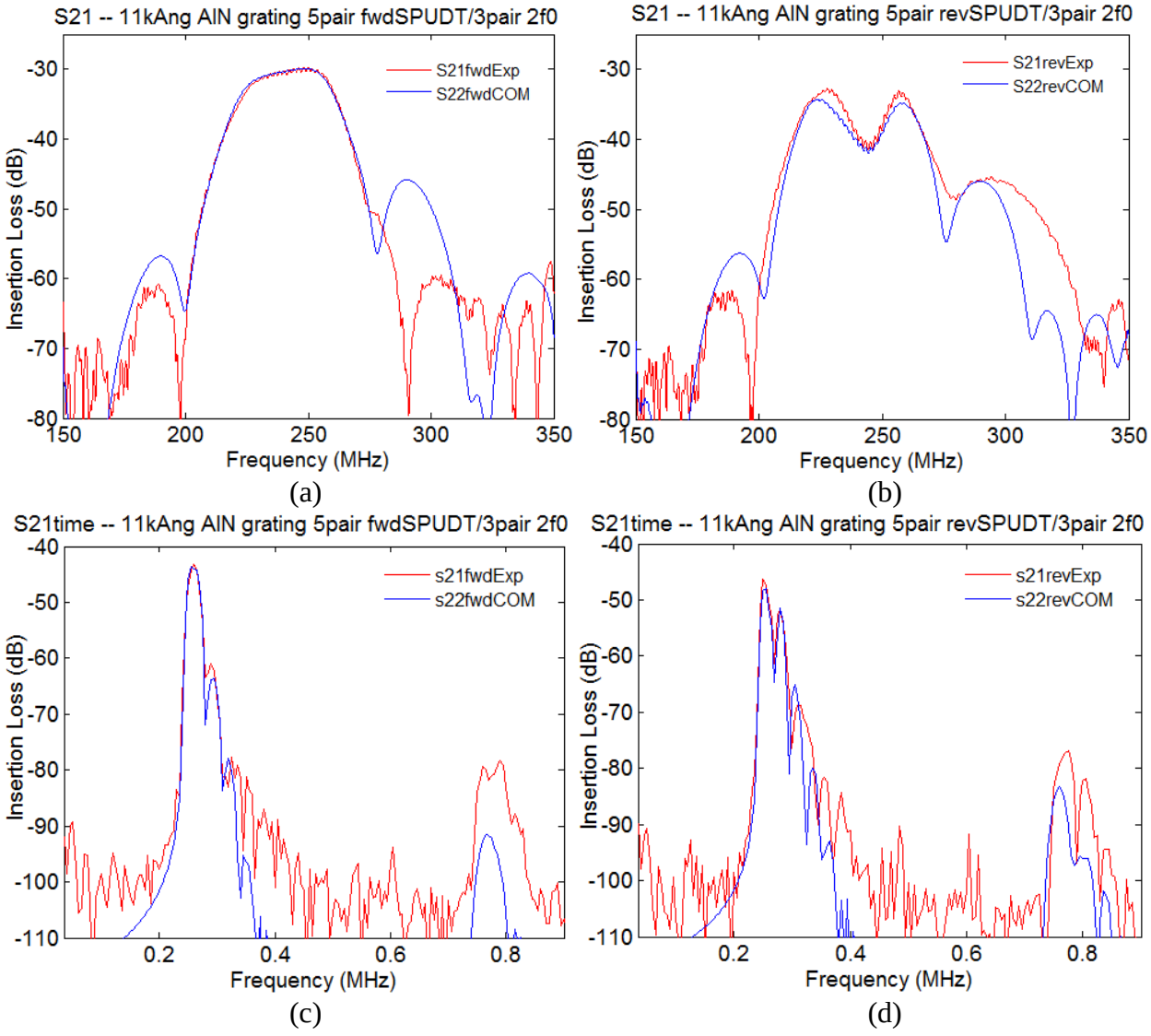

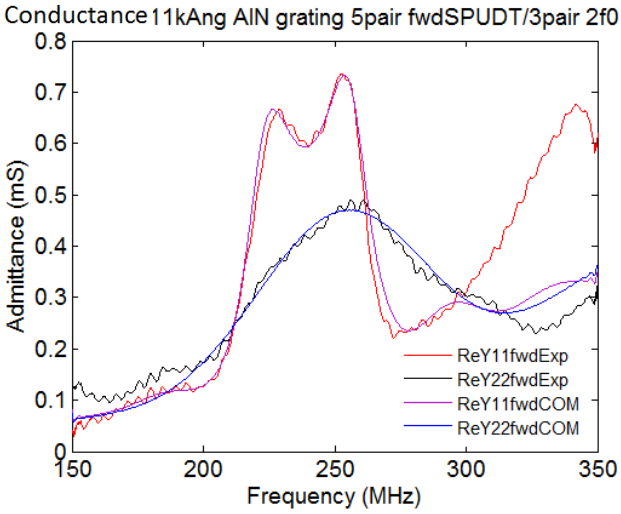
Conductance 11kAng AlN grating 5pair fwdSPUDT/3pair 2f0
Admittance (mS)
Frequency (MHz)
ReY11fwdExp
ReY22fwdExp
ReY11fwdCOM
ReY22fwdCOM

(e)

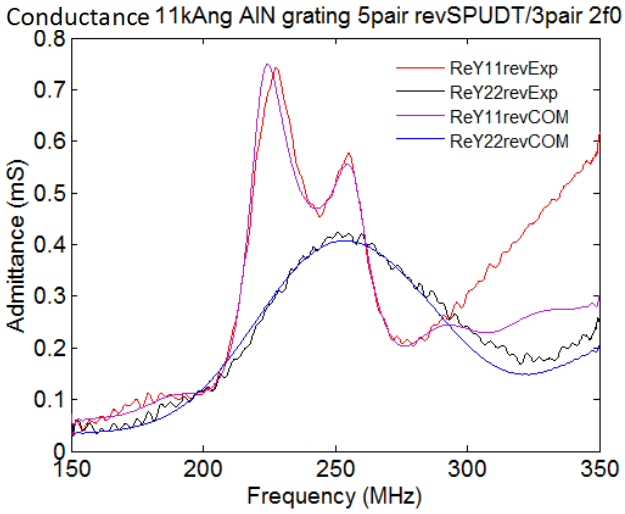
Conductance 11kAng AlN grating 5pair revSPUDT/3pair 2f0
Admittance (mS)
Frequency (MHz)
ReY11revExp
ReY22revExp
ReY11revCOM
ReY22revCOM

(f)

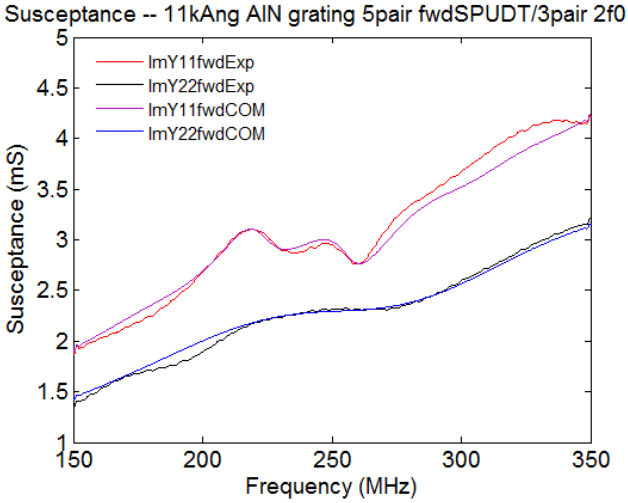
Susceptance -- 11kAng AlN grating 5pair fwdSPUDT/3pair 2f0
Susceptance (mS)
Frequency (MHz)
ImY11fwdExp
ImY22fwdExp
ImY11fwdCOM
ImY22fwdCOM

(g)

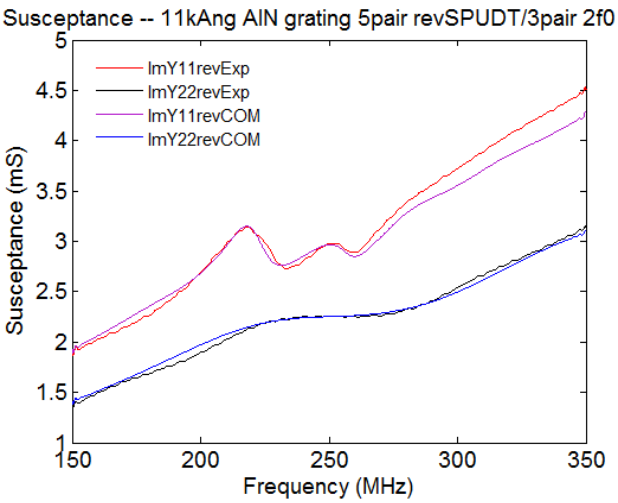
Susceptance -- 11kAng AlN grating 5pair revSPUDT/3pair 2f0
Susceptance (mS)
Frequency (MHz)
ImY11revExp
ImY22revExp
ImY11revCOM
ImY22revCOM

(h)

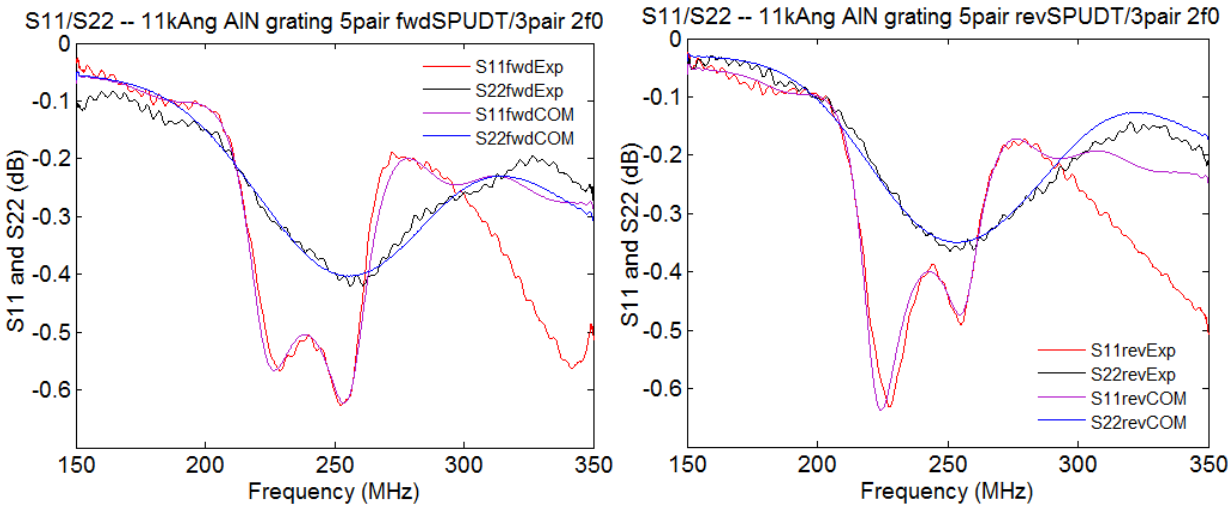

Figure I-3. Measured and COM simulated response for 5pair 11kAng SPUDT device. (a) Forward S21, (b) reverse S21, (c) forward S21 time, (d) reverse S21 time, (e) forward filter conductance, (f) reverse filter conductance, (g) forward filter susceptance, (h) reverse filter susceptance, (i) forward filter S11, (j) reverse filter S11.

The COM modeling parameters are given in Figure I-4. The parameters may not be phenomenologically accurate, the aim was only to match the measurement as best as possible with the model. The number of cells had to be increased by a factor, ScaleLength (SL), in order to achieve a good match. For this reason this factor is also included in the reflectivity and other parameters so that the number next to the factor might give a better estimate of the phenomenological quantity.

Table I-1. COM parameters for simulations of a 5 pair SPUDT using an 11kAng aluminum nitride grating.

Filter direction	Transducer Type	Harmonic	Length Scaling Factor (SL)	αSF	Cf	Rs	γLoss	|R|	ϕTCRC	Vidt
fwd	5pair 2f0 with AlN grat	1	1.25	1.5*1/SL	7.1584x10^-14	SL*1.2	3000*SL	.14/SL	80	3250
	3pair 2f0 bidirectional		1	1.5	2.859x10^-13	2	100	0.015	0	3300
rev	5pair 2f0 with AlN grat	1	1.35	1.5*1/SL	6.6281x10^-14	SL*1	3000*SL	.18/SL	60	3250
	3pair 2f0 bidirectional		1	1.55	2.7365x10^-13	1.1	100	0.015	0	3304

The 15kAng devices are also 5 pair devices. Three sets of filters will be shown, each with the AlN grating having a different shift.

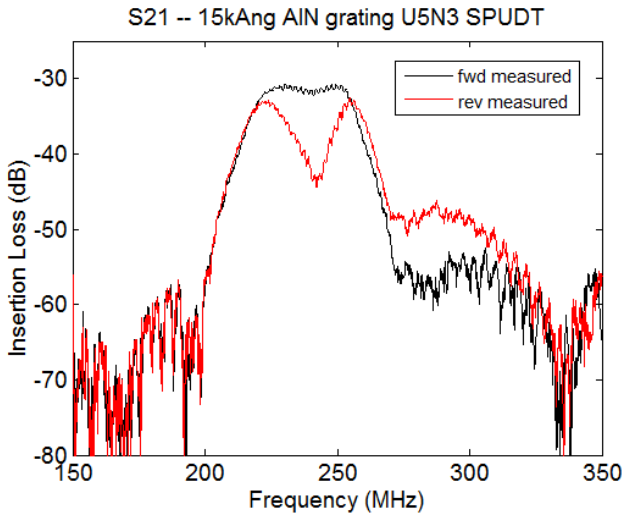
S21 -- 15kAng AlN grating U5N3 SPUDT
fwd measured
rev measured
Insertion Loss (dB)
Frequency (MHz)

(a)

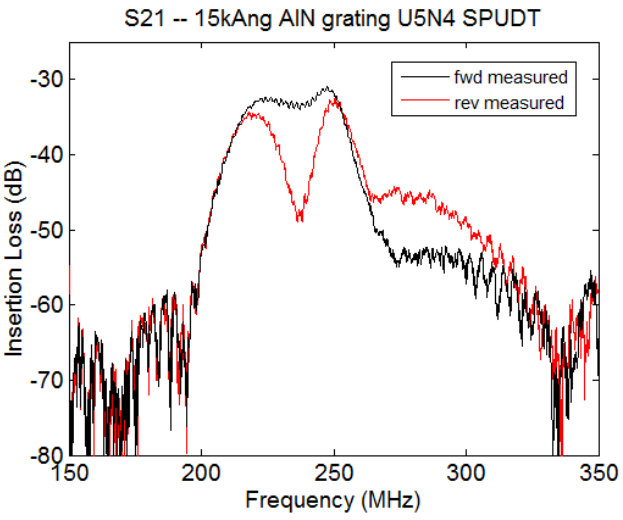
S21 -- 15kAng AlN grating U5N4 SPUDT
fwd measured
rev measured
Insertion Loss (dB)
Frequency (MHz)

(b)

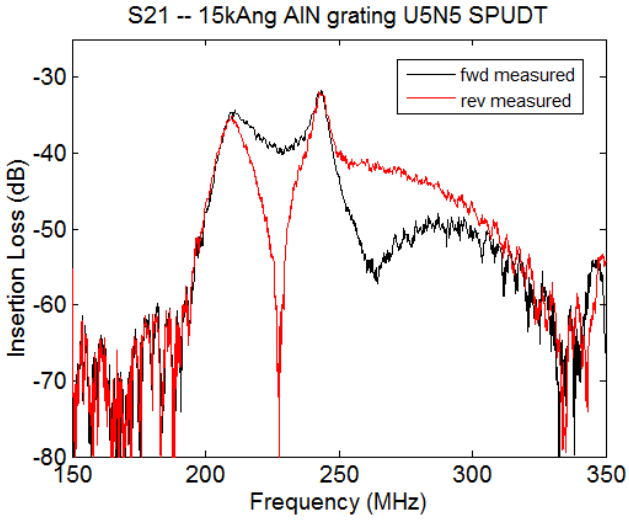
S21 -- 15kAng AlN grating U5N5 SPUDT
fwd measured
rev measured
Insertion Loss (dB)
Frequency (MHz)

(c)

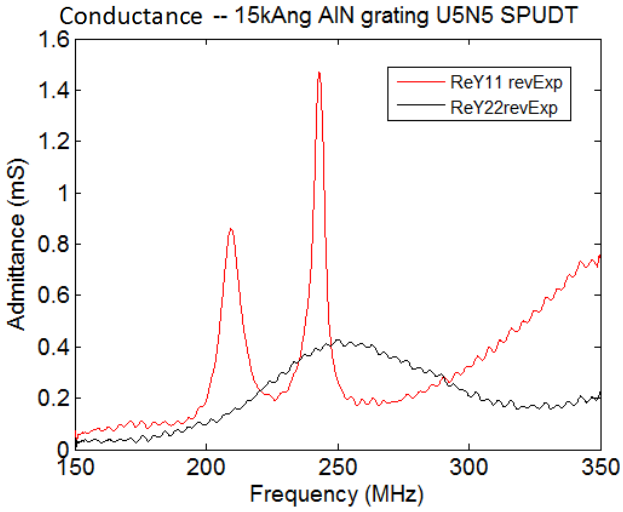
Conductance -- 15kAng AlN grating U5N5 SPUDT
ReY11 revExp
ReY22revExp
Admittance (mS)
Frequency (MHz)

(c)

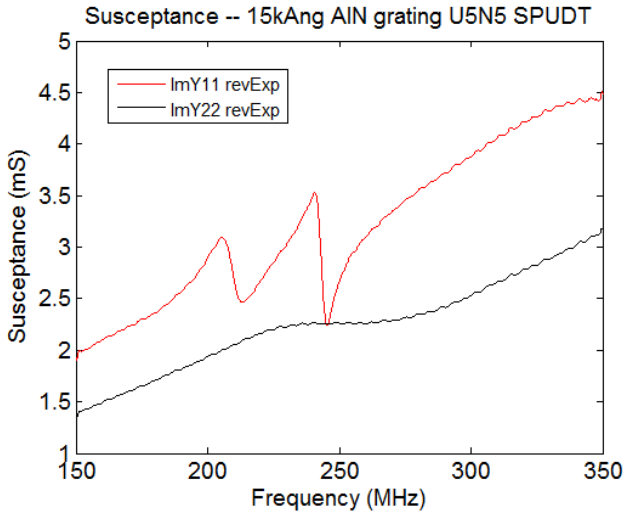

(d)

Figure I-4. Five pair, 15kAng SPUDT devices of different grating shifts. (a) S21 fwd and rev for grating shift N3, (b) S21 fwd and rev for grating shift N4, (c) S21 fwd and rev for grating shift N5. (c) Conductance of transducers in device U5N5, (d) susceptance of device U5N5. Device U5N5 may not be a practical device, but it is interesting to see almost perfect directionality (40dB) from the SPUDT effect with only 5 AlN reflector strips.

These devices may not be practical, but it is interesting to see what happens with very high reflectivity, approximately 10 times that of an aluminum electrode for the 11kAng grating devices.

REFERENCES

[1] B. A. Auld, *Acoustic fields and waves in solids*, 2 ed. Malabar, Florida: Krieger Publishing Company, 1990, p. 435.

[2] R. Varghese *et al.*, "Magnetostriction measurement in thin films using laser Doppler vibrometry," *Journal of Magnetism and Magnetic Materials*, vol. 363, pp. 179-187, 8// 2014.

[3] M. Penza and G. Cassano, "Relative humidity sensing by PVA-coated dual resonator SAW oscillator," *Sensors and Actuators B: Chemical*, vol. 68, no. 1–3, pp. 300-306, 8/25/ 2000.

[4] D. Puccio, D. C. Malocha, and N. Saldanha, "Multiple access SAW sensors using orthogonal frequency coding," in *IEEE Sensors, 2005.*, 2005, p. 4 pp.

[5] D. Malocha and B. Fisher, "Passive, wireless, surface acoustic wave identification tag with hydrogen gas sensor," ed: Google Patents, 2016.

[6] B. Fisher and D. Malocha, "Cryogenic liquid sensing using SAW devices," in *Frequency Control Symposium, 2007 Joint with the 21st European Frequency and Time Forum. IEEE International*, 2007, pp. 505-510: IEEE.

[7] D. C. Malocha, M. Gallagher, B. Fisher, J. Humphries, D. Gallagher, and N. Kozlovski, "A passive wireless multi-sensor SAW technology device and system perspectives," *Sensors*, vol. 13, no. 5, pp. 5897-5922, 2013.

[8] D. Puccio, "Design, analysis and implementation of orthogonal frequency coding in SAW devices used for spread spectrum tags and sensors," 2006.

[9] D. R. Gallagher, M. W. Gallagher, N. Saldanha, J. M. Pavlina, and D. C. Malocha, "Spread Spectrum Orthogonal Frequency Coded SAW Tags and Sensors Using Harmonic Operation," *IEEE Transactions on Microwave Theory and Techniques*, vol. 58, no. 3, pp. 674-679, 2010.

[10] N. Kozlovski, "Passive Wireless Saw Sensors With New And Novel Reflector Structures Design And Applications," 2011.

[11] N. Saldanha, "Modeling, design and fabrication of orthogonal and psuedo-orthogonal frequency coded SAW wireless spread spectrum RFID sensor tags," 2011.

[12] B. H. Fisher, *Surface acoustic wave (SAW) cryogenic liquid and hydrogen gas sensors. [electronic resource]*. Orlando, Fla. : University of Central Florida, 2012., 2012.

[13] D. Gallagher, "Ultra-wideband orthogonal frequency coded SAW correlators," 2007.

[14] M. Gallagher, "Design, Fabrication, and Interrogation of Integrated Wireless SAW Temperature Sensors," 2015.

[15] J. Humphries, "Passive, Wireless SAW OFC Strain Sensor and Software Defined Radio Interrogator," 2016.

[16] D. C. Malocha and C. D. Bishop, "The Classical Truncated Cosine Series Functions with Applications to SAW Filters," presented at the IEEE Transactions on Ultrasonics, Ferroelectrics, and Frequency Control, 1987.

[17] D. C. Malocha, D. Puccio, and D. Gallagher, "Orthogonal frequency coding for SAW device applications," in *IEEE Ultrasonics Symposium, 2004*, 2004, vol. 2, pp. 1082-1085 Vol.2.

[18] G. Ostermayer, A. Pohl, C. Hausleitner, L. Reindl, and F. Seifert, "CDMA for wireless SAW sensor applications," in *Spread Spectrum Techniques and Applications Proceedings, 1996., IEEE 4th International Symposium on*, 1996, vol. 2, pp. 795-799 vol.2.

[19] D. C. Malocha and M. Gallagher, "Coherent correlator multi-sensor receiver," in *2012 IEEE International Frequency Control Symposium Proceedings*, 2012, pp. 1-5.

[20] J. Kim, R. Luis, M. S. Smith, J. A. Figueroa, D. C. Malocha, and B. H. Nam, "Concrete temperature monitoring using passive wireless surface acoustic wave sensor system," *Sensors and Actuators A: Physical*, vol. 224, pp. 131-139, 2015.

[21] L. M. Rodriguez, D. R. Gallagher, M. W. Gallagher, B. H. Fisher, J. R. Humphries, and D. C. Malocha, "Wireless SAW Sensor Temperature Extraction Precision," *IEEE Sensors Journal*, vol. 14, no. 11, pp. 3830-3837, 2014.

[22] N. Y. Kozlovski, M. W. Gallagher, and D. C. Malocha, "SAW sensor correlator system performance parameters," in *2011 Joint Conference of the IEEE International Frequency Control and the European Frequency and Time Forum (FCS) Proceedings*, 2011, pp. 1-6.

[23] D. C. Malocha, B. Fisher, R. Youngquist, A. Weeks, and M. Gallagher, "Surface Acoustic Wave Pulsed-Correlator Transceiver for Aerospace Applications," *IEEE Sensors Journal*, vol. 14, no. 11, pp. 3775-3781, 2014.

[24] N. Y. Kozlovski and D. C. Malocha, "SAW passive wireless multi sensor system," in *2009 IEEE International Ultrasonics Symposium*, 2009, pp. 1541-1544.

[25] N. Saldanha, D. C. Malocha, and R. C. Youngquist, "Coherence multiplexed passive wireless SAW RFID tag system," in *2013 IEEE Topical Conference on Wireless Sensors and Sensor Networks (WiSNet)*, 2013, pp. 4-6.

[26] D. C. Malocha, J. Humphries, J. A. Figueroa, M. Lamothe, and A. Weeks, "915 MHz SAW wireless passive sensor system performance," in *2016 IEEE International Ultrasonics Symposium (IUS)*, 2016, pp. 1-4.

[27] M. W. Gallagher and D. C. Malocha, "Mixed orthogonal frequency coded SAW RFID tags," *IEEE Transactions on Ultrasonics, Ferroelectrics, and Frequency Control*, vol. 60, no. 3, pp. 596-602, 2013.

[28] N. Y. Kozlovski and D. C. Malocha, "SAW noise-like anti-collision code study," in *2009 IEEE International Frequency Control Symposium Joint with the 22nd European Frequency and Time forum*, 2009, pp. 616-621.

[29] D. C. Malocha *et al.*, "Orthogonal frequency coded SAW sensors and RFID design principles," in *2008 IEEE International Frequency Control Symposium*, 2008, pp. 278-283.

[30] D. R. Gallagher, N. Y. Kozlovski, and D. C. Malocha, "Ultra wide band communication systems using orthogonal frequency coded SAW correlators," in *2006 IEEE Ultrasonics Symposium*, 2006, pp. 1075-1078.

[31] D. R. Gallagher and D. C. Malocha, "Noise-like transducers for ultra wide band SAW correlators," in *2012 IEEE International Ultrasonics Symposium*, 2012, pp. 1774-1777.

[32] B. P. Abbott, *A coupling-of-modes model for saw transducers with arbitrary reflectivity weightin*. 1989., 1989.

[33] D. Malocha, "SAW reflective delay line multi-transit analysis," in *Frequency Control Symposium (IFCS), 2016 IEEE International*, 2016, pp. 1-4: IEEE.

[34] K.-y. Hashimoto and K.-Y. Hashimoto, *Surface acoustic wave devices in telecommunications*. Springer, 2000.
[35] H. Skeie and H. Engan, "Second-order effects in acoustic surface-wave filters: design methods," *Radio and Electronic Engineer*, vol. 46, no. 5, pp. 207-220, 1976.
[36] Y. Y. Chen, T. T. Wu, and K. T. Chang, "A COM Analysis of SAW Tags Operating at Harmonic Frequencies," in *2007 IEEE Ultrasonics Symposium Proceedings*, New York, NY, 2007, pp. 2347-2350.
[37] D. Gallagher, "Ultra-wideband Spread Spectrum Communications using Software Defined Radio and Surface Acoustic Wave Correlators," 2015.
[38] N. Saldanha and D. C. Malocha, "Improved reflectivity and velocity model for aluminum gratings on YZ LiNbO3," *IEEE Transactions on Ultrasonics, Ferroelectrics, and Frequency Control*, vol. 58, no. 4, pp. 798-807, 2011.
[39] C. Fu *et al.*, "Design and Implementation of 2.45 GHz Passive SAW Temperature Sensors with BPSK Coded RFID Configuration," *Sensors*, vol. 17, no. 8, p. 1849, 2017.
[40] D. Puccio, D. Malocha, and N. Saldanha, "Implementation of orthogonal frequency coded SAW devices using apodized reflectors," presented at the Proceedings of the 2005 IEEE International Frequency Control Symposium and Exposition, Vancouver, BC, 2005.
[41] N. Y. Kozlovski and D. C. Malocha, "SAW noise-like coded reflector structures," presented at the 2008 IEEE International Frequency Control Symposium, Honolulu, HI, 2008.
[42] P. Jankowski-Mihułowicz, G. Pitera, and M. Węglarski, "The impedance measurements problem in antennas for rfid technique," *Metrology and Measurement Systems*, vol. 21, no. 3, pp. 509-520, 2014.
[43] T. Koskinen, H. Rajagopalan, and Y. Rahmat-Samii, "Impedance measurements of various types of balanced antennas with the differential probe method," in *Antenna Technology, 2009. iWAT 2009. IEEE International Workshop on*, 2009, pp. 1-4: IEEE.
[44] S.-K. Kuo, S.-L. Chen, and C.-T. Lin, "An accurate method for impedance measurement of RFID tag antenna," *Progress In Electromagnetics Research*, vol. 83, pp. 93-106, 2008.
[45] R. Meys and F. Janssens, "Measuring the impedance of balanced antennas by an S-parameter method," *IEEE Antennas and Propagation Magazine*, vol. 40, no. 6, pp. 62-65, 1998.
[46] K. D. Palmer and M. W. van Rooyen, "Simple broadband measurements of balanced loads using a network analyzer," *IEEE Transactions on Instrumentation and Measurement*, vol. 55, no. 1, pp. 266-272, 2006.
[47] T. Sasamori, T. Tobana, and Y. Isota, "Input Impedance Measurement for Balanced Antenna by S-parameter Method."
[48] B. Wang, Y. Zhuang, X. Li, X. Ren, Z. Qi, and Y. Zhang, "A novel method for impedance measurement of balanced UHF RFID tag antennas," *Journal of Electromagnetic Waves and Applications*, vol. 28, no. 16, pp. 2059-2066, 2014.
[49] A. E. Abdulhadi and R. Abhari, "Tunable compact printed monopole antenna for passive UHF RFID tags," in *Proceedings of the 2012 IEEE International Symposium on Antennas and Propagation*, Chicago, IL, 2012, pp. 1-2.
[50] D. C. Malocha and B. J. Hunsinger, "Capacitive Tap Weighted SAW Transducers with Reduced Losses," presented at the 1977 Ultrasonics Symposium, Phoenix, AZ, USA, 1977.

[51] D. C. Malocha and B. J. Hunsinger, "Tuning of Group Type Unidirectional Transducers," *IEEE Transactions on Sonics and Ultrasonics*, vol. 26, no. 3, pp. 243-245, 1979.
[52] R. C. Rosenfeld, R. B. Brow, and C. S. Hartmann, "Unidirectional Acoustic Surface Wave Filters with 2 dB Insertion Loss," presented at the 1974 Ultrasonics Symposium, Milwaukee, WI, USA, 1974.
[53] K. Yamanouchi, F. M. Nyffeler, and K. Shibayama, "Low Insertion Loss Acoustic Surface Wave Filter Using Group-Type Unidirectional Interdigital Transducer," in *1975 Ultrasonics Symposium*, Los Angeles, CA, USA, 1975, pp. 317-321.
[54] G. Macchiarella and G. Viola, "Improved feed network for group-type unidirectional transducers," *Electronics Letters*, vol. 19, no. 17, pp. 680-681, 1983.
[55] H. Nogami, T. Shiba, Y. Noro, and A. Yuhara, "Design of phase shifters for a group type unidirectional transducer based on interaction analysis," presented at the IEEE 1991 Ultrasonics Symposium, Orlando, FL, 1991, 1991.
[56] K. Yamanouchi, J. K. Gautam, and T. Meguro, "New phase-shifting technique for group-type unidirectional transducers used in surface-acoustic-wave filters," *Electronics Letters*, vol. 19, no. 5, pp. 168-169, 1983.
[57] J. K. Gautam, T. Meguro, and K. Yamanouchi, "Low-loss unidirectional SAW filters using integrated microinductors," *Electronics Letters*, vol. 19, no. 20, pp. 858-860, 1983.
[58] S. M. Richie and D. C. Malocha, *Final report, three-phase unidirectional surface acoustic wave transducer and computer aided design implementation. principal investigators, Samuel M. Richie, Donald C. Malocha*. Orlando : Engineering and Industrial Experiment Station, College of Engineering, University of Central Florida, 1983., 1983.
[59] S. M. Richie, M. A. Belkerdid, and D. C. Malocha, "A General Analysis for SAW 3-Phase Unidirectional Transducers," presented at the 1983 Ultrasonics Symposium, Atlanta, GA, USA, 1983.
[60] J. K. Gautam, T. Meguro, and K. Yamanouchi, "1.03 GHz operation of a low-loss SAW filter using 3-phase unidirectional transducers with thin dielectric layered feed electrodes," *Electronics Letters*, vol. 19, no. 24, pp. 1042-1043, 1983.
[61] B. M. Cabalfin Santos, *SAW reflective transducers and antennas for orthogonal frequency coded SAW sensors. [electronic resource]*. Orlando, Fla. : University of Central Florida, 2009., 2009.
[62] D. Morgan, *Surface acoustic wave filters: With applications to electronic communications and signal processing*. Academic Press, 2010.
[63] V. M. Ristic, "Redefinition of the coupling coefficient for surface-acoustic-wave interdigital transducer," *Journal of Applied Physics*, vol. 49, pp. 5672-5678, 1978.
[64] V. M. Ristic, "Modeling of the Impulse Response in SAW Transducers," presented at the IEEE Transactions on Sonics and Ultrasonics, 1979.
[65] J. D. Galipeau, "Enhanced SPUDT cells for high coupling substrates," in *IEEE Ultrasonics Symposium, 2005.*, 2005, vol. 2, pp. 1052-1055.
[66] Y. Shui, J. M. Lin, H. Wu, N. Wang, and H. Chen, "Optimization of single-phase, unidirectional transducers using three fingers per period," *IEEE transactions on ultrasonics, ferroelectrics, and frequency control*, vol. 49, no. 12, pp. 1617-1621, 2002.

[67] P. Ventura, M. Solal, P. Dufilie, J. M. Hode, and F. Roux, "A new concept in SPUDT design: the RSPUDT (resonant SPUDT)," in *1994 Proceedings of IEEE Ultrasonics Symposium*, 1994, vol. 1, pp. 1-6 vol.1.

[68] P. V. Wright, "The Natural Single-Phase Unidirectional Transducer: A New Low-Loss SAW Transducer," in *IEEE 1985 Ultrasonics Symposium*, 1985, pp. 58-63.

[69] R. C. M. Li and J. Melngailis, "The Influence of Stored Energy at Step Discontinuities on the Behavior of Surface-Wave Gratings," *IEEE Transactions on Sonics and Ultrasonics*, vol. 22, no. 3, pp. 189-198, 1975.

[70] P. V. Wright, "Modeling and Experimental Measurements of the Reflection Properties of SAW Metallic Gratings," in *IEEE 1984 Ultrasonics Symposium*, 1984, pp. 54-63.

[71] N. Saldanha, D. Puccio, and D. C. Malocha, "Experimental Measurements and Modeling of Aluminum Reflection Gratings on YZ LiNbO3 for OFC SAW Sensors," in *2006 IEEE International Frequency Control Symposium and Exposition*, 2006, pp. 368-373.

[72] W. R. Smith, H. M. Gerard, J. H. Collins, T. M. Reeder, and H. J. Shaw, "Analysis of Interdigital Surface Wave Transducers by Use of an Equivalent Circuit Model," *IEEE Transactions on Microwave Theory and Techniques*, vol. 17, no. 11, pp. 856-864, 1969.

[73] G. Coquin and H. Tiersten, "Analysis of the excitation and detection of piezoelectric surface waves in quartz by means of surface electrodes," *The Journal of the Acoustical Society of America*, vol. 41, no. 4B, pp. 921-939, 1967.

[74] S. Datta and B. J. Hunsinger, "Redefined element factor for simplified i.d.t. design," *Electronics Letters*, vol. 14, no. 23, pp. 744-745, 1978.

[75] B. P. Abbott and C. S. Hartmann, "An efficient evaluation of the electrostatic fields in IDTs with periodic electrode sequences," in *1993 Proceedings IEEE Ultrasonics Symposium*, Baltimore, MD, 1993, vol. 1, pp. 157-160.

[76] S. V. Biryukov and V. G. Polevoi, "The electrostatic problem for the SAW interdigital transducers in an external electric field. I. A general solution for a limited number of electrodes," *IEEE Transactions on Ultrasonics, Ferroelectrics, and Frequency Control*, vol. 43, no. 6, pp. 1150-1159, 1996.

[77] S. V. Biryukov and V. G. Polevoi, "The electrostatic problem for the SAW interdigital transducers in an external electric field. II. Periodic structures," *IEEE Transactions on Ultrasonics, Ferroelectrics, and Frequency Control*, vol. 43, no. 6, pp. 1160-1170, 1996.

[78] S. Malocha and B. P. Abbott, "Calculation of COM parameters for an arbitrary IDT cell," in *2002 IEEE Ultrasonics Symposium, 2002. Proceedings.*, 2002, vol. 1, pp. 267-270 vol.1.

[79] C. S. Hartmann and B. P. Abbott, "Experimentally determining the transduction magnitude and phase and the reflection magnitude and phase of SAW SPUDT structures," presented at the IEEE Symposium on Ultrasonics, Honolulu, HI, 1990.

[80] V. PLESSKY and J. KOSKELA, "COUPLING-OF-MODES ANALYSIS OF SAW DEVICES," *International Journal of High Speed Electronics and Systems*, vol. 10, no. 04, pp. 867-947, 2000.

[81] C. S. Hartmann and B. P. Abbott, "A generalized impulse response model for SAW transducers including effects of electrode reflections," in *IEEE 1988 Ultrasonics Symposium Proceedings.*, 1988, pp. 29-34 vol.1.

[82] C. Hartmann and B. Abbott, "Experimentally determining the transduction magnitude and phase and the reflection magnitude and phase of SAW SPUDT structures," in *Ultrasonics Symposium, 1990. Proceedings., IEEE 1990*, 1990, pp. 37-42: IEEE.
[83] B. P. Abbott, C. S. Hartmann, and D. C. Malocha, "Transduction magnitude and phase for COM modeling of SAW devices," *IEEE Transactions on Ultrasonics, Ferroelectrics, and Frequency Control*, vol. 39, no. 1, pp. 54-60, 1992.
[84] D. P. Chen and H. A. Haus, "Analysis of Metal-Strip SAW Gratings and Transducers," *IEEE Transactions on Sonics and Ultrasonics*, vol. 32, no. 3, pp. 395-408, 1985.
[85] K. Ingebrigtsen, "Surface waves in piezoelectrics," *Journal of Applied Physics*, vol. 40, no. 7, pp. 2681-2686, 1969.
[86] K. Blotekjaer, K. A. Ingebrigtsen, and H. Skeie, "A method for analyzing waves in structures consisting of metal strips on dispersive media," *IEEE Transactions on Electron Devices*, vol. 20, no. 12, pp. 1133-1138, 1973.
[87] H. Bateman and A. Erdélyi, *Higher transcendental functions*. McGraw-Hill New York, 1953.
[88] S. Malocha, B. P. Abbott, C. Finch, E. B. Hamilton, and E. A. Halpern, "Accurate COM analysis for RSPUDT," in *IEEE Symposium on Ultrasonics, 2003*, 2003, vol. 2, pp. 1672-1675 Vol.2.
[89] J. C. Maxwell, *A treatise on electricity and magnetism*. Clarendon press, 1881.
[90] B. Auld and R. E. Green, "Acoustic Fields and Waves in Solids: Two Volumes," *Physics Today*, vol. 27, p. 63, 1974.
[91] B. P. Abbott, C. S. Hartmann, and D. C. Malocha, "A coupling-of-modes analysis of chirped transducers containing reflective electrode geometries," in *IEEE Ultrasonics Symposium*, 1989, vol. 1, pp. 129-134.
[92] K. M. Lakin, "Electrode Resistance Effects in Interdigital Transducers," *IEEE Transactions on Microwave Theory and Techniques*, vol. 22, no. 4, pp. 418-424, 1974.
[93] A. L. Lentine, S. Datta, and B. J. Hunsinger, "Charge Distribution for Non-Periodic Transducers Using a Circuit Model," presented at the 1979 Ultrasonics Symposium, New Orleans, LA, USA, 1979.
[94] Y. Satoh and K. Yamanouchi, "SAW unidirectional interdigital transducer with ultra-low insertion loss and wide band in 10MHZ-10GHZ range," in *Proceedings of the 2005 IEEE International Frequency Control Symposium and Exposition*, 2005, p. 3.
[95] K. Yamanouchi and Y. Satoh, "Unidirectional interdigital transducers and resonators using grating SAW substrates and application to low loss wide band filters," presented at the IEEE Symposium on Ultrasonics, 2003.
[96] Y. Satoh and K. Yamanouchi, "Phase linear flat wide band low loss filters using new configuration of unidirectional up-chirp and down-chirp dispersive inter digital transducers," presented at the 2009 IEEE International Ultrasonics Symposium, Rome, 2009.